PAUL UKPAAYEDO SUKPE

CRACK TIP CONSTRAINT IN TYPICAL HIGH STRENGTH STEEL COMPONENTS IN ARCTIC CONDITIONS

DEPARTMENT OF MECHANICAL AND AEROSPACE ENGINEERING

This thesis is submitted in partial fulfilment of the requirements for the degree of *Doctor of Philosophy*

July 2023

This page intentionally left blank

DEPARTMENT OF MECHANICAL AND AEROSPACE ENGINEERING

CRACK TIP CONSTRAINT IN TYPICAL HIGH STRENGTH STEEL COMPONENTS IN ARCTIC CONDITIONS

PAUL UKPAAYEDO SUKPE

This thesis is submitted in partial fulfilment of the requirements for the degree of *Doctor of Philosophy*

July 2023

ABSTRACT

Crack tip constraint is a significant issue in engineering components' design and repair decisions. The main reason is that the use of plane strain fracture toughness derived from deeply cracked and thick section specimens in structural integrity assessments is generally considered conservative. Generally, real components contain shallow cracks and thin sections that lead to significant variability in effective toughness due to loss of crack tip constraint. The overall objective of this research was therefore to develop test methods used in fracture assessment of high strength steel components operating in extreme low temperatures, by incorporating a reduction in the inherent conservatisms in assessment procedures, particularly BS 7910.

The work contained both experimental and numerical analyses of pin-loaded single edge notched tension (SENT) and three-point single edge notched bend (SENB) specimens at room and low (-120°C) temperatures under different constraint conditions. Finite element analyses (FEA) of steel pipelines containing surface flaws subjected to both internal pressure and bending were also conducted. Further, a method was proposed, based on the combined use of digital image correlation (DIC) to measure full-field displacements at room temperature and a finite element approach to extract the strain energy release rate of shallow cracks. A finite element model with imported DIC-measured full-field displacements acting as boundary conditions is solved and the *J*-integral was computed. Additional preliminary testing was carried out on aluminium 5083 coupons using X-ray computed tomography, intended for digital volume correlation (DVC) analysis.

The experimental and numerical results showed that a decrease in temperature leads to a reduction in fracture toughness and therefore, susceptibility to brittle failure. The numerical analyses also showed that loss of constraint in shallow and thin components can be quantified by a triaxiality parameter, *Q*, as characterised by the two-parameter fracture mechanics in terms of the *J*-*Q* locus. The DIC-FEA in this research forms a robust correlation of fracture conditions for the fracture specimens assessed. The enhanced toughness associated with constraint reduction using the constraint-modified failure assessment diagram (FAD) approach indicated an increased margin and allows realistic design and repair decision-making that can help prevent catastrophic failures.

DECLARATION

I hereby declare that the work presented in this thesis has not been submitted for any other degree or professional qualification, and that it is the result of my own independent work.

Paul Ukpaayedo Sukpe

Brunel University London, Uxbridge, 2023

LIST OF PUBLICATIONS/PRESENTATIONS

Oral presentations/Abstract publications

P. Sukpe, R. Vignjevic, K. Hughes and R. Kulka. "Crack tip constraint in typical high strength steel components in Arctic conditions: Literature review and experimental methods/PhD methodology", National Structural Integrity Research Centre, NSIRC Research and Innovation Conference proceedings/presentation, Cambridge, UK, 8th – 9th September 2021.

P. Sukpe, R. Vignjevic, K. Hughes and R. Kulka. "Crack tip constraint in typical high strength steel components in Arctic conditions: Experimental and numerical investigation", National Structural Integrity Research Centre, NSIRC Research and Innovation Conference proceedings/presentation, Cambridge, UK, 21st - 22nd July 2022.

P. Sukpe, R. Vignjevic, K. Hughes and R. Kulka. "Constraint-based failure assessment diagram for fracture assessment of API 5L X65 steel grade pipe at low temperature", Science, Technology and Engineering Conferences (STECONF) – World Conference in Mechanical Engineering, Berlin, Germany, 9th – 11th December 2022.

ACKNOWLEDGEMENTS

This work was made possible by sponsorship and support from Lloyd's Register Foundation. The Foundation helps to protect life and property by supporting engineering-related education, public engagement and the application of research. www.lrfoundation.org.uk. The research was enabled and undertaken at the National Structural Integrity Research Centre (NSIRC), a postgraduate state-of-the-art facility in structural integrity established in collaboration with Brunel University London and managed by TWI Ltd as well as through a network of selected UK and international universities.

I would like to extend my profound gratitude to my supervisors, Prof Rade Vignjevic, Dr Kevin Hughes and Dr Rob Kulka for their immense support, encouragement and patience over the course of my PhD. I am extremely grateful to my mentor, Dr Li Xu at Lloyd's Register Foundation who helped with the test material selection. Special thanks to the invaluable team at NSIRC, especially Hannah Stedman and James Brookman. I am also grateful for the support I received from Dr Yin Jin Janin and the laboratory team at TWI Ltd in carrying out my experimental work.

Last but not the least, I am most grateful to my family and friends, especially Dr Joseph Sukpen for the support and encouragement not to give up in the most difficult times that I nearly gave up when my daughter passed away in November 2020.

DEDICATION

To my parents, I have nothing but gratitude to you. My children, Maximilian and late Maya.

TABLE OF CONTENTS

LIST OF FIGURES

LIST OF TABLES

LIST OF TABLES FOR APPENDICES

NOMENCLATURE

Abbreviations

AB	Arc-shaped bend
API	American Petroleum Institute
ASME	American Society of Mechanical Engineers
ASTM	American Society for Testing and Materials
AT	Arc-shaped tension
BCC	Body centred cubic
BS	British Standard
CCT	Centre-Cracked Plate
CMOD	Crack Mouth Opening Displacement
CT	Compact Tension
CTOD	Crack Tip Opening Displacement
CVN	Charpy V-Notch
DBT	Ductile-to-brittle transition
DIC	Digital Image Correlation
DVC	Digital Volume Correlation
ECA	Engineering Critical Assessment
EDM	Electron Discharge Machining
EPFM	Elastic-Plastic Fracture Mechanics
FAD	Failure Assessment Diagram
FAC/FAL	Failure Assessment Curve/Line
FCC	Face centred cubic
FE	Finite Element
FEA	Finite Element Analysis
FFS	Fitness-For-Service
FGSS	Fuel gas supply systems
FSRU	Floating storage regasification units

HRR	Hutchinson-Rice-Rosengren
HSS	High strength steel
ID	Inside/Internal Diameter
ISO	International Organisation for Standardisation
LEFM	Linear Elastic Fracture Mechanics
LNG	Liquefied natural gas
LNGC	Liquefied natural gas carriers
LSY	Large-Scale Yielding
MBL	Modified Boundary Layer
MC	Master curve
MT	Middle-cracked tension
OD	Outside Diameter
OM	Optical microscope
SEM	Scanning Electron Microscope
SENB	Single Edge Notched Bend
SENT	Single Edge Notched Tension
SG	Strain Gauge
SIF	Stress Intensity Factor
SSY	Small-Scale Yielding
TMCP	Thermomechanical controlled process
TPFM	Two-parameter fracture mechanics
TWI	The Welding Institute
UTS	Ultimate Tensile Strength
YS	Yield Strength
XCT	X-ray computed tomography

Greek/Latin Symbols

$\tilde{\sigma}_{ij}$ and $\tilde{\varepsilon}_{ij}$	Dimensionless functions in HRR formulation
I_n	Integration constant that depends on $\tilde{\sigma}_{ij}$ and $\tilde{\varepsilon}_{ij}$
r_p	Plastic zone size
T_i	Traction Vector
ε_{ij}	Strain tensor
E'	Young modulus in plane strain
J_{el}	Elastic component of J
J_{pl}	Plastic component of J
J_{tot}	Total or elastic-plastic J
K_I	Mode I stress intensity factor
K_{II}	Mode II stress intensity factor
K_{III}	Mode III stress intensity factor
K_{eff}	Effective stress intensity factor
K_{mat}	Material fracture toughness measured by stress intensity factor
K_r	Fracture ratio of applied K and K_{mat}
L_r	Load ratio
r	the distance from the crack tip
T_Z	Out-of-plane constraint parameter
V_{p1} and V_{p2}	plastic parts of the clip gauge displacements of the knife heights of Z_1 and Z_2
Z_1 and Z_2	clip gauge displacements of the knife heights
a_0	Initial crack length
a_{eff}	Effective crack length
b_0/b	Uncracked ligament

u_i	Component of displacement vector T_i
δ_{ij}	Kronecker delta
ε_0	Reference strain
η_p	dimensionless function of geometry
σ_0	Normalising or Yield stress
$\sigma_{0.2}$	0.2% proof stress on true stress-strain curve
σ_{hoop}	Hoop stress induced by internal pressure in a pipe
σ_F	Flow stress
σ_Y	Yield stress
σ_{YS}	Yield stress
σ_{ij}	Stress tensor
σ_{ref}	Reference stress
$\sigma_{\theta\theta}$	Tangential component of crack tip in polar coordinate system
Π	Potential energy
B	Thickness of specimen
E	Total energy
E	Young's modulus in plane stress
E'	Young's modulus in plane strain
e	Engineering strain
G	Energy release rate
J	J-integral
J	Joules/unit of energy
K	Stress intensity factor
n	Strain hardening exponent
P	Applied load
P	Internal pressure
P_L	Limit Load
Q	Elastic-plastic constraint parameter

R	Radius of pipe
T	Elastic constraint parameter/T-stress
t	Thickness of pipe
U	Strain energy
W	Width of specimen
δ	Crack tip opening displacement
Γ	Arbitrary contour around the crack
Y	Shape factor
a	Crack length
α	Ramberg-Osgood fitting parameter
β	Biaxiality ratio
β	Normalised structural constraint parameter
θ	Angular position ahead of the crack tip in polar coordinate system
ν	Poisson's ratio
σ	Stress

1 Introduction

1.1 Background

This research work presents an important area of study that focuses on understanding the behaviour of cracks in high strength steel structures operating in extreme cold environments. The use of plane strain fracture toughness derived from deeply cracked and thick section specimens in structural integrity assessments is generally considered conservative. However, real components contain shallow cracks and thin sections that lead to significant variability in effective toughness due to loss of crack tip constraint. Moreover, in Arctic environments, structures and components face unique challenges due to extreme low temperatures, cyclic loading, the presence of ice/snow and corrosive agents. These conditions can significantly influence the crack growth behaviour and fracture toughness of high strength steels, leading to potential structural failures [1], [2]. Therefore, understanding and managing crack tip constraint is crucial for ensuring the structural integrity and reliability of high strength steel components in these harsh conditions.

High strength steels are commonly used in Arctic and other engineering applications due to their excellent mechanical properties, including high strength and toughness. However, the behaviour of these materials near the crack tip, where stress concentrations are highest, can significantly impact their resistance to crack growth and failure. Crack tip constraint, refers to the effect of local stresses and strain fields near the crack tip [3]. It is essential for accurately assessing the risk of crack propagation and the overall fracture behaviour of a material to ensure its safe operation in Arctic environments. Low temperatures in the Arctic can affect the mechanical properties of high strength steels. For instance, cold temperatures can reduce the ductility and fracture toughness of the material, making it more susceptible to brittle fracture. Additionally, temperature gradients within structures can affect the distribution of stresses near the crack tip, affecting the crack tip constraint and potentially influencing crack growth rates.

Further, environmental factors specific to Arctic conditions, such as ice loading, thermal cycling and the presence corrosive agents, can also impact crack tip constraint. Ice-induced loads, which can result from impact or interaction between ice and structures, introduces additional stresses and strain rates near crack tips, thereby affecting the crack propagation path. Thermal cycling due to temperature variations can result in fatigue and cyclic loading effects on crack growth. Corrosive agents such as saltwater or freezing and thawing cycles, can accelerate crack propagation and reduce the structural integrity of high strength steel components [2].

To ensure the reliability and safety of high strength steel structures in Arctic environments, it is necessary to study and quantify the effects of crack tip constraint under these unique conditions. This involves conducting experimental investigations to characterise the mechanical properties of high strength steels at low temperatures, as well as evaluating the influence of temperature gradients, environmental factors and microstructural features on crack tip constraint. Advanced numerical modelling techniques can also be employed to simulate crack behaviour and predict crack growth rates in low temperature conditions.

By gaining a comprehensive understanding of crack tip constraint in high strength steel components in Arctic conditions, engineers and researchers can develop more accurate assessment methodologies, design guidelines and mitigation strategies. These efforts aim to enhance the structural integrity and reliability of high strength steel structures operating in the challenging Arctic environment, ensuring their safe operation and minimising the risk of catastrophic failures. This research conducts experimental and numerical investigations on pin-loaded single edge notched tension (SENT) and three-point single edge notched bend (SENB) specimens to characterise the influence of temperature and fracture toughness on crack tip constraint. Plane-strain and 3D finite element computations are conducted for SENB and SENT specimens having different crack lengths (a) to specimen width (W) ratio in the range $0.1 \leq a/W \leq 0.5$. Finite element analyses (FEA) of steel pipelines containing surface flaws subjected to both internal pressure and bending were also conducted. Further, a novel method was proposed, based on the conjoint use of digital image correlation (DIC) to measure full-field displacements at room temperature and a finite element approach to extract the strain energy release rate of shallow cracks. A finite element model with imported DIC-measured full-field displacements acting as boundary conditions is solved and the *J*-integral was calculated. Additional testing was carried out on aluminium 5083 coupons using X-ray computed tomography (XCT), intended for digital volume correlation (DVC) analysis. This was aimed at extending the DIC two-dimensional surface measurements to three-dimensional volumetric measurements to study the through-thickness effects.

One aspect of this research was to provide a form of refinement to the inherent conservatism in structural integrity codes and standards, particularly improvement to BS 7910 Annex N on constraint assessment. The methods developed for the base metal should also be applicable to welds (with suitable corrections for the crack driving force applied as part of a defect tolerance analysis). Suitable guidance should be developed such that it can be incorporated into the existing

fracture mechanics assessment procedures (primarily, BS 7910) to justify the selection of a suitable test specimen for cracked pipes.

1.2 Challenges and industry Gap

The research topic is an area of ongoing research and faces several industry challenges and gaps. Here are some current challenges and gaps in this field:

Lack of Experimental Data: One significant challenge is the limited availability of experimental data specifically focused on crack tip constraint in high strength steel components under low temperature conditions. Arctic environments pose unique challenges, including low temperatures, cyclic loading and the presence of ice and snow. More experimental studies are needed to understand the behaviour of high strength steel components in these extreme conditions and quantify crack tip constraint effects.

Material Characterisation: High strength steels are commonly used in Arctic applications due to their superior mechanical properties. However, there is a need for comprehensive material characterisation, including fracture toughness and crack growth data, specifically tailored for high strength steels under Arctic conditions. Obtaining accurate material properties is crucial for reliable crack tip constraint assessment.

Modelling Crack Tip Constraint: Developing accurate and robust numerical models to simulate crack tip constraint in high strength steel components in Arctic conditions is a research gap. Modelling crack tip constraint requires consideration of various factors, including stress triaxiality, constraint loss due to low temperatures and the influence of microstructural features. Improved modelling techniques are necessary to predict crack growth behaviour and evaluate the structural integrity of components in Arctic environments.

Addressing these industry challenges and research gaps will contribute to a better understanding of crack tip constraint in high strength steel components under Arctic conditions. It will also aid in the development of improved design guidelines, assessment methodologies and mitigation strategies to ensure the integrity and reliability of structures operating in Arctic environments. Though there are several industry challenges to the topic as outlined above, this research will cover the aspect of experimental and numerical modelling to provide data for the treatment of constraint effects in high strength steel components used in Arctic environments. This is aimed at bridging the gap in the so-called constraint-matching approach such that the transferability of fracture toughness data obtained from a laboratory specimen to an actual structural component becomes less of an issue in defect assessment procedures, e.g., BS 7910.

1.3 Research Aims and Objectives

The significant petroleum reserves in the Arctic region in recent years has necessitated oil and gas companies to expand their activities further North. This results in the design of offshore facilities made of ferritic structural steels with the aim to withstand lower temperatures. However, as most structural materials have varying mechanical behaviour in such low temperatures, this must be accounted for during the design and construction stage to avoid accidents related to structural failure. In real structures, there is variability in effective fracture toughness due to structural geometry, crack size and the effect of constraint.

The main research aim is to investigate the effects of crack tip constraint on fracture toughness by incorporating a reduction in the inherent conservatisms in current assessment procedures. An intended outcome from this research is to provide recommendations to improve the BS 7910 procedure, enabling more cost-effective design and accurate analysis of steel structures operating in low temperature environments.

The research aim would be achieved through the following objectives:

1. To conduct and analyse experimental fracture tests on different geometries, with varying loading and crack tip constraint conditions of API 5L X65 steel under low (-120°C) and room temperatures.
    - Perform comprehensive material testing to determine fracture toughness, tensile properties and other mechanical properties at low (-120°C) and room temperatures. These include round bar and flat tensile specimens, SENB and SENT with DIC measurements at room temperature for enhanced determination of *J*-integral and aluminium specimens with XCT/ DVC.
    - Investigate the influence of low temperature and crack tip constraint on fracture toughness in the API 5L X65 steel grade.
    - Establish a database of material properties specifically tailored for the API 5L X65 steel grade in low temperature environments.
2. Develop numerical models to quantify crack tip constraint conditions within the API 5L X65 steel grade at low and room temperatures for SENB, SENT and cracked pipe
    - Relate the constraint results from the numerical models to experimental fracture toughness tests (i.e. SENB and SENT).
    - Constraint matching procedure using the constraint parameter, Q, to relate the same levels of constraint for the SENB, SENT and cracked pipe. That is, as long as any of the fracture

specimens (SENB, SENT) has the same level of constraint as the flawed pipe, it is deemed suitable for engineering critical assessments (ECAs) of real structural pipelines.

1.4 Research impact

The outcome from this research has several significant impacts:

Improved Structural Integrity: Understanding crack tip constraint in high strength steel components operating in Arctic environments can lead to improved structural integrity. By considering the effects of temperature, environmental factors and material properties on crack growth behaviour, engineers and designers can make more accurate assessments of the risk of failure. This knowledge can guide the development of design guidelines and maintenance strategies to ensure the safe operation of structures in Arctic conditions. The novel DIC-FEA methodology adopted in this research provided good agreement between the experimentally determined J values and those obtained from this new approach. This gives confidence in the results and engineers can rely on the analyses carried out in this research for defect assessments.

Enhanced Material Selection and Design: One area of this research is to investigate where it is that we overdesign by testing thin-walled and shallow cracked specimens. Research on crack tip constraint can contribute to the development of advanced high strength steels specifically tailored for Arctic environments. By characterising the material properties under low temperatures and investigating the effects of constraint on fracture toughness, researchers can identify steel compositions and processing techniques that enhance crack resistance and mitigate the impact of crack tip constraint. One can use the knowledge of the experimental specimens explored in this research as a guide for material selection and design decisions for components operating in Arctic conditions, leading to more reliable and durable structures.

Safer Arctic Operations: Low temperature environments present unique challenges for industries such as oil and gas, shipping and infrastructure development. Research on crack tip constraint can help mitigate the risk of structural failures in these sectors. By understanding the factors influencing crack growth in high strength steel components, industry stakeholders can develop appropriate inspection and maintenance protocols, implement structural health monitoring systems and adopt effective mitigation strategies. This ultimately contributes to safer operations and reduced downtime in Arctic conditions.

Environmental Sustainability: Arctic environments are ecologically sensitive, and the impact of structural failures can be detrimental to the delicate ecosystems. By ensuring the structural integrity of high strength steel components in Arctic conditions, research on crack tip constraint in this work can contribute to environmental sustainability. Reliable structures reduce the risk of

spills, leaks and other environmental hazards, minimising the ecological impact of industrial operations in the Arctic region.

Technological Advancements: Exploring crack tip constraint in high strength steel components in Arctic conditions requires advancements in materials testing, numerical modelling and structural health monitoring techniques. The work carried out for this research can be referred to for the development of novel testing methods capable of characterising material behaviour at low temperatures, the improvement of numerical models to accurately simulate crack growth under Arctic conditions and the innovation of advanced monitoring systems for real-time assessment of crack propagation. These technological advancements have broader applications beyond Arctic environments and can benefit other industries and research fields.

In summary, this research has the potential to improve on several aspects when assessing structural integrity, including material selection, operational safety, environmental sustainability and technological advancements. By addressing the unique challenges posed by Arctic environments, this research contributes to safer and more sustainable operations in these extreme conditions while advancing knowledge and innovation in the field of structural engineering.

These are particularly relevant to Lloyd's Register Foundation's vision on "engineering a safer world". Therefore, the results of this work would be considered by Lloyd's Register Foundation and inform the refinement of BS 7910 assessment procedure. Once the analyses approach for the fracture specimens are approved by the BS 7910 assessment committee, it can be incorporated and utilised by industry operators for defect assessment and failure prediction.

1.5 Summary of Methodology

A summary of the methodology used in this work is shown in Figure 1.1.

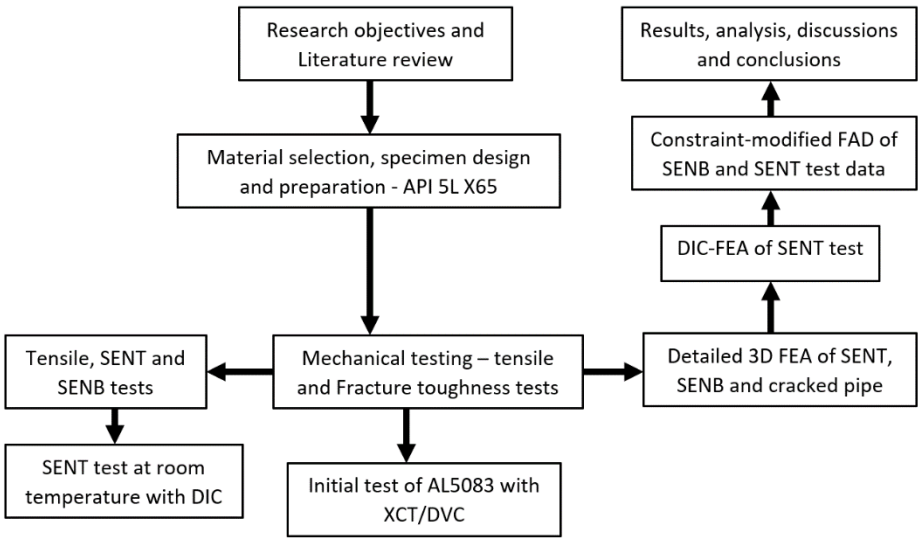

Figure 1.1: Flow chart of overall thesis methodology

1. A series of small-scale fracture mechanics tests (SENT and SENB) was carried out on an API 5L X65 grade pipe material with details of chemical composition and properties. Conditions for the test specimens was designed to closely match those of cracked pipes with through-thickness defects. Thus;

- Test material identical to the pipeline material under investigation
- Test temperature not exceeding -120℃ in liquid nitrogen chamber
- Specimen orientation/rolling direction
- Specimen design – most important dimension of fracture mechanics test specimen is the thickness which can be calculated using available formulae in fracture toughness test standards knowing the yield strength of the material and its fracture toughness
- Pre-cracking – fatigue pre-cracking for plane strain conditions

2. DIC was used for the fracture tests of SENT specimens at room temperature to capture the full-field surface displacements. A novel method was developed, that made use of the finite element approach to obtain the crack's surface strain energy release rate as the *J*-integral.
3. Detailed 3D FEA of SENB, SENT specimens and cracked pipe was conducted using Abaqus to derive in-plane constraint parameter, Q. This covered a wide range of specimen configurations and loadings in order to study different specimen and flaw behaviour and to investigate methods for recognising size effects in the test results (validation).

4. A constraint-modified FAD approach was utilised to investigate its applicability to the experimental tests data for SENT and SENB specimens at room and low temperatures.

1.6 Structure of Thesis

The work in this thesis comprises of both experimental and numerical study. The structure of the thesis is as described below:

- Chapter 1 gives the background, importance, the research gap and contributions to new knowledge/research impact.
- Chapter 2 reports on critical review into the current understanding of constraint and concepts of fracture mechanics for the treatment of constraint effects.
- Chapter 3 reports on the experimental analyses of the tensile and fracture tests carried out during this study – round and flat tensile, SENT and SENB fracture tests. Digital image correlation (DIC) was used to capture the full-field displacement of some crack configurations of SENT and flat tensile specimens at room temperature.
- Chapter 4 investigates the numerical analyses of crack tip constraint effects in terms of the Q-parameter of the fracture specimens (SENB and SENT) and cracked pipe. This was considering the transferability in constraint level from the fracture specimens to pressured pipes with defects.
- Chapter 5 presents a proposed novel methodology to calculate the strain energy release rate as characterised by the crack driving force (*J*-integral) from the DIC full-field displacement data obtained in chapter 3. The analysis method makes use of a finite element approach, that is versatile and easy to implement through its Python scripting capabilities in Abaqus.
- Chapter 6 investigates the work carried out on aluminium specimens using x-ray computed tomography (XCT) technique. An initial application of a novel approach to measure the strain and displacement fields within a three-dimensional volume based on digital image data obtained from XCT.
- Chapter 7 presents conclusions to the thesis and provide some recommendations for future work, possibly to build on the current research scope investigated in this thesis. The conclusions and recommendations drawn will help to reduce the inherent conservatisms in current assessment procedures (particularly, BS 7910), enabling a more cost-effective design and accurate analysis of steel structures operating in low temperature environments.

2 Literature review

2.1 Introduction

This chapter presents a comprehensive literature survey on the relevant concepts and previous studies. The fundamental concepts of fracture mechanics essential to the research work are introduced, focusing on stress field of a cracked body, crack driving force and crack tip constraint (linear and elastic-plastic fracture mechanics). Fracture mechanisms in metals and fundamentals of high strength steel grades are presented thereafter. The chapter further reviews current fracture toughness test methods and standards as well as relevant assessment codes and standards. The importance of crack tip constraint matching is highlighted. A baseline 3D SENB finite element verification analysis is carried out in this chapter that provide confidence for subsequent numerical work that would be performed in chapter 4. A summary and conclusion to the chapter is provided.

All engineering structures and components contain geometrical defects/discontinuities. The strength of these components/structures largely depend on the size and shape of the defects. The conventional approach to assess the strength of components or structures containing defects is by evaluating the stress concentration that is caused by the features of the discontinuity [4][5]. It is to be noted that such conventional approach would give erroneous results if the geometrical defects have very sharp radii.

Fracture mechanics involves a set of theories used to describe the behaviour of solids or structures with geometrical discontinuity at the scale of the structure. These theories have now evolved into a mature discipline of science and engineering that has dramatically changed our understanding of the behaviour of engineering materials [4], [6]. One of the impacts of fracture mechanics today is the establishment of the so-called damage tolerance design methodology which has now been incorporated in engineering design standards.

Fracture mechanics as can be inferred from the name is the study that combines the mechanics of cracked bodies and mechanical properties (deals with fracture phenomena and events). The history and establishment of fracture mechanics dates back to some well-known disasters where very few developments were made in the field until World War II (WWII), when several hundred liberty ships and some aircrafts fractured. Some of these disasters after WWII incidents are the Comet accidents in 1954 and the Melbourne Kings Bridge failure in July 1962 leading to significant progress in the understanding of fracture and fatigue [4]. The reader is encouraged to refer to books written by [4], [7] [5], [8] and the paper reviewed by [9] among several others to gain in-depth historical background on the development of fracture mechanics.

From the above concepts in fracture mechanics, one can define it as the study of the propagation of cracks in materials in the field of mechanics and an analytical and numerical solid mechanics tool is used for the calculation of crack driving force. Also, a materials' resistance to fracture characterisation is the experimental field of science.

2.1.1 Energy Release Rate, G

Alan Arnold Griffith's energy-based analysis of cracks in 1920 is considered to be the foundation in which the field of fracture mechanics is constructed [10]. During Griffith's pioneering work, he was aware of Inglis' work [11] in calculating the stress concentrations around elliptical holes and considered how it might be used in developing a fundamental approach to predicting fracture strengths. Inglis' solution, however, poses a mathematical difficulty: in the limit of a perfectly sharp crack, the stresses approach infinity at the crack. This prompted much discussion due to the fact that no material can support an infinite stress without yielding and failing, implying that all structures would fail under small loads [4].

In 1920, Griffith applied the idea from the First Law of Thermodynamics (energy can neither be created nor destroyed in an isolated system) to propose a (linearly elastic) energy-based failure criterion that effectively superseded Inglis' infinite-stress prediction. This approach by Griffith was developed for brittle materials, specifically glass rods. As the atomic bonds in glass rupture would be different to that of metals (ductile – plastic deformation), considering the surface energy alone fails to provide an accurate model for fracture. Another shortcoming of the Griffith approach is that it is based on global energy balance and it does not attach any significant importance to the stress field near the crack-tip [4][12].

This deficiency was later remedied independently by Irwin (1948) and Orowan (1949, 1955) [4]. They suggested that in a ductile material, most of the released strain energy was not through creating surfaces, but via energy dissipation due to plastic flow in the material near the crack tip.

The energy approach was later developed in the 1950s by Irwin [13], where he defined the energy release rate, G as a measure of the energy required for an increment of crack extension. The formulation of the energy release rate is carried out by utilising the conservation of energy. For instance, consider the case of an incremental increase in the crack area ΔA, therefore, to cause crack growth, an incremental external work done, ΔW_{ext} by an external force, results in the strain energy within the body of the structure/component to increase by ΔU. Then the available energy GΔA, provides the energy balance as follows in equation (2.1):

$$G\Delta A = \Delta W_{ext} - \Delta U \quad (2.1)$$

Dividing equation (2.1) by ΔA and taking the limit ΔA→ 0, we obtain equation (2.2) as:

$$G = -\frac{d}{dA}(U - W_{ext}) \quad (2.2)$$

Knowing that potential energy, Π= $U - W_{ext}$, for a wide plate with a through-thickness crack of length, 2a subjected to a remote/nominal tensile stress σ, the energy release rate, G is given by equation (2.3):

$$G = -\frac{d\Pi}{dA} = \frac{\pi\sigma^2 a}{E} \quad (2.3)$$

where Π is the potential energy supplied by the internal strain energy and external forces, dA is the incremental increase in the crack area and E is modulus of elasticity (Young's modulus). Nowadays, G is invariably referred to as the strain energy release rate. It is noted that G is dependent on the fracture stress or critical stress in the presence of crack size 2a. Re-writing equation (2.3) in terms of critical stress σ_c , critical crack size, a_c and critical strain energy release rate, G_c for the unstable crack extension gives:

$$\sigma_c = \sigma_f = \sqrt{\frac{EG_c}{\pi a}} \quad (2.4)$$

where $G_c = 2\gamma_s =$ energy required per unit area of crack extension and γ_s is the surface energy. G_c is also considered to be a material property and is known as the crack resistance, R to brittle fracture. Therefore, G_c must be at least equal to R before crack propagation can occur.

Irwin made further fundamental step few years later by showing a relationship between the critical stress intensity causing fracture, K_{IC} and a critical value of the strain energy release rate, G_c. The realisation that the strain energy and stress intensity approaches to the prediction of fracture are equivalent led to a rapid development in the discipline of Linear Elastic Fracture Mechanics (LEFM) which allows engineers to predict what defects are tolerable in a given structure under known loading conditions forming the basic goal of Fracture Mechanics [4] [5], [14], [15]. This would be discussed further next in the section 2.2.

2.2 Linear Elastic Fracture Mechanics (LEFM)

As outlined in the previous section, the basis of fracture mechanics stems from the work of Griffith [10] where he demonstrated that the strain energy released during crack extension is the driving force for fracture.

Fracture mechanics is made of two main branches: linear-elastic fracture mechanics (LEFM) and the elastic-plastic fracture mechanics (EPFM). While LEFM describes the behaviour of a material when plastic deformation is restricted to a small region at the crack tip known as small scale yielding (SSY), EPFM generally applies to large scale yielding (LSY) conditions when there is significant plasticity in a region surrounding the crack-tip [4]. Further, in the SSY regime, the plastic zone size (region of plastic deformation) is relatively small compared to the crack size and the stress field near the crack tip is well approximated by linear elastic behaviour, except with a very localised plastic zone. LSY on the other hand occurs when the plastic zone near the crack tip is significant, extending over a considerable portion of the over structure or specimen being tested. The stress field near the crack tip is no longer accurately described by linear elastic behaviour, and non-linear plastic deformation plays a significant role. Therefore, the determination of whether a crack falls into the SSY or LSY regime involves calculating the plastic zone size (r_p) relative to the crack size (a) based on the material properties, stress state and loading conditions [12], [16]. This is discussed later in the next section.

2.2.1 Stress Intensity Factor and Plastic Zone Correction

The energy-balance approach developed by Griffith and later modified by Irwin and Orowan provides a great insight to the fracture process in fracture mechanics. An alternative method that examines the stress state near the crack-tip of a sharp crack has also proven useful in engineering practice and Westergaard [17], Irwin [18] and Williams [19] were among the first to define the stress field at the crack-tip.

There are three typical loading modes in fracture mechanics based on the loading position and direction with respect to the crack as illustrated in Figure 2.1.

- **Mode I** (opening): has the crack opening under the influence of a stress at right angles to the crack plane.
- **Mode II** (in-plane shear): involves in-plane sliding normal to the crack front under the influence of a shear stress parallel to the crack plane.
- **Mode III** (out-of-plane shear): involves in-plane sliding parallel to the crack front under the influence of a shear stress parallel to the crack plane.

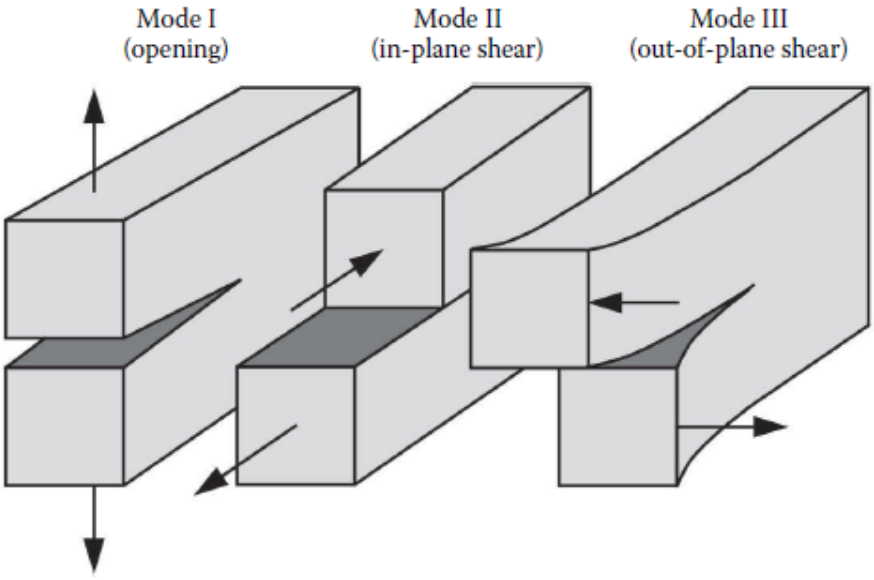

Figure 2.1: Three typical fracture modes [4]

Consider an isotropic linear elastic material containing a through-thickness Mode-I crack with length 2a as shown in Figure 2.2 with a polar coordinate system defined with the origin located at the crack-tip subjected to a remote tensile stress, the stress field can be written as given by Westergaard [17], Irwin [18] and Williams [19]:

$$\lim_{r\to 0} \sigma_{ij}^{(I)} = \left(\frac{K_I}{\sqrt{2\pi r}}\right) f_{ij}^{(I)}(\theta) \tag{2.5}$$

where σ_{ij} is the stress tensor, r is the distance from the crack tip, f_{ij} is a dimensionless function of the angle θ and K_I is the so-called stress intensity factor (SIF) in the units of $MPa\sqrt{m}$. The SIF is a function of crack length, applied force and specimen geometry and it describes the crack tip stress field.

$$\lim_{r\to 0} \sigma_{ij}^{(II)} = \left(\frac{K_{II}}{\sqrt{2\pi r}}\right) f_{ij}^{(II)}(\theta) \tag{2.6}$$

and

$$\lim_{r\to 0} \sigma_{ij}^{(III)} = \left(\frac{K_{III}}{\sqrt{2\pi r}}\right) f_{ij}^{(III)}(\theta) \tag{2.7}$$

Mixed mode loading problems arises when any two or three of these modes occur concurrently and their individual contributions to a given stress component is mathematically illustrated as a total of the three modes:

$$\sigma_{ij}^{(total)} = \sigma_{ij}^{(I)} + \sigma_{ij}^{(II)} + \sigma_{ij}^{(III)} \tag{2.8}$$

The general form of the loading mode equations can therefore be written as;

$$\lim_{r\to 0} \sigma_{ij} = \left(\frac{K}{\sqrt{2\pi r}}\right) f_{ij}(\theta) \qquad (2.9)$$

which describes a stress singularity at the crack-tip indicating σ_{ij} approaches infinity as $r \to 0$.

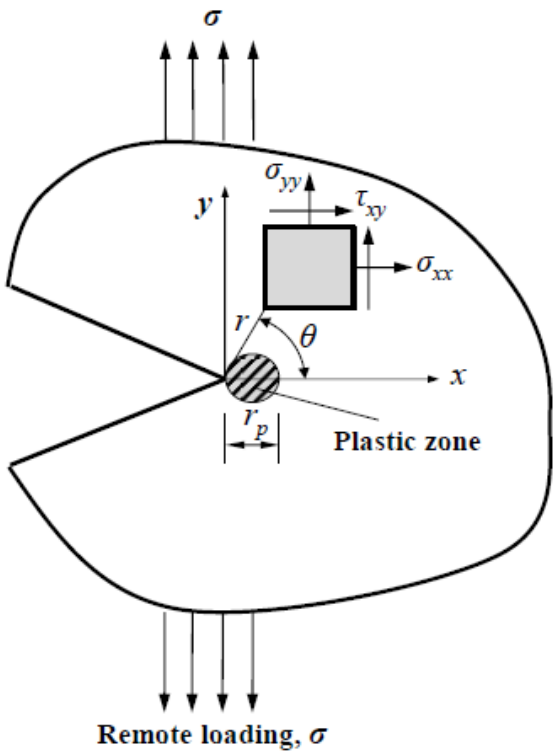

Figure 2.2: Stress field near crack tip [4]

For instance, if a crack in any structure and under any loading condition is investigated, after determining the SIF (K_I, K_{II}, K_{III} or combination of them) and depending on the loading condition, the material fracture toughness, K_{mat} is a benchmark to understand whether the material fails due to existence of the crack or not. Stress singularities refer to the behaviour where stresses and strains become infinite or approach very high values in the vicinity of the crack tip. As a result, the stress and strain distribution near the crack tip become highly concentrated and exhibit singular values. One example of stress singularity is the stress intensity factor, *K*, which is used to characterise the stress field near the crack tip (common in sharp crack analysis). The presence of stress singularities poses challenges in the analysis of fracture mechanics assessments and requires techniques, such as finite element analysis or application of fracture mechanics principles to accurately predict the behaviour and failure of materials containing cracks [4]. It is worth noting that stress singularities are idealisations and may not fully represent the behaviour of real-world materials that have non-sharp (blunted) crack tip.

It is also important to understand plane stress and plane strain in fracture mechanics problems. In plane stress, the stress normal to the plate plane is zero ($\sigma_z = 0$). An example of plane stress problem is in the aviation design of very thin plates loaded only by forces or displacements in the plane of the plate. Similarly, when the value of the strain normal to the plate is zero, it is known as a plane strain condition ($\varepsilon_z = 0$). For these two conditions, the modulus of elasticity has been redefined as E′. Considering triaxiality at the crack front, when a tensile load is applied to a cracked block as shown in Figure 2.3, the block experiences stretching in the *y* direction and contraction in the *z* direction. Depending on the *z*-coordinate at a point on the crack plane and located ahead of the crack front, the state of stress (triaxiality) varies. For a point *J* or *K* very close to the surface, ($z = B/2$), there is no constraint in the *z* direction because the outer surfaces are free of any normal stress σ_z or σ_3. On the other hand, for a point I near the centre, tendency of contraction is restrained, some stress σ_3 develop in the z direction because of the interaction between inner and outer layers. This constraint gradually increases from zero at the surface (plane stress) to higher values at the inner (plane strain) locations. For thicker specimens, it may develop to full constraint of plane strain even before the mid-thickness location is reached [12]. Hence, there is triaxiality at the inner locations and state of stress for the two points are illustrated in Figure 2.3c and Figure 2.3d, respectively. There is thus, a state of plane stress near the surfaces ($z = \pm B/2$) and a state of plane strain near the centre. High constraint conditions therefore describe a high stress triaxiality and low constraint conditions describe a low stress triaxiality. A reduction in crack tip stress triaxiality leads to increased resistance to fracture as crack tip is no longer fully plane strain conditions [20].

Shear stresses are a fundamental concept in fracture mechanics and material science and plays a crucial role in understanding the behaviour of materials in various conditions, particularly in yielding and failure criteria such as Von Mises and Tresca criteria. Shear stress is a measure of the internal resistance of a material to deformation caused by the applied forces or loads acting parallel/tangential to a specific plane or surface within the material. This stress arises due to sliding or deformation of adjacent layers of material along that plane. The Von Mises and Tresca criteria are two commonly used in material science and engineering to predict the onset of yielding (permanent deformation) and ultimately, failure in materials subjected to various stress states. The Von Mises criterion (also known as the Von Mises stress/the distortion energy criterion) is based on the concept of equivalent stress and postulates that yielding will occur when the equivalent Von Mises stress exceeds a critical value ($\sigma_{VM} > \sigma_Y$). The equivalent Von Mises stress is a combination of the normal stress ($\sigma_x, \sigma_y, \sigma_z$) and shear stress ($\tau_{xy,}\tau_{yz,}\tau_{zx,}$) in three dimensions and is given by:

$$\sigma_{VM} = \sqrt{\frac{(\sigma_x - \sigma_y)^2 + (\sigma_y - \sigma_z)^2 + (\sigma_z - \sigma_x)^2 + 3(\tau_{xy}^2 + \tau_{yz}^2 + \tau_{zx}^2)}{2}} \qquad (2.10)$$

The Tresca criterion, also know known as the maximum shear stress criterion or the Coulomb-Mohr criterion is much simpler and states that yielding will occur when the maximum shear stress, $\tau_{max,}$ at any point within the material exceeds a critical value, $\tau_{y,}$ ($\tau_{max,} > \tau_y$). The maximum shear stress at a point is typically calculated as the difference between the maximum and minimum principal stresses at that point:

$$\tau_{max} = \frac{1}{2}(\sigma_{max} - \sigma_{min}) \qquad (2.11)$$

Therefore, yielding occurs in materials when the applied stresses exceed a critical threshold (usually, yield strength or yield stress) required to cause permanent deformation [21][22] [6].

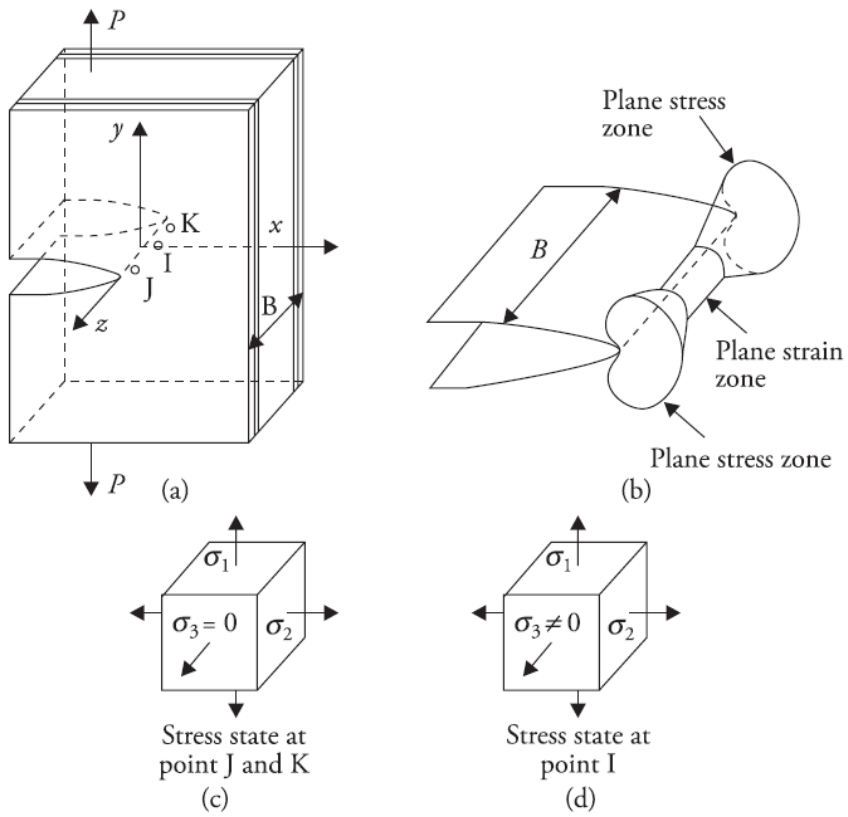

Figure 2.3: Plastic zone size variation along thickness (a) Specimen (b) Plastic zone shape around crack front (c) Stress state at point J and K (d) Stress state at point I [12]

Under SSY conditions, Irwin [18] showed that the energy release rate, G can be related to the SIF K_I, for Mode-I loading configuration as;

$$G = \frac{K_I^2}{E'} \tag{2.12}$$

where $E' = E$ for plane stress

and $E' = \frac{E}{1-\upsilon^2}$ for plane strain

E is the elastic modulus and υ is the Poisson's ratio. Irwin further showed that G is related to K when all the three modes of loading occur for a given geometry and loading configuration as:

$$G = \frac{K_I^2}{E'} + \frac{K_{II}^2}{E'} + \frac{K_{III}^2}{2\mu} \tag{2.13}$$

where μ is the shear modulus

From the SIF relation stated above, for an initial case of infinite plate/material subjected to uniform stresses, the SIF can be written generally as:

$$K = \sigma\sqrt{\pi a} \tag{2.14}$$

which for an infinite plate is justifiable as the only known dimension is the crack length. In general, the SIF depends on the geometry of a cracked body (including the crack length) and it is usually expressed as in equation (2.15) as found in several fracture mechanics text books, SIF handbooks as well as assessment procedures BS 7910 [23] R6 [24] and ASME API 579-1 [25]:

$$K_I = Y\sigma\sqrt{\pi a} \tag{2.15}$$

where Y is a shape factor and is a function of body geometry and crack length, f(a/W). It is worth noting that, the SIF can have a simple relation to applied stress and crack length, or the relation could involve complex geometry factors for complex loading, different structural configurations and various crack shapes. The reader is encouraged to refer to [4], [15] and other SIF handbooks for calculation of the shape factor for various crack shapes (e.g. centre crack, single edge crack and double edge crack).

The stress intensity factor, K (SIF) as given by [4] and [14] completely defines the amplitude of the stress singularity (the stresses, strains and displacements) near the crack-tip. This single-parameter characterisation by K strictly relies on the satisfaction of the SSY condition that the zone of plastic deformation to be well confined within the singularity fields [14]. As previously stated, as $r \to 0$ (confined within the singularity dominated zone), the stresses at the crack tip

tends to infinity but in reality, there is no infinite stress. This is due to plastic deformation of the crack tip and the crack tip stresses remain finite. Two main correction approaches were postulated to account for yielding near the crack tip: Irwin small-scale yielding (SSY) approach and the strip yield model [4] [14].

Assuming the existence of plastic zone, Irwin defined the size of the plastic zone ahead of the crack-tip, r_p, for plane-stress and plane-strain respectively, as equation (2.16) and (2.17):

for plane stress

$$r_p = \frac{1}{\pi}\left(\frac{K}{\sigma_{YS}}\right)^2 \tag{2.16}$$

and

for plane strain

$$r_p = \frac{1}{3\pi}\left(\frac{K}{\sigma_{YS}}\right)^2 \tag{2.17}$$

where σ_{YS} is the yield strength. As a result of triaxial stress state (higher constraint), the Irwin approach showed that the plastic zone is smaller for plane strain conditions and yielding is suppressed. It is worth to note that the ASTM standard for experimentally determining the linear-elastic plane-strain fracture toughness of metallic materials [26] requires the crack length and the uncracked ligament of the test specimen to be no less than $25r_p$ at the point of fracture in order to satisfy SSY condition expressed as:

$$B \geq 25 \times \frac{1}{3\pi}\left(\frac{K_{IC}}{\sigma_{YS}}\right)^2 \tag{2.18}$$

and

$$B \geq 2.5\left(\frac{K_{IC}}{\sigma_{YS}}\right)^2 \tag{2.19}$$

where B is the thickness of the plate and it can be seen from equations (2.18) and (2.19) that the plate thickness has a strong influence on the fracture behaviour. It should be noted also that SIF (K) is independent of the specimen thickness, whereas fracture toughness testing and measurement of material fracture toughness, K_{mat} depends on specimen thickness.

As another illustration for conditions within the plastic zone, consider a crack loaded in a thick test specimen, which causes the opening of the crack and a small plastic zone formed in front of the crack tip. Increasing the load will increase the size of the plastic zone until a critical value (i.e.

SIF reaches the plane strain fracture toughness of material), when the crack starts to extend inside the larger plastic zone. This crack extension with the plastic zone will continue straight in plane strain condition because of surrounding material on the crack tip stresses. As the minimum stresses are perpendicular to the crack plane, the in-plane stress components in the crack grow at a 45° angle, resulting in visible shear lips forming.

Further, the redistributed stress in the elastic region will be higher, which implies a higher effective stress intensity factor, K_{eff}. By this, Irwin further found that a good approximation of K_{eff} can be obtained by placing the effective crack tip in the centre of the plastic zone and inserting the effective crack size in the appropriate SIF solution for the geometry correction [4]:

$$a_{eff} = a + \frac{r_p}{2} \tag{2.20}$$

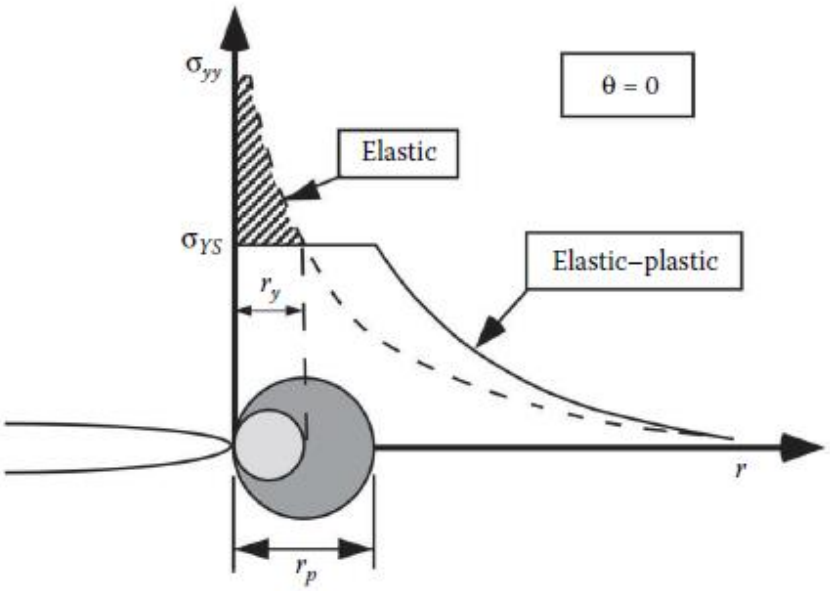

Figure 2.4: Estimate of plastic zone size, r_p [4]

The strip-yield model was first proposed by Dugdale [27] and Barenblatt [28] where they assumed a long slender plastic zone at the crack tip in a nonhardening material in plane strain. It should be noted that further discussion of this model is limited to a through-crack in infinite plate. The strip-yield model is also a classical application of the principle of superposition as it approximates the elastic-plastic behaviour by superimposing two elastic solutions [4]:

- A through-crack under remote/nominal tension and
- A through-crack with closure stresses at the tip

Dugdale [27] and Barenblatt [28] idea is based on the fact that, since the stresses at the strip-yield zone are finite, there cannot be a singularity at the crack tip (the SIF at the tip of the plastic zone must be equal to zero). Thus, the plastic zone length ρ, is found from the condition that the stress intensity factors from the remote tension and closure stress cancel out. The mathematical derivation of the strip-yield model for the prediction of the effective SIF is beyond the scope of this research. The reader is referred to Anderson [4] for a step-by-step derivation of the more realistic estimate of K_{eff} by Burdekin and Stone [29] shown below [4]:

$$K_{eff} = \sigma_{YS}\sqrt{\pi a}\left[\frac{8}{\pi^2}\ln\sec\left(\frac{\pi\sigma}{2\sigma_{YS}}\right)\right]^{\frac{1}{2}} \tag{2.21}$$

It should be noted that the plastic zone shapes predicted by the strip-yield model produce crack tip zones in many polymers as shown in Figure 2.5, which bear little resemblance to the actual plastic zones in metals. Furthermore, the Irwin approach and strip-yield model are valid for LEFM theories only and beyond these limits, can only be considered approximations [4].

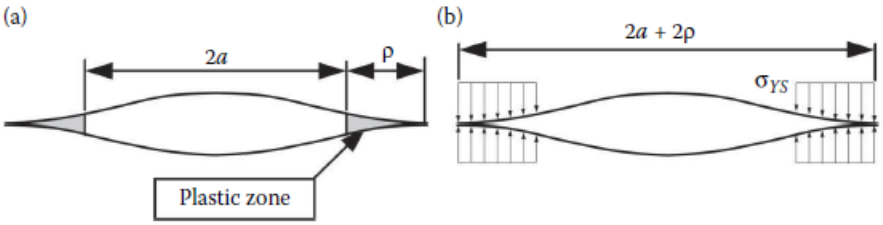

Figure 2.5:Strip-yield Model Plastic Zone Correction [4]

2.2.2 Stress Intensity Factor of a Pipe

Consider the case of a longitudinal crack in a pipe under internal pressure, a solution has been presented by Tada et al [30]. As illustrated in Figure 2.6 and Figure 2.7, the longitudinal crack length is shown as $2a$ and the pipe is under an internal pressure loading of P, with thickness given as t. The SIF for this scenario is depicted as follows:

$$K_I = \sigma\sqrt{\pi a}F(\lambda) \tag{2.22}$$

where σ and $F(\lambda)$ are:

$$\sigma = P\frac{R}{t} \tag{2.23}$$

and

$$F(\lambda) = (1 + 1.25\lambda^2)^{0.5} \quad \rightarrow 0 < \lambda \leq 1 \tag{2.24}$$

$$F(\lambda) = 0.6 + 0.9\lambda \quad \rightarrow 1 \leq \lambda \leq 5 \tag{2.25}$$

where

$$\lambda = \frac{a}{\sqrt{Rt}} \tag{2.26}$$

σ is the hoop stress due to the internal pressure P and R is the mean pipe radius.

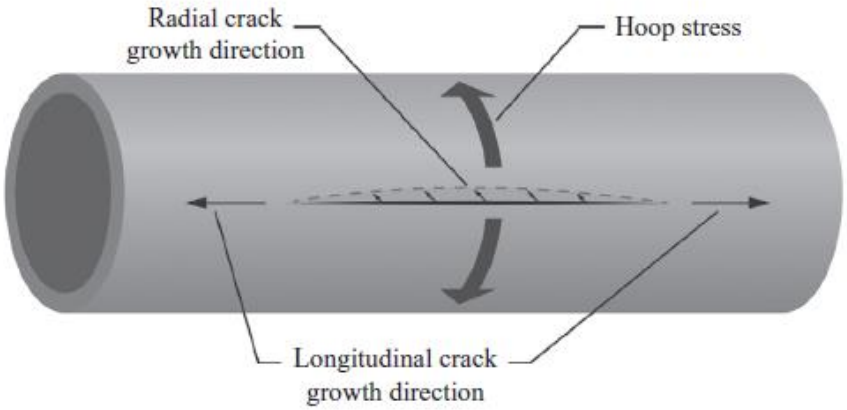

Figure 2.6: Pipeline illustrating the orientation of hoop stress resulting from internal pressure and the preferential orientation of crack growth [31]

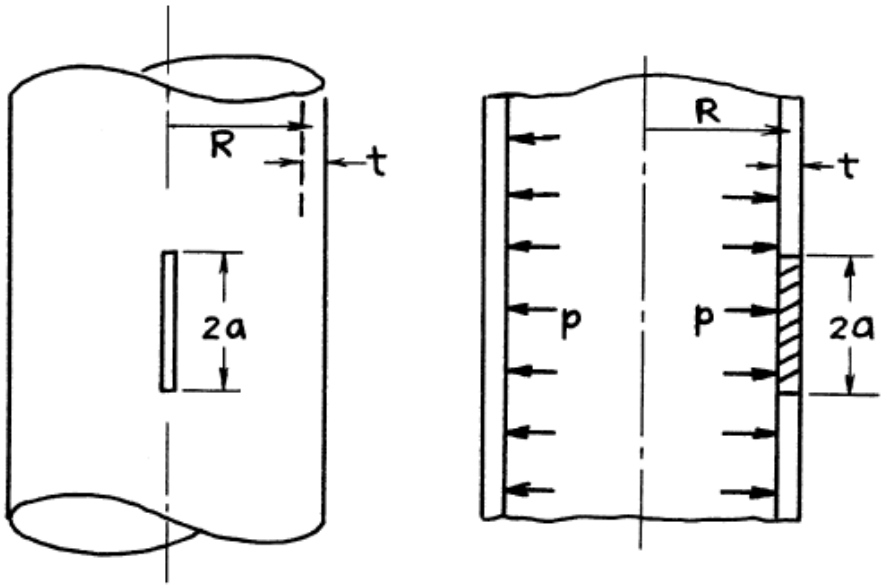

Figure 2.7: Longitudinal crack in a pipe [31]

2.2.1 Limitations of LEFM

Severe size limitation has been a major issue in the application of LEFM to ensure that the plasticity is restricted to a local disturbance around the elastic field. K_{IC} becomes a measure of

fracture toughness when components fail in an elastic manner. ASTM E399 shows a valid K_{IC} test can be performed using different specimen size requirements [26]:

$$a \geq 2.5\left(\frac{K_{IC}}{\sigma_{YS}}\right)^2 ;\ W - a \geq 2.5\left(\frac{K_{IC}}{\sigma_{YS}}\right)^2 ;\ \mathrm{B} \geq 2.5\left(\frac{K_{IC}}{\sigma_{YS}}\right)^2 \qquad (2.27)$$

where a is the crack length, W is the width and B is the thickness of the specimen. K_{IC} is calculated from a critical applied load P_Q given in ASTM E399 [26] as:

$$K_{IC} = \frac{P_Q}{B\sqrt{W}} f\left(\frac{a}{W}\right) \qquad (2.28)$$

These limits ensure that the radius of the plastic zone which is directly proportional to $(K_I/\sigma_{YS})^2$, is far smaller than the relevant in-plane dimensions of the material. The thickness requirement is to ensure plane strain conditions while the in-plane dimensions $a, (W - a)$ ensures the macroscopic response is linear elastic and that the plasticity endures less disturbance, meaning the problem is governed by the field characterised by K_I.

Research and experiments have shown that structural metals often exhibit extensive plasticity prior to failure and there is reduction in the thickness of the component, thereby, increasing fracture toughness. This limits the practical application of LEFM to tough structural materials such as ferritic steels requiring large test specimens that are expensive to prepare and difficult to test.

2.3 Elastic Plastic Fracture Mechanics (EPFM)

The application of linear-elastic fracture mechanics becomes difficult when the fracture processes are accompanied by significant plastic deformation in the region surrounding the crack tip [4]. In structural ferritic steels, this limits the use of LEFM as a means of assessing structural integrity. Thus, there is the need to rely on elastic-plastic fracture mechanics (EPFM) to characterise the crack tip fields and define the energetics of crack extension in non-linear materials.

In elastic-plastic fracture mechanics, two key methods have been proposed: the *J*-integral by Rice (1968) [32] and the crack-tip opening displacement (CTOD or δ) by Wells (1961) [33] to describe crack-tip conditions in elastic-plastic materials and can be used as a fracture criterion [4] [15]. The intention for the development of these methods was to provide specialised measurements of fracture properties [15]:

- **CTOD**: full range of fracture toughness for slow loading rates
- ***J*-integral**: Elastic-plastic fracture toughness for slow loading rates

2.3.1 Path independent integral (*J*)

The *J*-integral, like the energy release rate, *G* and the stress intensity factor, *K*, is a parameter used to characterise the stress state near the crack tip. Not only is the *J*-integral applicable to linear and non-linear elastic materials but is useful in the characterisation of materials that exhibit elastic-plastic behaviour near the crack tip. Thus, for large scale plasticity, the elastic solution for crack tip stress is no longer valid and the stresses in the plastic zone should be determined using plasticity theory [32], [34]. The *J*-integral is based on the first Law of thermodynamics: energy can neither be created nor destroyed, but can be transformed from one state to another state. In deriving the *J*-integral from first principles, it can be expressed in the rate form as [12], [16], [32], [35]–[37]:

$$\dot{W}_{external} + \dot{Q}_{heat} = \dot{K}_{velocity} + \dot{W}_{strain} + \dot{U}_{thermal} + \dot{D}_{crack} \tag{2.29}$$

where

$\dot{W}_{external}$ = work done by the external force

$\dot{Q}_{heat}$ = heat input to, or generated by, the material

$\dot{K}_{velocity}$ = kinetic energy

$\dot{W}_{strain}$ = mechanical strain energy

$\dot{U}_{thermal}$ = internal energy related to temperature

$\dot{D}_{crack}$ = dissipated mechanical energy due to breaking of atomic bonds (as crack grows) are the rate at which each of the energy term changes with time.

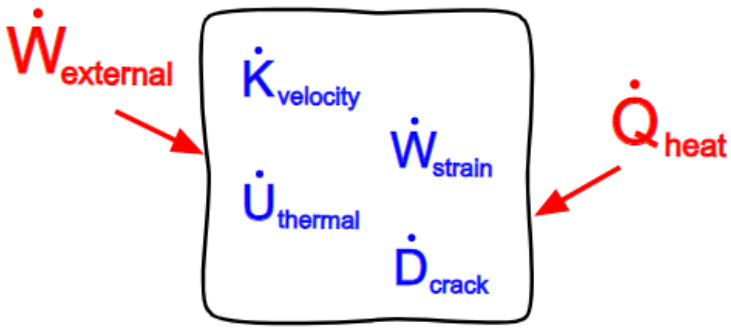

Figure 2.8: Conservation of energy

The terms on the left side of equation (2.29) represent energy input into an object in the forms of mechanical and heat. The terms on the right side represent the several forms of energy into which the external energy can go within an object as illustrated in Figure 2.8. Three of these four: kinetic

energy, strain energy and thermal energy are reversible, can be stored in an object and subsequently used to do work on other objects. An example of this is in a billiard ball when external work and heat are transferred into the ball's kinetic energy, causes the ball to move to strike another ball, using its newly acquired 'speed-energy'. The exception to this example is the energy that causes crack propagation as it is not reversible, not stored within an object and cannot subsequently do work on others. Therefore, considering a situation involving only quasi-static mechanical loading such that kinetic energy, internal energy and heat input terms are negligible, we have:

$$\dot{W}_{external} = \dot{W}_{strain} + \dot{D}_{crack} \tag{2.30}$$

Equation (2.30) shows that as work energy is input into a test specimen under quasi-static mechanical loading (external forces), it is divided into internal strain energy and the energy required to break the atomic bonds, i.e., crack growth. The *J*-integral is directly related to this energy release associated with bond breaking and crack growth. As an example, if we consider a case where there is no crack propagation in a specimen, $\dot{D}_{crack} = 0$, and all the work of the external forces, $\dot{W}_{external}$, goes into stored internal strain energy, $\dot{W}_{strain}$. On the other hand, when the test specimen experiences crack propagation, then, $\dot{W}_{strain}$ will likely be negligible with much of the external energy, $\dot{W}_{external}$, going directly to cause the crack to propagate, $\dot{D}_{crack}$. Applying a chain rule identity to the time derivatives:

$$\frac{d(\,)}{dt} = \frac{d(\,)}{da}\frac{da}{dt} = \frac{d(\,)}{da}\dot{a} \tag{2.31}$$

where a is crack length. This leads to:

$$\frac{dW_{external}}{da}\dot{a} = \frac{dW_{strain}}{da}\dot{a} + \frac{dD_{crack}}{da}\dot{a} \tag{2.32}$$

Factoring $\dot{a}$ out gives the conservation of energy per unit crack growth as:

$$\frac{dW_{external}}{da} = \frac{dW_{strain}}{da} + \frac{dD_{crack}}{da} \tag{2.33}$$

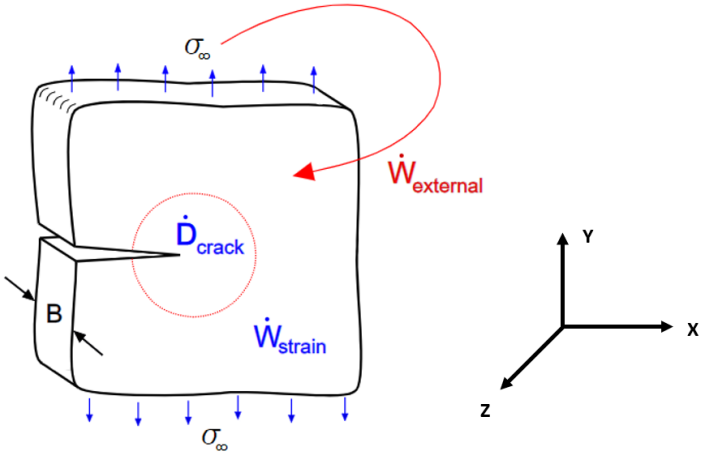

Figure 2.9: Cracked block showing the workdone, internal strain energy and the energy required for crack growth

Dividing equation (2.33) above by the material thickness, B (see Figure 2.9) and rearranging, we have definition of J to be:

$$J = \frac{1}{B}\frac{dD_{crack}}{da} = \frac{1}{B}\frac{dW_{external}}{da} - \frac{1}{B}\frac{dW_{strain}}{da} \tag{2.34}$$

where (Bda) is the increment of area created by the crack growth, da. Equation (2.34) clarifies that J is a measure of the energy lost per unit increase in crack surface area with dimensions in *Energy/Area.* In metric units, this could be *Joules/*m^2 *or* $N.m/m^2$, which reduces to the rather confusing N/m. Re-writing (Bda) as a new crack area, dA_{crack}, i.e., $Bda = dA_{crack}$, the following expression for J can be defined:

$$J = \frac{1}{B}\frac{dD_{crack}}{da} \equiv \frac{dD_{crack}}{dA_{crack}} \tag{2.35}$$

Simple algebra can be applied to obtain an alternative expression for *potential energy* in terms of J. Equation (2.30) can be written as $W_{external} = W_{strain} + D_{crack}$, where the time derivative has been dropped for convenience. Solving for D_{crack}, gives $D_{crack} = W_{external} - W_{strain}$, such that J can be expressed as:

$$J = \frac{dW_{external}}{dA_{crack}} - \frac{dW_{strain}}{dA_{crack}} \tag{2.36}$$

Knowing that potential energy, Π, is:

$$\Pi = W_{strain} - W_{external} \tag{2.37}$$

This can be re-written in terms of D_{crack} as:

$$\Pi = D_{crack} = -(W_{external} - W_{strain}) \tag{2.38}$$

Substituting the above equation (2.38) into equation (2.36) for the J definition gives:

$$J = \frac{dD_{crack}}{dA_{crack}} = -\frac{d\Pi}{dA_{crack}} \tag{2.39}$$

The above relationship leads to J being introduced as the rate of change of an object's potential energy relative to its crack growth. In practice, it is useful to express $W_{external}$ and W_{strain} in terms of directly measurable quantities as:

$$W_{external} = \int \boldsymbol{T}.\boldsymbol{u}dS \tag{2.40}$$

where $\boldsymbol{T}$ is the traction vector, $\boldsymbol{u}$ is the displacement vector and S is the exterior surface area.

The strain energy, W_{strain}, is expressed in terms of strain energy density, w, and volume, V.

$$W_{strain} = \int wdV \tag{2.41}$$

Strain energy density is the amount of energy per unit volume used to deform an object and this is usually the area under a stress-strain curve as shown in Figure 2.10. Also, recall from continuum mechanics that energy, W, is:

$$W = \int \boldsymbol{F}.d\boldsymbol{x} \tag{2.42}$$

While strain energy density, w, is:

$$w = \int \boldsymbol{\sigma}:d\boldsymbol{\epsilon} \tag{2.43}$$

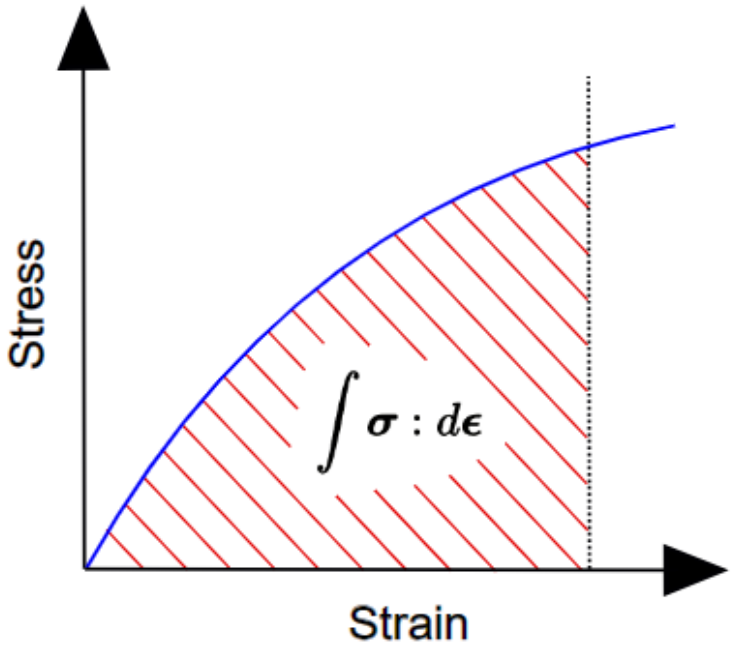

Figure 2.10: Example stress-strain curve to illustrate strain energy density

For linear elastic material, the integral can be evaluated as:

$$w = \frac{1}{2}\boldsymbol{\sigma}:\boldsymbol{\epsilon} \tag{2.44}$$

Inserting equations (2.40) and (2.41) into the energy conservation equation (2.34) gives:

$$J = \frac{1}{B}\frac{dD_{crack}}{da} = \frac{1}{B}\int \boldsymbol{T}.\frac{d\boldsymbol{u}}{da}dS - \frac{1}{B}\int \frac{dw}{da}dV \tag{2.45}$$

The above equation shows the integrals over the surface and volume enclosing the crack tip.

Rice [32] postulated that the change in stresses, strains, displacements etc., due to increment in crack length, da, would be the same as the differences in the values between two different locations separated by the distance, da, while the crack length is held constant. Thus:

$$\frac{d(\,)}{da} = -\frac{\partial(\,)}{\partial x} \tag{2.46}$$

where the x coordinate is measured along the direction of the crack. The J-integral expression then becomes:

$$J = \frac{1}{B}\int \frac{\partial w}{dx}dV - \frac{1}{B}\int \boldsymbol{T}.\frac{\partial \boldsymbol{u}}{\partial x}dS \tag{2.47}$$

Using Divergence Theorem [38], [39] which states:

$$\int \nabla w dV = \int w \boldsymbol{n} dS \tag{2.48}$$

Applying the divergence theorem to the first term, we obtain:

$$J = \frac{1}{B}\int w n_x dS - \frac{1}{B}\int \boldsymbol{T}.\frac{\partial \boldsymbol{u}}{\partial x} dS \tag{2.49}$$

where n_x is the value of the x component of the unit normal to the surface.

Since only ∂w/∂x is present in the volume integral of the J-integral equation (2.47), application of the Divergence Theorem includes only the wn_x term:

$$\int \left(\frac{\partial w}{\partial x}\right) dV = \int w n_x dS \tag{2.50}$$

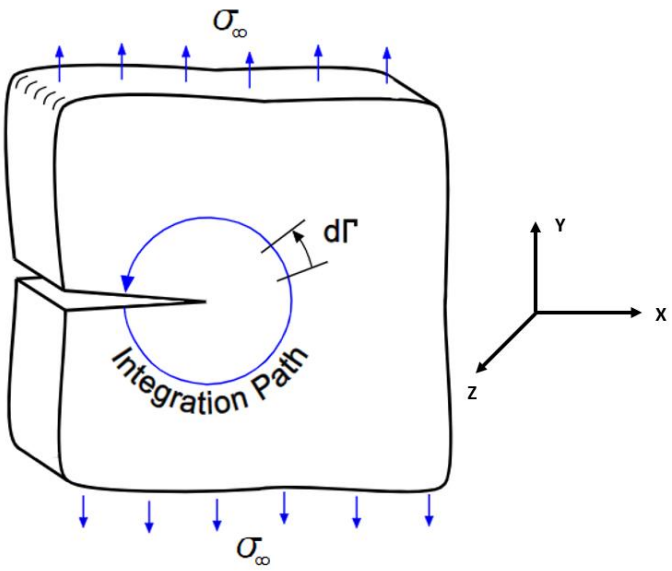

Figure 2.11: *J*-integral arbitrary contour around the crack tip

Generally, cracks propagate through objects that inherently have a *thickness, B,* such as the block shown in above. Assuming that the thickness direction is perpendicular to x, the crack propagation dimension, $n_x = 0$ on the faces of the plate, and the *J*-integral's first term is zero as well. That is, on front and back faces:

$$\frac{1}{B}\int w n_x dS = 0 \tag{2.51}$$

Also, the faces are negligibly loaded, if at all and so, $\boldsymbol{T} = 0$. Therefore, the second integral is zero too:

$$\frac{1}{B}\int \boldsymbol{T}.\frac{\partial \boldsymbol{u}}{\partial x}dS = 0 \tag{2.52}$$

The only contribution to the J-integral occur within the plate, and in it, the surface increment, dS, can be expressed as $Bd\Gamma$ (i.e., $dS = Bd\Gamma$). Inserting this relationship into the J-integral equation and expressed as path integrals gives:

$$J = \frac{1}{B}\oint wn_x Bd\Gamma - \frac{1}{B}\oint \boldsymbol{T}.\frac{\partial \boldsymbol{u}}{\partial x}Bd\Gamma \tag{2.53}$$

The thickness, B, cancels out, giving:

$$J = \oint wn_x d\Gamma - \oint \boldsymbol{T}.\frac{\partial \boldsymbol{u}}{\partial x}d\Gamma \tag{2.54}$$

Noting that, $n_x d\Gamma = dy$ and therefore, if we consider an arbitrary counter clockwise path Γ around a crack tip (see Figure 2.11), the *J*-integral was first applied to fracture mechanics by Rice [32] in 1968 for plane strain problems and is defined as:

$$J = \oint wdy - \oint \boldsymbol{T}.\frac{\partial \boldsymbol{u}}{\partial x}d\Gamma = \oint \left(wdy - \boldsymbol{T}.\frac{\partial \boldsymbol{u}}{\partial x}d\Gamma\right) \tag{2.55}$$

The *J*-integral is a path-independent parameter and Rice (1968) [32] showed that the value of *J* is independent of the integration path, Γ around the crack tip. Rice (1968) [32] and [4] further showed that *J* is equivalent to the energy release rate, *G* for nonlinear elastic cracked bodies, resulting in *J* being defined as the nonlinear energy release rate. The *J* -integral can be related to linear-elastic material theories through the application of the boundary layer approach in equation (2.13), with the assumption that Γ is a circle with radius *r* and given as:

$$J = G = \frac{{K_I}^2}{E'} \tag{2.56}$$

Consider a two-dimensional cracked body that is characterised by the deformation plasticity, Hutchinson and Rice and Rosengren (HRR) independently characterise crack tip conditions in a nonlinear elastic material. The Ramberg-Osgood stress-strain relationship is given by [4]:

$$\frac{\varepsilon}{\varepsilon_0} = \frac{\sigma}{\sigma_0} + \alpha\left(\frac{\sigma}{\sigma_0}\right)^n \tag{2.57}$$

where σ_0 is the reference stress, usually equal to the yield strength, ε_0 is the reference strain, n is the strain hardening component and α is a dimensionless constant. The HRR solution (singularity) for the actual stress and strain derivation are as follows [4]:

$$\sigma_{ij} = \sigma_0 \left(\frac{J}{\alpha\sigma_0\varepsilon_0 I_n r}\right)^{\frac{1}{n+1}} \tilde{\sigma}_{ij}(n,\theta) \tag{2.58}$$

$$\varepsilon_{ij} = \alpha\varepsilon_0 \left(\frac{J}{\alpha\sigma_0\varepsilon_0 I_n r}\right)^{\frac{n}{n+1}} \tilde{\varepsilon}_{ij}(n,\theta) \tag{2.59}$$

where I_n is an integration constant that depends on n, $\tilde{\sigma}_{ij}$ and $\tilde{\varepsilon}_{ij}$ are dimensionless functions of n and θ. Therefore, just as K provides a single-parameter characterisation of the crack tip fields in LEFM, J provides a single-parameter characterisation of crack tip fields in EPFM. Therefore, the J -integral is limited as only applicable for elastic-plastic materials for monotonic loading (no unloading) and small deformation theory is used in developing the path independence of J.

2.3.2 Crack Tip Opening Displacement (CTOD)

The crack tip opening displacement (CTOD or δ) was proposed by Wells (1961) [33] to describe crack tip conditions for materials that exhibit elastic-plastic behaviour. Wells found that for materials with high toughness, the initial sharp crack tip prior to plastic deformation is blunted. He also noticed that as crack blunting increases, the fracture toughness increases and therefore concluded that CTOD could be used to characterise the fracture toughness of materials that did not exhibit LEFM behaviour.

Within the limit of SSY, the value of CTOD is related to K or G by [4];

$$\delta = 2u_y = \frac{4}{\pi}\frac{K_I^2}{E\sigma_{YS}} \tag{2.60}$$

or

$$\delta = \frac{4}{\pi}\frac{G}{\sigma_{YS}} \tag{2.61}$$

where u_y is half the displacement at the crack tip (see Figure 2.12) that relate the CTOD approach to the SIF K and the elastic potential energy release rate, G which are both equivalent in SSY. There are two widely known definitions of CTOD: the displacement at the original crack tip proposed by Wells (1961) [33] by measuring the crack mouth opening displacement (CMOD) and

90-degree line intercept construction, commonly used for the evaluation of CTOD in finite element analysis suggested by Rice (1968) [32]and Shih (1981) [40].

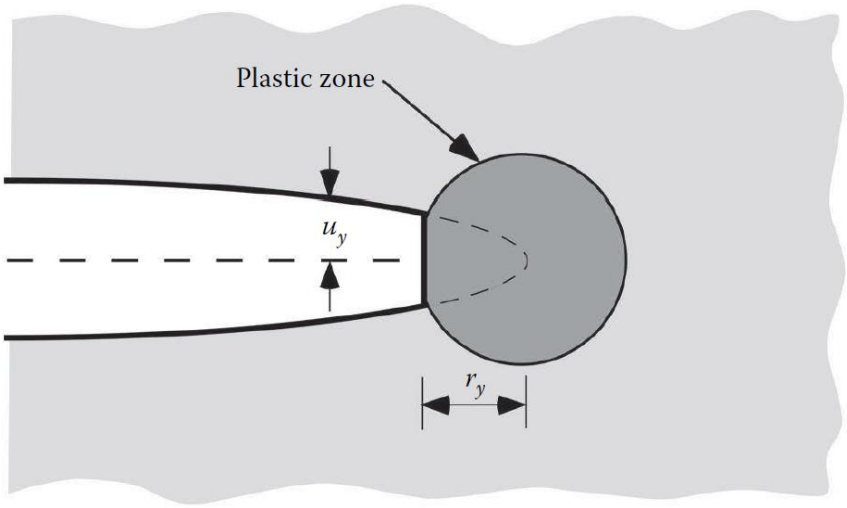

Figure 2.12: Estimation of CTOD from the displacement, u_y of an effective crack [4]

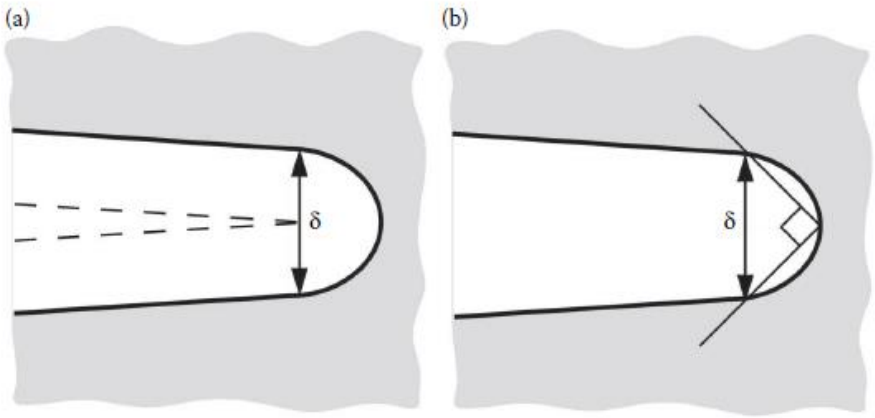

Figure 2.13: CTOD definition: (a) displacement at the original crack tip and (b) displacement at the intersection of 90-degree [4]

The *J*-integral is related to the CTOD for linear elastic fracture mechanics materials as well as applicable to non-linear conditions and given by:

$$J = m\sigma_{YS}\delta \qquad (2.62)$$

where m is a dimensionless constant that depends on stress state and material properties that is approximately unity for plane stress condition and '2' for the plane strain condition. Shih [40] further proved the *J*-CTOD relationship applies well beyond the validity limits of LEFM and therefore, *J* and CTOD are equally valid as fracture toughness parameters in EPFM.

2.3.3 Crack Growth Resistance

Crack growth in structural components or test specimen may be stable or unstable and for plane stress conditions, the Griffith energy criterion ($R = G$) is applicable. This was modified by Irwin [18] when he proposed that crack instability should occur when:

$$\frac{dG}{da} = \frac{dR}{da} \tag{2.63}$$

From the R-curve diagram in Figure 2.14, the condition for stable crack growth can therefore be expressed as:

$$R = G \tag{2.64}$$

$$\frac{dG}{da} \leq \frac{dR}{da} \tag{2.65}$$

The shape of the crack resistance curve (*R*-curve) is horizontal for ideally brittle materials because the surface energy is an invariant material property and R is independent of crack size. However, the *R*-curve can be of a variety of shapes when nonlinear behaviour accompanies fracture [4]. The characterisation of the fracture criterion anticipates that R increases when the plastic zone at SSY increases and strain hardens. Although the initiation toughness is usually not sensitive to the geometry of the structure or test specimen, it is difficult to determine the precise moment of crack initiation in most materials. The engineering definition of fracture initiation analogous to the 0.2% offset yield strength in tensile tests is usually required. Another drawback of initiation toughness is that it characterises only the onset of crack growth and does not provide further details on the shape of the *R*-curve [4].

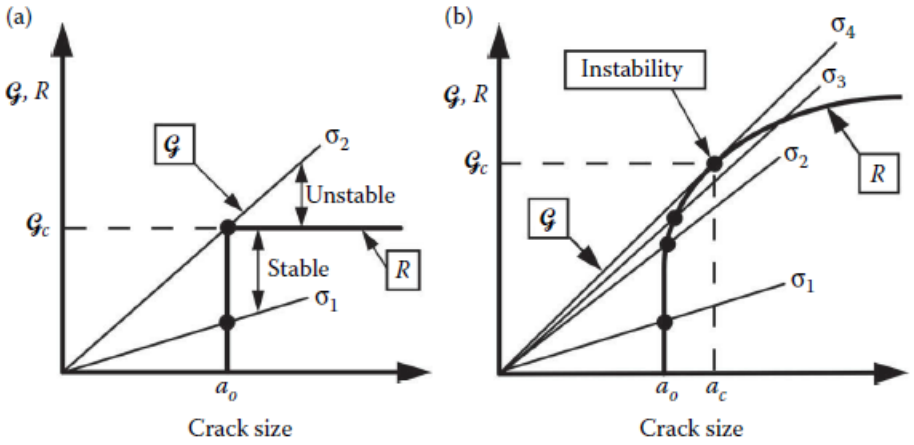

Figure 2.14: *R*-curve diagrams: (a) horizontal *R*-curve (b) rising *R* curve [4]

2.3.4 Limitations of EPFM

The application of the principles of EPFM to practical engineering problems is not as widespread as LEFM, due to the unavailability of solutions for CTOD or *J*-integral for practical geometries and materials with varieties of hardening characteristics. Numerical techniques such as the finite element method has helped to eliminate this drawback. At the same time, research and developments in relation to the transfer of laboratory material data to real life engineering components have increased the confidence in both design and safety assessments [41], [42]. Full-scale testing is also on the increase for practical applications of the principles of EPFM. For instance, burst have been conducted on pipeline until failure to determine the pipeline's burst strength and to provide information about its maximum allowable pressure [43][44].

2.4 Constraint Effects in Fracture Mechanics

Constraint is the restriction of a plastic zone within a material by the surrounding elastic region. The size of the plastic zone (constraint experienced by a specimen) can be influenced by the crack depth, specimen thickness, specimen size, crack geometry and loading configuration. Constraint can be described and measured as in-plane constraint (due to crack depth) or out-of-plane constraint (due to section thickness) [20], [45]. Constraint is an important factor in fracture toughness testing as it can have significant effects on the resultant fracture toughness values.

2.4.1 Single Parameter Fracture Mechanics

Fracture toughness experimental studies have shown that different standard cracked specimens made of similar materials have varying toughness values. This indicates that fracture toughness is not just a material property but also depends on the crack geometry, crack depth, section thickness, specimen size and loading configurations. All these can have a significant effect on the fracture toughness measurements (*K*, *J* and CTOD) [46]. Research in the past decades show that the geometry dependency of fracture toughness is attributed to the effect of crack tip constraint.

It is also known that cracked specimens which at fracture load exhibit a larger plastic zone around the crack tip have higher fracture toughness. This is due to more energy been consumed for plastic deformation and remainder of the less energy for breaking the atomic bonds ahead of the crack tip. In contrast, for specimens with smaller plastic zone that is highly constrained, more energy is present for the occurrence of brittle fracture and therefore, the fracture toughness is low. For instance, the fracture toughness of plane strain specimens is lower than plane stress ones and the effect of stress triaxiality in plane strain conditions limits the extent of the plastic zone [47].

In order to obtain a unique result for K_{IC} that is geometry independent, ASTM E399 [26], ASTM E1820 [48] and BS 12135 [49] provide restrictions for length parameters in different fracture test specimens. For the three-point bend or compact tension specimens, the following requirement must be met:

$$B, (W - a) \geq 2.5 \left(\frac{K_{IC}}{\sigma_o}\right)^2 \tag{2.66}$$

where B is the specimen thickness, W is the width and a is the crack depth. The size limits vary for different specimens providing conditions necessary for J-dominance where the crack tip fields are described only by J. As the plastic zone expands further (e.g., in elastic-plastic materials), the single parameter described by J alone loses its validity to quantify the stresses at the crack tip and a second constraint parameter is then employed.

2.4.2 Two Parameter Fracture Mechanics

Extensive research has been conducted in quantifying the effect of constraint on standard specimen geometries as well as typical cracked structural configurations. In all the investigations, the proposed remedy in both the elastic and elastic-plastic cases have been to define a second parameter in conjunction with K or J. This is related to non-singular stress expansions that it quantifies and so can be used to correct variations in crack tip constraint. The elastic-plastic HRR field solution has therefore been improved by introducing second parameters and corresponding two-parameter crack tip field. The K-T or J-T approach, J-Q theory and J-A_2 three-term solution are examples with parameters T, Q and A_2 used to quantify the constraint effect on the crack-tip field and fracture toughness in elastic and elastic-plastic conditions [46], [47], [50].

2.4.2.1 The Elastic T-Stress Approach

For linear-elastic materials, the singular stress field in equation (2.67) is the leading term of the expansion proposed by Williams [19]. Larsson and Carlsson [51] were the first to denote that, the second, non-singular term in the Williams' expansion has significant effect on the shape and size of the plastic zone near the crack tip under SSY condition.

Rice [32] researched further the limitations of the SSY approximation and rewrote the first two terms of the Williams' series expression as:

$$\sigma_{ij} = \frac{K_I}{\sqrt{2\pi r}} f_{ij}(\theta) + T\delta_{1i}\delta_{1j} \tag{2.67}$$

where the first term represents the singular elastic K field with K_I as the SIF, and the second term is non-singular with magnitude denoted by a parameter T and δ_{ij} (Kronecker delta). This leading

term parameter is called the elastic *T*-stress since *T* represents the tensile stress acting parallel to the crack plane. Equation (2.67) shows clearly that the second term, or *T*-stress, influences the crack tip field and therefore, if an applied *T*-stress varies at a constant *K*, the plastic zone will vary in size and shape.

Different numerical and FEA calculations have been developed over the years to determine the *T*-stress for a variety of fracture specimens and geometries. Leevers and Radon [52] introduced the biaxiality ratio parameter in reference to the *T*-stress and *K*-factor that is widely used:

$$\beta = \frac{T\sqrt{\pi a}}{K_I} \tag{2.68}$$

As an example, a through-thickness crack in an infinite plate subjected to a remote tensile stress, σ (Griffith's problem) has a biaxiality ratio of:

$$\beta = \frac{T}{\sigma} = -1 \tag{2.69}$$

and thus, the remote stress, σ induces a compressive *T*-stress equal in magnitude to the remote tensile stress in the direction parallel to the crack plane in the plate [50]. A compilation of the *T*-stress solutions available at that time through the biaxiality ratio, β for different geometries, including the conventional M(T), SENB, CC(T) and C(T) specimens with full range of a/W ratios was by Sherry et al [53]. When the measured T-stress is small or positive, there is a variation causing the crack tip opening stress field to be slightly greater than SSY limit (high constraint conditions). However, when the measured T-stress is negative, there is a reduction in the out-of-plane stress which reduces triaxiality at the crack tip and reduces the crack tip opening stress fields (low constraint conditions). These trends are evidenced in Figure 2.15 and Figure 2.16, the *T*-stress as a function of crack size varies between different test geometries

Also, the T-stress can be determined either by numerical analysis or experimentally. Though, the later can be challenging, there are some indirect methods and techniques that can provide insights into its value. Combined use of digital image correlation (DIC) and FEA can be used to validate and find T-stress estimates experimentally since *T*-stress and *J*-integral are related through the stress intensity factor, *K*. Similarly, *T*-stress can be obtained indirectly from *J*-integral fracture testing but again, this may require a combination of techniques and careful analysis. The *T*-stress approach is also based on a linear elastic analysis and applies to defect problems where plastic deformation is limited to a small region ahead of the crack tip as in Figure 2.17. When the plastic deformation becomes larger, other approaches such as the *J*-*Q* are explored, as discussed in the next section.

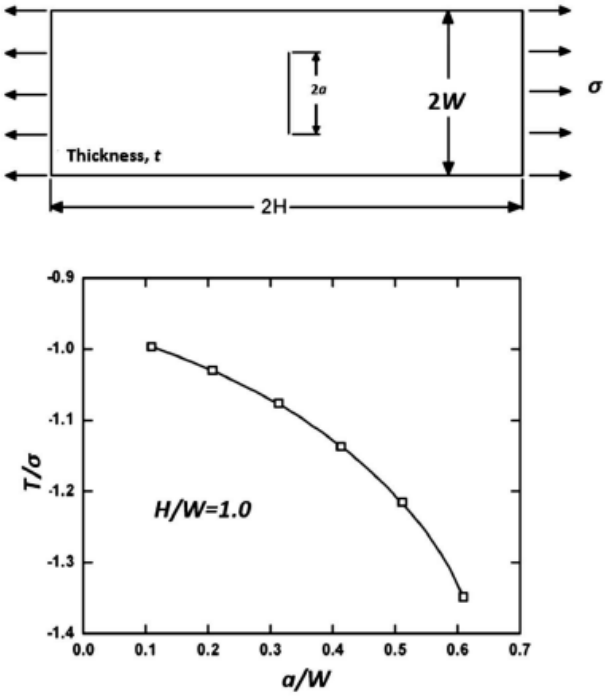

Figure 2.15 Schematic diagram of the CC(T) specimen analysed and the T-stress as a function of crack size [53]

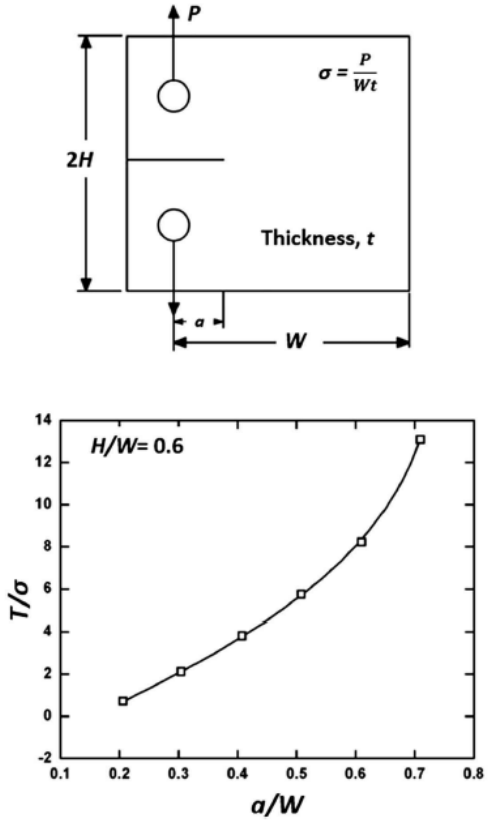

Figure 2.16: Schematic diagram of the C(T) specimen analysed and the T-stress as a function of crack size [53]

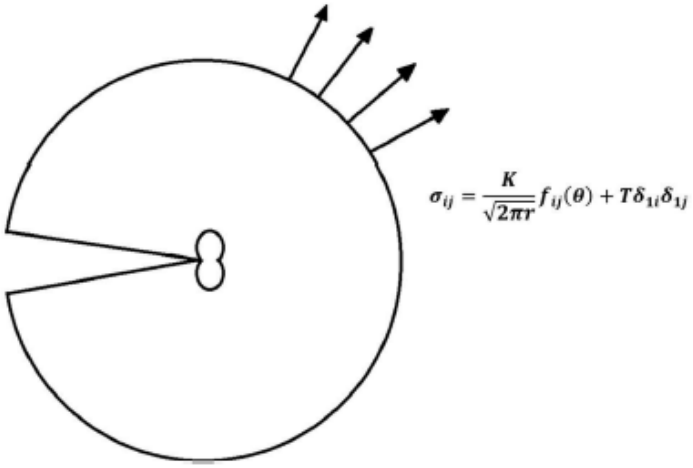

Figure 2.17: Modified boundary layer model to study the effects of T-stress on the crack opening stress [5]

2.4.2.2 The *J*-*Q* Theory

The *T*-stress approach has limitations since the *T*-stress is an elastic constraint parameter. It becomes invalid as the plastic zone expands at the crack tip leading to a new second parameter, *Q*, for elastic-plastic crack under SSY and LSY conditions. O'Dowd and Shih [54] performed a series of detailed elastic-plastic FEA calculations for various geometries. Based on the theory of deformation plasticity, they developed the *J*-*Q* theory as a numerical solution to describe the elastic-plastic crack tip field. By performing full-field FEA, they found the difference between the full-field numerical solution σ_{ij} and the HRR field $(\sigma_{ij})_{HRR}$ is approximately a uniform hydrostatic stress ahead of the crack tip. The following two-term crack tip stress field was proposed:

$$\sigma_{ij} = (\sigma_{ij})_{HRR} + Q\sigma_0\delta_{ij}\,; \text{for } r > \frac{J}{\sigma_0} \quad and\ |\theta| \le \pi/2 \tag{2.70}$$

where $(\sigma_{ij})_{HRR}$ is the HRR field, σ_0 is the yield stress and Q is a stress triaxiality parameter to reflect the hydrostatic stress level at the crack tip. The Q parameter is defined from the FEA results of the required crack opening stress $(\sigma_{\theta\theta})_{FEA}$:

$$Q = \frac{(\sigma_{\theta\theta})_{FEA} - (\sigma_{\theta\theta})_{HRR}}{\sigma_0};\ \ at\ r = \frac{2J}{\sigma_0}\ \ and\ \theta = 0 \tag{2.71}$$

Furthermore, O'Dowd and Shih [54] and O'Dowd [45] suggested an alternative reference stress field to replace the HRR solution using the SSY stress field $(\sigma_{ij})_{SSY}$ with *T*=0, where $(\sigma_{ij})_{SSY}$ is determined by FEA using the boundary layer model. These two reference stress fields result in

two formats of Q definition and O'Dowd [45] discussed the difference in Q caused by these two reference stress fields. However, caution should be taken to ensure consistent choice of a reference stress field and the corresponding Q definition when using the J-Q theory. Generally, Q has been used extensively to quantify the constraint effect on the fracture toughness parameters, J_C and J_{IC} as shown by O'Dowd and Shih [54], Joyce and Link [50] and other authors.

A limitation of the Q parameter is that it varies (Q is distance and load dependent under LSY) on the J-R curve during ductile crack growth as reviewed by Faleskog [55] and thus, is not appropriate to describe the constraint effect on a crack growth resistance curve.

Aside the J-T and J-Q approaches, there are other two-parameter constraint theories such as the three-term solution, J-A_2, which is based on the theory of deformation plasticity under plane strain conditions. This approach will not be considered in this thesis and the reader is referred to papers by Chao et al [56] and Yang et al [57] for further details on this approach.

2.4.3 Out-of-Plane Constraint Parameter

There have been progress and wide use of the two-dimensional plane strain method in engineering structural integrity standards such as the R6 [24] and BS 7910 [23] to quantify fracture toughness data in relation to the level of constraint at the crack tip. However, these standards are still limited to materials that exhibit the behaviour of thick specimens, such as deeply cracked bars under bending that provide conservative defect assessment.

In real structural components, cracks are relatively shallow and subjected mostly to 3-dimensional mixed mode loading. Fracture toughness does not only depend on the geometry and loading configurations (in-plane constraint) but also depends on the thickness (out-of-plane constraint). Several researchers including [58]–[66] have shown that fracture toughness depends on the 3D out-of-plane stress near the crack front and established that fracture toughness also depends on the thickness of the test specimen.

Guo [66]–[68] extended the HRR analysis series and introduced the T_z factor that has been shown to be an important parameter to characterise the out-of-plane constraint effect in 3D cracked body accurately:

$$T_z = \frac{\sigma_{33}}{\sigma_{11} + \sigma_{22}} \tag{2.72}$$

where σ_{33} is the out-of-plane stress and σ_{11}, σ_{22} are the in-plane stress components as illustrated in Figure 2.18. The subscripts $(1,2,3) = (x, y, z)$ are the Cartesian coordinates or (r, θ, z) for

polar coordinates. The effect of T_z on three-dimensional crack front-fields and fracture toughness have been systematically investigated by Guo [65], [66]. The principles and applications of $K-T_z$, $J-T_z$, $K-T-T_z$ and $J-Q-T_z$ to fracture and fatigue have been demonstrated by [58], [65], [69], [70]. However, Zhang and Guo [67], [71] have shown that except for some numerical results and approximate expressions for crack under the mode I loading, the detailed distribution of T_z near the crack front under the mixed-mode loading has not been obtained simply because of its complicated 3D characteristics. The outcome of this investigation has limited the application of the $K-T_z$, $J-T_z$, $K-T-T_z$, or $J-Q-T_z$ theory.

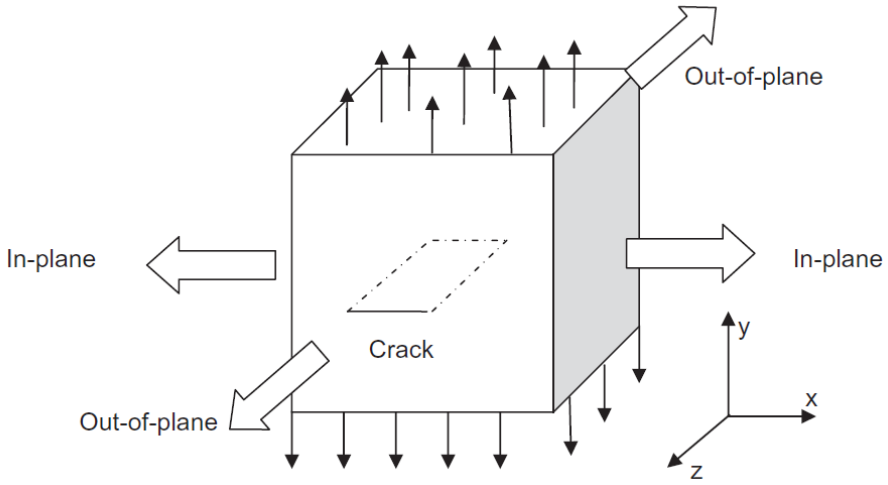

Figure 2.18: In-plane and out-of-plane directions for a through thickness crack in 3D structural component [62]

Figure 2.19 illustrates the historical journey for estimation of crack tip fields by including the in-plane (crack depth) and out-of-plane (wall thickness) constraint parameters that are sufficient to guarantee appropriate level of crack tip triaxiality.

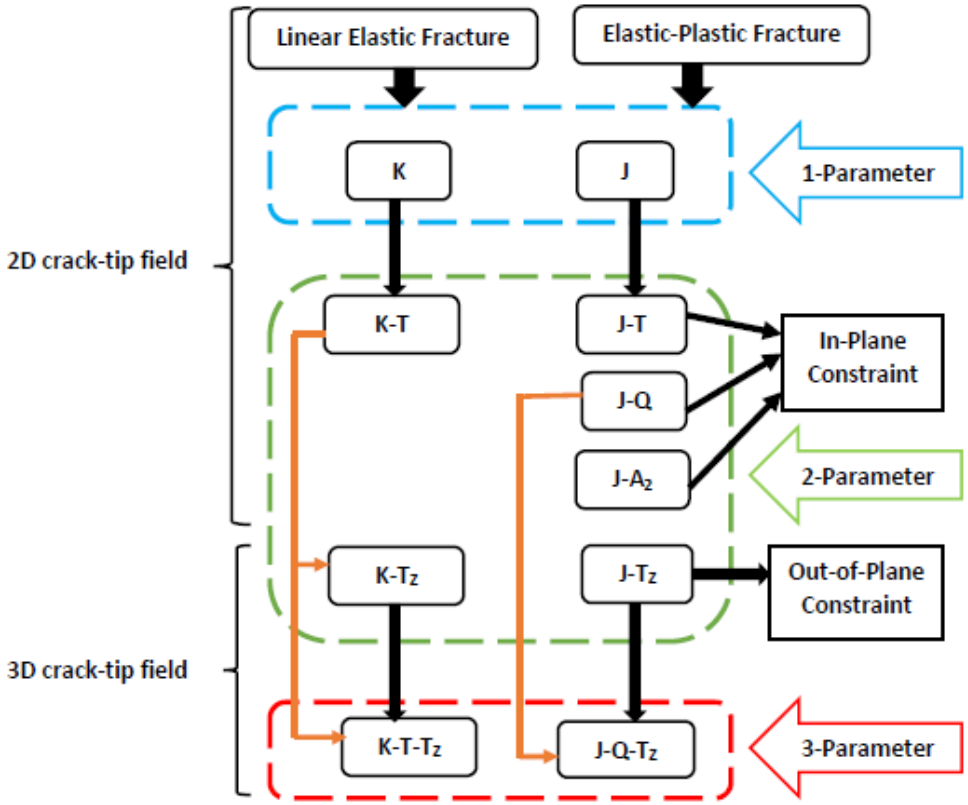

Figure 2.19: Development of crack-tip fields estimation by including in- and out-of-plane constraint parameters

2.5 Fracture Mechanisms in Metals

The study of fracture mechanisms plays a key role in the development of engineering metallic alloys, manufacturing and assessment of mechanical integrity of structures. In the steel industry, due to the changing and challenging environments, the development of new alloys occurs rapidly to replace existing compositions for more robust dual-phase and multi-phase steels. At present, these steels are used in structural applications where they have replaced more conventional high strength low alloy steels, offering opportunities for weight reduction [72].

Detailed composition knowledge is required in the development of new high strength steels in terms of understanding their deformability and cracking resistance. Also, the study of the micro-mechanisms of failure is important in the assessment of mechanical integrity of structures for flaws that appear either during manufacturing or under in-service conditions. Therefore, developing damage-tolerant microstructures is of significant importance in many fields of engineering [72], [73].

The three most common fracture mechanisms in metals and alloys are ductile fracture, cleavage fracture and intergranular fracture (Figure 2.20). Ductile materials often fail as result of nucleation,

growth and coalescence of microscopic voids that initiate at inclusions and second-phase particles. This mechanism is characterised by a slow stable crack extension or growth that absorbs more energy [4]. High strength steels tend to have lower toughness and increased susceptibility to brittle facture at low temperatures, leading to catastrophic failure without significant plastic deformation.

Cleavage fracture involves separation along specific crystallographic planes, where fracture can be preceded by large-scale plasticity and ductile crack growth. Intergranular fracture occurs when the grain boundaries are the preferred fracture path in the material. It is also worth to note that brittle fracture includes both cleavage and intergranular fracture [4], [72]. In high strength steels, the presence of high levels of alloying elements and the presence of residual stresses can promote cleavage. Cold temperatures further increase the susceptibility to cleavage fracture.

Other fracture mechanisms for high strength steels in Arctic/low temperature environments may include:

Hydrogen embrittlement: In Arctic conditions, the presence of hydrogen can significantly affect the fracture behaviour of components made of high strength steels. Hydrogen embrittlement can initiate through sources such as corrosion or exposure to hydrogen gas and this reduces the ductility and increases brittle fracture [74].

Fatigue fracture: High strength steel components in Arctic regions are often subjected to cyclic loading (e.g., wave-induced loading on offshore structures). Fatigue fracture can occur due to the accumulation of microcracks, which can propagate and lead to sudden failure under cyclic loading conditions. Cold temperatures can further accelerate fatigue crack growth and reduce the fatigue life of the steel [75].

Stress Corrosion Cracking (SCC): In the presence of corrosive environment, such as seawater, high strength steels can be prone to stress corrosion cracking. SCC occurs due to the combined action of tensile stress and a corrosive environment, leading to crack initiation and propagation [76].

Therefore, the influence of crack tip constraint and stress triaxiality on ductile and cleavage fracture is of considerable importance for the assessment of structural integrity of many industrial components. Linear and non-linear fracture mechanics concepts are usually employed for these assessments. In contrast, micromechanical models developed in the framework of a local approach to fracture have advantage that the corresponding material parameters for fracture toughness can be transferred in a more general way between various specimen geometries. Though the

development of such models has been in existence for over 50 years, these approaches are not generally accepted or incorporated into international engineering standards [72].

In this thesis, an overview of the methodologies associated with cleavage and ductile fracture mechanisms at the microscopic scale (local) and through a multiscale approach is given. The transfer of this local information to the macroscale, over which the performance of structural components as well as materials characteristics are usually defined shall be presented.

2.5.1 Cleavage Fracture

Cleavage fracture is the term used to describe the process by which material separation occurs by breaking atomic bonds along certain crystallographic planes. The fracture is transgranular (fracture that follows the edges of lattices in a granular material, ignoring the grains in the individual lattices) and the cleavage planes are those with fewer bonds and greater pacing between the planes [4], [5]. Cleavage may be brittle, but can be preceded by large scale plastic flow and ductile crack growth as pointed out by Knott [7]. This type of fracture is possible in body centred cubic (BCC) materials, such as ferritic steels, that cleavage occurs along the planes (1 0 0). Fracture by cleavage takes place with the lowest expenditure of energy and the overall deformation is small since fewer bonds must be broken and distances between planes is greater [4].

The grains in polycrystalline materials are crystallographically disoriented with respect to each other and cleavage fracture changes its orientation each time it encounters a grain boundary as in Figure 2.20b. The fracture planes in each grain can be seen to be highly reflective, given a shiny appearance on the overall cleavage fracture surfaces. Cleavage fracture in BCC materials is promoted by low temperature and high strain rates as a result of limited number of active slip systems.

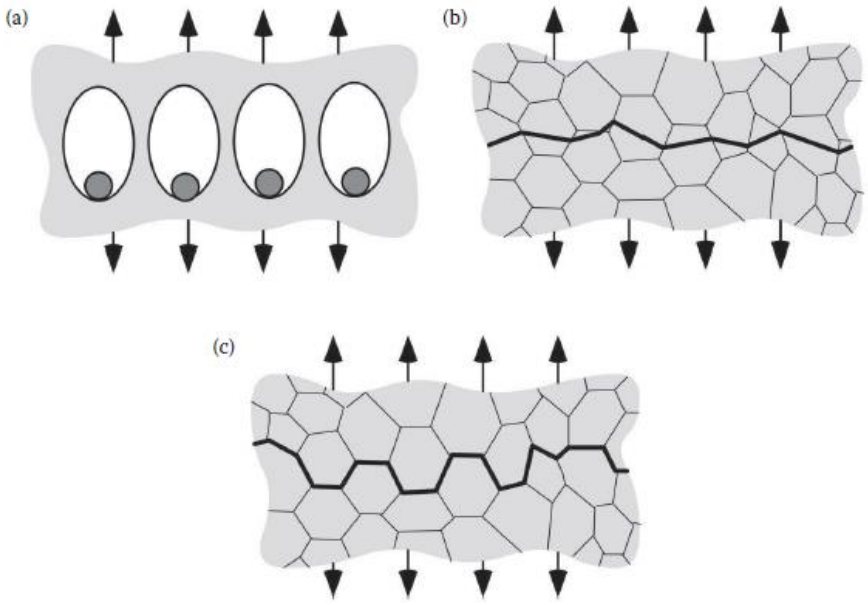

Figure 2.20: Three micromechanisms of fracture in metals: (a) Ductile fracture (b) Cleavage fracture (c) Intergranular fracture [4]

Fracture surfaces observed on ferritic steels are shown in Figure 2.21 where these micrographs reveal that the orientation of cleavage facets change when they cross sub-boundaries, twin boundaries or grain boundaries. Steps or ridges appear on the fracture surface to compensate for the local misorientation, at grain boundaries (see Figure 2.21). For BCC metals such as ferritic steels and in the case of mechanical twins, these steps look like indentation marks which look like "tongues" (Figure 2.23). In order to maintain equilibrium of the crack front, the nearest steps gather to form a single step of higher height, leading to the formation of "rivers" in Figure 2.22.

Cleavage fracture in ferritic steels is often initiated from brittle second phase particles such as carbides that have a spherical shape. As a result of fibre loading mechanism, spherical or oblong carbides experience very high stresses as the surrounding ferrite matrix is plastically deformed. As illustrated in Figure 2.23, spherical carbides are more prone to the initiation of cleavage fracture. Non-metallic inclusions such as manganese sulphides (MnS) can also act as initiation sites for cleavage fracture in ferritic steels [4], [5], [72].

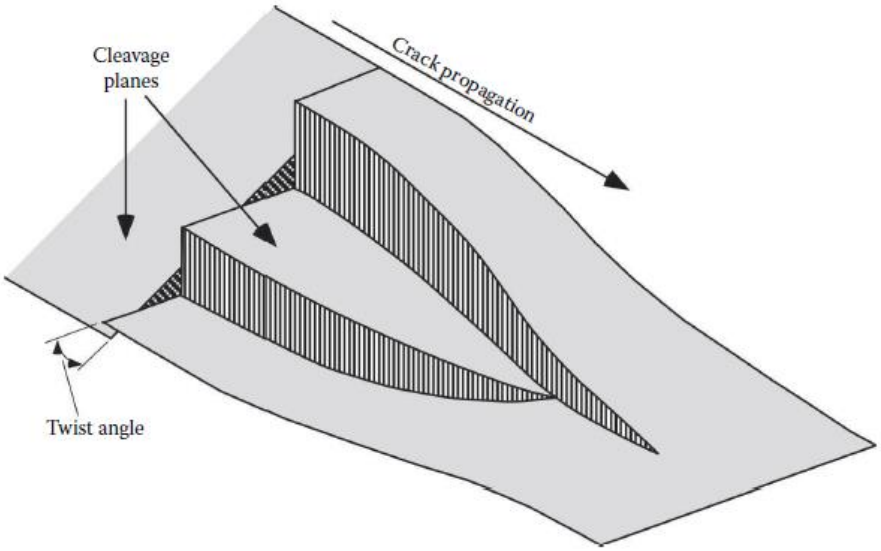

Figure 2.21: Formation of river patterns as a result of a cleavage crossing a twist boundary between grains [4]

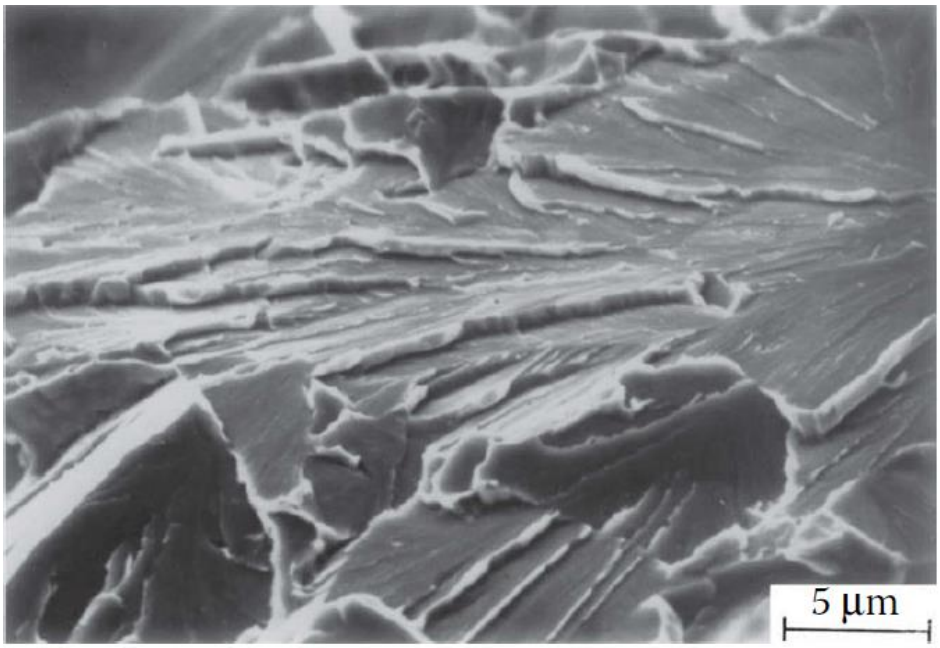

Figure 2.22: River patterns in A 508 Class 3 steel showing tearing between parallel cleavage planes [4]

Various micromechanical models have been developed for nucleation of cleavage fracture. The Smith model is of particular significance as it incorporates the important microstructural features of grain boundary carbides. The model considers stress concentration as a result of a dislocation pile-up at a grain boundary carbide [7].

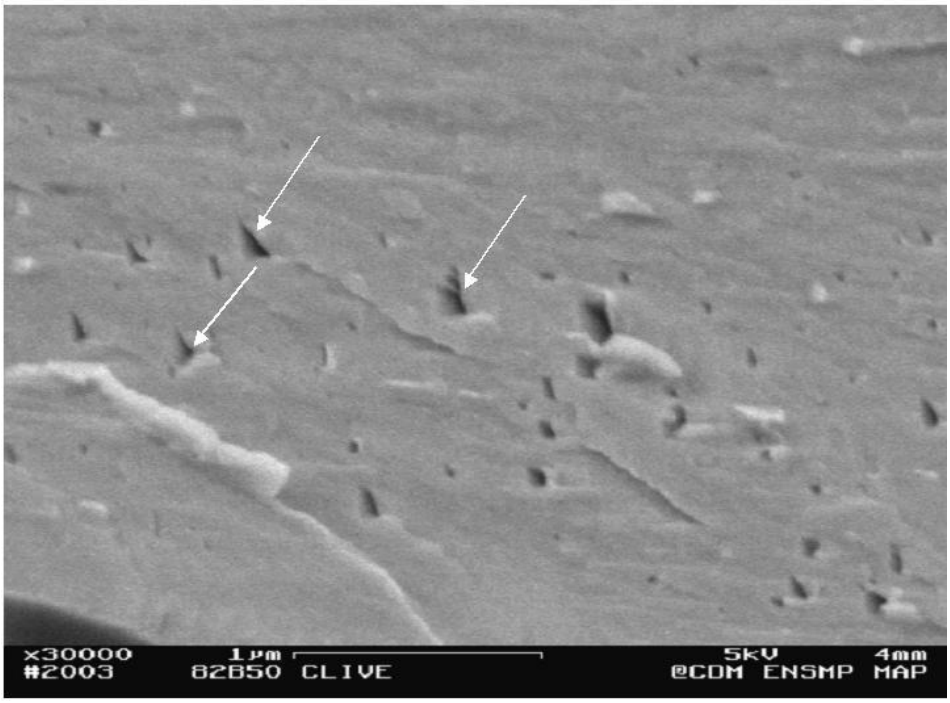

Figure 2.23: SEM micrograph of a fracture surface of low ally steel where the arrows identify tongue features

Aside the approaches outlined in section 2.4 in quantifying constraint, there are other methods such as the statistical and the Master Curve (MC) techniques. The statistical approach is based on the fact that scatter in fracture toughness data can also be caused by the effect of constraint, in particular when the data is based on specimens with different size and geometry leading to variations in plasticity and constraint between specimens [5]. The most widely used statistical models are those derived from the work of Beremin (1983) [77] and is based on the Weibull weakest link theory. The weakest link concept postulates that failure of the body of a material containing a large number of statistically independent volumes is triggered by the failure of one of the reference volume. The reference volume is the material volume related related to likelihood of finding cracked carbide [4], [5], [72] [78]. The weakest link theory as can be drawn from the name depicts an analogy between the material's reliability and a chain composed of individual links. In this analogy, the material is only as string as its weakest link and if one link in the chain is weaker than others, it will break first, causing the material material or structure to fail. It takes into account the probability distribution of strengths and failure charcteristics of individual sites or mechanisms [78]. The Master Curve concept on the otherhand, is based on the fact that the size effects on the fracture toughness data obtained from laboratory specimen do not directly describe the fracture behaviour of real flawed structures, posing a transferability problem for structural integrity engineers. The technology associated with the MC developed by Wallin [79] has the capability of

defining the position and shape of the ductile-to-brittle transition range more accurately in ferritic steels [80]. A significant part of the MC technology has been the observation that most grades of ferritic steels share a common transition shape. Readers are advised to refer to these concepts for further details as they are not treated in detail in this thesis.

As previously mentioned, fracture toughness data in the cleavage regime such as the ductile-to-brittle transition region can have large amount of scatter requiring statistical methods to analyse data. Further, scatter in fracture toughness data can also be caused by random variation in microstructural level and the effect of constraint, in particular in the latter, when the data is based on specimens with different size and geometry (different stress states) leading to variations in triaxiality and plasticity between specimens [5]. In addition, constraint has more influence on maximum stress and therefore is of more concern during cleavage fracture, and is less important for ductile fracture which is strain controlled [4], [5].

2.5.2 Intergranular Brittle Fracture in Ferritic Steels

From the literature, intergranular fracture should be observed preferentially in many multiphase/polycrystalline metals rather than transgranular cleavage fracture. However, in ferritic steels due to the reinforcement effect of a number of elements segregated along the grain boundaries especially in carbon, brittle fracture occurs at low temperatures by transgranular cleavage [4] [81]. One key factor that contribute to intergranular brittle fracture in ferritic steels relevant to this research is the stress state. The state of stress, including the presence of tensile stresses, can promote crack initiation and propagation along grain boundaries. High stresses acting perpendicular to the grain boundaries can cause grain boundary separation and facilitate intergranular crack propagation [4].

2.5.3 Ductile Fracture

Ductile fracture involves extensive plasticity and rough fracture surfaces that manifest in various ways depending on the material system, level of constraint and boundary conditions. This type of fracture is seen in face-centred-cubic (FCC) pure metals in which polycrystalline tensile specimen neck down to a stage just before separation. Failure may occur by void coalescence or mechanical instability of the specimen itself, where voids nucleate at inclusions and grow plastically. When they finally coalesce, a crack forms and the material fractures. Therefore, the commonly observed stages in ductile fracture are [4]:

- Formation of a free surface at an inclusion or second-phase particle by interface decohesion or particle cracking

- Growth of the void around the particle by means of plastic strain and hydrostatic stress
- Coalescence of the growing void with adjacent voids

2.5.4 Ductile-to-Brittle-Transition

Fracture in the ductile-to-brittle region is mostly controlled by the competition between ductile tearing and cleavage fracture as illustrated in Figure 2.24 in the transition region [5]. When loading is initially applied to a test specimen or structural component in the upper transition region, cleavage does not occur because there are no critical particles present near the crack tip. As the crack grows, more material is sampled and cleavage fracture eventually occurs when the growing crack samples a critical particle [4]. The fracture toughness locus is plotted in a typical three-region behaviour where the upper-shelf corresponds to ductile fracture and the lower-shelf to cleavage fracture and the transition region where both types of fracture are observed.

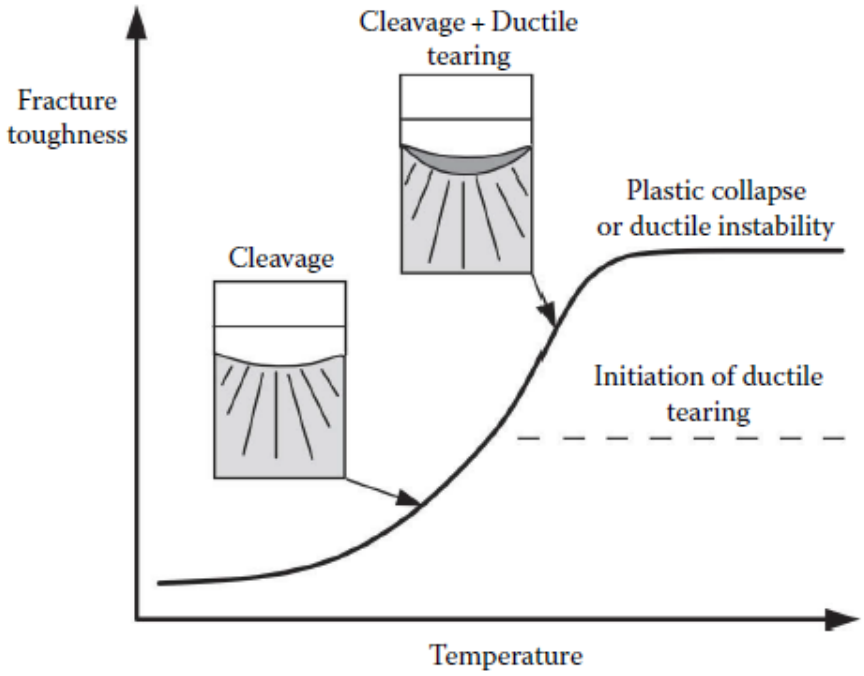

Figure 2.24: Ductile-to-brittle transition curve [4]

Depending on the chosen geometry and specimen size, either ductile or brittle fracture can occur since a high crack tip constraint promotes cleavage fracture conditions and low constraint can promote ductile void growth mechanism at temperatures from mid-ductile to brittle transition regime.

2.6 Fundamentals of High Strength Steels

High strength steels (HSS) are advanced structural steels that have nominal yield strengths of 460 MPa or greater, possess satisfactory ductility for either conventional plastic design or performance-based design, toughness and weldability for practical use in engineering. These steels have been available for many years, but their use in offshore, marine and construction engineering is limited except in specialised applications. This is largely due to the fact that, in general, satisfactory performance can be achieved with cheaper, more readily available lower strength conventional steels that have yield strengths in the range 250 MPa to 350 MPa [82]. Also, in comparison to the HSS, lower strength steels are well documented in existing codes and standards [83].

With the significant petroleum reserves in the Arctic regions in recent years, there have been increasing application of structural steels in critical conditions with ambient temperature as low as $-70℃$. At low ambient temperature, ferritic steels often experience unstable brittle failure that occurs at a remote stress level significantly lower than the material yield strength; without noticeable prior deformations and with a significant scatter in the critical driving forces at the crack front which leads to catastrophic consequences [84][85].

Though HSSs are susceptible to brittle fracture at low temperatures, they offer numerous benefits in terms of structural weight reduction, less material consumption and welding needs, lower manufacturing, transportation and assembly costs. Therefore, a more economic design and safety when strength to weight ratio is important. The increasing use of HSSs in a range of steel structures in the construction industry such as buildings and bridges, offshore and marine industries for structures such as jackets, topsides, pinions, jack-up structure legs, racks, vessel cranes and offshore wind has necessitated their failure assessment to be included in codes and standards [83].

In recent years, considerable amount of research has been undertaken on high strength steels providing data to support their application especially in the offshore sector. However, there is limited information on the long-term use of high strength steels in seawater particularly under the severe environment conditions to which structures in the Arctic regions are subjected. Further, most codes and standards relate to medium strength steels and most cases the use of design formulae is limited to steels with yield strengths less than 500 MPa which is a significant drawback for the use of HSSs. Despite the increasing amount of data available from research and testing, very little of this has yet found itself into codes and standards especially in terms of constraint effect on fracture toughness.

2.6.1 Production Routes and Chemical Composition

The advances in material and production technology in recent years have allowed the production of steels with not only higher strength, but also with better toughness, higher weldability, corrosion resistance and improved cold formability making HSS an attractive material for engineering structural applications. Generally, the strength of steel is controlled by its microstructure which varies according to the chemical composition, thermal history and deformation processes it undergoes during the production times [83][86]. In order to meet the requirements of HSS to be readily weldable as well as showing a higher strength, heat treatment techniques are implemented and depending on the carbon content, austenite, martensite, bainite, pearlite and ferrite are formed [87].

The common heat treatments methods applied for the development of high strength steels are: normalising (N), quenching and tempering (Q+T) and Thermomechanical Controlled Process (TMCP). Most moderate strength of up to 460 MPa and 690 MPa are produced by normalising and TMCP respectively. For higher strength up to 1100 MPa, quenching and tempering production process is employed to obtain a finer grain size [82], [83], [86]. Producing structural steel by normalising is generally carried out by hot rolling at high temperatures above 950℃, followed by reheating the hot-rolled plates to some 900℃ and subsequent free cooling in air to obtain a refined microstructure of ferrite and pearlite as illustrated by process A in Figure 2.25. The disadvantage of this process is that there are still higher alloying contents that can influence plate weldability [86], [88].

The Q+T heat treatment (process C in Figure 2.25) is applied after hot rolling and consists of an austenitisation, quenching in water or a suitable medium that cools fast enough so that there is no time for the formation of ferrite and pearlite which require a diffusion process. A tempering process is then applied to the plate that offer the possibility to relax the effect that strength decreases while increasing toughness to obtain a steel plate with the satisfactory combination of tensile and toughness properties [86]. Another heat treatment method to create extremely fine-grained microstructure is by the thermomechanical controlled process by a skilled combination of rolling steps at a certain temperature and a close temperature control (processes D to G in Figure 2.25). The gain in strength obtained by the grain refinement allows to reducing effectively the carbon and alloying content of the TMCP steel as compared to the normalised of the same grade. The improved weldability that results from the thinner steel composition is a major benefit of the TMCP plates [88][82], [86]. Using the TMCP technique in conjunction with accelerated cooling

(AC), thicker plates and higher yield strength grades are obtainable with the use of very few alloying elements [86].

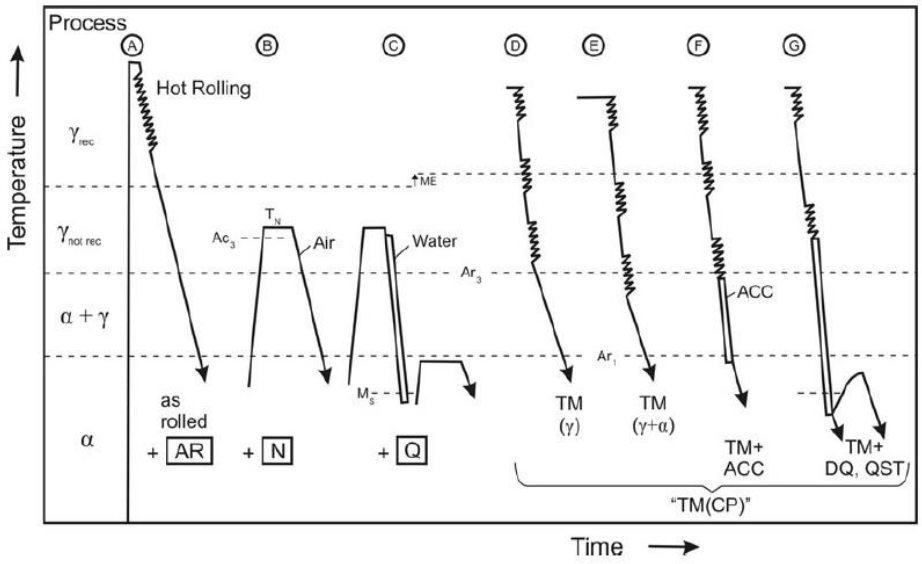

Figure 2.25: Temperature-time procedures used in plate production: normalise (process A+B), quenched and tempered (process A+C) and different TMCP processes (D-G) [88]

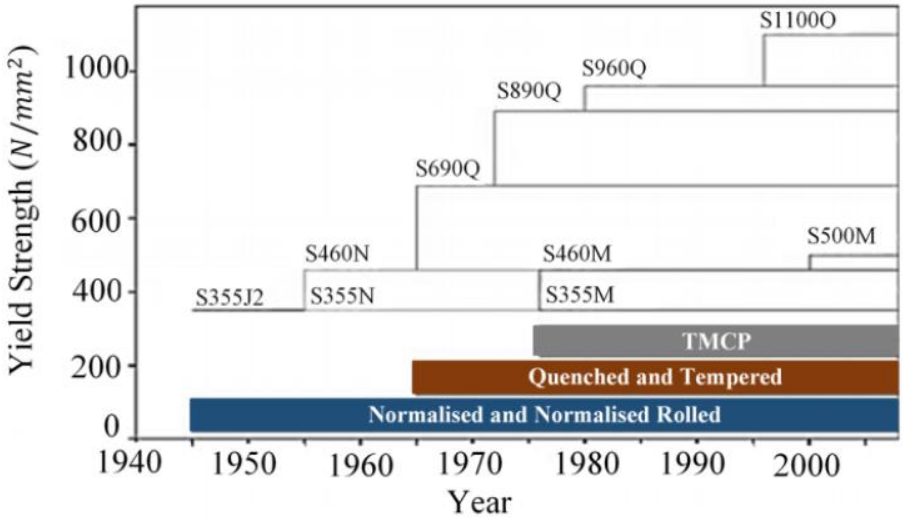

Figure 2.26: Historical development of steel grades and processes [86]

Figure 2.26 shows the historical development of higher strength steel grades over the last decades using the quenching and tempering technique to produce steels with very high yield strengths (S690Q, S890Q, S960Q and S1100Q). Similarly, TMCP steels with moderate yield strength but higher toughness (S355M, S460M and S500M) are also presented in Figure 2.26.

Aside the thermal history of steel, the chemical composition has effect on the formation of its microstructure and the mechanical properties, where strength is primarily controlled by the amount

of carbon. Increasing carbon content increases hardness and strength and improves hardenability, but carbon also increases brittleness (reduction in toughness) and reduces weldability because of the tendency to form martensite. Therefore, well understood and established metallurgical principles can be used to satisfy the overall mechanical property requirements for HSS by [83]:

- Reduction in carbon content to improve weldability and toughness
- Decreased grain size (ferrite and/or bainite) by microalloying with Niobium (Nb), Vanadium (V) or Aluminium (Al) through some form of thermomechanical process increases strength and toughness
- Increased strength is also achieved by Manganese (Mn) and molybdenum (Mo) and increased fracture toughness by addition of nickel (Ni), chromium (Cr) and copper (Cu)
- Decreased impurity content of sulphur (S), phosphorus (P) and oxygen (O) to increase toughness in particular and through thickness homogeneity

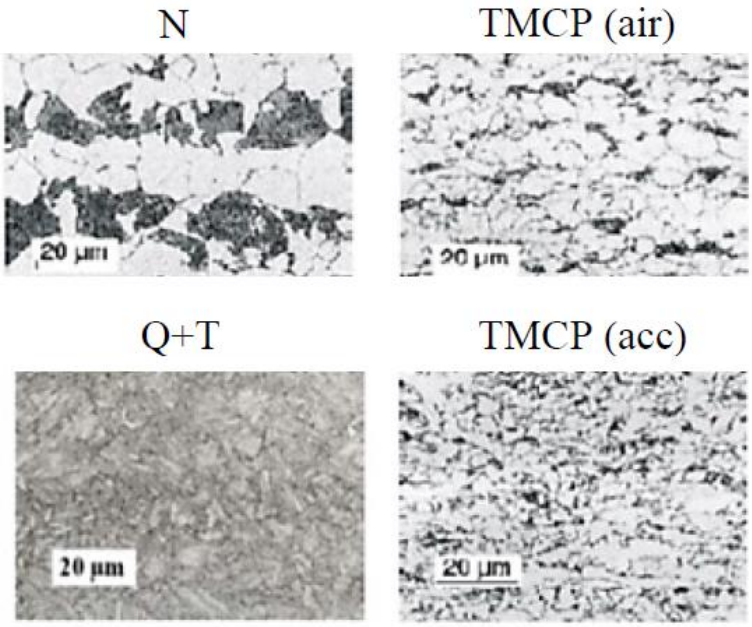

Figure 2.27: Heat treatment applied in high strength steels [86]

2.6.2 Structural Integrity of HSS Pipelines

Over the years, the need to guarantee the structural integrity of pipelines has attracted much attention to researchers and engineers alike. The results of a catastrophic failure would not only cause damage to the environment, but also potential injury, loss of life as well as economic loss. Such a guarantee of security can only be achieved through an integrated approach, involving all aspects of quality control during steel production, pipeline fabrication, assembly, installation, operation and maintenance.

In practice, this is complicated by the fact that oil and gas pipelines, when in service, routinely must withstand high operating pressure as well as high levels of CO_2, H_2S and chloride. Therefore, the high strength steels used in these applications must be resistant to various aspects of in-service degradation [89]. High strength steels should be examined for possibility of hydrogen damage and crack-like defects in-service both in the parent metal and weldments [83].

2.6.3 Stress-Strain Curves for HSS

The primary tensile properties of high strength steels are the yield stress (YS), the ultimate tensile strength (UTS), the strains at failure (ε) and strain hardening (n), reduction in area and yield to tensile strength ratio. An example of stress-strain curves of various steel grades with increasing strength are shown in Figure 2.28 where it is observed that, with an increase in the yield strength, the yield plateau becomes shorter and eventually disappears when the yield strength is less than 500 MPa. Furthermore, the strains corresponding to ultimate tensile strengths are lower for steels with higher yield strengths, which implies worse ductility. It should be noted that steels demonstrating rounded response utilises an offset yield point (permanent deformation) at 0.2% plastic strain (the so-called proof strength) for the estimation of yield strength or 0.5% for total deformations [90]. The 0.2% offset value is usually used for steels with no clearly defined yield plateau.

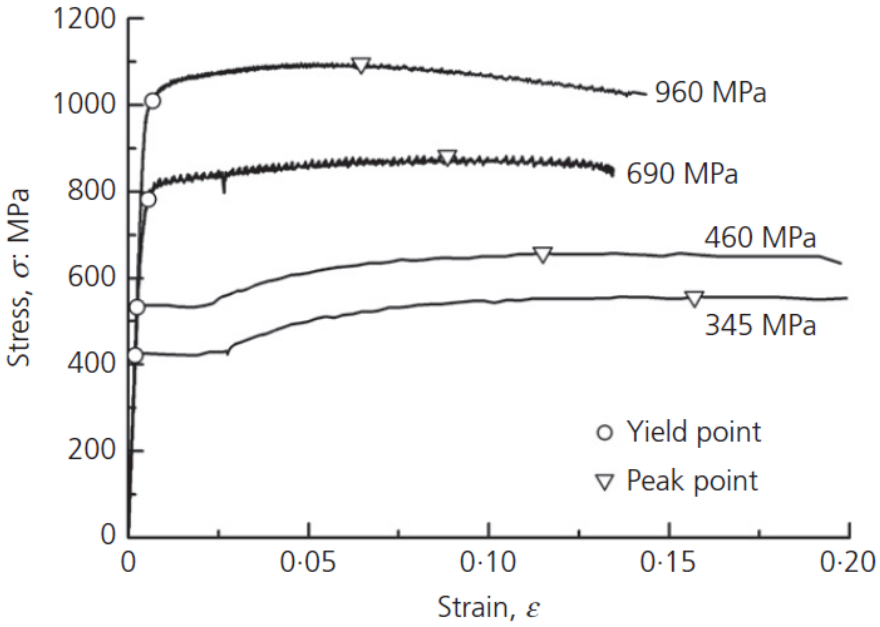

Figure 2.28: Comparison of stress-strain curves for different steel grades [90]

2.6.4 Fracture toughness of high strength steels at low temperature

The effect of low temperature on fracture toughness is generally dependent on the alloy base. Alloy steels normally exhibit decreasing fracture toughness as the test temperature is decreased through transition temperature range, when the structure contain ferrite or tempered martensite. This is because, low temperature reduce the ability of the material to deform plastically, making it more brittle and prone to fracture The transition temperature is influenced by the alloy content, grain size and heat treatment [91], [92].

High strength steels increasingly are used for transporting oil and gas and offshore structural installation. The installation of these pipelines sometimes takes place in severe environments, such as in low temperature region, where the pipelines must have low temperature toughness. Thus, the major motivation for the improvement of HSSs has been provided by the demands for higher strength as well as improved toughness, ductility and weldability at low temperatures. Though, HSSs own the excellent properties of tensile strength and ductile to brittle transition (DBT), research has shown that the DBT on the basis of microscopic mechanism occurs with decreases of temperature [92] [93] [94].

Fracture toughness at low temperatures is often assessed through tests such as Charpy V-notch impact testing or fracture toughness testing using specimens such as SENB, C(T) or SENT. These measure the energy absorbed by the material before it fractures and provide critical information for design and safety considerations [48], [49], [95]. Therefore, the fracture toughness of high strength steels at low temperatures is a critical factor in engineering design and material selection. It requires a balance between achieving high strength and maintaining sufficient toughness to resist fracture at cold environments. Careful alloying, heat treatment and testing are essential to ensure that HSSs meet performance requirements at low temperatures.

2.7 Fracture Toughness Test Methods and Standards

2.7.1 Fracture Toughness Test Methods

Fracture toughness test is employed as a method in structural integrity assessment of engineering components to determine a material's resistance. The fracture toughness is a material property that is used to determine the resistance of the material with crack growth under applied load in a particular environment.

The fracture toughness test specimen in the laboratory is fabricated such that they have similar crack tip constraint conditions that real structural components might be subjected. This is normally done by the introduction of a sharp crack through fatigue pre-cracking by applying a controlled

alternating force using three-point bending such that the total crack depths reaches the intended value [4]. To ensure the test specimen conforms to the general fracture mechanics on fracture toughness, the crack tip radius of the specimen at failure must be greater than the originally fatigue pre-cracked radius. The plastic zone at fracture must also be larger than the one during pre-cracking [46]. It is worth noting that in general, a crack propagates in mixed mode (combination of Mode I, II and III) and as stated earlier in section 2.2, it is found that Mode I dominates in most of the failures in real life cases. Therefore, for the rest of this thesis, more emphasis will be placed on Mode I test techniques and standards/codes.

Fracture toughness tests and standards play an important role in the application of fracture mechanics methods for structural integrity assessment, damage tolerance design and fitness-for-service (FFS) evaluation of various engineering components and structures. The data obtained from fracture toughness tests may also be used to characterise the material, evaluate its performance and quality assurance in typical engineering components/structures including oil and gas pipelines, pressure vessels, automotive, ship, aircraft and construction structures [46].

The most common fracture parameters used in fracture mechanics are the stress intensity factor, *K*, the *J*-integral and the crack tip opening displacement (CTOD). As these parameters are able to characterise both the crack driving force and the material toughness in the analysis of a structural component containing a crack, they have been used in engineering critical assessment/analysis (ECA) for unstable fracture mechanisms [4].

Fracture toughness testing forms an important part of fracture mechanics methods and during the past decades, extensive research has been done to develop reliable fracture measurement methods. There are a range of conventional fracture test specimens that are used in fracture test standards and they include compact tension (C(T)) specimen, single-edge-notched bend (SENB) specimen in three-point bending, single-edge notched tension (SENT) specimen, middle-cracked tension (M(T)) panel, disk-shaped compact tension DC(T) specimen, arc-shaped tension A(T) specimen and arc-shaped bend (A(B)). However, the most commonly used are the (C(T)), SENB, SENT specimens and (M(T)) panel [4]. There are three significant characteristic dimensions that each specimen configuration has: crack length (a), thickness (B) and width (W) with a standard test loading span of 4W as illustrated in Figure 2.29.

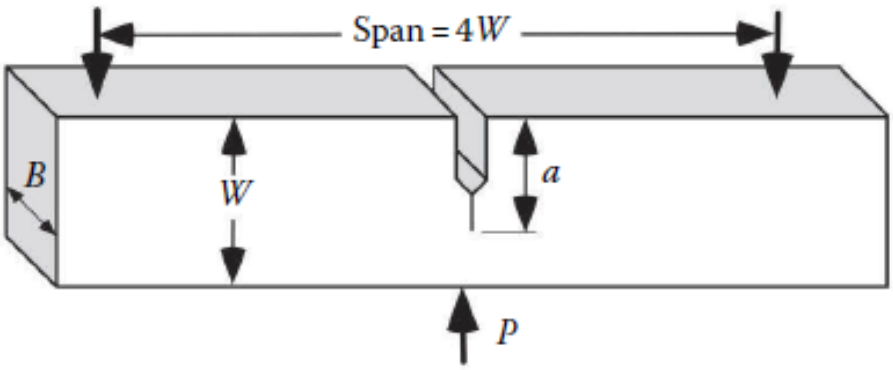

Figure 2.29: SENB specimen [4]

Most fracture test standards adopt deep-cracked bending specimens with high crack tip constraint conditions to obtain conservative resistance/toughness values. Among the fracture toughness specimens stated above, the C(T) and SENB specimens are the ones often used for testing. However, many experiments by [50], [96], [97] showed that the levels of crack tip constraint as a result of crack size, specimen geometry and loading type have a major effect on the fracture toughness of the material in terms of *J*-*R* and CTOD-*R* curves. Generally, a high-constraint specimen determines a lower *R*-curve (or decrease in fracture toughness), whereas a low-constraint specimen gives a higher *R*-curve (or increase in fracture toughness) [46].

Nonhomogeneous materials are generally sensitive to loading and the direction of crack propagation due to their microstructure and mechanical properties and it is important to define the sensitivity to orientation carefully in fracture toughness testing [4] [98]. As a result of the importance of specimen orientation in fracture toughness measurements, all ASTM and BS ISO fracture testing standards require that the orientation be recorded together with the measured fracture toughness [4], [49], [95].

The American Society for Testing and Materials (ASTM), the British Standards Institution (BSI) and the International Organisation for Standardisation (ISO) are the common accepted standards for fracture toughness testing. The two ASTM standard fracture test methods are E399 [26] and E1820 [48]. ASTM E399 was the first fracture test standard developed in the USA for measuring the elastic plane strain fracture toughness K_{IC} for brittle materials. ASTM E1820 is a combination of fracture test standards to determine the elastic-plastic plane strain fracture toughness J_{IC} or critical CTOD and J-R or CTOD-curves for ductile materials. The BSI fracture test standard developed are the BS 7448 [98]–[101] and the BS ISO 12135 [49] corresponds to the ASTM E1820. BS 8571 [95] is the current standard for low constraint fracture toughness testing of pipeline components.

The basic requirement during fracture toughness testing is the measurement of applied load and the accompanying displacement. In some cases, additional instrumentation is attached to the specimen to monitor crack growth or measure more than one displacement. Modern fracture toughness testing machines are equipped with a load cell that makes measuring the applied load a straightforward process. A clip gauge is commonly used to measure displacement during fracture toughness tests and must be attached as shown in Figure 2.30, ensuring the free rotation of the clip gauge beams [4]. In this thesis, in addition to the clip gauges, digital image correlation (DIC) is employed to measure full-field surface displacements. (The general techniques and procedure of DIC is presented in chapter 3).

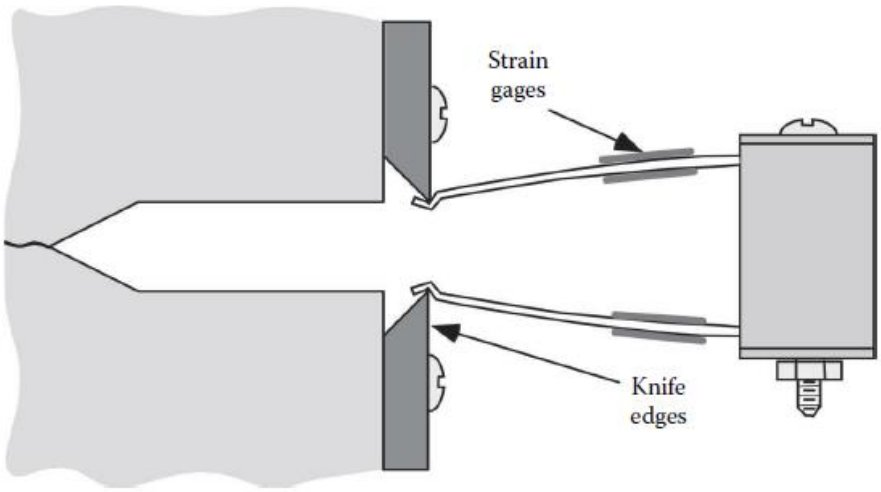

Figure 2.30: Measurement of crack tip opening displacement with a clip gauge [4]

Side grooves in test specimen are necessary and are often machined into the sides of the specimen for the purpose of maintaining straight crack front during both pre-cracking and testing. Experience has shown that a specimen without a side groove could be subjected to tunnelling and shear lip formation as a result of the low stress constraint/triaxiality at the outer surfaces of the material. Side grooves are done to remove these outer free surfaces where plane strain conditions are common, leading to straight crack front. They are also done to allow integral knife edges for the attachment of clip gauges. Generally, side-grooved test specimens have a net thickness of about 80% of the gross thickness. Side grooves should be machined to this approximation as much as possible to avoid lateral singularities being produced, causing a rapid crack growth at the outer edges of the test specimen [4]. It should be noted for the specimen type selected for the fracture tests (SENT and SENB) in this thesis would not be side-grooved due to thinner thickness used to represent the thickness of an actual pipeline steel. Instead, clip gauges would be instrumented on attached knife edges for the measurement of displacement.

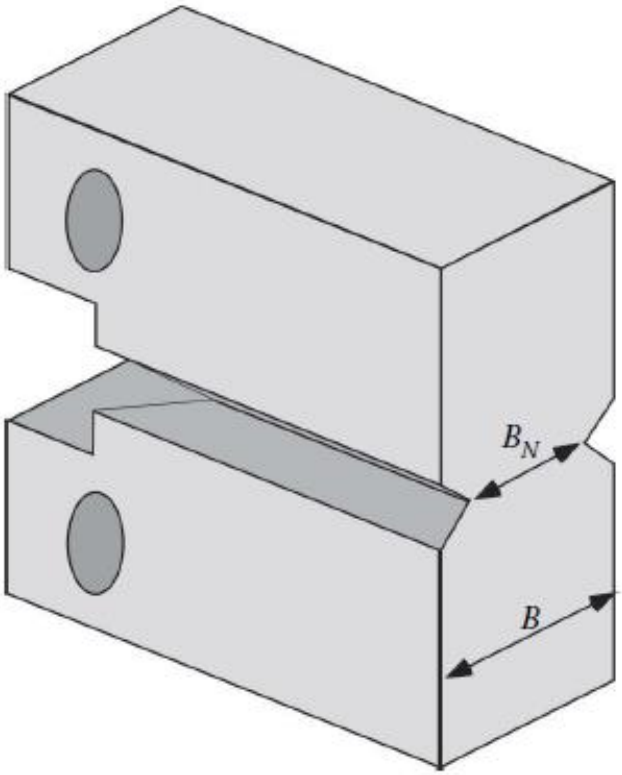

Figure 2.31: Side groove in typical fracture toughness specimen [4]

ASTM E399 [26] and BS 12135 [49] provide standard methods for the experimental determination of the critical stress intensity K_{IC} for linear elastic materials. It is also shown that the apparent toughness K_C decreases with increasing specimen size until a plateau is reached and there are strict rules on specimen size requirements in ASTM E399 and BS 12135 to ensure K_{IC} measurement corresponds to a lower bound at the plane strain plateau. Aside the initial crack size requirement, the following two validity requirement equations must be met [26], [49]:

$$B, a \geq 2.5\left(\frac{K_{IC}}{\sigma_Y}\right)^2 \tag{2.73}$$

$$P_{max} \leq 1.1P_Q \tag{2.74}$$

where;

P_{max} = maximum applied load, P_Q=critical load

The size requirement in equation (2.73) and (2.74) makes it difficult to measure a valid K_{IC} for most of the structural materials as shown by Anderson [4]: the material must be relatively brittle, or the test specimen must be large with a width W, greater than 1 m for the 95% secant offset procedure in ASTM E399 [26] to correctly estimate the load at crack initiation. In characterising

lower shelf (brittle) fracture toughness for steels, these tests are valid. However, the *J*-integral and CTOD are required for the fracture toughness in the ductile-to-brittle transition region and upper shelf.

A general equation for calculating the stress intensity factor K is given as:

$$K = \frac{P}{B\sqrt{W}} f\left(\frac{a}{W}\right) \tag{2.75}$$

where; P=applied load, B=specimen thickness, W=specimen width and a=crack length

For materials that exhibit low yield stress, thickness required for K_{IC} test specimen is high and it is not practical for a K_{IC} test to be performed. This makes it difficult to prepare specimens for materials like mild steel, HSS and commercially available aluminium, etc. and this has motivated researchers to formulate the *J*-integral test discussed in the next section.

2.7.2 Measurement of *J*-Integral

In contrast to the experiments designed for the determination of K_{IC} where the plastic zone size is controlled to remain small in comparison to the crack length; experiments to find critical *J*-integral, J_{IC} are designed such that a large amount of plastic deformation is allowed in the vicinity of the crack tip. The *J*-integral test in ASTM E1820 [48] and BS 12135 [49] is also more relaxed than the E399 standard test method because it allows a a_o/W range of $0.45 \leq a_o/W \leq 0.70$ and provides a means to test a specific specimen geometry without knowing the type of test required.

In addition, the characteristic values of elastic-plastic fracture mechanics are generally deduced from a *J*-*R* curve using equation (2.76). A *J*-*R* curve is generated by calculating the *J*-integral incrementally while recording the continuous crack length values. The plane strain initiation toughness J_{IC} is an important parameter that provides a measure of crack growth resistance near the onset of stable crack growth in Mode-I cracks. ASTM E1820 has adopted an engineering definition of J_{IC} at the intersection of 0.2 mm offset construction line to the *J*-*R* curve [48].

$$J = f(\Delta a) \tag{2.76}$$

For a single specimen test under Mode-I loading, the construction line on a typical *R*-curve is given by:

$$J_{\mathrm{I}} = \mathrm{m}\sigma_y \Delta a \tag{2.77}$$

$$\sigma_F = \frac{\sigma_Y + \sigma_{UTS}}{2} \tag{2.78}$$

where; σ_F=Flow stress, or effective yield strength

σ_Y=Yield strength

σ_{UTS}=Ultimate tensile strength

m =2 (representing the slope)

The size requirement for *J*-controlled crack extension are given as:

$$B, b_o \geq \frac{10J_{max}}{\sigma_Y} \tag{2.79}$$

$$\Delta a_{max} \leq 0.25 b_o \tag{2.80}$$

where; B=thickness, $b_o = W - a$= crack ligament and W=width.

Furthermore, *J* can be determined from a load-displacement curve as in Figure 2.32 for both linear-elastic and elastic-plastic and therefore, according to BS 12135 [49], the generalised total *J*-integral and its components for Mode-I quasi-static configuration are of the form [4]:

$$J = J_{el} + J_{pl} = \frac{K^2}{E'} + \frac{\eta_p U_p}{B b_0} \tag{2.81}$$

where J_{el} and J_{pl} are the elastic and plastic components of J respectively; K is the elastic stress intensity factor at force applied to the specimen at the start of unloading; E' is the longitudinal elastic modulus in plane strain; η_p is a dimensionless function of geometry; U_p is the plastic area under the load-crack mouth opening displacement (CMOD) curve. Double-clip gauges are placed at the knife edges for the measurement of the crack opening, from which CMOD and CTOD can be calculated [4]:

$$CMOD = V_{p1} - \frac{Z_1}{Z_2 - Z_1}(V_{p2} - V_{p1}) \tag{2.82}$$

where V_{p1} and V_{p2} are the plastic parts of the clip gauge displacements of the knife heights of Z_1 and Z_2 respectively.

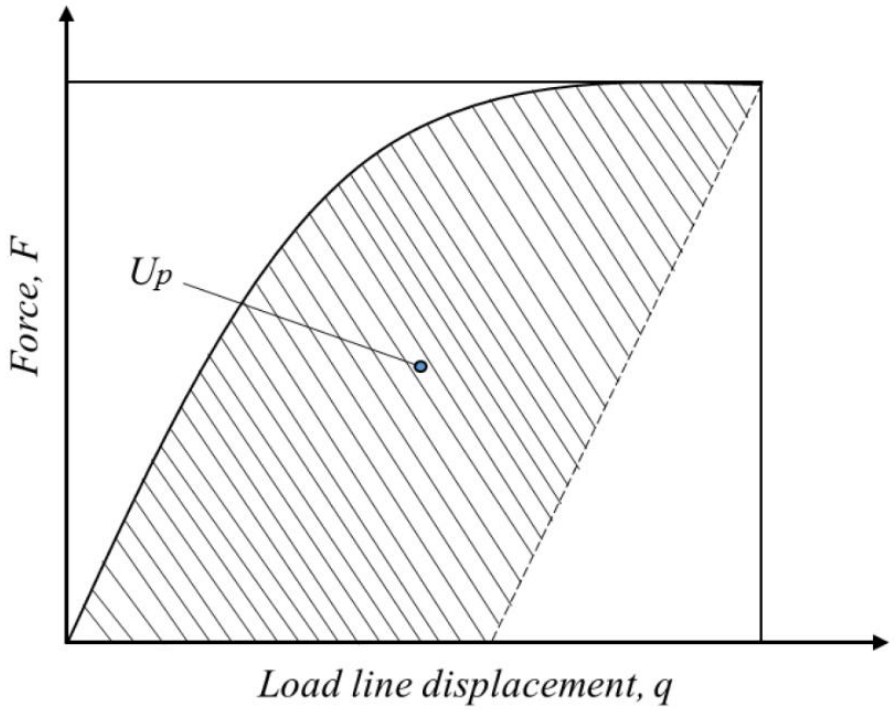

Figure 2.32: Load-displacement curve for the determination of *J* [49]

2.7.3 CTOD Testing

The first CTOD standard is the BS 5762 [102] developed by the British Standards Institution (BSI) and published in 1979. The plastic hinge model in equation (2.83) was adopted for estimating the critical δ_c from CMOD measurements. The plastic hinge model was still in used in the last edition BS 7448-1991 [98], now superseded by BS 12135 [49]. ASTM E1820 [48] published a similar CTOD test standard using a plastic hinge model that incorporates three-parameters, K, J, δ.

The CTOD laboratory measurement of the critical δ_c is usually associated with the onset of cleavage fracture under plane strain conditions. Just like the *J*-integral separation, the plastic hinge model for the total δ is also divided into elastic and elastic-plastic components as shown [49]:

$$\delta = CTOD = \delta_{el} + \delta_{pl} = \frac{(1-\nu^2)K^2}{1.5R_{p0.2}} + V_{p1} - \frac{a_0 + Z_1}{Z_2 - Z_1}(V_{p2} - V_{p1}) \qquad (2.83)$$

where $R_{p0.2}$ is the 0.2% offset yield strength of the parent metal at the temperature of the fracture toughness test. It should be noted that the factor 1.5 replaces the value of m=2 based on the information in the comparative study of CTOD-resistance curve test methods for SENT specimens.

2.8 Design Codes and Standards in Engineering Assessment

2.8.1 Application of Constraint in Structural Integrity Assessments

Engineering structures containing defects might be susceptible to structural failure during fabrication or service life. The structural integrity assessments for defects usually require the fracture toughness of the component to be determined in terms of SIF from *J*-integral, CTOD or K_{IC} tests. There has been much research on how to transfer the small-scale laboratory test specimens to real structures being analysed. However, the assessment of structural defects has traditionally been based on the single parameter toughness data obtained from high constraint deeply cracked bend and compact tension specimens according to established experimental standards and strict validity criteria. This provides lower bound conservative fracture toughness leading to unnecessary repairs and maintenance cost.

Fracture assessment standard procedures for engineering structures containing flaws have been published, such as BS 7910 [23], R6 [24] and ASME API 579-1 [25]. These standards are based on the failure assessment diagram (FAD) which was first proposed by Dowling and Townley [103] from the two-criteria approach when they worked at Central Electricity Generation Board (CEGB) in the United Kingdom. A failure assessment line/curve (FAL/FAC) is constructed by the relationship between the fracture ratio K_r and applied load ratio, L_r. Failure is possible when the assessment point on the FAD lie on or outside the FAC as in Figure 2.33 [23]. Therefore, the use of high constraint specimens, along with assessment procedures such as BS 7910:2019 [23], R6 [24] and ASME API 579-1 [25] have proven itself as a conservative approach in preventing failures of engineering structures.

2.8.2 Constraint effects in BS 7910:2019

Constraint is responsible for some of the reserve factors in a fracture assessment conducted in accordance with clause 7 of BS 7910. In the previous and most recent editions of BS 7910, a new annex (Annex N: "Allowance for constraint effects") has been added in an attempt to quantify constraint. The procedure originated from the UK nuclear flaw assessment procedure, R6 [24] and was incorporated into the European SINTAP and FITNET procedure [104], before being adopted by BS 7910. Annex N in BS 7910 is intended to be used as a supplement to the main fracture clause, clause 7 of BS 7910 to estimate the likely increase in reserve factors due to constraint effects [23].

Annex N essentially allows the structural integrity engineer to quantify the constraint conditions associated with the structure being assessed and the small-scale laboratory specimens used to

assess it, using either the elastic *T*-stress or *Q* parameter. The *T*-stress requires elastic calculations, so it is often used for initial analysis when plasticity is not widespread. It is convenient to express the constraint parameter in terms of normalised structural constraint parameter, $\beta_T = T/\sigma_Y L_r$ for primary loading. The *T*-stress is an elastic parameter and does not depend on the stress-strain characteristics of the material under investigation. It depends only on the geometry of the specimen/structure, the flaw size and loading type (not the load magnitude). Thus, it can be expressed by simple polynomials which are given in Annex N of BS 7910 for various geometries including SENT and SENB used in this study [23].

The assessment of constraint effects using the elastic-plastic *Q* parameter gives very similar results to the elastic T-stress when plasticity is limited ($L_r < 1$). However, under conditions of widespread plasticity ($L_r > 1$), the predictions of constraint from the *T*-stress and *Q* parameter diverge. When this is the case, the *Q* parameter provides a more accurate description of constraint. For most geometries though, the *T*-stress can provide a conservative description of constraint even for ($L_r > 1$). That is, constraint is overestimated, and fracture toughness underestimated. Therefore, care must be taken in basing assessments on *T*-stress for $L_r > 1$. It is recommended that the *T*-stress is used for $L_r \leq 1$, while for ($L_r > 1$), the *Q* parameter should be used for accurate prediction of constraint assessment, as demonstrated by Cravero and Ruggieri [105] investigating failure of axially cracked pipelines. As the *Q* parameter depends on the stress-strain characteristics of the material and the magnitude of the loading, it cannot be easily standardised in the same way as the *T*-stress and is therefore not addressed in detail in Annex N of BS 7910 [23].

BS 7910 Option 1 is a conservative procedure that is quite simple to employ and does not need detailed stress/strain data for the material being analysed. The FAC for continuously yielding material is expressed as a relationship between K_r and L_r is as shown below [23]:

$$K_r = f(L_r) = [1 + 0.5L_r^2]^{-0.5}[0.3 + 0.7\exp(-\mu L_r^6)] \quad (2.84)$$

for $L_r < 1$, where $\mu = min\left[0.001\frac{E}{\sigma_Y}; 0.6\right]$

$$K_r = f(L_r) = f(1)L_r^{(N-1)/2N} \quad (2.85)$$

For $1 < L_r < L_{r,max}$, where N is the estimate of strain hardening exponent given by:

$$N = 0.3\left(1 - \frac{\sigma_Y}{\sigma_{UTS}}\right) \text{and } L_{r,max} = \frac{\sigma_Y + \sigma_{UTS}}{2\sigma_Y} \quad (2.86)$$

The proximity to plastic collapse is given as:

$$L_r = \frac{\sigma_{ref}}{\sigma_Y} = \frac{P}{P_L} \tag{2.87}$$

σ_{ref}= the reference stress, σ_Y= yield strength, P_L=limit load and P=applied load

The proximity to failure is quantified by the ratio of the applied stress intensity factor, K_I to the experimentally measured material fracture toughness, K_{mat} [23]:

$$K_r = \frac{K_I}{K_{mat}} \tag{2.88}$$

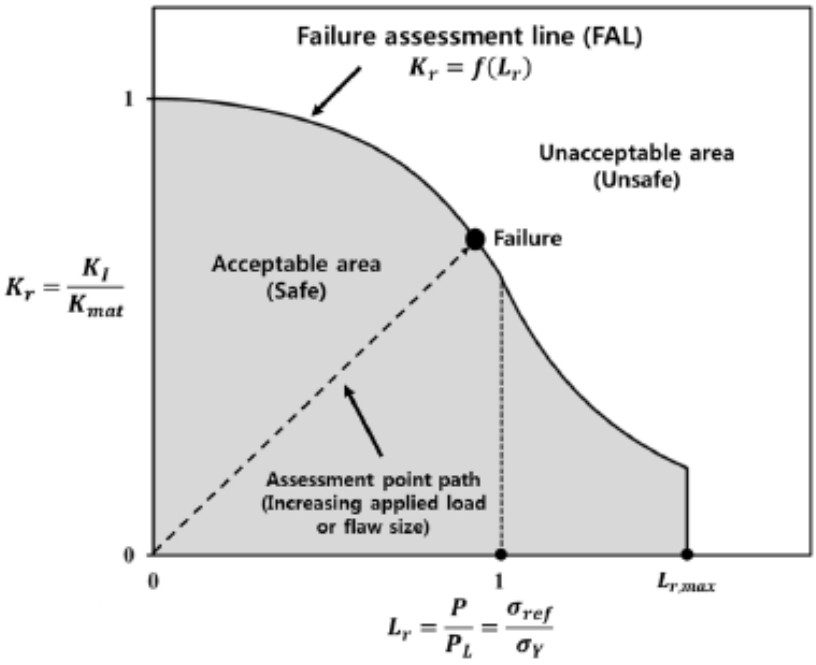

Figure 2.33: Example of failure assessment diagram (FAD) [106]

2.8.3 Limitations of Annex N of BS 7910:2019

The use of constraint correction procedures in order to analyse safety-critical structures is considerably more complex than implied by the approaches outlined in Annex N of BS 7910. In practice, constraint correction is normally used to show the existence of a larger safety margin than would be implied by the use of the standard Option 1 FAD (rather than to determine if the assessment is safe or unsafe). Some of the factors that could limit the use of constraint correction may include:

- Generally, large quantities of data are required to support evidence in order to demonstrate constraint-sensitivity analysis.

- For ferritic steels such as the API 5L X65 used in this study, failure mode is likely to switch from cleavage fracture to ductile tearing as crack tip constraint is lowered, introducing both high data scatter and uncertainties in the analysis of the data.
- The different solutions available in the literature for the reference stress, σ_{ref} to calculate the load ratio, L_r and for the T-stress. This could change the results of a constraint analysis significantly depending on which reference stress, σ_{ref} solutions are chosen. Sensitivity study should therefore be conducted to determine the consequences of using the different solution assumptions.
- Limited user experience with methods for determining fracture toughness under low constraint conditions.
- The treatment of residual stresses is not straightforward. This is because, these residual stresses are usually associated with significant bending components but are often treated in BS 7910 as membrane stresses for simplicity. Therefore, it is conservative to treat secondary stresses as primary and bending stresses as membrane stresses might not be valid due to changes in constraint conditions.
- Validation of the approach against experimental data is currently limited especially for low temperature testing

2.8.4 Constraint Matching

In matching the constraint of a laboratory test specimen to the actual structural component, the fracture toughness that corresponds to the constraint experienced by the structural crack/defect is used to predict failure. In contrast, the available integrity assessment methods utilise standard specimen with strict size requirement resulting in high state of constraint [16]. This is because actual structural flaws involve low constraint state and the transfer of fracture toughness data from standard laboratory specimens to the real cracked components will produce conservative results. The matching of constraint between real structural defects and standard laboratory specimens forms an important part in developing an accurate structural integrity assessment method.

Therefore, understanding crack tip constraint matching is crucial for accurately predicting crack propagation and designing structures to withstand fracture. It helps engineers assess the influence of various factors on crack growth behaviour and make informed decisions regarding material selection and structural integrity assessments.

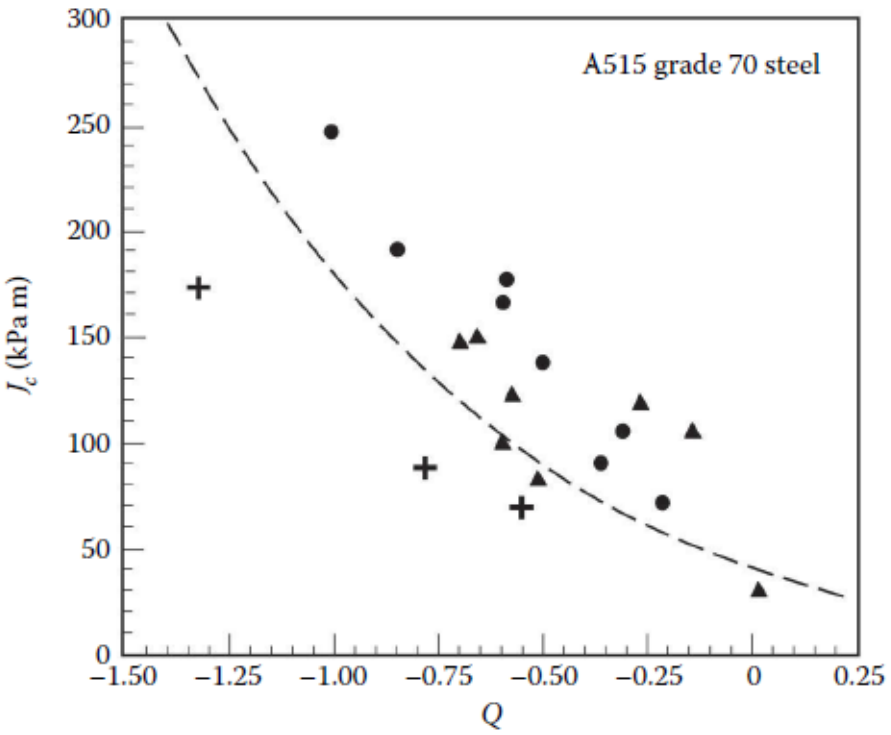

Figure 2.34: *J-Q* toughness locus for SENB specimens of A515 Grade 70 Steel [4]

As constraint is dependent on the geometry of the specimen or structural component being assessed, it is not possible to obtain a single value of fracture toughness J_C by testing different specimens. Through the testing of specimens of different sizes and geometry however, it is possible to obtain a variation of fracture toughness with constraint, Q or T (see Figure 2.34) [4]. In applying this material data to real engineering component to illustrate constraint matching, it is necessary to ensure that the fracture toughness, J_{Design} of the component to be designed is equal to the fracture toughness, J_C measured from the small-scale laboratory test specimen. That is, the constraint factor in the design example has the same value as the one associated with J_C as illustrated in Figure 2.35 using the constraint parameter, Q. If the fracture toughness, J_C of the material varies with constraint, Q as shown by curve OAB and the loading on the structural component being designed made of the same material leads to the variation of the applied toughness, J with Q along curve OAC, then the fracture load corresponds to point A. Point A is where both cases have the same Q [12] and shows how laboratory test data can be transferred to practical engineering components for the assessment of constraint.

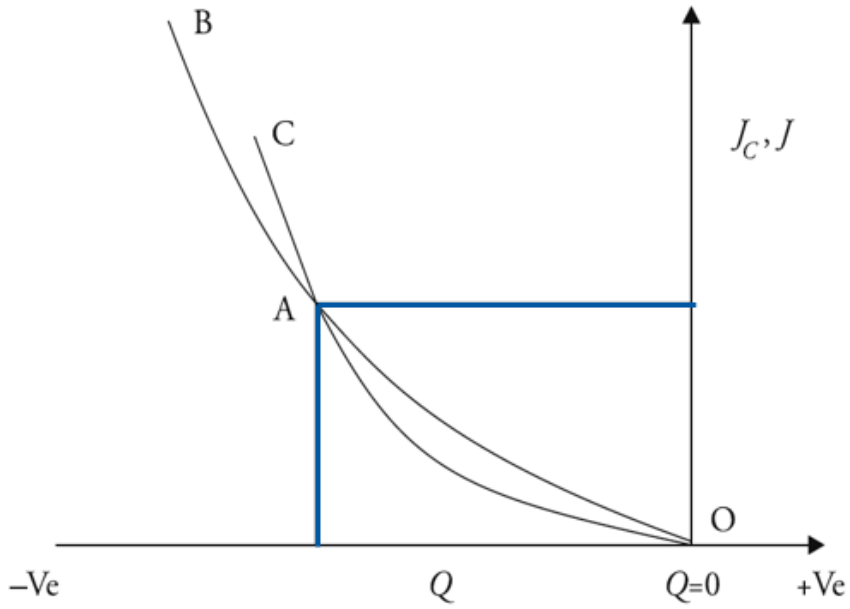

Figure 2.35: Variation of fracture toughness with constraint parameter, *Q*

2.9 Baseline finite element verification of three-point SENB

This section aims to confirm the values of *J*-integral and *T*-stress obtained from analyses with finite element program, Abaqus, to provide confidence to the key research topics that can be represented numerically.

Shallow cracked three-point SENB test specimens are useful for the systematic investigation of the influence of crack tip constraint loss on cleavage fracture toughness of a material in the ductile-to-brittle transition temperature range. For linear elastic behaviour, the *T*-stress can be used as a measure of crack tip constraint loss. In this section, the 3D *T*-stress solutions were obtained by running finite element analyses (FEA) for SENB specimens with a wide range of crack length-to-width ratio (a/W=0.1 to 0.5) to study in-plane constraint loss.

The *J*-integral is also an important parameter when discussing fracture mechanics of cracked bodies. *J*-integral along the crack front is one of the most important crack driving force parameters used recently in elastic-plastic fracture mechanics methodology. It defines the strength of the singular stress field under small to large scale yielding conditions.

Crack tip constraint, which is the resistance against plastic deformation has attracted attention in fracture mechanics research for the past years. The level of constraint at the crack front plays a significant role in the fracture behaviour of cracked components and can be used for accurate description of crack-tip stresses and deformation fields. As stated above, in linear elastic fracture

mechanics, the level of constraint due to geometry and loading configuration can be quantified by the elastic *T*-stress. This work aims to confirm the values of *J*-integral and *T*-stress obtained from analyses with finite element program, Abaqus.

Finite element (FE) analysis was used to investigate the stress state in the SENB specimen using Abaqus. For this case, a 150 mm x 30 mm x 15 mm (L x W x B) is considered and is as shown in Figure 2.36. Due to symmetry, one-quarter of the total geometry of the specimen is created to reduce computational costs and time.

The FE model is intended to be a representation of the laboratory test specimen and tensile properties of the selected high strength steel specimen should be used. To define elastic properties, Young's modulus of 210 GPa and Poisson's ratio of 0.3 was assumed for API 5L X65 steel pipe since experimental work was not conducted yet. Contact between the rollers and the specimen were modelled using surface-to-surface contact as shown in Figure 2.38. The SENB specimen was loaded in three-point bending with the rollers modelled as analytical rigid shells.

In modelling cracks in FE, focused meshes are normally used in small-strain fracture mechanics evaluations as the strain field become singular at the crack tip. Mesh refinement and crack tip element type are chosen carefully to account for the singularity at the crack tip [107]. Singularity in FE analysis mostly improves the accuracy of the *J*-integral, as the stresses and strains near the crack tip region closely follow the HRR solution for high constraint conditions. However, according to the Abaqus manual [107], accurate contour integral values can be obtained without the use of singularity if sufficiently fine meshes are employed.

The analyses used focused mesh at the crack tip with collapsed element edges at the crack tip and the model was meshed using first order, reduced integration brick elements, C3D8R. The 3D non-linear finite element model was run to extract fracture parameters, *J*, *K* and constraint parameter, T-stress. The crack tip region was refined and focused meshed at the crack position with 15 elements around the semi-circles. The mesh and close-up view of the mesh around the blunted crack are shown in Figure 2.36 and Figure 2.37 respectively. Note that even though the entire model is 3D geometry, the crack itself is 2D. This was achieved from Rice's [32] idealisation of 2D problem for 3D where the crack was modelled within the 3D model using the contour integral approach. Other techniques such as extended finite element method (XFEM) may be used [107].

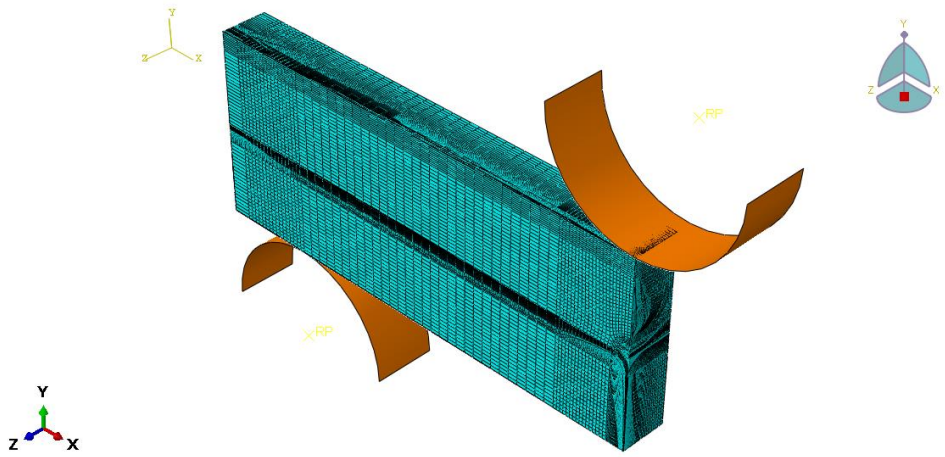

Figure 2.36: Mesh applied on the quarter model

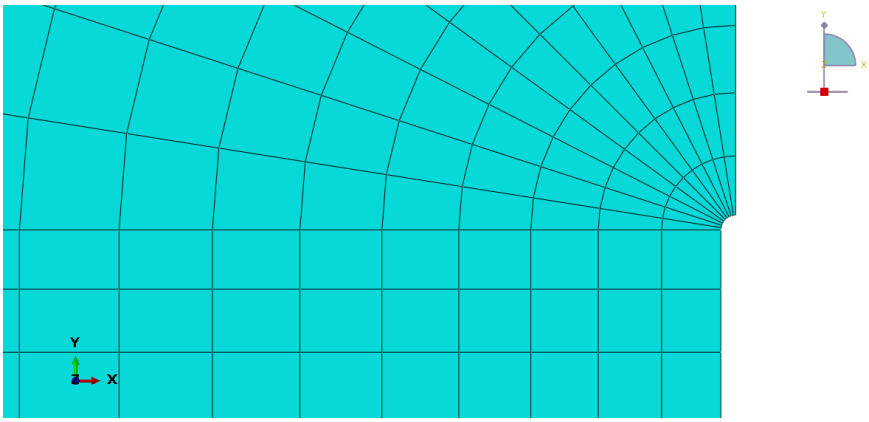

Figure 2.37: Close-up view of the mesh around the crack region

A displacement was applied to a reference point, constrained to all nodes of the upper face representing the location of the top test rig roller as shown in Figure 2.38.

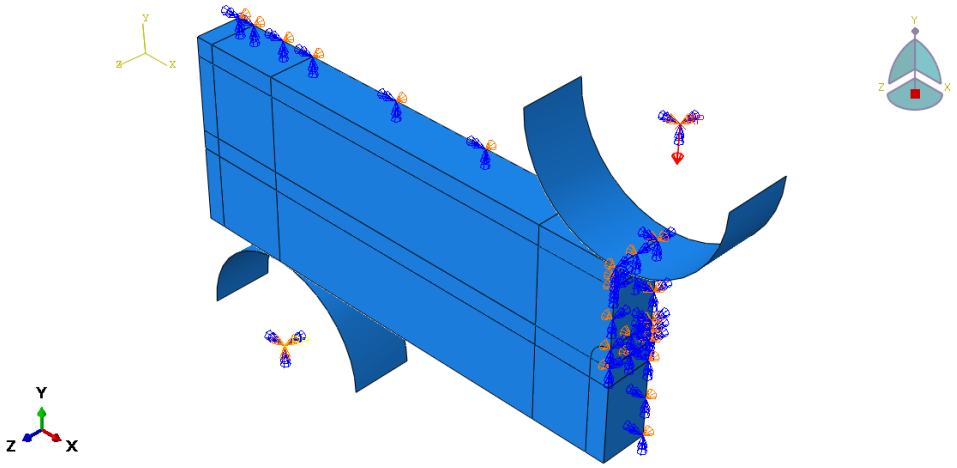

Figure 2.38: Loading and Boundary Conditions

2.9.1 Results and discussions

J-integral is quantified as the energy release rate in the vicinity of the crack and calculated in Abaqus based on the contours around the crack tip. The design of this model allows 15 valid contours around the crack tip for the calculation of the *J*-integral. The contours nearer the crack tip have lower values as compared to contours further away from the tip of the crack. As deformation at the crack tip increases, the difference between the *J* calculated to the contour close to the crack tip and the contour further from the crack tip will increase. In fracture mechanics, the *J*-integral is path independent and therefore, only contours which are sufficiently similar give appropriate representative values of *J* and this has been demonstrated in this model.

Figure 2.39 and Figure 2.40 below illustrate the evaluation of contour *J*-integral and elastic *T*-stress (as biaxiality ratio: $\beta = (T\sqrt{\pi a})/K_I$) respectively, in a 3-dimensional crack configuration of three-point SENB specimen. This is to provide a method for linear elastic response validation for comparative results available in literature. Figure 2.39 illustrates the variation of *J*-integral across the contour integrals at the mid-plane and free surface for the deep straight crack. They show contour independence for the *J*-integral values if the first two contours are excluded. This behaviour is consistent with planar crack front geometries. The biaxiality ratio in terms of the T-stress determined from the FEA considered in this current study is illustrated Figure 2.40 alongside the solution obtained by Sham [108]. These analyses form the basis in showing the effect of geometry on the *T*-stress and the significance of examining contour integrals across the crack front when determining *J*-integral values with path independence. Figure 2.41 shows good agreement of stress intensity factors, *K* as a function of crack depth (a/W) from this study and the solution from BS 7910.

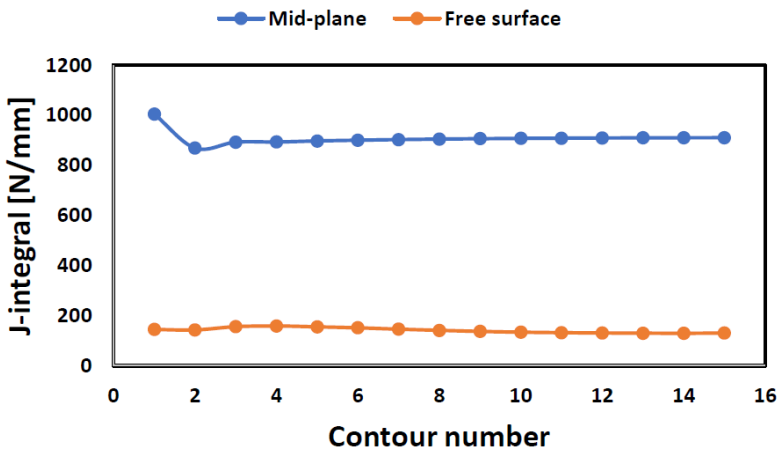

Figure 2.39: Linear elastic analysis: *J*-integral vs. Contour Number, mid-plane and surface of through-thickness crack, a=10 mm for 1000 N applied load.

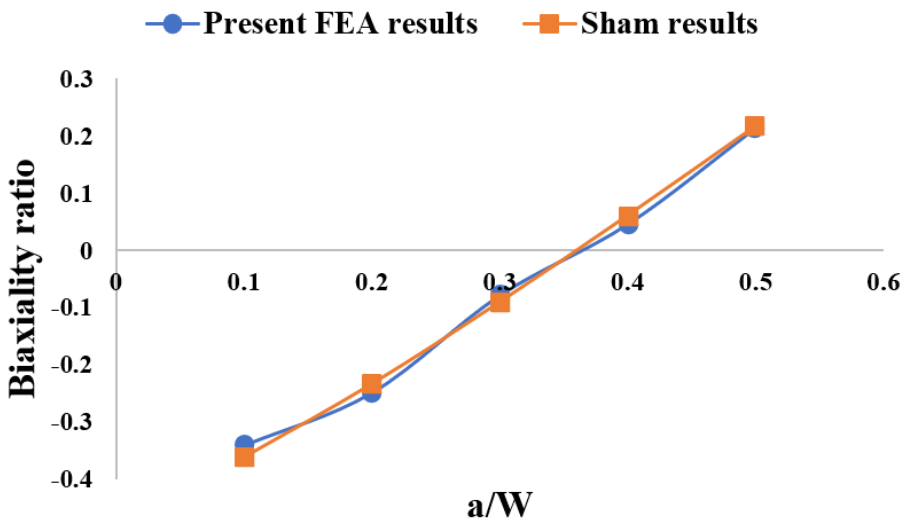

Figure 2.40: Biaxiality ratio as a function of crack length to width ratio (present FEA results comparison with Sham [108] solution)

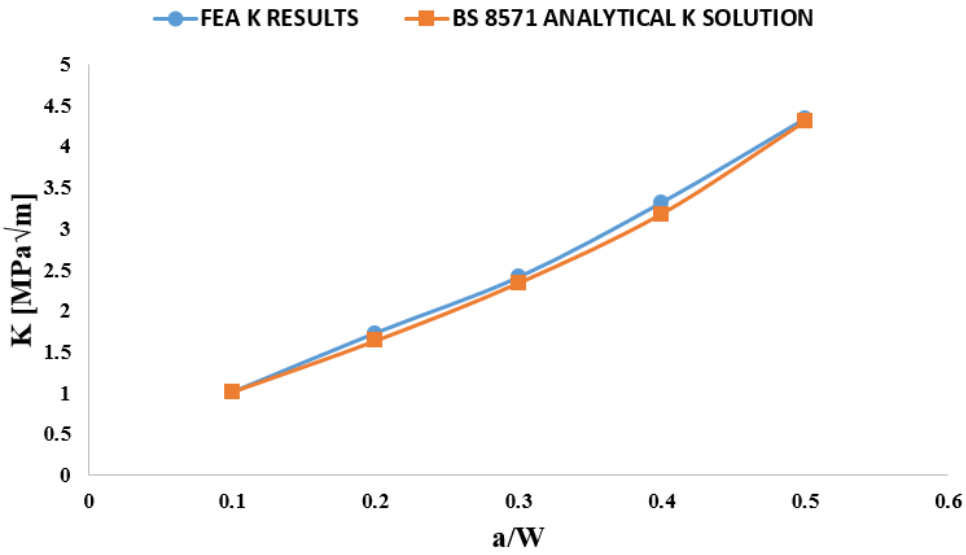

Figure 2.41: Elastic analysis: stress intensity factor vs crack length, 20000N applied load (comparison with BS 7910 solution)

Figure 2.42 shows the normalised constraint parameter, β_T, variation with crack depth, derived using the reference stress solution for three-point SENB specimen given in BS 7910. The FE analyses yield similar results to those used to derive the β_T solution in BS 7910. It can be seen in Figure 2.42 that shallow cracked SENB specimens, which are intended to be representative of real structural components, are associated with negative values of β_T (low constraint condition). Deeply notched ($a/W > 0.4$) SENB specimen, typically used to generate the fracture toughness

information for conservative fracture assessment, show high constraint (positive β_T). This preliminary investigation gives confidence in conducting further finite element analyses for this research which are detailed in chapter 4.

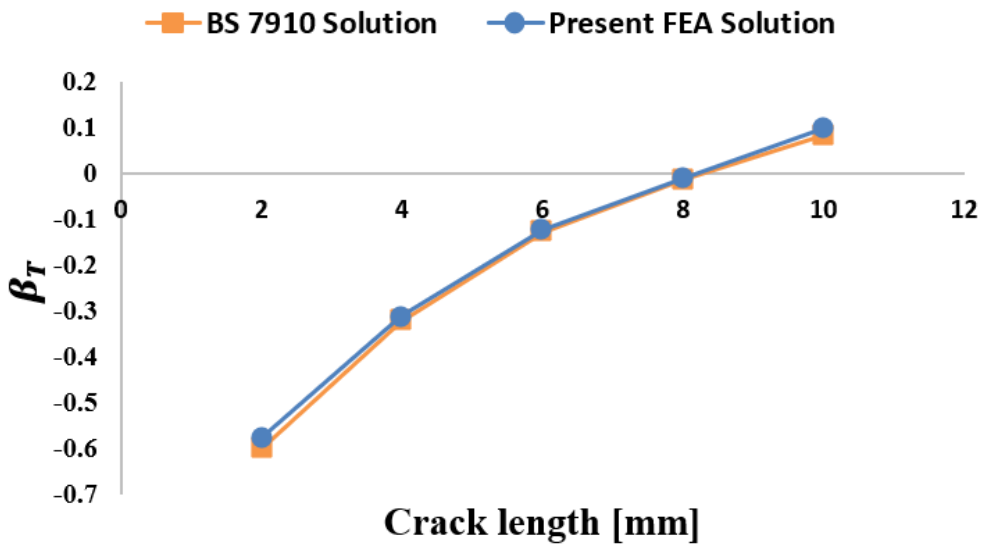

Figure 2.42: β_T solution for different crack lengths of three-point SENB specimen (comparison of BS 7910:2019 [23] and present FEA study)

2.10 Summary from Literature Review

A thorough review on the effects of constraint on the fracture toughness of offshore pipelines has been conducted in this Chapter. Current engineering critical assessment methods available in the literature was further reviewed to highlight the need to investigate the fracture response with the effect of constraint. Based on these, the following conclusions are drawn:

- The application of the principles of EPFM to practical engineering problems has not been possible to the same extent as the case of LEFM. This is due to the non-availability of solutions for CTOD or *J* for practical geometries and materials with varieties of hardening characteristics. Numerical techniques such as the finite element method has helped in eliminating many of these limitations. At the same time, research and developments in relation to the transfer of laboratory material data to real engineering components have increased the confidence in both design and safety assessments.
- There is the desire to conduct further research on fracture mechanics assessment procedures to reduce the conservatism inherent in the assessment codes of structural integrity structures. Minimising these conservatisms could enable safe extension of the

lifetime of offshore structures, particularly, pipelines operating in Arctic conditions. These structures are prone to brittle fracture and may allow more efficient designs of these components in the future, thereby reducing costs and maintenance times.

- Single-parameter fracture mechanics has been well developed with rigorous testing methods available for fracture criteria. There is also a wide understanding on how the single-parameter theory can be applied to fracture assessment of engineering structures.
- The two-parameter fracture mechanics is also well understood and there are methods for predicting in-plane constraint loss. The *J-T* two-parameter approach has been implemented into fracture assessment codes, but it is only applicable to linear elastic materials. Therefore, there is some argument about how to incorporate two-parameter theory into assessment codes to account for both linear and elastoplastic materials. Two-parameter fracture assessment has also benefited only when constraint correction and local approach models are used in conjunction with large material testing data.
- Out-of-plane constraint loss is still not well developed in fracture assessment procedures. Recent research has focussed on manipulation of stress triaxiality used to define an out-of-plane constraint parameter. This can then be used to describe the effect on fracture toughness. It is still however, unclear on how the out-of-plane three-parameter approach can be transferred into fracture criteria for use in assessment codes.
- There seem not to be a robust method to account for constraint effects on the fracture toughness of offshore high strength steel pipelines at low temperatures in the ductile-to-brittle transition curve.
- The FEA work conducted in this chapter gives confidence in creating other models for constraint analyses using SENT and SENB specimens. It should be noted that in reality, components fail by plastic collapse as well as fracture and therefore, both failure mechanisms should be considered in any fracture assessment.
- This thesis will adopt the modified-constraint based method to illustrate the interaction between the two failure mechanisms for the SENT and SENB geometries and setup, K_r and L_r parameters for each specimen configuration plotted on failure assessment diagrams (FADs).

3 Experimental investigation of crack tip constraint effects

3.1 Introduction

The development of Arctic oil and gas infrastructure requires fixed offshore structures and pipelines capable of operating safely at low temperatures and typically manufactured from steel. This is due to its relatively low cost, ease of fabrication and high strength and fracture resistance properties. However, the Arctic environment is hazardous from a structural integrity standpoint, as steel has increased susceptibility to brittle fracture at low temperatures that can result in catastrophic failure, irreparable damage and potential loss of life [81].

Therefore, an appropriate material toughness criterion is needed to ensure high strength steels with adequate fracture resistance at low temperatures are used in Arctic constructions. In the past decade, significant efforts have been made in the development of fitness-for-service (FFS) procedures applicable to defect assessments and life-extension programs of critical engineering components. These methodologies, called Engineering Critical Assessment (ECA) procedures, provide a concise framework to relate crack size with applied loading using failure assessment diagrams (FADs). These approaches rely on the use of lower-bound fracture toughness data determined from deeply notched bend and compact tension (CT) specimens to guarantee representative levels of stress triaxiality, which drive the fracture process [109], [110]. A single geometry-independent failure locus provides a highly effective but conservative acceptance criterion for cracked structural components under such conditions. Several assessment methodologies are now well established, e.g. BS 7910 [23], R6 [24] and API 579 [25], among others, which are based upon the FAD concept and are widely employed to analyse structural defects.

However, the most common defects in pipelines are surface cracks that have low levels of crack-tip stress triaxiality. This significantly differs from the stress states present in deeply notched specimens. ECA procedures applicable to offshore pipelines rely on the direct application of crack growth resistance curves (*R*-curves) determined using small laboratory specimens to define acceptable defect sizes for conservative assessments. Therefore, the applicability of experimentally determined fracture toughness data for structural steel piping components is of high importance for accurate predictions of in-service residual strength and remaining life, to reduce maintenance downtime and costs [104].

At present, BS 7910 does not offer guidance for refinement/enhancement of estimation of toughness for shallow cracks in thin-wall structures, apart from testing the exact component

geometry, which may not always be practicable or appropriate. To quote BS 7910 Clause 7 [23]: "It is common practice to use fracture toughness specimens that are representative of the thickness of the component being assessed". This chapter focuses on evaluating the effects and influence of constraint on material fracture resistance for API 5L X65 high strength steel.

3.2 Current approach to the treatment of constraint and limitations

Experimentally determined fracture toughness / resistance curves typically exhibit a significant dependency on specimen geometry, crack size (characterised by the a/W ratio) and loading mode (bending vs tension) [111]. For the same material, high constraint configurations, such as deeply notched SENB and compact tension (CT) specimens produce low fracture toughness. In contrast, shallow-notched SENB and predominantly tension-loaded designs (SENT) are associated with higher toughness values for similar amounts of crack extension [58], [105].

The primary motivation to use SENT fracture specimens in defect assessment procedures for structural offshore steel pipes is the similarity in crack-tip stress and strain fields driving the fracture process for both crack configurations, as previously reported by Nyhus et al [112]–[114]. Xu et al [115][116] also investigated the effects of constraint on ductile fracture toughness for clamped SENT and deeply notched SENB fracture specimens. By correlating experimental results with ductile fracture behaviour in circumferentially cracked pipes, the authors concluded that SENT and shallow cracked SENB have crack-tip constraint conditions similar to circumferentially cracked pipes. Cravero and Ruggieri [111] generated a range of *J*-resistance curves for pin-loaded and clamped SENT fracture specimens using the unloading compliance method. Their results provided further support for the development of standard test procedures for SENT specimens applicable in measuring crack growth resistance for pipelines [95].

These previous investigations represent a significant milestone in engineering applications of SENT fracture specimens that relate directly to structural integrity assessments of pipelines. A common approach is comparing SENT configurations having varying crack depths against a standard, deeply cracked SENB specimen with a/W = 0.5. In these cases, the evolving levels of crack-tip constraint with increased remote loading in the SENT specimens are closely related to the corresponding levels of stress triaxiality for a surface cracked pipe under predominantly tensile loading. However, a more systematic investigation of the toughness dependency as a function of constraint is required to assess the similarity between SENT and circumferentially surface cracked pipes. Nevertheless, the use of SENT fracture specimens to characterise fracture resistance

properties in steel pipelines has been effective in reducing over-conservatism that arises when measuring fracture toughness using high-constraint specimens [91], [105], [117].

Despite SENT specimens being routinely used in pipeline fracture testing, some difficulties are associated with test fixture and gripping conditions, low constraint conditions and high loads required to propagate the crack. This raises concerns about the validity and accuracy of the measured fracture resistance curves. Often viewed as nonconventional and slightly more conservative, shallow-notch bend SENB configuration testing may become more attractive due to its simpler testing procedures and smaller loads required for crack propagation. Therefore, using smaller specimens that guarantee adequate levels of crack-tip constraint to measure the material's fracture toughness represents an attractive alternative [118].

Motivated by these observations, this research investigates the applicability of the constraint-based FAD method in the assessment of cracked SENT and SENB specimens at low (-120℃) and room temperatures. The fracture tests were performed for three different crack configurations, a_0/W = 0.1, 0.3 and 0.5 (where a_0 is the initial crack length and W is the width of the specimen). As part of the constraint-modified FAD calculations, CrackWISE software [119] was used to derive the respective FADs. One of the objectives of this work was to improve and refine defect assessment procedures that include the effects of constraint variation on fracture toughness.

3.3 Experimental tests on tensile and fracture specimens

Tensile and fracture toughness tests were performed on API 5L X65 steel. Mechanical properties and fracture toughness were determined at room (23℃) and low temperatures (-120℃ $\pm$2℃). The methods developed for the base metal should also be applicable to welds (with suitable corrections for the crack driving force applied as part of a defect tolerance analysis). This is generally true, as the behaviour of welds is closely related to that of the base metal. The same principles and techniques used in assessing the performance of base metal can also be applied to welds. However, it is important to note that the presence of a weld can introduce additional factors that may need to be considered when assessing its performance. For example, welding can result in residual stresses, which can increase the susceptibility of the material to fracture. In addition, the presence of a weld can create a region of altered microstructure which can affect the material's properties and behaviour. Therefore, while the methods developed for the base metal can be applied to welds, it may be necessary to make certain corrections or adjustments to account for these additional factors. A defect tolerance analysis can help identify the critical defects that may be present in the weld and determine the appropriate level of inspection and testing required to ensure its integrity.

3.3.1 Material and tensile tests

Chemical compositions for the API 5L X65 steel pipe, as provided by the supplier, are presented in Table 3.1. Samples were manufactured using electron discharge machining (EDM) from pipe sections as shown in Figure 3.1. The pipe had a wall thickness, t = 23.8 mm and outside diameter, D_o = 1219 mm (D_o/t = 51). This geometry typifies the current trend of deep-water submarine pipelines made of high-grade pipeline steels. The notch orientation was machined parallel to the pipe rolling direction (L-C) as shown in **Figure 3.2**. First letter indicates the direction normal to crack plane and the second letter indicates the crack growth direction, where C=circumferential direction, L=longitudinal direction and R=radial direction. The orientation circled in red represents the orientation used in study machined out from sections as shown in Figure 3.1. Mechanical properties (see Table 3.2) and stress-strain behaviour of the X65 steel were tested according to BS EN ISO 6892 [120], using standard round specimens (diameter of 10 mm and a gauge length of 60 mm) at room temperature and -120°C.

Table 3.1: Chemical Composition of the tested steel grade (wt%)

Material	C	Mn	Si	Cr	Mo	Cu	Ni	P	S
X65	0.12	1.60	0.45	0.50	0.50	0.50	0.50	0.25	0.015

Figure 3.1: Pipe section from which all specimens are extracted

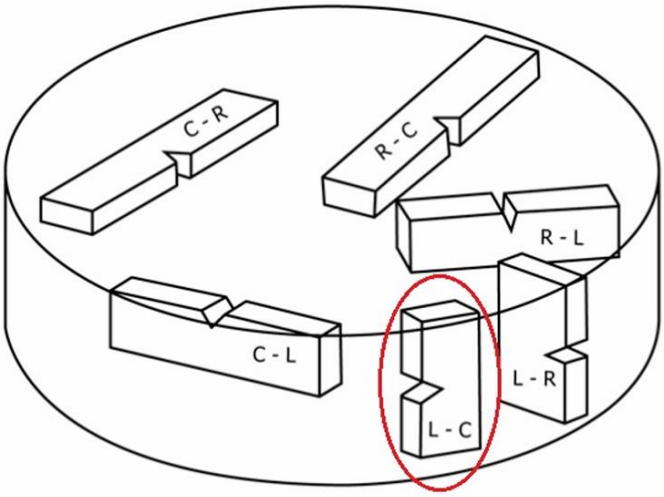

Figure 3.2: Sample orientations within a cylindrical section of material [26]

3.4 Digital Image Correlation (DIC) and Tensile Tests

3.4.1 Principles of DIC

Digital image correlation (DIC) is an effective non-contact optical technique. DIC measure the evolving deformation fields on the surface of a test specimen by calculating the strains, displacements and analysing the images of the specimens captured throughout a mechanical test. Prior to testing, a random speckle pattern is applied to the specimen surface to be tested. The pattern can be generated using either a spray or marker. The characteristic speckles applied to the specimen enables the observation of their relative changes in position during deformation, which follows the deformation of the underlying test specimen [121]. Thus, the images of the test piece taken throughout the test can be correlated to produce full-field coordinates representative of the shape, motion and deformation of the surface of the test specimen.

The DIC-measured images of the deformed test specimen are divided into a two-dimensional matrix of nodes or facets. At each of the nodes, a grey-scale intensity is evaluated as a weighted average of a square box surrounding the node. The size of the box is determined by a subset size parameter expressed in pixels (units of 2D image) [121]. Two consecutive images taken before and during the deformation process record the changes in the location of the nodes/facets. A specialised DIC software (GOM Correlate 2019) [122] performs the calculation of the displacements/deformation fields for the entire test specimen surface using a correlation algorithm.

3.4.2 Plain sided flat tensile specimen

The two plain tensile specimens, denoted M03-03, M03-04 are identical and have a rectangular cross-section of 20 x 3 mm and a gauge length of 80 mm. Both specimens are installed with strain gauges. M03-03 is tested at room temperature for a larger area of DIC measurement on one side (front - Figure 3.3a) with strain gauges installed on the other side (back - Figure 3.3b). Speckle patterns were applied to the M03-03 specimen surface by using a black spray which was effective enough to create the stochastic black dots. An image of the speckle pattern applied to the test specimen surface is shown in Figure 3.3a. The strain and displacement maps of the flat tensile specimen tested at room temperature are shown in Figure 3.4 and Figure 3.5 respectively, showing the *Y*-components at the start of the test and at necking. M03-04 is tested at the low temperature of -120℃. Note that DIC was not used for any of the low temperature tests due to frost and the environmental chamber needed to be closed for uniform low temperature and may affect the feasibility of applying DIC directly. Notwithstanding, the data obtained from room temperature DIC tests can be used to gain a deeper insight of the material behaviour and deformation mechanisms under different conditions. This would be discussed further in chapter 5.

During the test, the specimens were loaded quasi-statically under displacement control at a rate of 1.35 mm/min using a servo-hydraulic testing machine, INSTRON 8802 B790 with a loading capacity of 250 kN sufficient to load the specimens to failure. DIC was used for the room temperature test specimen throughout the testing to monitor the full-field deformations. The DIC system consists of a high-resolution camera with a Titanar A 75 mm lens (ARAMIS 5M with a resolution of 2448 x 2050 pixels). The lighting was supplied by a halogen light fitted on the tripod and the test proceeded until failure.

Further, flat tensile specimens (3mm thickness and gauge length of 80 mm) were used to obtain the true plastic stress-strain data at room and -120℃ (Figure 3.6), which shows yield strength increasing with decreasing temperature.

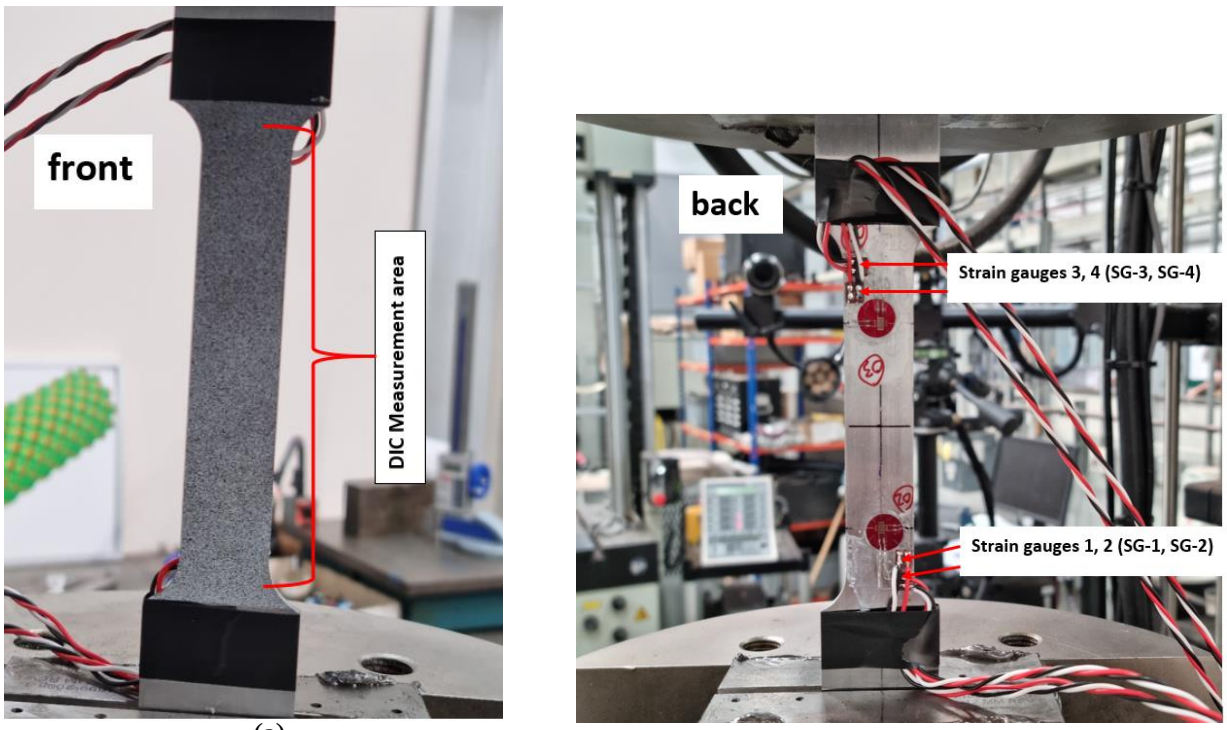

(a) (b)

Figure 3.3: M03-03 tensile specimen (a) speckle patterns applied at the front surface (b) 4 strain gauges installed at the back surface

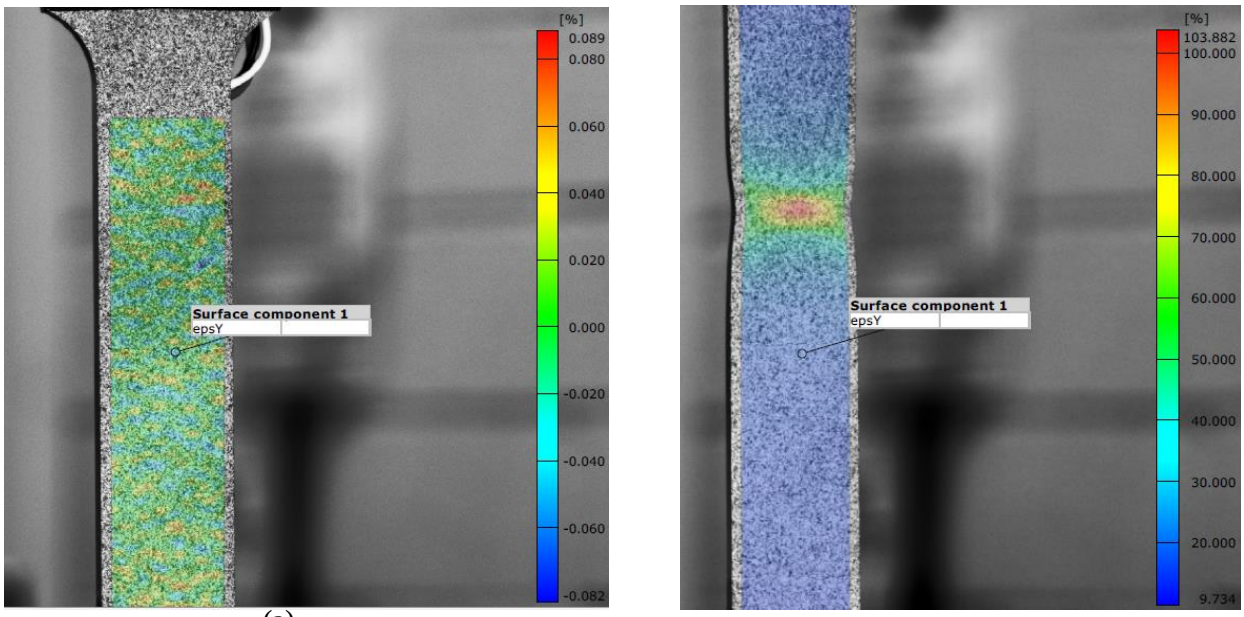

(a) (b)

Figure 3.4: Flat tensile test at 23℃ (a) *Y*-strain at the start of test (b) *Y*-strain at the start of necking

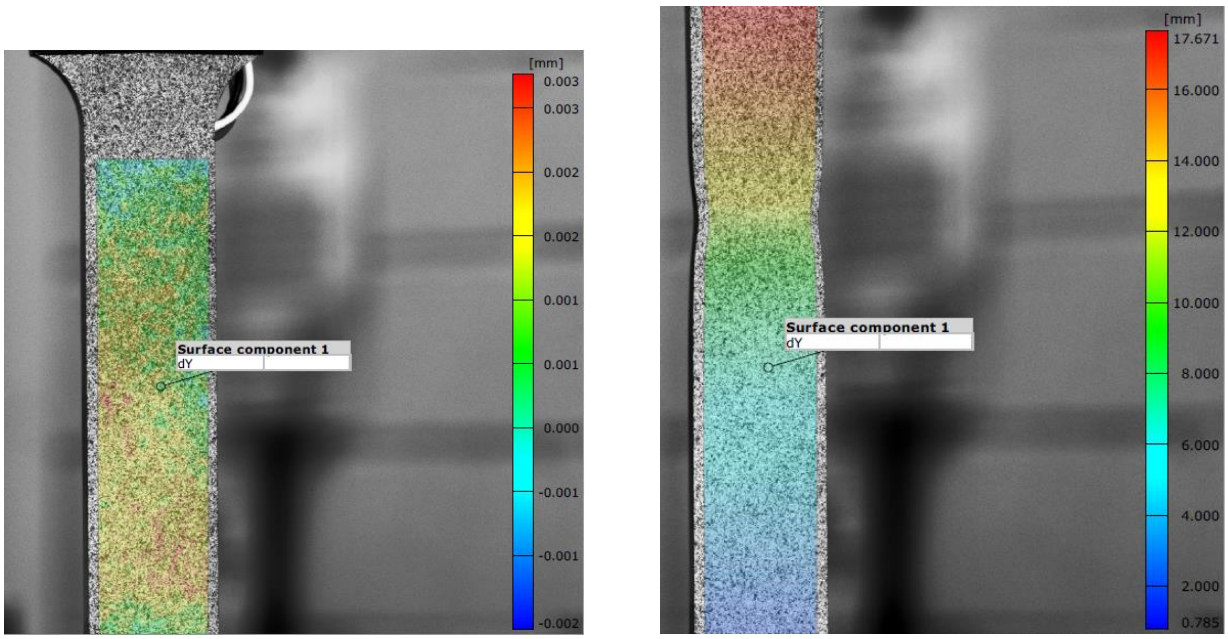

(a) (b)

Figure 3.5: Flat tensile test at 23℃ (a) *Y*-displacement at the start of test (b) *Y*-displacement at the start of necking

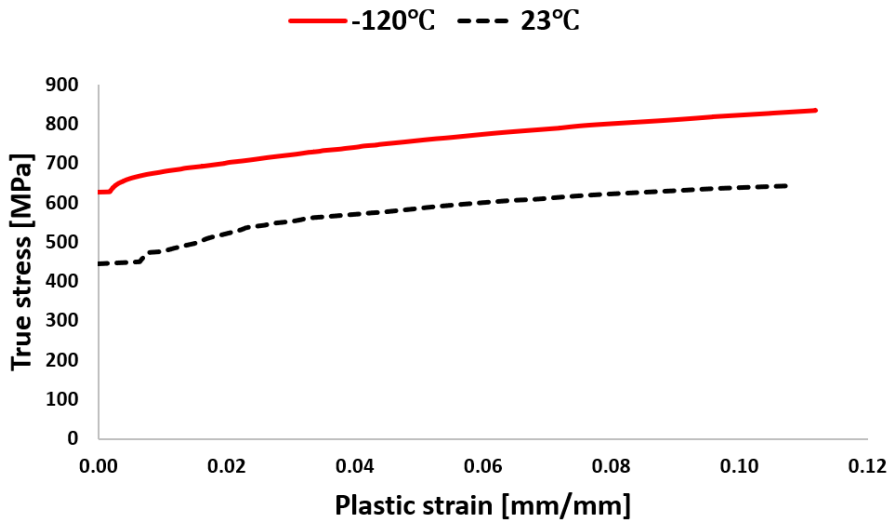

Figure 3.6: True plastic stress – strain characteristics of flat tensile specimen at room and low temperature

3.4.3 Round-bar tensile specimen

The mechanical properties and stress-strain behaviour of the X65 steel were tested according to BS EN ISO 6892 [120]. Standard round specimens (diameter of 10 mm and a gauge length of 60 mm) were used to obtain the yield and the ultimate tensile strength, elongations and elastic modulus at room temperature and -120℃ as shown in Table 3.2.

Table 3.2: Mechanical properties of tested API 5L X65 steel at room and low temperatures offset at 0.2%

$\sigma_{0.2\%YS}$ [MPa]	σ_{UTS} [MPa]	E [MPa]	ν	Elongation [%]	$(\sigma_{UTS}/\sigma_{YS})$
Room temperature (23℃)					
446	579	207000	0.3	27.3	1.3
Low temperature (-120℃)					
593	746	213000	0.3	32.8	1.3

For the crack propagation analyses, the mechanical and flow properties for an API 5L X65 pipe steel are employed to generate the required numerical solutions. Round bar tensile test was therefore, conducted at room (denoted M03-01) and -120℃ (denoted M03-02). During the test, the specimens were loaded quasi-statically under displacement control using a servo-hydraulic testing machine, INSTRON 8500 B488 with a loading capacity of 100 kN sufficient to load the specimens to failure.

3.5 Charpy V-notched specimen

Offshore structures including oil and gas pipelines are often designed for quasi-static loading conditions. Though, there are occasions when dynamic loading such as impact loading affects the response of the structure. Chary V-notch (CVN) has been used over the years as a standardised qualitative method to qualify the property of material under impact loading. Therefore, in order to simulate the loading at the appropriate test temperature, CVN impact test was carried out to determine the impact resistance of absorbed energy for API 5L X65 pipe.

Charpy V-notch specimens of width equal to the thickness (W = B =10 mm) were prepared and tested according to BS 148-1[123]. The tests were conducted at a range of temperatures between room and low temperature: -150℃, -120℃, -110℃, -100℃, -90℃ -60℃, -40℃, 0℃ and 21℃. This was necessary to estimate the lower shelf temperature for fracture testing. Specimens were extracted in the rolling direction with a through thickness V-notch perpendicular to the rolling direction. As per BS 148-1, the V-notch has an angle of 45°, a crack depth of 2 mm and a root radius of 0.25 mm. A total of 10 specimens were tested using a 450 energy (J) capacity Zwick testing machine (see Figure 3.7) calibrated to a 2 mm striker head. At the end of each test, the absorbed energy, crystallinity and lateral expansion were measured, and the data curve fitted using a tanh function as shown later in Figure 3.19.

Figure 3.7: Zwick RKP450 Charpy test machine. Courtesy of TWI Ltd

3.6 Fracture toughness tests of SENT and SENB

Fracture toughness tests for three-point SENB and pin-loaded SENT were conducted for the API 5L X65 steel following BS ISO 12135 [49] and BS 8571 [95], respectively. The dimensions of the respective configurations tested are shown in Table 3.3. Localised cooling can be applied to SENT specimens clamped and loaded vertically, using a flow of liquid nitrogen vapour within insulation around the notch location. This method is effective for modest cooling, down to around -60°C, below which it can be difficult to establish a sufficiently constant and stable temperature for the duration of the soak time. Therefore, the pin-loaded SENT specimen was selected for test, so to be able to test at the lower temperature of -120°C in an environmental chamber, without the need for insulation. The choice of dimensions and configurations of the specimens were based on numerical analysis conducted to ascertain suitability of slenderness for testing. The crack depth-to-width ratios, a_0/W = 0.1, 0.3 and 0.5, were achieved using fatigue pre-cracking. In total, 36 specimens were tested, with three repetitions per crack configuration. Force and crack mouth opening displacements (CMOD) were obtained from load cell and displacement clip gauges at a crosshead rate of 0.5 mm/min for SENB and 1 mm/min for SENT.

The CMOD was calculated from the displacement measurement through the relation below [49], [95]:

$$CMOD = V_{p1} - \frac{Z_1}{Z_2 - Z_1}(V_{p2} - V_{p1}) \tag{3.1}$$

where V_{p1} and V_{p2} are the plastic parts of the clip gauge displacements of the knife heights of Z_1 and Z_2, respectively.

Figure 3.8 illustrates the knife height positions on SENT specimen to further illustrate the definitions in equation (3.1).

Table 3.3: Fracture specimen dimensions

B [mm]	**W [mm]**	$\boldsymbol{a}$ **[mm]**	$\boldsymbol{a/W}$
Pin-loaded single edge notched tension (SENT)			
15	30	3	0.1
15	30	9	0.3
15	30	15	0.5
Three-point single edge notched bend (SENB)			
15	30	3	0.1
15	30	9	0.3
15	30	15	0.5

The manufactured SENT and SENB specimens are shown in Figure 3.9 and Figure 3.10 respectively. The SENT and SENB setup, shown in Figure 3.12 (a) and (b) respectively, were tested at -120℃ (using liquid nitrogen) in an environmental chamber as shown in Figure 3.11.

Similar to the flat tensile specimens, speckle patterns were applied to the surface of the SENT (see Figure 3.13) at room temperature to capture the deformation using DIC. The tested SENT specimen at maximum load is shown in Figure 3.14. During the test for the SENT, the load is applied through the pin and clevis of the specimen of a tensile machine (INSTRON B107) with a load capacity of 500kN. The clevis and pin mating surfaces are machined smooth to permit free rotation of the specimen during loading. The SENB specimens on the other hand were tested in three-point bending, supported on rollers, which move freely on the surface of the fixture of the same test machine as the SENT test. The test load was applied via a roller and the variation of the applied load with the CMOD is recorded by two clip gauges mounted on the attached knife edges during the fracture tests for the room and the low temperatures. The setup for DIC for the SENB test at room temperature is shown in Figure 3.15 and the speckle pattern with the tested specimen are illustrated in Figure 3.16 (a) and (b).

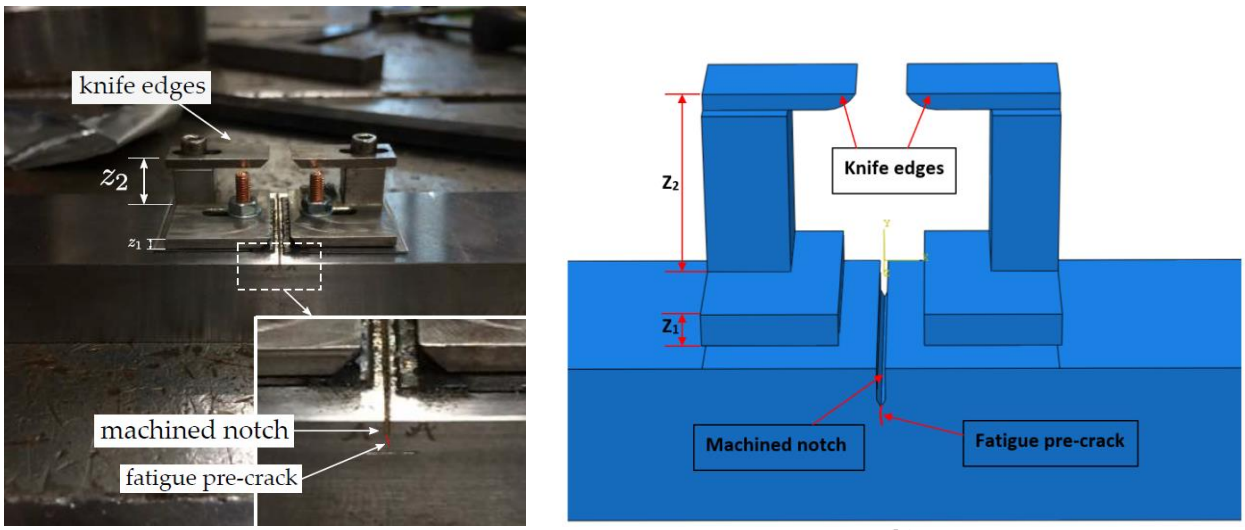

(a) (b)

Figure 3.8: SENT specimen configuration showing knife edges and clip gauge displacement of knife height positions, Z_1 and Z_2 with: (a) close-up view of machined notch and pre-crack (Photo courtesy by TWI) (b) drawing to illustrate knife height positions on the photo

The *J*-integral was calculated at the assessment point based on equations given in BS 8571: 2018 [95] and BS ISO 12135 [49]:

$$J = J_{el} + J_{pl} = \frac{K^2}{E'} + \frac{\eta_p U_p}{B b_0} \tag{3.2}$$

where J_{el} and J_{pl} are the elastic and plastic components of *J*, respectively; *K* is the elastic stress intensity factor (SIF) determined for the force acting on the specimen at the start of unloading; E' is the longitudinal elastic modulus in plane strain; η_p is a dimensionless function of geometry; U_p is the area under the plastic part of the load versus CMOD curve; B is the specimen thickness and b_0 is the crack ligament length $(W - a)$. The values of *K* and η_p were obtained for the calculation of *J* based on the respective equations provided in BS 8571: 2018 [95] and BS ISO 12135 [49].

In addition to the *J*-integral, the CTOD is also calculated as the sum of the elastic and plastic components as [49], [95]:

$$CTOD = \delta = \delta_{el} + \delta_{pl} = \frac{(1-\nu^2)K^2}{1.5R_{p0.2}} + V_{p1} - \frac{a_0 + Z_1}{Z_2 - Z_1}(V_{p2} - V_{p1}) \tag{3.3}$$

where $R_{p0.2}$ is the 0.2% offset yield strength of the steel grade at the temperature of the fracture toughness test.

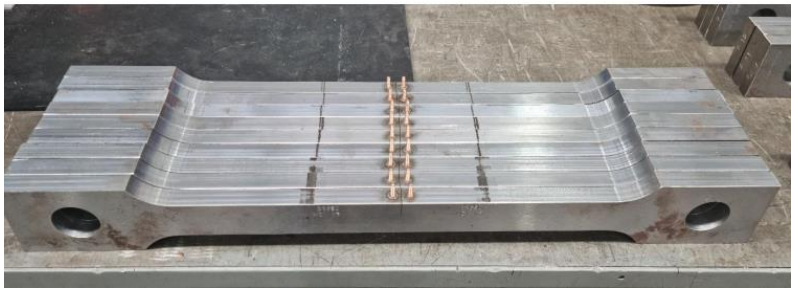

Figure 3.9: Pin-loaded SENT specimens' configuration to be tested using single point unloading method

Figure 3.10: SENB specimens to be tested at -120℃ using single specimen unloading method

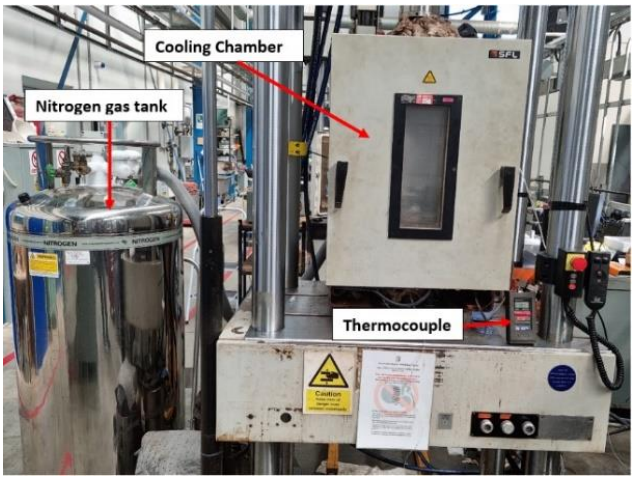

Figure 3.11: Test apparatus used for SENB and SENT low-temperature fracture tests

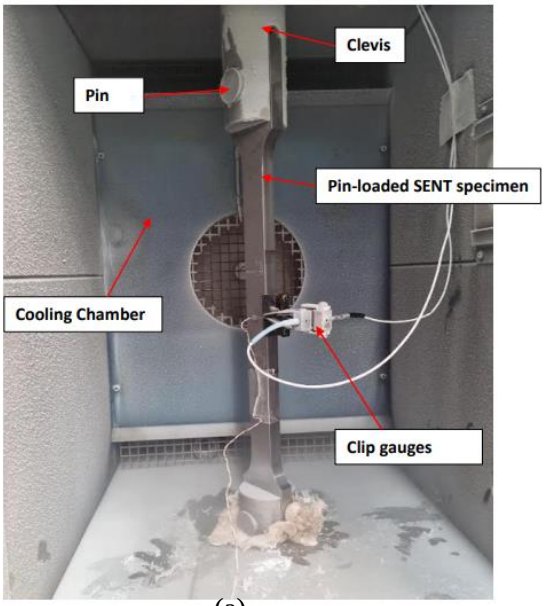

(a)

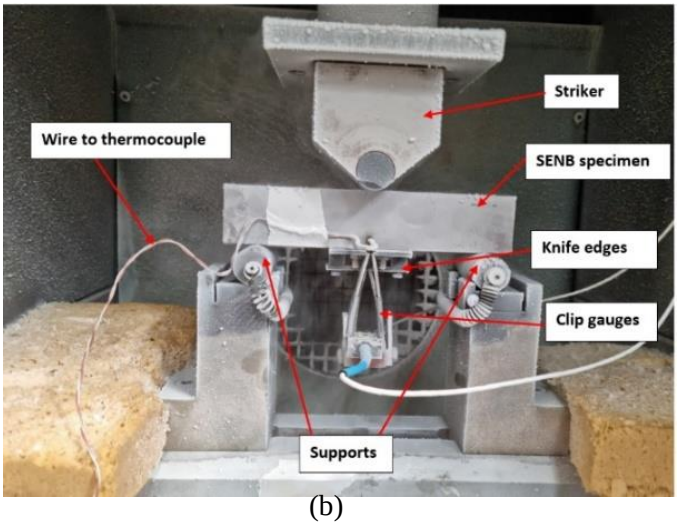

(b)

Figure 3.12: Fracture test set up at -120℃ in a cooling chamber based on liquefied nitrogen gas for single point specimen method: (a) pin-loaded SENT (b) three-point SENB

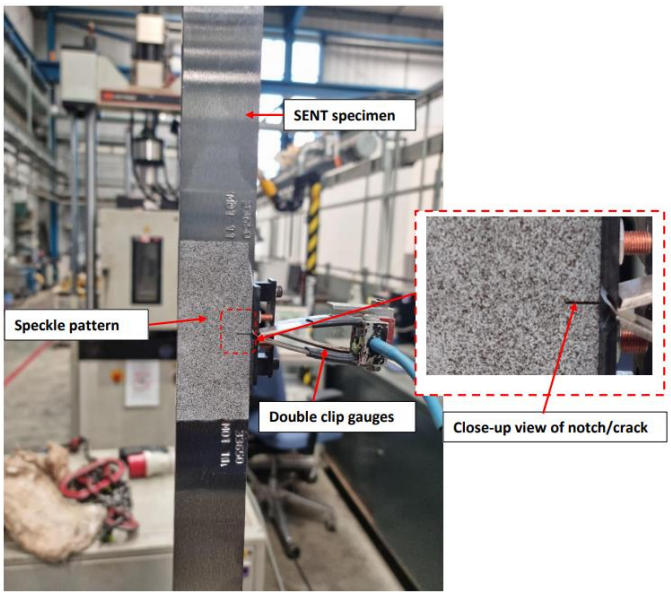

Figure 3.13: Pin-loaded SENT specimen showing close-up view of the machined notch region for DIC measurement at room temperature for 3 mm crack length (a/W= 0.1)

Figure 3.14: Pin-loaded SENT specimen, a/W= 0.1 tested to maximum load

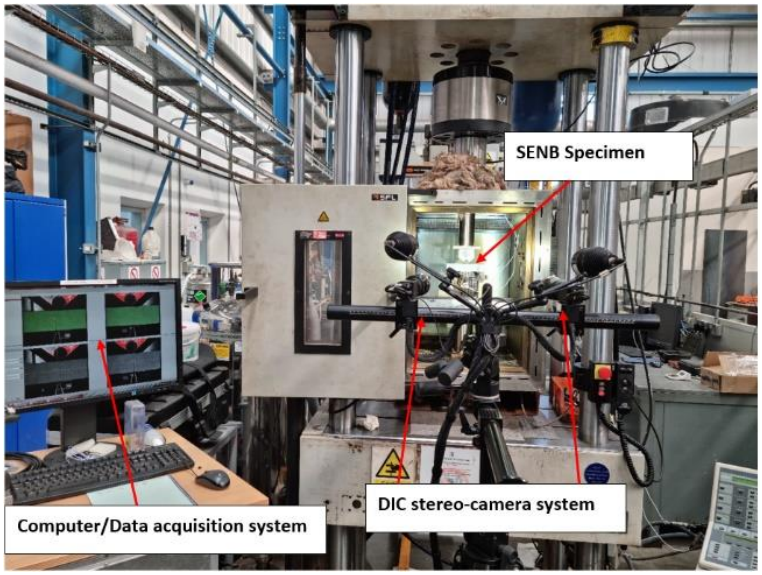

Figure 3.15: DIC system setup with the SENB specimen mounted in the test rig

(a)

(b)

Figure 3.16: SENB specimen for room temperature test, a/W= 0.5: (a) Speckle pattern generated on the surface of for DIC measurement (b) tested to maximum load

3.7 Constraint analysis for SENB and SENT specimens

To apply constraint-sensitive defect assessment procedures in BS 7910 Annex N [23], the fracture toughness (J_0 values) obtained from experiments for various crack configurations were re-indexed in terms of the elastic T-stress ($\beta_T L_r$). The procedure described in BS 7910 Annex N [23] was used to calculate the relative collapse load, L_r, and T-stress in this study, as summarised in Figure 3.17.

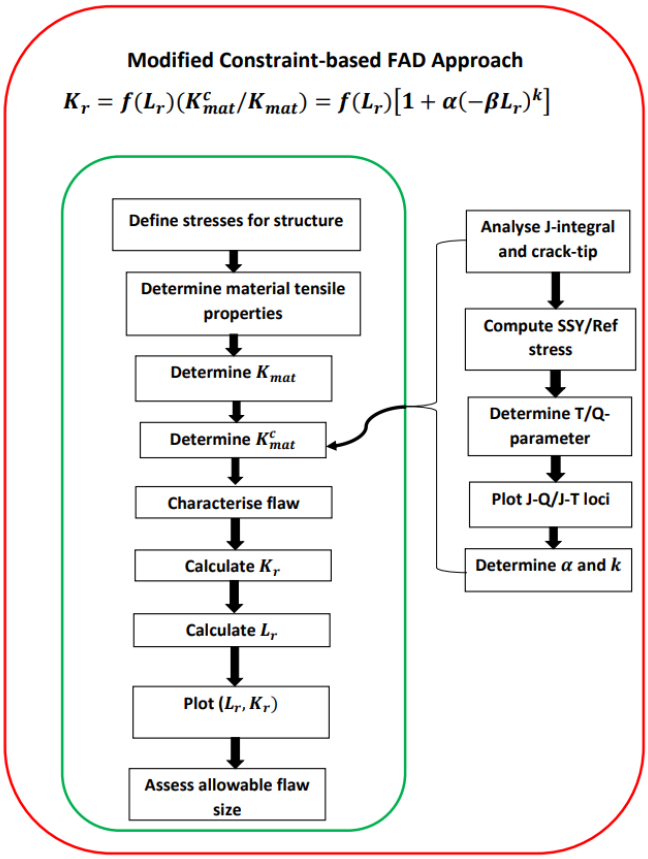

Figure 3.17: Constraint-based procedure used in this study

Structural integrity assessment of engineering components is assessed in terms of parameters that measure the proximity to either plastic collapse or fracture within linear elastic fracture mechanics (LEFM). The applied load, P, is compared with the plastic collapse load, P_L, through a parameter, L_r. This can also be defined in terms of the reference stress (σ_{ref}) that characterises the distribution of stress in the vicinity of a flaw and yield strength (σ_y), as defined in BS 7910 [23]:

$$L_r = \frac{\sigma_{ref}}{\sigma_y} = \frac{P}{P_L}\left(= \frac{applied\ load}{limit\ load}\right) \tag{3.4}$$

where

L_r is the collapse ratio on the horizontal axis of FAD

σ_y is the yield strength taken as the lower yield strength, or 0.2% proof strength [MPa]

σ_{ref} is the reference stress [MPa]

When $L_r = 1$, then σ_{ref} is equal to σ_y. The limit load in FAD is required for the calculation of σ_{ref}. For instance, the reference stress which characterises the increase in stress in the vicinity of a flaw for a through-thickness flaw in plates under combined tension and bending is calculated as

given in Annex P of BS 7910, as defined in equation (3.5). Please, refer to Annex P of BS 7910 for other equations for the calculation of reference stress for different geometries.

$$\sigma_{ref} = \frac{P_b + ({P_b}^2 + 9{P_m}^2)^{0.5}}{3\left\{1 - \left(\frac{2a}{W}\right)\right\}} \tag{3.5}$$

where,

P_b is the primary bending stress (MPa)

P_m is the primary membrane stress (MPa)

a is half crack length for through-thickness flaw (mm)

W is the plate width (mm)

Primary stresses are set-up in a structure due to mechanical loads and contribute to plastic collapse. The primary bending stress, P_b, is the local average stress across the thickness of a component/structure developed due to mechanical loads and includes the effect of discontinuities. The primary membrane stress, P_m, on other hand is the average stress across the thickness of a component or structure developed due to the mechanical loads [23].

Similarly, the possibility of fracture under LEFM is quantified by the ratio of the applied stress intensity factor, K_I to an experimentally measured material toughness, K_{mat}. In order to use the notation of *J*-based fracture mechanics, the ordinate of the FAD is written in terms of the fracture toughness J_{mat} and the elastic component of the driving force $J_{elastic}$:

$$K_r = \frac{K_I}{K_{mat}} = \sqrt{\frac{J_{elastic}}{J_{mat}}} \tag{3.6}$$

where K_I is the applied stress intensity factor, and K_{mat} and J_{mat} are measures of the material's fracture toughness.

BS 7910 [23] provides a method for defect assessment which may be related to *J* and crack opening displacement approaches. BS 7910 [23], however, has conservatisms introduced in approximate failure assessment curves (FACs) and also in the use of fracture toughness data from deeply cracked bend specimens. Improvement in the methods used to reduce this conservatism by consideration of constraint effects has been the subject of ongoing research.

Flaws in real structural components are typically surface cracks (low constraint) that contrasts significantly with fracture toughness testing of deeply cracked specimens. Therefore, Ainsworth

[124] and Ainsworth and O'Dowd [125] incorporated constraint effects through modification of the failure assessment curve (FAC) by quantifying constraint through the normalised structural parameter, β, and a function of material behaviour through the parameters α and k. The normalised constraint parameter, β, can be expressed by either elastic T stress or Q parameter, using:

$$\beta_T = \frac{T}{L_r \sigma_y} \tag{3.7}$$

$$\beta_Q = \frac{Q}{L_r} \tag{3.8}$$

where β_T and β_Q are the normalised structural constraint parameters, which both depend on the geometry, crack size and loading configurations. Negative values of β_T or β_Q correspond to low constraint, whereas positive values, as in deeply cracked bend geometries, correspond to high constraint.

The limit load required for calculation of L_r for SENB specimens is given by [24]:

$$P_L = \left(\frac{W^2 B \sigma_Y}{S}\right) f_L \tag{3.9}$$

where W, B and S are specimen width, thickness, and span respectively, σ_Y is offset yield strength and f_L is the Von-Mises yield factor.

For plane strain conditions, the Von-Mises yield factor, f_L, for SENB is given by [24]:

$$f_L = \frac{2}{\sqrt{3}}\left(1.12 + 1.13\left(\frac{a}{W}\right) - 3.194\left(\frac{a}{W}\right)^2\left(1 - \frac{a}{W}\right)^2\right) for\ \left(0 \le \frac{a}{W} \le 0.18\right) \tag{3.10}$$

$$f_L = \frac{2.44}{\sqrt{3}}\left(1 - \frac{a}{W}\right)^2 \ for\ \left(0.18 \le \frac{a}{W} \le 1\right) \tag{3.11}$$

Negative values of β_T (or β_Q) are associated with a loss of crack-tip constraint and an increase in fracture toughness. Since β_T depends only on specimen geometry, flaw size and loading type (not magnitude), this can be defined by simple polynomial expressions as per Annex N of BS 7910 for various geometries [23].

The normalised constraint parameters, β_T for three-point SENB and SENT specimens for $0 \le \frac{a}{W} \le 0.8$ are summarised in equations (3.12) and (3.13) respectively:

$$\textbf{SENB}:\ \beta_T = -0.7887 - 0.1795\left(\frac{a}{W}\right) + 32.9014\left(\frac{a}{W}\right)^2 - 153.45\left(\frac{a}{W}\right)^3 + 316.11\left(\frac{a}{W}\right)^4 - 308.47\left(\frac{a}{W}\right)^5 + 115.18\left(\frac{a}{W}\right)^6 \quad (3.12)$$

$$\textbf{SENT}:\ \beta_T = -0.5889 - 0.0128\left(\frac{a}{W}\right) + 0.5512\left(\frac{a}{W}\right)^2 + 4.651\left(\frac{a}{W}\right)^3 - 4.6703\left(\frac{a}{W}\right)^4 \quad (3.13)$$

The plane strain Von-Mises limit load solution for pin-loaded SENT specimens [24] is:

$$P_L = WB\sigma_Y f_L \quad (3.14)$$

where

$$f_L = (\gamma/1.702)\left(1 - \left(\frac{a}{W}\right) - 1.232\left(\frac{a}{W}\right)^2 + \left(\frac{a}{W}\right)^3\right) for\ \left(0 \le \frac{a}{W} \le 0.545\right) \quad (3.15)$$

$$\gamma = 3.404/\sqrt{3}$$

3.7.1 Modification of Failure Assessment Diagram (FAD)

The combination of standard approach in BS 7910 clause 7 and Annex N: "Allowance for constraint effects", is an attempt to characterise constraint quantitatively using a two-parameter fracture mechanics (TPFM) approach, through the elastic *T*-stress or *Q*-parameter [23].

Essentially, Annex N of BS 7910 [23] allows the user to quantify the constraint conditions associated with the structure being assessed and the small-scale specimens used to assess it, typically using either the elastic T-stress or Q parameter. Because, the *T*-stress requires only elastic calculations, it is used for the initial analyses in this study. It should be noted that the use of the elastic-plastic Q parameter gives very similar results to the linear-elastic *T*-stress when plasticity is not widespread ($L_r < 1$).

A failure assessment diagram (FAD) represents a simple geometry-dependent failure locus (Failure Assessment Curve, FAC), defined by the fracture ratio, K_r as a function of the applied load ratio, L_r [23]:

$$K_r = f(L_r) \quad (3.16)$$

By evaluating these two parameters using equations (3.4) and (3.6), failure could be avoided if the point (K_r, L_r) lies within the failure assessment diagram as shown in Figure 3.18. A point within the FAC would suggest that the procedure is non-conservative. Assessment point farther outside

the FAC might hint at inherent safety factors that could be reduced by carrying out a more detailed assessment.

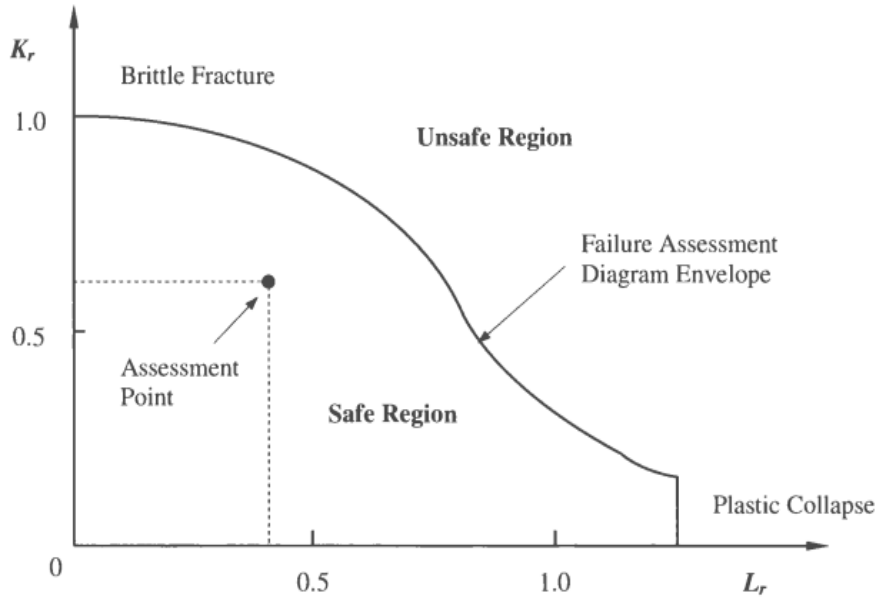

Figure 3.18: Failure assessment diagram (FAD) [126]

To conduct a fracture assessment, both brittle and plastic collapse parameters are implemented in the FAD. This is an essential tool in order to assess the integrity of components or structures containing crack-like flaws. Both failure modes (brittle and ductile tearing) should be considered for fracture evaluation (structural integrity assessment). Note that the FACs are independent of geometry and material strain-hardening properties [125].

To examine the constraint effect, it is essential to have a measure of not only the structural constraint parameter, but also the dependence of the material toughness on constraint. There is guidance provided in the R6 [24] and BS 7910 [23] assessment procedures on an approach to account for constraint using a simple two-parameter model based on the work of Ainsworth and O'Dowd [125]. With respect to the *T*-stress and *Q*-parameter, the model proposed is described as:

$$K_{mat}^{C} = \begin{Bmatrix} K_{mat};\ \beta L_r, Q \geq 0 \\ K_{mat}[1+\alpha(-\beta L_r)^k];\ \beta L_r < 0 \\ K_{mat}[1+\alpha(-Q)^k];\ \ Q < 0 \end{Bmatrix} \tag{3.17}$$

where α and k are constants that define the sensitivity of toughness to constraint variation for the material and temperature of interest. This model has the advantage that for a given material, the effect of any state of constraint can be modelled with two parameters, α and k. Sherry et al. [127] noted that α and k depend on the material properties and the fracture mechanisms, with ductile

fracture initiation toughness generally exhibiting a lower sensitivity to constraint than cleavage fracture toughness.

Two modifications to the constraint-based FAD approach are provided in BS 7910 Annex N [23] to account for constraint effects. First, the material toughness used to define K_r is set equal to K_{mat}^c, rather than K_{mat}. In this way, the failure assessment curve remains unchanged from equation (3.16). However, since K_{mat}^c is a function of constraint and hence applied load, the loading curve becomes a non-linear function of L_r. Instead, a modified FAD may be obtained by constructing the FAC using the relationship [125]:

$$K_r = f(L_r)\left(\frac{K_{mat}^c}{K_{mat}}\right) \tag{3.18}$$

Substituting equation (3.17) for $\beta L_r < 0$ into equation (3.18), the modified FAD can be expressed as:

$$K_r = f(L_r)[1 + \alpha(-\beta L_r)^k] \tag{3.19}$$

This method of constraint-based fracture assessment involves the modification of the FAD but retains the definition of K_r given by equation (3.6). In other words, the fracture toughness obtained from the geometry with high constraint remains unchanged, but the failure assessment curve is modified by low constraint factors. Several authors, including but not limited to [106], [128]–[132], have shown that constraint-modified FAD can be used for a reduction in structural integrity conservatism.

There are several procedures that exist for the treatment of constraint loss such as the BS 7910 [23], R6 [24] and API 579/ASME [25] based on the work of Ainsworth and O'Dowd [125]. The procedure from BS 7910 [23] was adopted in this thesis for the construction of the FAD and are summarised as follows (see also Figure 3.17)

I. Measure the high constraint fracture toughness K_{mat} using standard deeply cracked bend fracture specimens.
II. Evaluate the standard BS 7910 parameters K_r and L_r for the defective component.
III. Perform a FAD assessment using the standard failure assessment curve, $K_r = f(L_r)$
IV. Evaluate the structural constraint parameters, β, for the defective component. In this thesis, the elastic constraint parameter, $\beta_T = T/L_r\sigma_y$ is used, where T is the T-stress.
V. Using a range of test specimen geometries and cracked sizes (here, SENT and shallow-cracked SENB), and hence a range of constraint levels, β, measure the low constraint toughness K_{mat}^c.

VI. Fit the data from step V with a function of the form, $K_{mat}^{c} = K_{mat}[1 + \alpha(-\beta L_r)^k]$

VII. Construct a constraint modified FAD using the failure assessment curve $f(L_r)[1 + \alpha(-\beta L_r)^k]$ and compare the assessment point (K_r, L_r) for the defective component with this modified curve.

These procedures were performed in CrackWISE software [119] to produce the FADs illustrated in Figure 3.34 to Figure 3.37 which show the increased margin against fracture which are possible with constraint-based methods.

3.8 Results and Discussions

Figure 3.19 presents the transition curve for the Charpy V-notch test conducted to identify the temperature for the tensile and fracture tests. When the load is applied to the test specimen in the upper transition region, cleavage does not occur due to the absence of critical particles near the crack tip. In the transition region, fracture is mostly controlled by the competition between ductile tearing and cleavage fracture showing the ductile-to-brittle behaviour. Therefore, the fracture toughness locus plotted in a typical three-region behaviour show the upper shelf corresponding to ductile fracture, lower shelf to cleavage fracture and the transition region experiences both ductile and cleavage behaviour. At room temperature this material presents fully ductile fracture with a Charpy impact energy of 226 J, whereas at a low temperature of -120℃, cleavage fracture occurs with a Charpy impact energy of 10 J. This value is selected as the Charpy-V notch energy to correlate with a lower bound value to the lower shelf fracture toughness, K_{IC} or J_C/J_0.

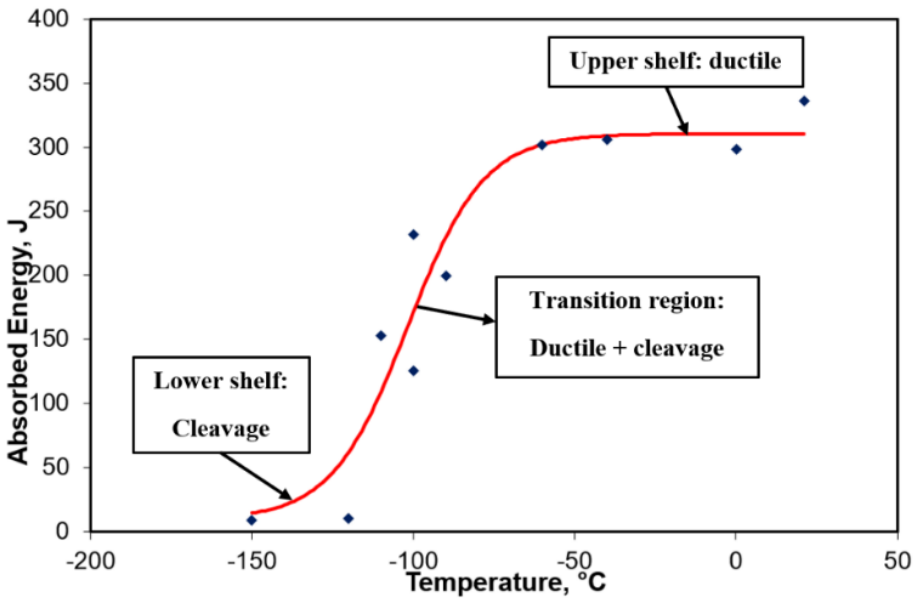

Figure 3.19: Transition curve for Charpy V-notch test

Figure 3.20 illustrates the SENB specimens with crack depth, a/W = 0.5 oxidised surfaces at the end of the fracture test, for the specimens tested to maximum load at room temperature. This technique is used to identify the contrast between cracked material and uncracked ligament. The test specimens that did not fracture after being subjected to maximum load were frozen in liquefied nitrogen for easier breaking/fracture to reveal fracture surfaces. Distinct line between the end of tearing during the test and the start of brittle fracture due to the freezing is shown. The crack faces then allow observation and measurement of the crack. The fracture surface of the a/W = 0.1 tested at -120℃ is also shown in Figure 3.21.

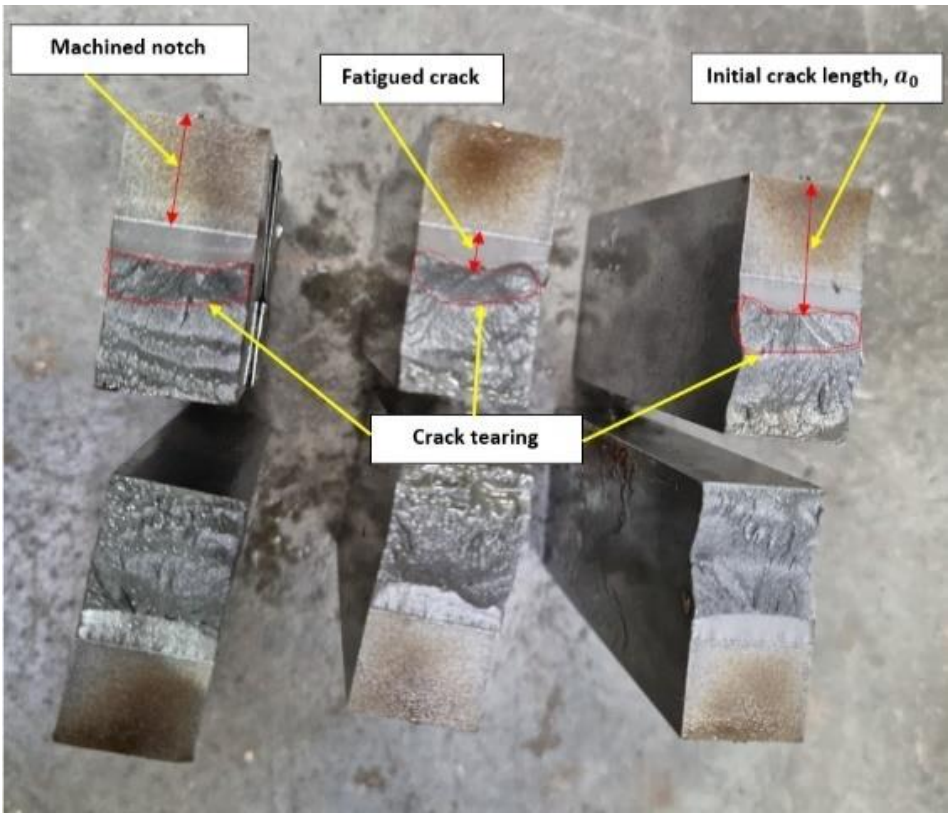

Figure 3.20: Oxidised crack faces for easy identification of the start and end of crack tearing for SENB specimen with crack depth a/W=0.5 tested at room temperature

Figure 3.21: Fracture surface of SENB with crack depth, $a/W = 0.1$ tested at -120℃

As discussed in chapter 2, section 2.5, ferritic steels undergo a transition in fracture mechanism with a change in temperature in the ductile-to-brittle transition (DBT) regions. At low temperatures, fracture proceeds by a cleavage mechanism, whereby fracture occurs at a rapid rate by the initiation and catastrophic propagation of a crack along crystallographic planes. Cleavage initiates at microcracks resulting from secondary phase particles within a plastically deformed material. Cleavage fracture is random, and failure occurs when the first critically sized microcrack propagates and this is illustrated in Appendix D and E for tests at -120℃. As temperature and plastic zone size increase from the lower shelf to the upper shelf on the DBT curve, cleavage fracture becomes less representative of the mechanism of failure. At higher temperatures, such as the upper shelf temperature of 23℃ used in this fracture test, fracture occurs as a result of the initiation, growth and coalescence of voids that form around the secondary phase particles in the form of inclusions or carbides. In most cases, this fracture mechanism is stable, requiring increasing load or displacement to progress to failure. This type of ductile behaviour is also shown in the fracture test reports in Appendix D and E at the room temperature tests.

Figure 3.22 to Figure 3.25 illustrate the relationship between crack depth, a/W and fracture toughness, J_0, at fracture/maximum load for the SENB and SENT specimens at -120℃ and 23℃ (cleavage and ductile fracture toughness respectively). J_0 is the J-value at 0.2 mm stable crack extension. It can be observed that J_0 increases under low constraint ($a/W = 0.1$), but $a/W = 0.3$

and $a/W = 0.5$ ratio are insensitive to fracture toughness, J_0. Further, there was an increase in fracture toughness by a factor of between two and six between the deeply-cracked and shallow-notched SENB specimens. The fracture test results are presented in Appendix B of this thesis.

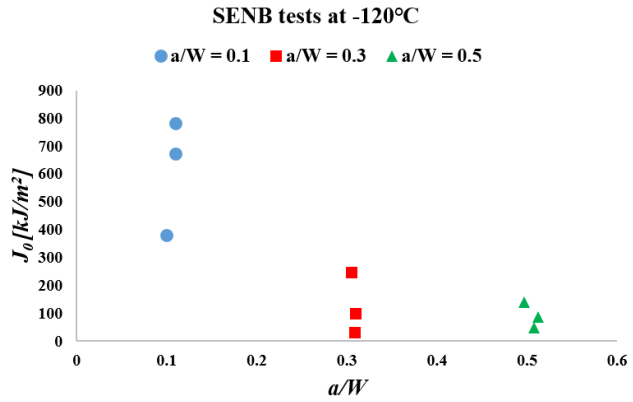

Figure 3.22: Relationship between fracture toughness and crack depth for SENB at -120°C, cleavage fracture

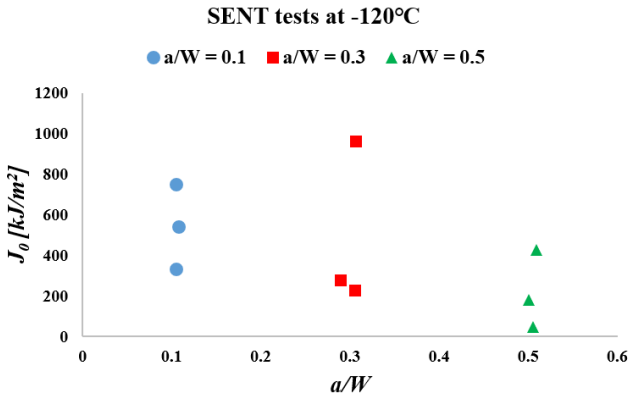

Figure 3.23: Relationship between fracture toughness and crack depth for SENT at -120°C, cleavage fracture

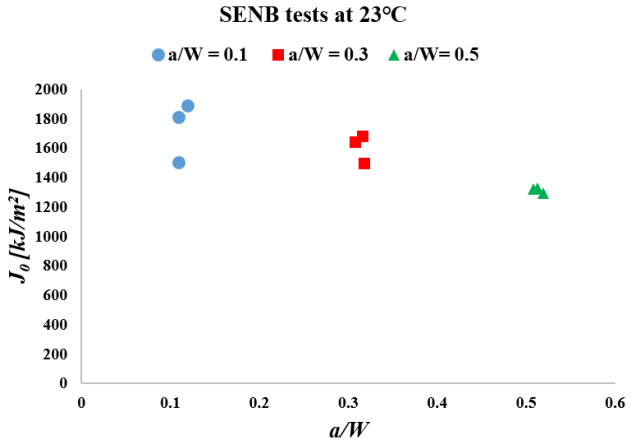

Figure 3.24: Relationship between fracture toughness and crack depth for SENB at 23°C, ductile fracture at maximum load

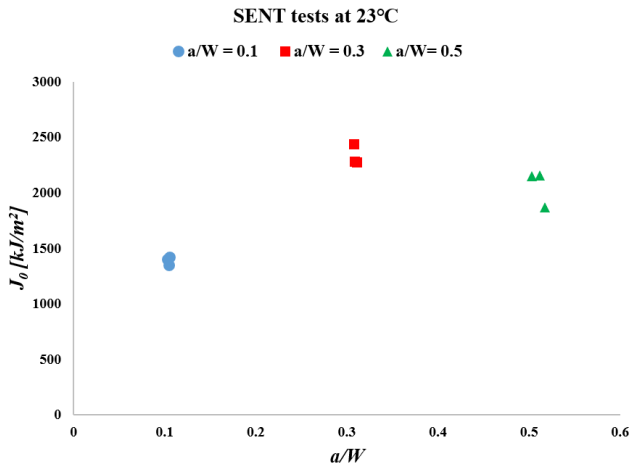

Figure 3.25: Relationship between fracture toughness and crack depth for SENB at 23°C, ductile fracture at maximum load

Figure 3.26 to Figure 3.29 illustrate the relationship between fracture toughness, J_0, and the amount of ductile tearing, Δa, for all experiments (a/W = 0.1, 0.3 and 0.5 at -120°C and 23°C for SENB and SENT). The increasing value of fracture toughness was observed to be highly dependent on the amount of ductile tearing, Δa, which in turn depends on the crack depth, a/W. In all the low temperature (-120°C) tests, no significant amount of stable tearing was observed, as expected, because this is close to the lower shelf temperature for this steel (-100°C). At room temperature (23°C), the toughness was defined at the maximum load in the test, and ductile tearing was observed in each case. The cleavage and ductile fracture toughness properties play a significant role in the constraint-modified FAD procedure. It involves comparing the applied loading conditions with the material's fracture toughness properties to determine the structural integrity. These two different fracture toughness measures are important in the use of the constraint-modified FAD procedure and should be taken into account to define crack sizes and loadings where brittle or ductile fracture is likely to occur.

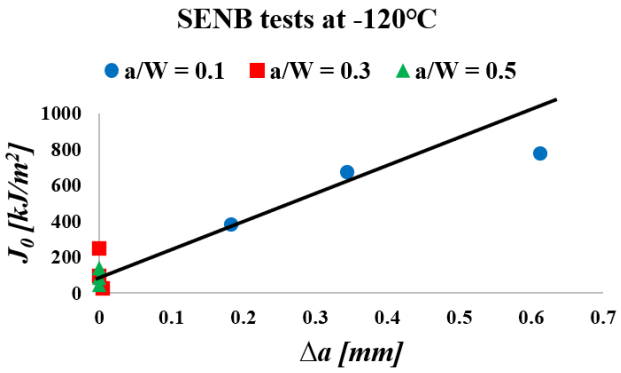

Figure 3.26: Relationship between fracture toughness and tear length for a/W = 0.1, 0.3 and 0.5 for SENB at -120°C

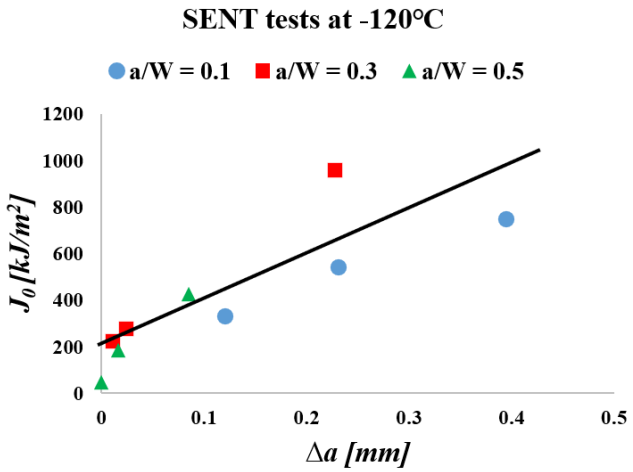

Figure 3.27: Relationship between fracture toughness and tear length for a/W = 0.1, 0.3 and 0.5 for SENT at -120°C

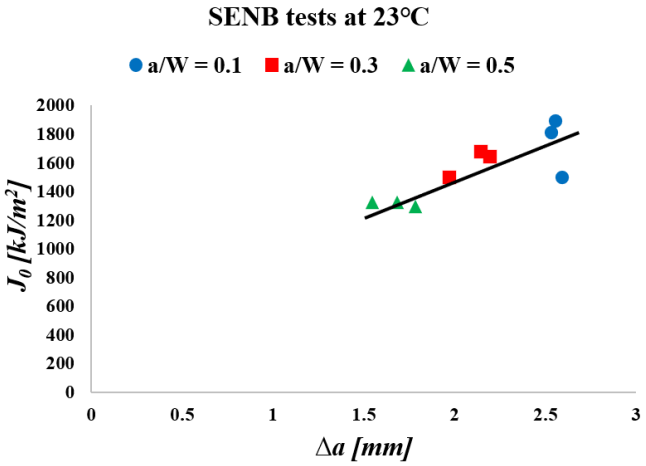

Figure 3.28: Relationship between fracture toughness and tear length for a/W = 0.1, 0.3 and 0.5 for SENB at 23°C

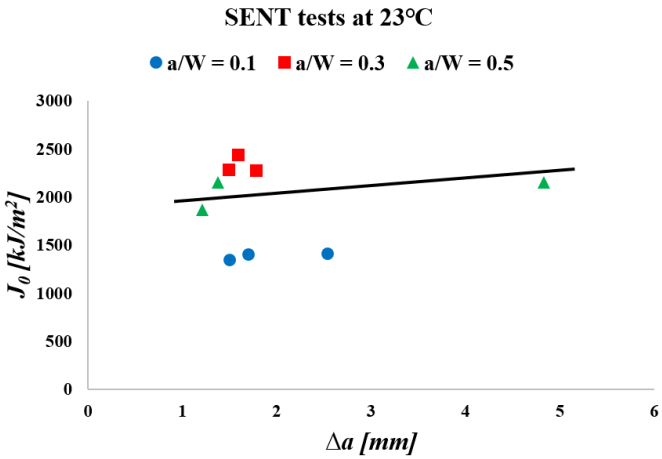

Figure 3.29: Relationship between fracture toughness and tear length for a/W = 0.1, 0.3 and 0.5 for SENT at 23°C

Figure 3.30 to Figure 3.33 show that shallow-notched bend specimens (those that have a loss of crack-tip constraint and exhibit negative values of T). This result in enhanced fracture toughness at both low (-120°C) and room temperatures (typically, cleavage and ductile tearing mechanisms respectively) compared to deeply cracked SENB geometries. Therefore, the resistance to fracture of the material in the presence of a crack is increased due to the low stresses near the crack tip. In contrast, deeply notched a/W=0.5 feature positive values of T and a geometry-independent toughness associated with a highly constrained flow field. The geometry with a negative T-stress indicates a low constraint level near the crack tip, whereas zero or positive T-stress corresponds to a higher constraint level. This behaviour is consistent with previous research carried out by [105], [117], [131], [133], [134], among others. Note in Figure 3.33 the low fracture toughness values for the low constraint SENT specimen (a/W=0.1) which should normally not be the case but this behaviour could not be ascertained as why this occurred during the test.

Further, it is observed that additional testing is recommended to determine a consistent relation between fracture toughness and constraint T/σ_Y, since data scatter is high under high fracture toughness/low constraint conditions for SENB and all SENT crack configurations at -120°C.

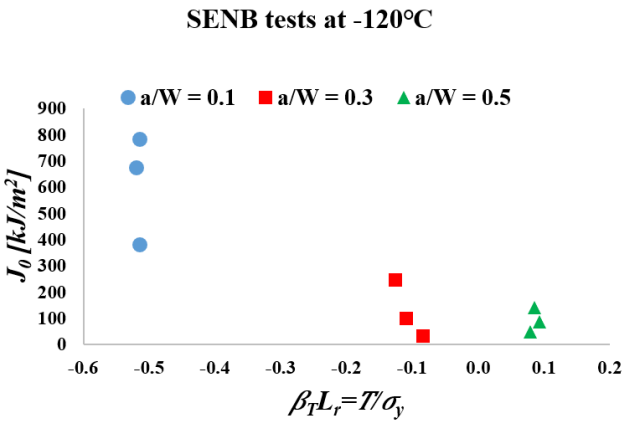

Figure 3.30: Fracture toughness as a function of T-stress for SENB at -120°C

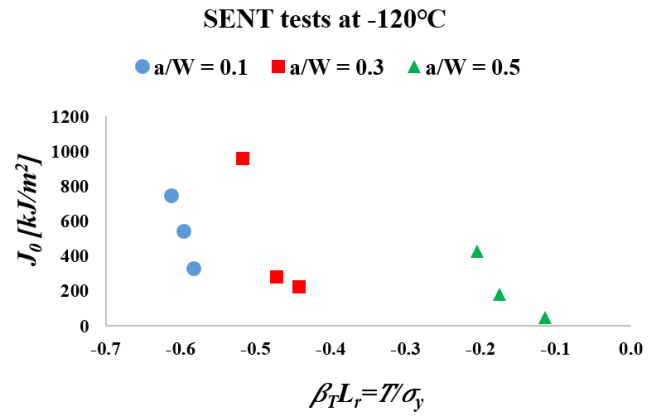

Figure 3.31: Fracture toughness as a function of T-stress for SENT at -120°C

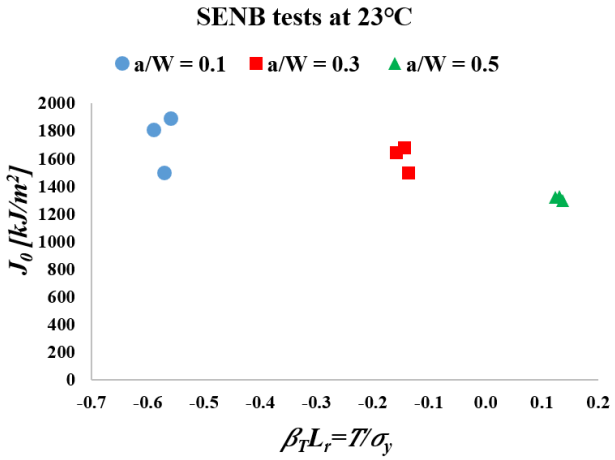

Figure 3.32: Fracture toughness as a function of T-stress for SENB at 23°C

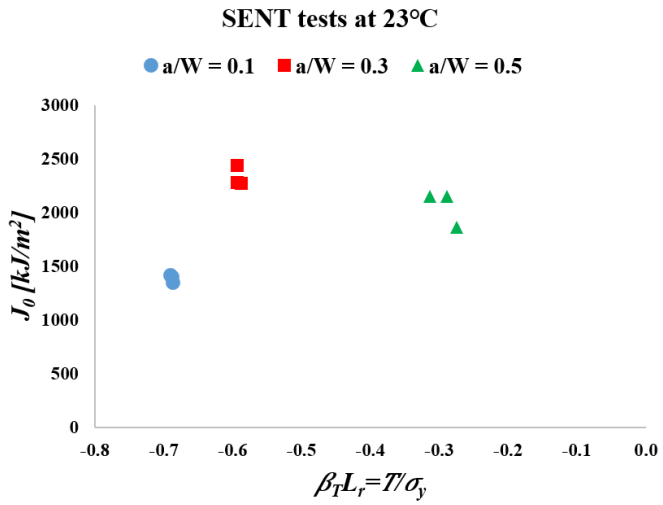

Figure 3.33: Fracture toughness as a function of T-stress for SENT at 23°C

The work of Beremin et al [77] describes a widely adopted model based on the simple weakest link statistics to define the functional as a relationship between the macro and microscale driving

forces for cleavage fracture. Their work provides a Weibull distribution for the probability of cleavage fracture (P_f) as a function of the scalar Weibull stress, σ_w:

$$P_f = 1 - exp\left[-\left(\frac{\sigma_w}{\sigma_u}\right)^m\right] \quad (3.20)$$

where σ_u and m are parameters of the model. The Weibull parameter, m provides a quantitative description of the loss of constraint using material fracture toughness and proper judgement of the Weibull parameter for different material is desirable for practical needs. The calibration of the Weibull exponent, m is a subject of ongoing research and current best practice is to use data derived from both high and low constraint fracture toughness specimens, such as deep and shallow-cracked bend specimens. When such datasets are available, Gao et al [78], provides a suitable methodology for determining m and σ_u.

Sherry et al [135] provides a set of look-up tables that define the material parameters, α and k in equation (3.17) and these have been incorporated in BS 7910 [23] to define the constraint sensitivity of material toughness for cleavage fracture behaviour. The material parameters, α and k are given as a function of tensile properties (E/σ_Y), work hardening exponent (n) and the Weibull model exponent, (m), with constraint quantified in terms of $\beta_T L_r$ or T/σ_Y. Once identified, these parameters may be applied to equation (3.17) for the material and at the appropriate temperature of interest. In order to generate the best possible interpretation of equation (3.17), the approach adopted in this study for the construction of the FAD was to choose the appropriate candidate values of α and k from the look-up tables in BS 7910 Annex N. Based on the work hardening exponent, n = 15, for ferritic steels at -120°C (E = 213000 MPa, σ_Y = 593 MPa, $E/\sigma_Y \approx 350$) and at room temperature, 23°C (E = 207000 MPa, σ_Y = 446 MPa, $E/\sigma_Y \approx 450$), for a range of Weibull exponents ($(5 \leq m \leq 20)$, the choice of α and k values are shown in Table 3.4 and Table 3.5.

In cases where sufficient test data is available, a value of m can be selected that gives the α and k values which provide the best fit to the data. Alternatively, m can be calibrated directly using test data from high and low constraint test specimens. This requires not only an extensive testing programme, but also, detailed cracked-body large strain elastic-plastic finite element analysis of the test specimens, as well as a suitable post-processor to calculate the Weibull stress, σ_w [127]. Therefore, the approach is analytically complex, labour intensive and unsuitable for routine engineering application. Hence, it was convenient to select a value of m that gave α and k values which provided an increased margin in the FADs. Generally, lower values of m are insensitive to constraint and higher values of m are constraint sensitive.

The work hardening exponent, *n* (also employed in this thesis) is a measure of a metal's ability to resist plastic deformation after it has yielded under stress. This is defined as the slope of the logarithmic relationship between stress and strain during plastic deformation phase of a tensile test. A high work hardening exponent indicates that the material can withstand significant plastic deformation without fracturing or cracking. The value of the work hardening exponent varies depending on the material being tested and the testing conditions.

From the parametric study conducted for different values of *m*, (a value of *m* = 15) and work-hardening exponent, *n* (*n* =15) gave results with an increased margin in the FADs. Therefore, these were chosen for this study as can be seen from Figure 3.34 to Figure 3.37 at the respective temperatures and cracked specimens.

Table 3.4: α and k defined with respect to $\beta_T L_r = T/\sigma_Y$ for n = 15, $E/\sigma_Y \approx 350$ for low (-120°C) temperature

m	**10**	**15**	**20**
α	3.434	6.821	9.652
k	2.38	2.57	2.48
m	**5**	**7.5**	**12.5**
α	0.759	1.929	5.118
k	2.26	2.29	2.49

Table 3.5: α and k defined with respect to $\beta_T L_r = T/\sigma_Y$ for n = 15, $E/\sigma_Y \approx 450$ for room temperature (23°C)

m	**10**	**15**	**20**
α	3.508	6.907	9.721
k	2.38	2.56	2.47
m	**5**	**7.5**	**12.5**
α	0.945	2.033	5.192
k	2.47	2.35	2.47

Constraint-modified FADs are shown in Figure 3.34 to Figure 3.37 for the SENB and SENT test specimens of a constraint-sensitive material based on experimental data. By combining the applied loading conditions, the material properties and dimensions of the defect, the structural integrity

can be assessed and the likelihood of failure can be determined. The constraint-correction FADs are compared to those of the standard Option 1 approach in BS 7910. For Option 1 of BS 7910, deep notched specimen is typically used to populate the failure assessment diagram (FAD). The lower values of the toughness was adopted in all analyses. The deep cracked specimens are designed to simulate the behaviour of cracked components or structures, allowing for safe but conservative assessment of their integrity. Therefore, there is merit in applying the experimental data from shallow cracked SENB and SENT specimens to provide some form of refinement to the inherent conservatism in defect assessment procedures, particularly BS 7910.

The values of assessment points (L_r, K_r), primary bending and primary membrane stresses are shown in Table 3.6 and Table 3.7 respectively for SENT and SENB specimens. These primary bending and primary membrane stresses were used alongside other mechanical properties obtained from the experiment to derive the FADs with constraint-correction factors in this study.

At small fractions of the limit load ($L_r \rightarrow 0$), there is no effect of constraint or geometry, as failure occurs under essentially elastically-controlled conditions. However, with increasing load, the constraint-enhanced toughness for shallow cracked SENB configuration (a/W = 0.1) increases. For SENT (a/W = 0.1 and 0.3), an enlargement in the FAD is observed for both temperatures analysed, with the largest adjustment at loads close to the limit load (L_r=1), see Figure 3.34 to Figure 3.37. Therefore, there are significant advantages to be gained from this approach for applied loads with magnitudes close to the limit load (these stresses may be close to those at which engineering components are expected to operate). The analysis of the tests conducted on the SENB specimens at the low temperature generated assessment points that lie farther from the FAC, as all these specimens failed during the test. Noticeably, the high constraint SENB specimen at low temperature (-120°C) in Figure 3.34 has K_r value of 3.1. Further, it is observed that, assessment points for the SENT at the same low temperature for the Option 1 and a/W= 0.3 cases have both the points within the FAC (indicating failure did not occur), but all the low temperature specimens fractured. This raises concerns about the specimens that have their assessment point lying in the safe zone of the FACs, even though failure occurred. A possible explanation to this could be microstructural difference due to the low temperature, however, this was not verified as part of this research.

For the test conducted at room temperature, SENB specimens have the assessment points that are almost in a straight line and lie farther outside the FAC (all tests tested to maximum load, failure did not occur). The SENT on the other hand, have the assessment points outside the FAC which are almost clustered at the bottom end of the FAC.

Table 3.6: Results of assessments and primary membrane stresses for SENT

a/W	L_r	K_r	P_m
SENT at -120℃			
0.1	1.138505	0.251601	607.62
0.3	0.986967	0.49958	409.69
0.5	1.001315	1.754101	151.56
SENT at 23℃			
0.1	1.341754	0.111957	538.58
0.3	1.311115	0.159502	409.33
0.5	1.331345	0.281218	296.89

Table 3.7: Results of assessment and primary bending stresses for SENB

a/W	L_r	K_r	P_b
SENB at -120℃			
0.1	2.759765	0.851189	2209.33
0.3	1.376905	2.744127	857.33
0.5	1.205171	3.104173	536.00
SENB at 23℃			
0.1	3.160488	0.374988	1902.93
0.3	2.454837	0.55212	1149.60
0.5	1.804096	0.686588	609.47

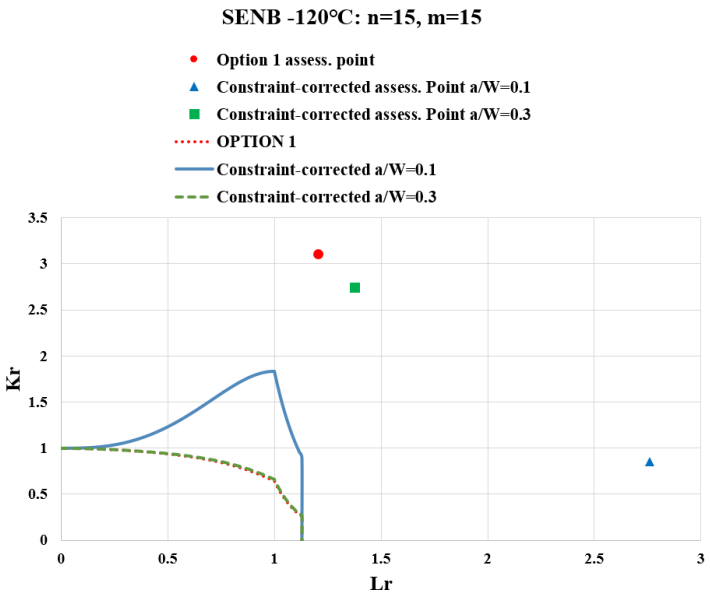

Figure 3.34: FAD for a constraint-sensitive material, *m* = 15, SENB at -120℃

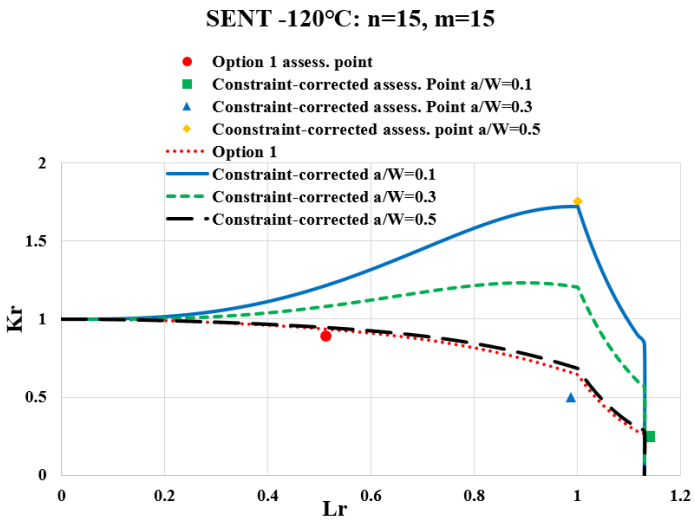

Figure 3.35: FAD for a constraint-sensitive material, *m* = 15, SENT at -120°C

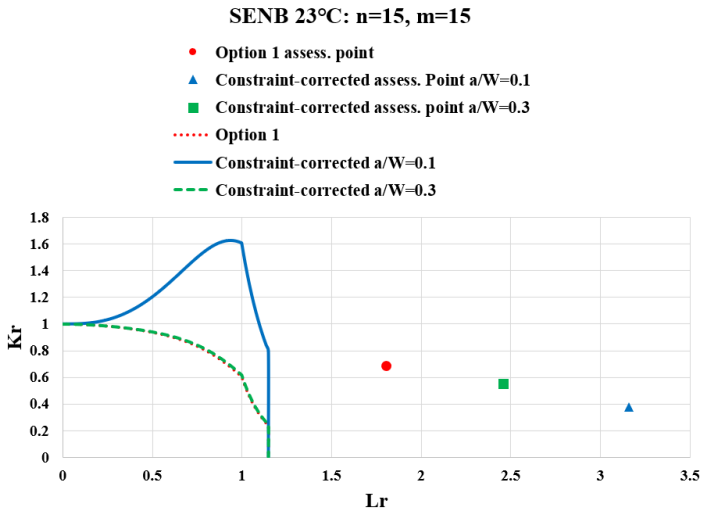

Figure 3.36: FAD for a constraint-sensitive material, *m* = 15, SENB at 23°C

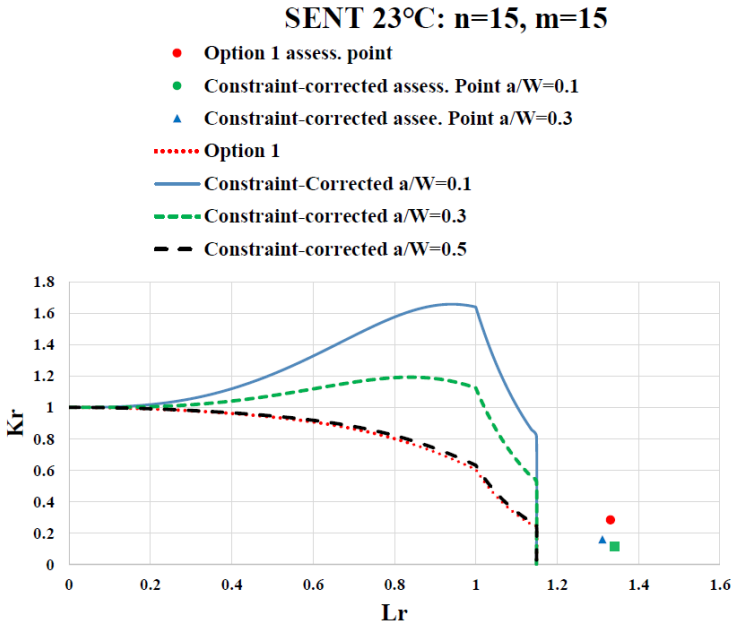

Figure 3.37: FAD for a constraint-sensitive material, m = 15, SENT at 23°C

3.9 Summary and conclusions to this chapter

Thirty-six fracture toughness tests have been carried out on API 5L X65 steel for SENT and SENB specimens at low (-120°C) and room temperatures. Crack lengths were 3, 9 and 15 mm, giving a_0/W ratios of 0.1, 0.3 and 0.5 respectively. A range of the experimental data for SENT and SENB has been analysed where failure occurred by cleavage at temperatures of -120°C, where the material had a yield stress of 593 MPa. At room temperature, ductile tearing occurred when the specimens were loaded to maximum load without failure, where the material had a yield stress of 446 MPa. The strain hardening characteristics were described by n = 15 based on the Beremin parameter, m using the constraint-based FAD fracture assessment approach with varying crack depth (a/W) ratios.

It has been demonstrated that enhanced levels of toughness associated with loss of constraint occur in both ductile and cleavage-controlled fracture. These effects have major advantages for safety cases which seek to demonstrate the integrity of engineering structures. Based on the constraint-based FAD methodology, fracture assessments were conducted with constraint-correction in the presence of cracks and compared to the conventional fracture assessment procedure in BS 7910 Option 1.

The following concluding remarks were drawn from this study:

- The work demonstrated that a decrease in temperature leads to reduction in fracture toughness and therefore, susceptibility to brittle failure for specimens tested at low temperature. This needs to be verified for real structures to ensure they are fit-for-service/purpose when operating in low temperature environments.
- SENT specimens exhibited larger fracture toughness (*J*-values) than SENB specimens for both temperatures tested. This is because the SENT specimen is loaded in tension perpendicular to the notch and this creates a mixed mode loading condition (both opening- mode I and shearing- mode III) stresses acting on the crack tip. The SENT specimen is designed to simulate more complex loading conditions that occur in real-world structures. For the SENB specimen, the notch is positioned on the tension side and the load is applied to the opposite side. This creates a pure mode I loading condition with opening stress acting on the notch tip. Therefore, low constraint (SENT and shallow-cracked bend) specimens showed higher values of fracture toughness than that associated with standard deeply-cracked bend specimens at low (-120℃) and room temperatures.
- The *T* stress was found to decrease rapidly with increasing applied load for shallow cracks than for deep cracks.
- The conventional fracture assessment method based on BS 7910 Option 1 FAD produces over-conservative results if the constraint effect is not considered properly. Based on the work in this thesis, the constraint-based FAD procedure may help to reduce excessively conservative predictions of failure. The enhanced toughness associated with loss of constraint implies that there is, in fact, an increased margin (as shown in the enlargement of the FAC for shallow cracked SENT and SENB specimens).
- By understanding the degree of crack tip constraint in a structure, engineers can design and develop accurate fracture mechanics models and prediction methods specific to low temperature operation to minimize the risk of crack propagation and failure. Therefore, this research demonstrates the advantages of incorporating representative (enhanced) fracture toughness at low temperatures, to support more realistic design and repair decisions.

4 Numerical Analysis of crack-tip constraint of fracture specimens and cracked pipe

4.1 Introduction

This chapter presents a numerical investigation of the effects of crack-tip constraint on fracture toughness of a cracked X65 pipeline steel and fracture specimens. A two-parameter description of near-tip stress fields based on the *J*-*Q* approach which enables a more accurate quantification of constraint in fracture specimens is employed. This incorporates the evolution of near-tip stresses with values of the crack driving force as characterised by the *J*-integral. 3D finite element computations are performed for three-point SENB and pin-loaded SENT specimens with varying crack length, a, to specimen width, W, ratio in the range $0.1 \leq a/W \leq 0.5$.

In addition, 3D finite element analyses are conducted for circumferentially cracked X65 pipeline steel with a surface flaw of fixed length having different crack length (a) over pipe wall thickness (t) ratios in the range $0.1 \leq a/t \leq 0.5$. Laboratory testing fracture specimens often use standard, deeply notched compact tension (CT) and SENB specimens to guarantee high levels of stress triaxiality which drive the fracture process resulting in over-conservative fracture toughness values. The study investigates the use of shallow cracked SENB and SENT specimens to derive fracture toughness values that can be used to describe the measuring toughness capacity of circumferentially cracked pipes under remote bending and internal pressure.

Finite element analysis (FEA) is a powerful tool for simulating the behaviour of structures and systems under different loads and conditions. Abaqus is a widely-used software package for FEA, and it can be used to perform a wide range of simulations: static and dynamic analyses, fatigue assessment, progressive damage analyses of materials and structures, design optimization etc. [107]. However, the process of setting up and running an Abaqus simulation can be time-consuming and error-prone, especially when performing complex simulations or parametric studies. One way to overcome these challenges is by using Python scripts in Abaqus, which greatly improves the efficiency and accuracy of FEA simulations [136]. In this thesis, Python scripts were written for a modified boundary layer (MBL) model generation in Abaqus for finite element analyses. Further, Python scripts were developed to automate the post-processing of the MBL, SENT, SENB and cracked pipe models.

4.2 Finite Element Models

Nonlinear 3D finite element models were created using Abaqus for SENT, SENB and cracked pipe. The analyses were carried out for 3D models of tension and bend loaded crack configurations covering the pin-loaded SENT and SENB fracture specimens with a fixed thickness B = 15 mm, width, W = 30 mm and varying crack lengths, a = 3, 6, 9, 12 and 15 mm. The analysis matrix included pin-loaded SENT (H/W =10) and SENB (S/W = 4) for a variety of crack depths, a_0/W ranging from 0.1 to 0.5 at room and low temperature, resulting in a total of 20 FE cases for the fracture specimens. Here, a_0 is the initial crack size, W is the specimen width, S defines the specimen span for the bend configuration and H is the distance between the pin-loading for the tension specimen.

Three-dimensional solid quadratic brick elements with reduced integration (C3D20R) were used to create all FE models. This element type and reduced integration was chosen as it required fewer calculations of integration points compared to the Gauss integration (full integration) to minimise computational time, yet given accurate results for this study. Even though reduced integration can provide computational benefits and accuracy in some situations, it should however, be applied with caution [107]. The element type, material behaviour and specific characteristic of the problem being investigated should be considered to ensure accurate and reliable results. Figure 4.1, Figure 4.2 and Figure 4.3 show the mesh configuration for the SENT, SENB and cracked pipe FE models respectively. Symmetry boundary conditions permit modelling of one-quarter of the specimens for the SENT and SENB specimens. Conventional mesh configuration having a focused ring of elements surrounding the crack tip front is used with root notch radius, ρ_0= 0.0025 mm (blunt tip) to enhance computation of *J*-values at low deformation levels. The quarter-symmetric models had approximately 36,000 nodes and 31,000 3D elements defined over the half-thickness (B/2). Previous numerical analyses [118], [137] show that such mesh design provides detailed resolution of the near-tip stress-strain fields which is needed for accurate numerical evaluation of *J*-values.

Table 4.1 and Table 4.2 summarise the FEA carried out for the constraint analysis of fracture test specimens and cracked pipe respectively.

Table 4.1: Summary of FEA cases for the analysis of crack-tip constraint of fracture test specimens

FE Model	B [mm]	W [mm]	a_0/W
SENT [B x 2B]	15	30	0.1, 0.2, 0.3, 0.4, 0.5
SENB [B x 2B]	15	30	0.1, 0.2, 0.3, 0.4, 0.5

Further, nonlinear 3D finite element analyses are also performed on a circumferentially cracked pipe with external surface flaws subjected to internal pressure and bending. The analysed pipe models have a wall thickness, t = 15 mm with outside diameter, OD = 1219 mm. This geometry is typical of current trends in deep water oil and gas pipelines of high-grade steels. Similar to the fracture models, the FEA of the cracked pipe had crack depths, a_0/t ranging from 0.1 to 0.5. The internal pressure level in terms of the hoop stress to yield stress ratio, σ_{hoop}/σ_Y was 0.8 resulting to a total of 10 FE cases for both room and low temperatures analysed.

Table 4.2: Summary of FEA cases for the analysis of crack-tip constraint of fracture cracked pipe

FE model	**OD [mm]**	t **[mm]**	a_0/t	**Internal pressure**
Cracked pipe	1219	15	0.1	σ_{hoop}/σ_Y = 0.8
			0.2	σ_{hoop}/σ_Y = 0.8
			0.3	σ_{hoop}/σ_Y = 0.8
			0.4	σ_{hoop}/σ_Y = 0.8
			0.5	σ_{hoop}/σ_Y = 0.8

Figure 4.3 shows the FE half-symmetric model constructed for the pipe with a_0/t = 0.5 taking advantage of symmetry boundary conditions. The numerical models for the cracked pipes also employ a conventional mesh configuration have a focussed ring of elements surrounding the crack front. The X65 steel plastic true stress-strain curves (see Figure 3.6) obtained from the flat tensile tests in chapter 3 at the corresponding temperatures are applied for all the 3D model calculations. The material property used at both temperatures are shown in Appendix I. The half-symmetric models for these analyses had approximately 78,000 nodes and 87,000 3D elements with appropriate constraints imposed on the nodes defining the longitudinal symmetry plane. The bending moment of the pipe with diameter, D_o= 1219 mm, thickness, t = 15 mm, length, L=1500 mm and internal pressure of 2 MPa is calculated to be approximately 1.368 MN-m. This was used alongside the internal pressure for the cracked pipe FE analyses and details of the calculation is shown in Appendix H. Even though it is observed in Figure 4.1 and Figure 4.2 that there is large aspect ratio at the vicinity of the crack tip (due to difficulty in getting very refined mesh at the crack tip), the results obtained using these models appear to fall within the range of experimental tests.

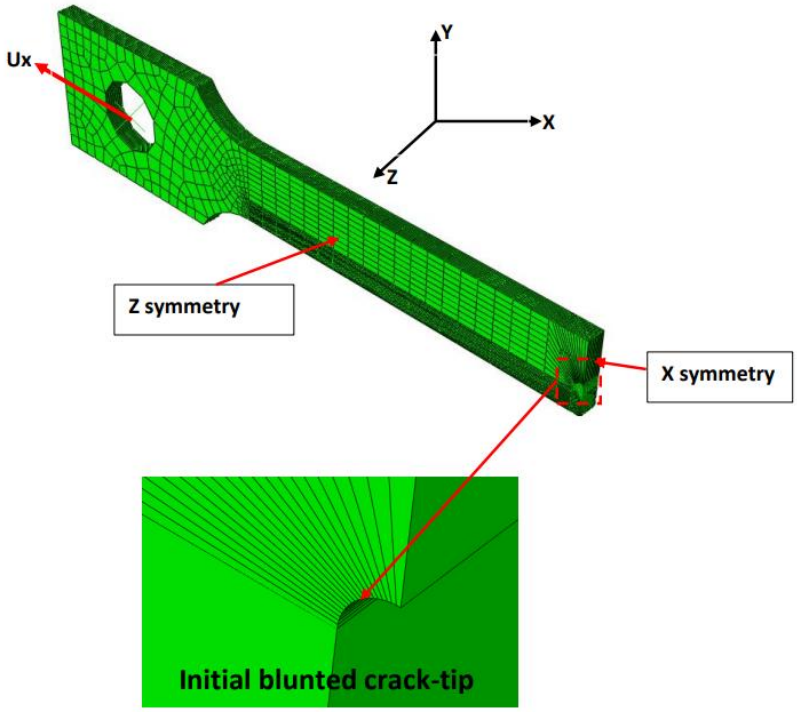

Figure 4.1: Mesh configuration of pin-loaded SENT specimen model with applied boundary conditions and close-up view of the initial blunted crack-tip radius, $\rho_0 = 0.0025\ mm$

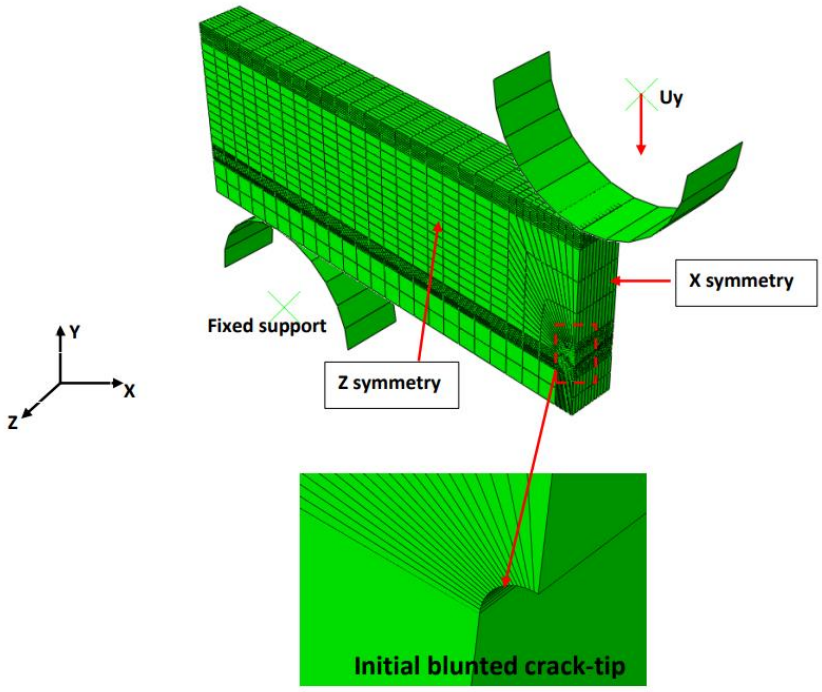

Figure 4.2: Mesh configuration of SENB specimen model with applied boundary conditions and close-up view of the initial blunted crack-tip radius, $\rho_0 = 0.0025\ mm$

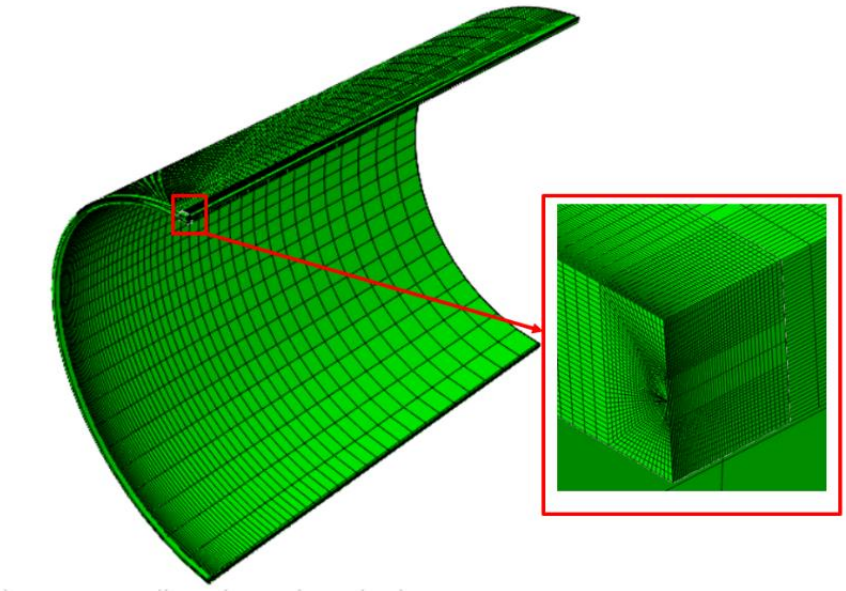

Figure 4.3: Cracked pipe showing the close-up view of the 15 mm crack length

4.3 Modified boundary layer (MBL) model

The modified boundary layer (MBL) model is used for testing the crack-tip behaviour in elastic-plastic materials under load without considering the finite geometry of the specimen or component. The MBL model is a disc-shaped plane strain finite element model where a crack is introduced with the crack-tip located in the centre of the disc. Typically, they are circular or semi-circular with a radius, R being at least 10^5 times larger than the crack tip dimension, ρ_0 [54], [138]. For the model used in this study, $\rho_0 = 0.005\ mm$ and $R = 5\ m$. For a crack in an isotropic elastic material subjected to plane strain Mode I loading, the first two terms of the William's solution are given by the singular and non-singular terms [19]:

$$\sigma_{ij} = \frac{K_I}{\sqrt{2\pi r}} f_{ij}(\theta) + \begin{bmatrix} T & 0 & 0 \\ 0 & 0 & 0 \\ 0 & 0 & \nu T \end{bmatrix} \qquad (4.1)$$

where, σ_{ij} is the stress tensor, r is the distance from the crack tip, f_{ij} is a dimensionless function of the angle θ and K_I is the stress intensity factor, T is a uniform stress in the x-direction, which induces a stress νT in the z-direction in plane strain. The second term of the expansion, the T stress, has the effect of changing the constraint state at the crack tip, with compressive T stresses reducing the crack tip constraint.

In computing the elastic-plastic constraint parameter, Q, the MBL model solution with $T = 0$ is adopted to represent the reference stress field. T is the elastic T-stress which is defined as the constant stress acting parallel to the crack plane and its magnitude is proportional to the nominal

stress in the vicinity of the crack. Due to symmetry, only a half of the MBL model was constructed. The global finite element mesh and details of the mesh in the local region of the crack tip as well as boundary conditions are shown in Figure 4.4. The MBL is a plane strain model with similar mesh arrangement in front of the crack tip with a root notch radius, $\rho_0 = 0.005\ mm$ as in the 3D fracture specimens (SENT and SENB). Prescribed displacements were applied to the nodes at the outer circumference of the MBL model to generate the reference crack-tip stress field for the calculation of the *Q*-parameter. The displacements are based on the first two terms of the William linear elastic singularity solution, which takes the form [20]:

$$U_x(r,\theta) = K_I \frac{1+\nu}{E}\sqrt{\frac{r}{2\pi}}cos\left(\frac{1}{2}\theta\right)(3-4\nu-cos\theta) + T\frac{1-\nu^2}{E}rcos\theta \qquad (4.2)$$

$$U_y(r,\theta) = K_I \frac{1+\nu}{E}\sqrt{\frac{r}{2\pi}}sin\left(\frac{1}{2}\theta\right)(3-4\nu-cos\theta) + T\frac{\nu(1-\nu^2)}{E}rsin\theta \qquad (4.3)$$

where $K_I = \sqrt{EJ/(1-\nu)^2}$ under plane strain conditions, r and θ are polar coordinates centred at the crack with $\theta = 0$ corresponding to the uncracked ligament ahead of the crack tip.

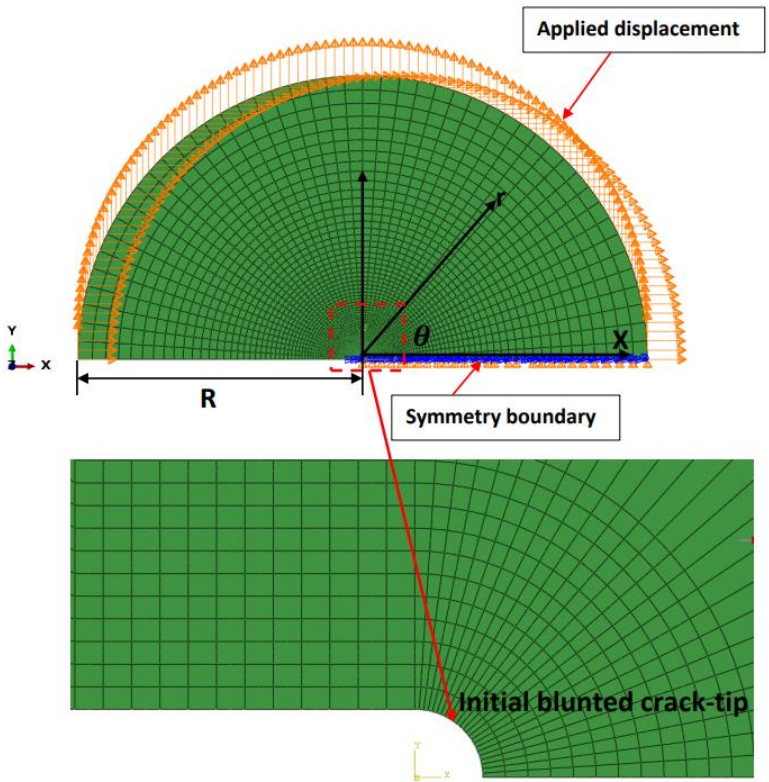

Figure 4.4: Mesh configuration of MBL model with applied boundary conditions and close-up view of the initial blunted crack-tip radius, $\rho_0 = 0.005\ mm$

4.4 Overview of $J - Q$ approach

The development of a two-parameter characterisation of the elastic-plastic crack-tip fields consider a cracked body subjected to a remote stress. The crack-tip deformation scales with a J/σ_Y where J is the J-integral and σ_Y is the yield stress. At load levels sufficiently small so that the crack-tip plasticity is limited, the mode I plane-strain near-tip fields can be described by a single family of crack-tip fields with varying stress triaxiality. This motivated O'Dowd and Shih [20], [54] to propose an approximate elastic-plastic crack-tip fields based upon a triaxiality parameter, Q, more applicable to small scale yielding (SSY) and large scale yielding (LYS) conditions. A review of the Q-parameter was given in chapter 2 and for brevity, will not be discussed in detail here again. The Q-parameter is often defined as the amount by which the crack opening stress in the fracture specimen, $(\sigma_{yy})_{FS}$, differ from the adopted high triaxiality reference SSY solution, $(\sigma_{yy})_{MBL(SSY)}$. For all the 3D analyses, the MBL model shown in Figure 4.4 was used and Q calculated as:

$$Q = \frac{(\sigma_{yy})_{FS} - (\sigma_{yy})_{MBL(SSY)}}{\sigma_Y}; \;\; at\ r = \frac{2J}{\sigma_Y} \;\; and\ \theta = 0 \qquad (4.4)$$

where $(\sigma_{yy})_{FS}$ is the crack opening stress component of interest (SENT/SENB), $(\sigma_{yy})_{MBL(SSY)}$ is the reference stress component characterised by the MBL model solution with $T = 0$, σ_Y is the yield stress and r is the distance from the crack tip along the crack plane ($\theta = 0$). The effects of temperature and specimen geometry as quantitatively characterised by the crack tip constraint (Q-parameter) on the fracture toughness was studied.

4.5 Abaqus CAE and Python scripting

A Python script is a text file that contains commands using Python syntax (variables, loops, conditions, functions etc.). By means of this file, we can tell Abaqus what it has to do: the dimensions in our FE model, the element size of the mesh, the odb file that will be opened to read some J-integral values, crack opening stresses etc. The easiest way to execute a Python script in Abaqus is from CAE, by going to: File > Run Script, and then select the Python script. Abaqus will start reading and executing the commands from that Python file.

The main advantages of using Python in Abaqus is automation and increased flexibility in creation of models and analyses of results. This can save time and reduce the risk of errors, making it easier to perform large-scale simulations or parametric studies. Python scripts enable the automation of every stage in the finite element analysis workflow, not only the pre-processing, but also the post-

processing and even more sophisticated tasks like iterative optimization processes [136]. For the scope of this work, Python scripts were used for the MBL model generation as well as postprocessing of the fracture specimens, cracked pipe and MBL model. Python is a highly versatile programming language and it can be used to customize and automate all aspects of Abaqus simulations, including functionalities that may not be available through the standard user interface (Abaqus/CAE) [107], [136].

The main motivation to use Python scripts in this thesis was to enable faster computations of the crack tip stress from the MBL, fracture specimens and cracked pipe for the calculation of the *Q*-parameter. The general approach to calculate the elastic-plastic constraint parameter, *Q* using FEA is outlined as:

Step A: Perform FEA of the specimens to be analysed (in our case, SENT, SENB and cracked pipe)

Step B: In the odb file, for each time increment or selected time increment, conduct the following:

B1.1: Extract crack opening stress (assuming to be σ_{yy}) along a path ahead of crack tip

B1.2: Extract *J*-integral values

B1.3: Interpolate σ_{yy}, that is $(\sigma_{yy})_{FS}$ at a distance of $r = 2J/\sigma_y$

B1.3: Obtain $(\sigma_{yy})_{FS}$ versus *J*-integral values

Step C: For each *J* or selected *J* extracted from Step B, run an MBL model with the applied *J*, then in the odb file, perform the following:

C1.1: Extract crack opening stress (σ_{yy}) along a path ahead of crack tip

C1.2: Extract *J*-integral values

C1.3: Interpolate σ_{yy} (which is the $(\sigma_{yy})_{MBL(SSY)}$) at a distance of $r = 2J/\sigma_y$

Step D: An alternative approach to Step C is to run an MBL model with an applied *J* sufficiently large and a sufficiently large radius so that we only need to run a single MBL model, rather than for each *J* at which we want to calculate *Q*. Then, in the odb file, carry out the following:

D1.1: Extract crack opening stress (σ_{yy}) along a path ahead of crack tip

D1.2: Extract *J*-integral value

D1.3: Interpolate σ_{yy} (i.e., $(\sigma_{yy})_{MBL(SSY)}$) at a distance of $r = 2J/\sigma_y$

D1.4: Obtain $(\sigma_{yy})_{MBL(SSY)}$) versus *J*-integral

D1.5: Interpolate $(\sigma_{yy})_{MBL(SSY)}$ at the same *J*-integral as that from Step B (SENT/SENB/cracked pipe)

Step E: Calculate Q at each J or selected J:

$$Q = \frac{(\sigma_{yy})_{FS} - (\sigma_{yy})_{MBL(SSY)}}{\sigma_Y}; \ \ at\ r = \frac{2J}{\sigma_Y} \ \ and\ \theta = 0$$

The above procedure is tedious and time-consuming when done manually. Thus, Python scripts used in this work to automate the process become handy. The Python scripts at hand perform Step B (B1.1 to B1.3) and the alternative Step C or Step D (C1.1 to C1.3 or D1.1 to D1.3) separately. Step D1.5 can be done manually in Excel spreadsheet using linear interpolation and then the Q-parameter computed. The Python scripts used in this thesis are given in Appendix H and can be obtained from the author upon request.

4.6 Results and discussions

Constraint is a major issue in structural integrity of engineering components. As a result of the stress concentration inherent in a cracked body, the material in the vicinity of the crack is highly stressed. Further, this material is constrained by the surrounding material due to strict testing requirements. This constraint produces a triaxial stress state near the crack tip which raises the flow stresses locally. This elevation in the flow stress makes it easier for the material to reach the fracture stress. In shallow cracked or thin-walled fracture specimens or real structures, a small amount of material surrounds the crack tip and therefore, constraint is relatively low, or fracture toughness is high. In a thick-walled or deeply cracked fracture specimen, constraint is high because a large volume of material surrounds the crack tip. This results in low fracture toughness and high constraint. The results of the effect of constraint due to crack length (in-plane constraint) and type of loading are discussed in this chapter.

An MBL analysis was conducted for a sufficiently large, applied loading (J-integral value) with zero T-stress to obtain the SSY normalised opening stress curve. Figure 4.5 and Figure 4.6 illustrate the normalised opening stresses for a range of applied loading plotted against the normalised distance ahead of the crack tip for room and low temperatures respectively. These figures show that the normalised opening stress fields collapse onto the SSY curve as a single curve. Similar plots have been carried out in the literature where the SSY curves were used for the calculation of the Q parameter [20], [54], [51], [139].

The variation of the constraint parameter, Q was examined for the deviation in the stress fields for the finite cracked body (fracture specimen) from the reference SSY fields (MBL model). The J-Q trajectories were computed at a normalised distance, $r = 2J/\sigma_Y$. Figure 4.7 to Figure 4.12 illustrate Q-values calculated at varying normalised distance, r, for SENB, SENT and cracked pipe

at room and low temperatures. These figures display the general effects of specimen geometry and loading mode (tension vs. bending) on the *J*-*Q* trajectories for the analysed cracked configurations. In all plots, *Q* is defined by equation (4.4) at the normalised crack-tip distance ($r = 2J/\sigma_Y$).

The crack driving force, *J*, normalised by $b\sigma_Y$, with b denoting the remaining $(W - a)$ crack ligament. It is observed in all the figures that; the evolution of *Q* depends on crack size as characterised by the a/W-ratio. There is a uniform shift of the *J*-*Q* trajectories with decreased crack size, particularly, SENB and SENT at low temperature. Shallow notched SENB ($a/W \leq 0.3$) have *Q*-values similar to those of all SENT configurations analysed. Further, the constraint levels (*Q*-values) of the SENT are similar to that of the cracked pipe. The large *Q*-values with the loading, $J/b\sigma_Y$ are associated with reduction in the crack tip stresses experienced by the specimens earlier in the loading. Indeed, the figures illustrate that the crack tip opening stress decreases rapidly with increasing loading (applied normalised *J* values) and distance away from the crack tip. This is due to the strong stress gradient across the specimen ligament – stress is compressive near the free surface and gradually becomes tensile as the crack tip (centre of specimen) is approach. Recall similar behaviour in Figure 2.3 when triaxiality at the crack front and plastic zone size for plane stress and plane strain conditions were considered. The normalised *J* values plotted against *Q*-values may be helpful in determining the effective toughness during testing of low constraint fracture specimens. For all the analyses carried out, there is a general trend of increasing *J* values with decreasing *Q*-values.

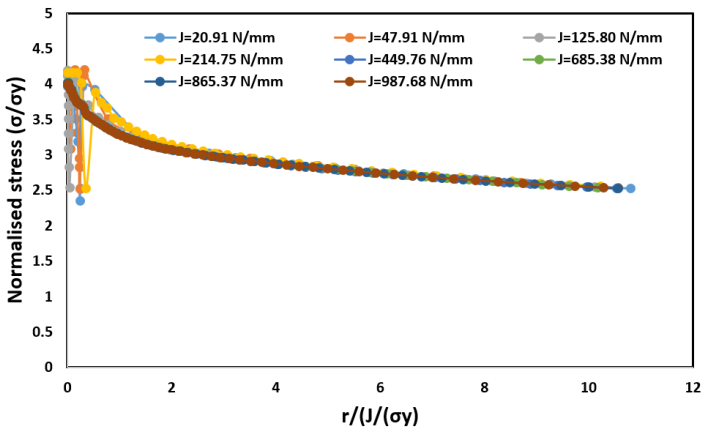

Figure 4.5: Normalised opening stresses (S11) for SSY solution with *T* = 0 MPa at various applied *J*-integral loadings at room temperature

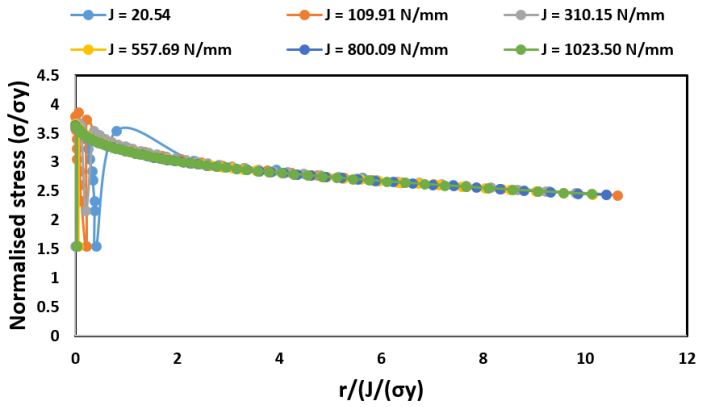

Figure 4.6: Normalised opening stresses (S11) for SSY solution with $T = 0$ MPa at various applied J-integral loadings at low temperature

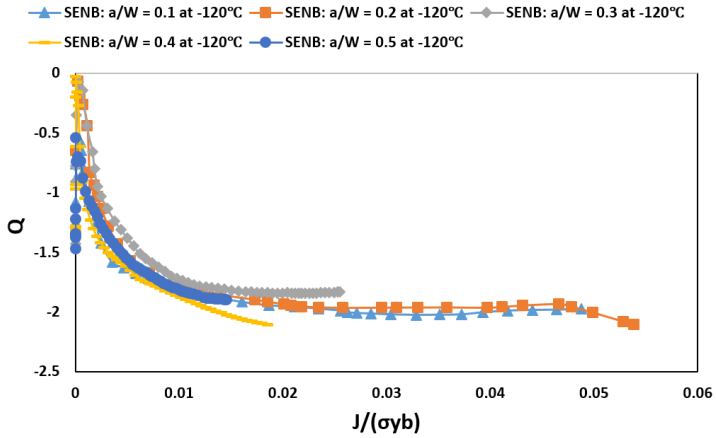

Figure 4.7: Relationship between in-plane crack-tip constraint, Q and normalised loading, $J/b\sigma_Y$ for SENB at low temperature

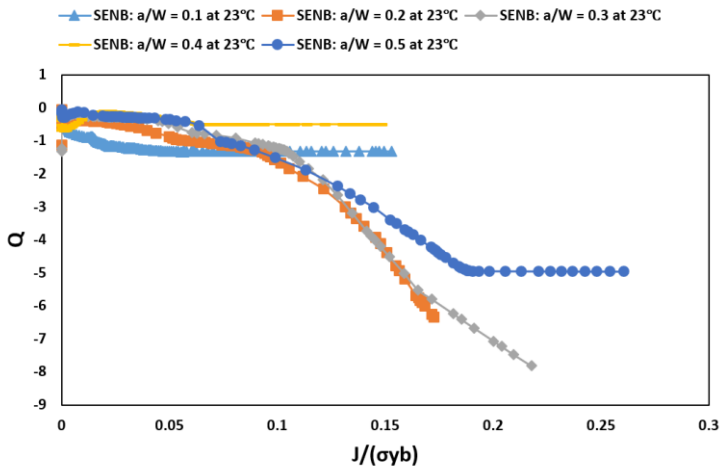

Figure 4.8: Relationship between in-plane crack-tip constraint, Q and normalised loading, $J/b\sigma_Y$ for SENB at room temperature

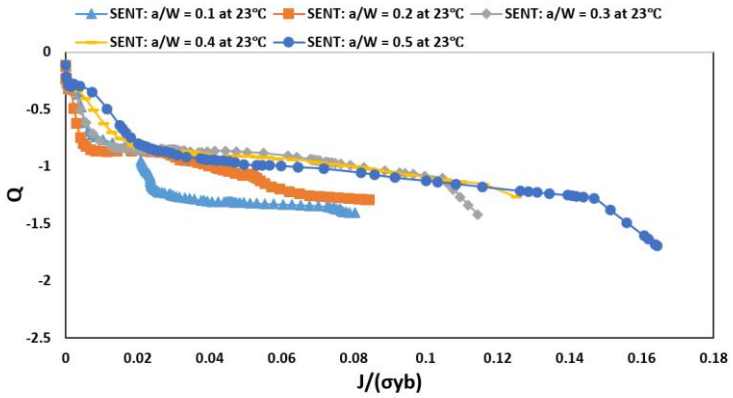

Figure 4.9: Relationship between in-plane crack-tip constraint, Q and normalised loading, $J/b\sigma_Y$ for SENT at room temperatures

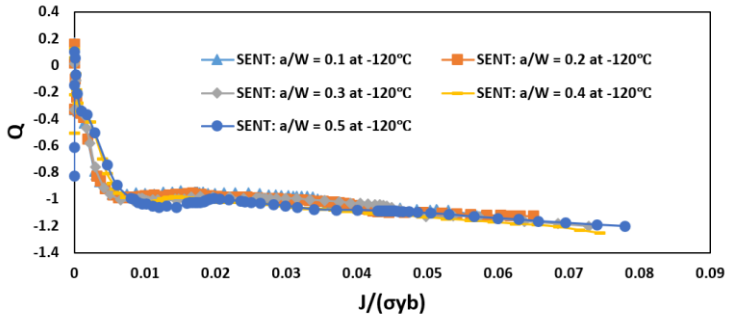

Figure 4.10: Relationship between in-plane crack-tip constraint, Q and normalised loading, $J/b\sigma_Y$ for SENT at low temperatures

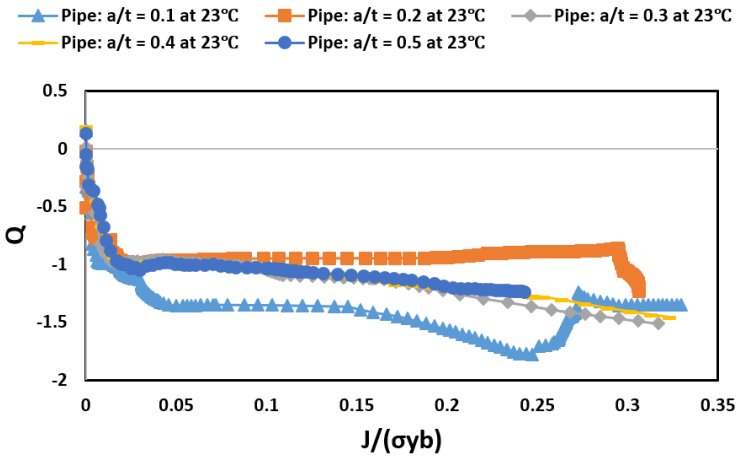

Figure 4.11: Relationship between in-plane crack-tip constraint, Q and normalised loading, $J/b\sigma_Y$ for cracked pipe at room temperature

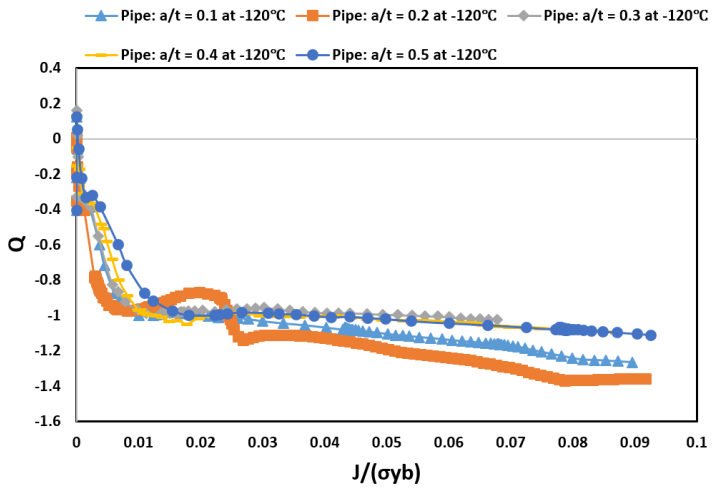

Figure 4.12: Relationship between in-plane crack-tip constraint, Q and normalised loading, $J/b\sigma_Y$ for cracked pipe at low temperature

Figure 4.13 to Figure 4.16 illustrate the *Q*-values plotted against the crack depth, a/W, for SENB, SENT and cracked pipe at various crack-tip loadings ($J/b\sigma_Y = 0.005$, 0.01, 0.03 and 0.06). This is to gain a better understanding on the effect of each parameter on *Q*, with a consistent loading measure, $J/b\sigma_Y$. It is observed that the *Q*-values for all the loadings and the temperatures analysed for SENB specimens are higher than those of other geometries, particularly those at low temperature. The *Q*-values further display increased radial dependence under increasing loading ($J/b\sigma_Y$). This behaviour is due to the interaction of remote plastic bending field acting on the remaining ligament ($b = W - a$) which impinges strongly upon the crack tip resulting in steeper stress gradients at higher deformation levels. O'Dowd and Shih [20], [54], Nevalainen and Dodds [140] had previously shown such trend of analyses. In addition, due to the low fracture toughness (*J*-values) obtained for the low temperature tests, high constraint levels (high *Q*-values) are achieved and is consistent with the experimental fracture tests. For the SENT specimens, room temperature analyses have higher *Q*-values than those analysed at low temperature. It is also observed that for all the loadings analysed, there is a steady increase in *Q*-values with increasing crack depth, a/W, indicating that shallow notched specimens exhibit low constraint levels and deep cracked configurations show high levels of crack-tip constraint. The trend is in good agreement with previous studies [20], [118], [137], [141] that, 'constraint loss' is severest in shallow crack geometries, while the deeply cracked geometries are generally 'high constraint'.

The effect of crack size on the *J*-*Q* trajectories for different a/W or a/t may justify the choice of narrowing an appropriate crack size and fracture specimen type which adequately matches the fracture behaviour of circumferentially cracked pipe. It can be seen in these figures that for all the

applied loadings, the shallow cracked SENB specimen with a/W between 0.1 and 0.2 encompasses the corresponding evolution of crack tip constraint for the SENT and cracked pipe. On the other hand, all the SENT specimens exhibit similar crack front behaviour to that of the cracked pipe for all the applied loadings considered. This provides additional understanding of the correlation of fracture behaviour for the fracture specimens and cracked pipe based on a stress triaxiality parameter, Q. This supports important implications for current defect assessment procedures and specification of tolerable flaw size in cracked pipes (girth welds of reeled pipelines).

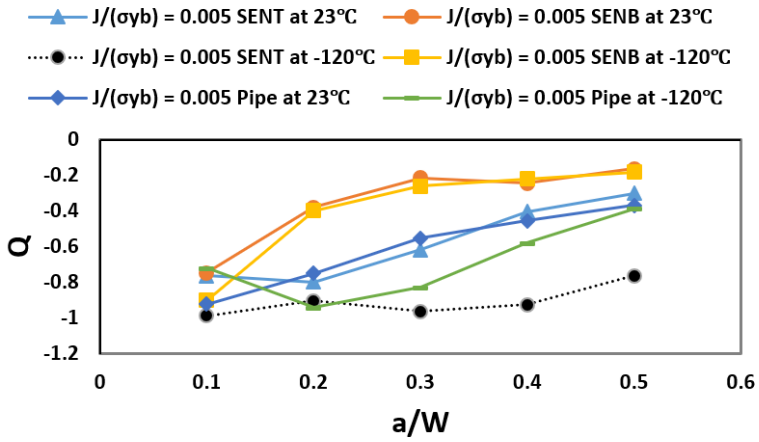

Figure 4.13: Relationship between constraint parameter, Q and crack depth, a/W (a/t) at crack tip loading $J/b\sigma_Y = 0.005$ at room and low temperature

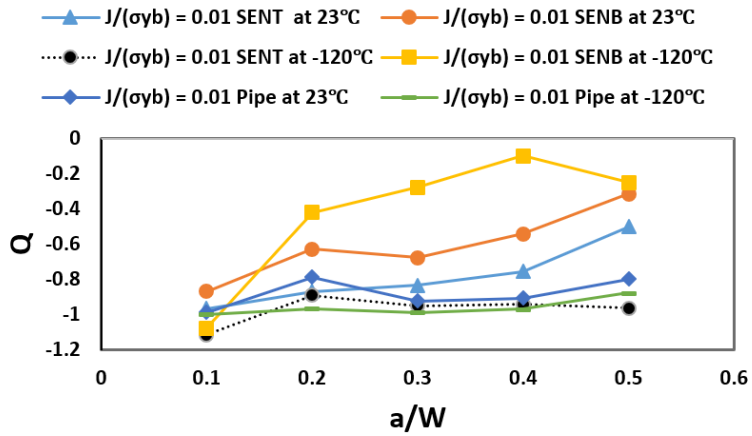

Figure 4.14: Relationship between constraint parameter, Q and crack depth a/W (a/t) at crack tip loading $J/b\sigma_Y = 0.01$ at room and low temperature

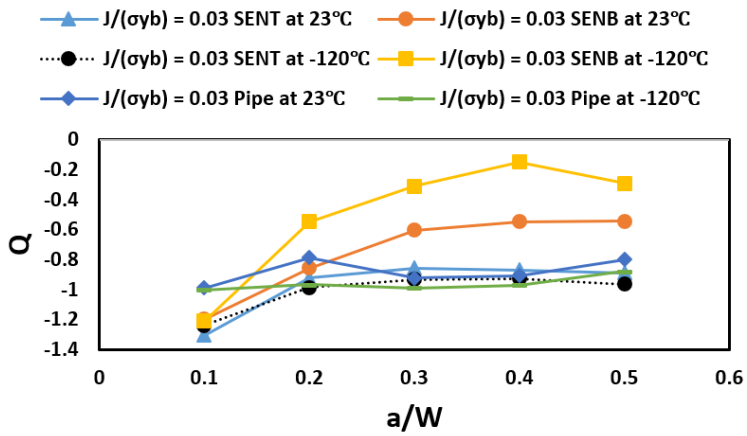

Figure 4.15: Relationship between constraint parameter, Q and crack depth a/W (a/t) at crack tip loading $J/b\sigma_Y = 0.03$ at room and low temperature

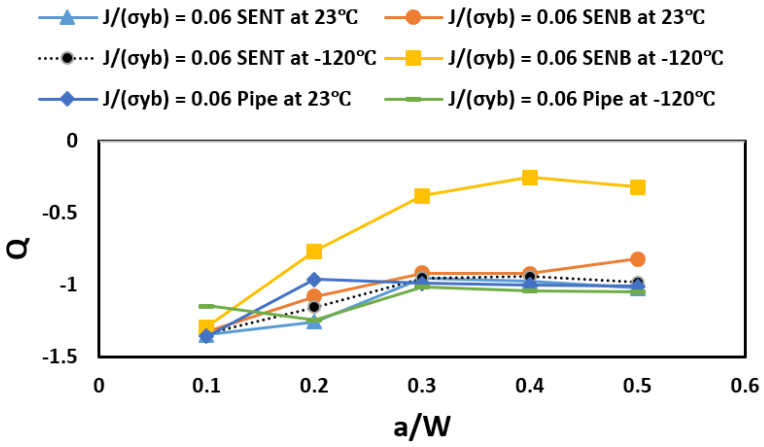

Figure 4.16: Relationship between constraint parameter, Q and crack depth, a/W (a/t) at crack tip loading $J/b\sigma_Y = 0.06$ at room and low temperature

4.6.1 Summary and conclusions from this chapter

The analysis of crack-tip constraint has important practical applications in the field of fracture mechanics. For example, it can be used to predict the behaviour of structures and components under different loading conditions and to design more effective fracture-resistant materials. In the case of cracked pipes, numerical analysis of crack-tip constraint can be used to determine the critical crack sizes and maximum allowable operating pressure, which is important for ensuring the safety and reliability of pipelines. Therefore, numerical analysis of crack-tip constraint in fracture specimens and cracked pipes is essential for understanding the underlying mechanics of fracture behaviour. It can help engineers design more robust structures and develop effective strategies for preventing catastrophic failures due to cracks.

This chapter described a numerical investigation on the effects of crack tip constraint in a cracked pipe subjected to internal pressure/bending moment load and fracture specimens (SENB and SENT) at room and low temperatures. These fracture specimens are commonly employed to measure ductile tearing properties in pipeline grade steels.

This research has demonstrated the distinct roles of J and Q in the two-parameter fracture mechanics approach (J-Q theory). J sets the deformation level over which large stresses and strains develop while Q scales the crack-tip stress distribution and the stress triaxiality ahead of the crack tip. Representations of the stress distributions in terms of the Q-parameter were given in this chapter. In summary, the numerical analysis of crack-tip constraint in fracture specimens, specifically SENT, SENB and cracked pipe, provides valuable insights into the behaviour and fracture resistance of these /specimens/structures. The following conclusions can be drawn from this chapter:

- The Q-parameter is dependent on geometry and loading – different values of the Q-parameter are obtained for SENT, SENB and cracked pipe under tension, bending and internal pressure/bending moment loadings respectively, which are characterised by the same material properties.
- The FEA configurations analysed indicate that a slight decrease in the hydrostatic stress level (Q-parameter) can result in a significant increase in fracture toughness – cleavage fracture depends on crack-tip constraint.
- The J-Q theory provides a framework for toughness locus to be measured and utilised. Based on this framework, we can systematically develop toughness loci based on cleavage and ductile failure mechanisms – allowing the competition between cleavage and ductile fracture to be examined.
- As crack length increases, the J-Q trajectories are characterised by rapid changes with the increasing applied loading ($J/b\sigma_Y$) – for deeper cracks, the Q-parameter decreases rapidly than for shallow-cracks.
- Shallow cracked SENB specimens with crack sizes in the range $0.1 \leq a/W \leq 0.2$ provide fracture response in good agreement with corresponding fracture behaviour of cracked pipe and SENT specimens.
- The pipe models analysed have similar constraint, independent of the loading condition and length of the crack. The SENT specimens have constraint levels somewhat higher than the pipe models, while the SENB specimens have the highest constraint level as expected.

- For relevant crack lengths in the pipe, the constraint level in the SENT specimens is similar to the constraint level in the pipe models than the SENB specimens. This reduces conservatism in defect assessment analyses, if SENT specimens are used to establish the fracture toughness (rather than the current defect assessment analyses that rely on deeply notch bend specimens fracture toughness to establish conservative acceptance criteria).
- This new insights and understanding gained from this work encourages investigations in direct correlations between small-scale laboratory fracture specimens and cracked pipes (e.g. subsea pipeline installation by reeling method with the application of internal pressure/bending moment to prevent wringling and local buckling).
- Since we have not examined other loading conditions such as cracked pipes subjected to tensile loading, the trends and results obtained in this study are limited to the analyses of cracked pipe subjected to internal pressure/bending moment loading. This approach can therefore, be utilised for the fracture assessment of cracked pipelines subjected to bending load (e.g. girth welds of reeled pipelines)

The findings from this study can contribute to the development of design guidelines, fracture mechanics models/fracture specimens that enables better assessment of structural integrity, enhances safety and facilitates informed decision-making in engineering applications.

5 Finite element optimised *J*-integral computations from DIC-measured displacements

5.1 Introduction

In this chapter, a novel and robust method is developed and demonstrated to obtain the crack's strain energy field as the *J*-integral by using measurements of the surface displacement fields from digital image correlation (DIC). The analysis method makes use of a finite element approach that is highly versatile and easy to implement, being able to locate crack direction and crack tip position.

Digital image correlation (DIC) is a non-contact optical method that can be used to measure full-field displacements and strains on the surface of a specimen undergoing mechanical testing. Thus, it provides a non-contact, non-destructive method to quantify the deformation and strain distribution over the entire surface of an object. The method involves capturing a sequence of images of the specimen before and after loading, and then using image processing algorithms to track the movement of small patterns or markers on the surface of the specimen [121]. The resulting displacement data can be used to calculate the *J*-integral, which is a measure of the fracture toughness of the material.

The *J*-integral is a parameter that characterises the energy release rate associated with the initiation and propagation of a crack. It can be calculated using different methods, such as the compliance or energy balance methods. In the case of DIC, the *J*-integral is typically calculated using the path-independent contour integral method, which involves integrating the stress-displacement curve along a contour that encircles the crack front [142]. To use DIC for *J*-integral calculation, the first step is to apply a crack to the specimen, either by pre-cracking or by using a specimen with a pre-existing crack. The specimen is then loaded under displacement-controlled conditions, while high-resolution images captured at regular intervals. The images are then analysed using DIC software, which identifies the patterns or markers on the surface of the specimen and tracks their movement over time.

The *J*-integral presented in chapter 2 allows calculation of the strain energy release rate from full-field displacement data. In engineering structural integrity assessment, reliable measurement of fracture resistance remains an essential input and various methods have emerged to quantify fracture toughness of standard fracture specimens. Among them, BS 8571 [95], BS 12135 [49] and ASTM E1820 [48] present standard test procedures based on the load-deformation response

of the specimen. These methods have been applied in testing various specimens and structural components. The development of the digital image correlation (DIC) technique [143] provides alternative methods to compute the energy release rate directly from a local crack tip full-field analysis. In this chapter, a finite element approach is utilised to extract the *J*-integral from the DIC-measured displacement fields for a shallow cracked (3 mm) SENT specimen to demonstrate the potential benefits of this approach to validate the experimental results.

The resulting displacement data can be used to generate displacement and strain maps, which provide a detailed visualisation of the deformation behaviour of the specimen. Overall, DIC is a powerful technique for the measurement of full-field displacements and strains, which can be used to calculate the *J*-integral and other fracture mechanics parameters (e.g., stress intensity factor, *K*).

5.2 Digital Image Correlation (DIC) Analysis

The principles of DIC have been outlined in chapter 3 for tensile and fracture test specimens and is a similar approach when applied to cracked components or specimens. Due to advancements in post-processing, fracture parameters such as *J*-integral, CTOD and SIFs can be directly calculated from DIC measurements. Directly measuring these parameters from DIC techniques offers an advantage over conventional methods of fracture parameter determination for a range of reasons. These include: the ability to assess the specimen using a non-contact technique, the ability to work far away from the specimen (in cases of unfavourable environmental conditions), the ability to obtain 3D displacement fields and an increase in the amount of data that can be obtained compared to using traditional clip gauge measurements [144]. Here, the DIC analysis is to measure the variation in the displacement field when a load is applied to a crack, and to identify the crack path and crack tip location. DIC-measured data was obtained from SENT fracture test specimens for this study and the dataset is analysed using a two-step approach. Step 1 is to retrieve the displacement vectors from the DIC dataset with optimal precision. In step 2, the crack tip position and crack path are determined.

5.3 Finite Element Treatment for *J*-integral Calculation

In recent years, there has been an increasing interest in using DIC data for *J*-integral calculation using the finite element method (FEM). The finite element treatment of DIC data for *J*-integral calculation involves acquiring DIC data, generating a finite element mesh, conducting FEM analysis, computing *J*-integral using VCE method and validating the results. This technique is

widely used in fracture mechanics research and engineering applications for predicting material fracture behaviour and structural response and follows the procedure:

1. Acquire DIC data: First, DIC data were obtained by taking images of the material surface (SENT specimens) under load using two cameras. The images were then analysed using DIC software (GOM Correlate 2019) to obtain the displacement field.
2. The displacement fields were imported into a MATLAB code that generated a Python code for the Abaqus finite element analysis.
3. Mesh generation: A finite element mesh is created using commercial software such as Abaqus through the Python script created in procedure 2, where the mesh should be sufficiently fine to capture deformation and strain fields around the crack tip.
4. FEM analysis: The displacement field obtained from the DIC data is applied as boundary conditions in the FEM analysis. The analysis is typically conducted using the displacement-based finite element method.
5. *J*-integral calculation: *J*-integral is calculated using the virtual crack extension (VCE) method. Through this method, the crack is extended incrementally, and the energy release rate is computed at each increment. *J*-integral is then obtained by integrating the energy release rate over the crack extension.
6. Validation: the results of the FEM-based *J*-integral calculation must be validated against the experimental measurements and/or other numerical methods. This helps to ensure the accuracy and reliability of the *J*-integral calculation

Figure 5.1 depicts the flowchart of the procedure for the DIC-measured displacement fields to compute *J*-integral. This work adopt a similar method outlined in Figure 5.2 by Barhli [145]. In this approach, the raw DIC-obtained displacement field was processed in a MATLAB code where the crack path and crack tip location are identified and segmented (see Figure 5.8).

After the DIC analysis, a Python code was generated where a finite element model was registered to the DIC-obtained displacement field with an automatic coarse mesh. The crack tip position was assessed, and a horizontal crack was inserted in the mesh. To accommodate the crack and for accurate *J*-integral values, the crack tip region was re-meshed with a fine mesh. The data points obtained by DIC were injected as local boundary conditions, point by point. The material properties are then defined in the FE model and a plane stress finite element analysis was performed to obtain the stress and strain fields. Finally, the *J*-integral was calculated using the inbuilt algorithms (VCE) in the finite element software Abaqus.

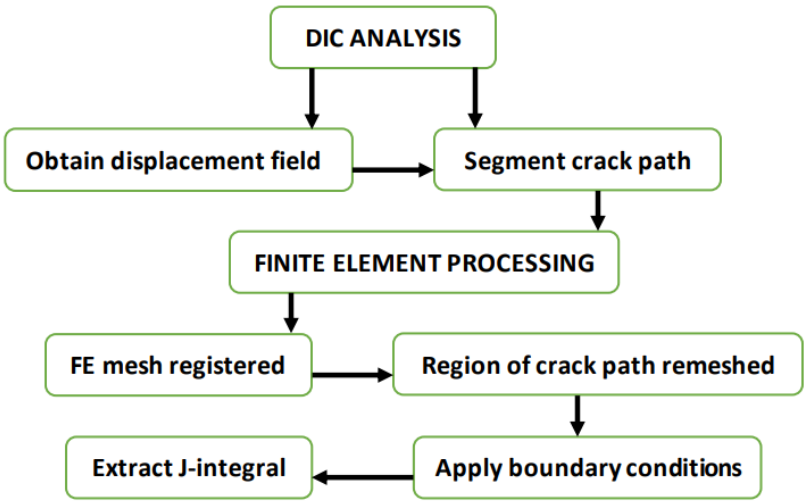

Figure 5.1: Steps of the DIC-obtained displacement field - finite element

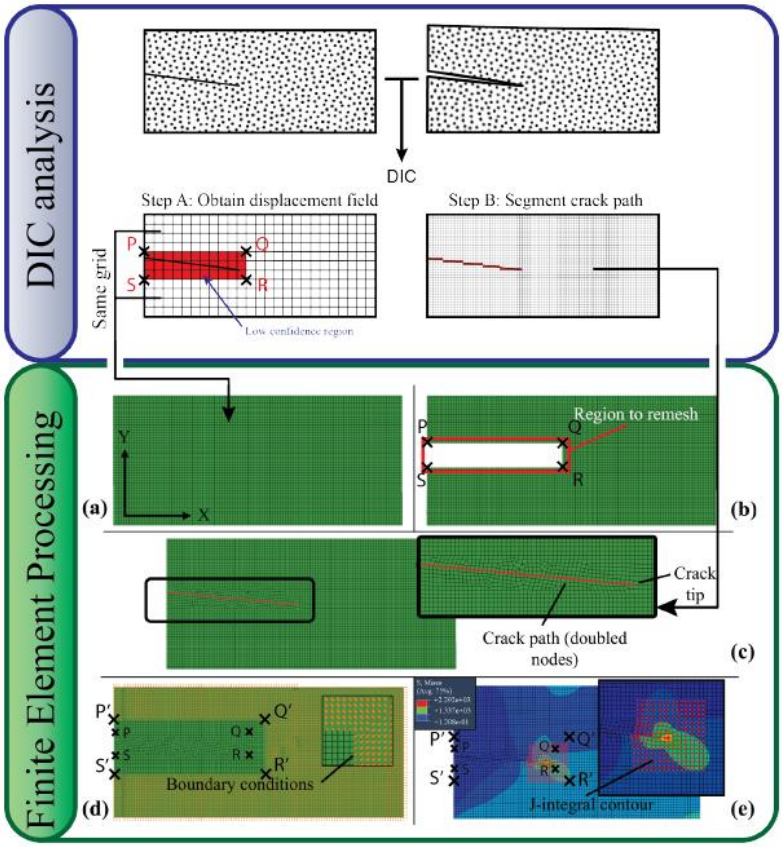

Figure 5.2: Steps to extract *J*-integral from DIC-measured data [146]

5.4 Results and discussions

Following the steps in Figure 5.1 and Figure 5.2, the DIC-measured displacement data was input into a MATLAB code that was written to treat the displacement data for finite element extraction of *J*-integral via its Python scripting capabilities.

The MATLAB code is robust and was able to segment the crack path, giving the user the option to select the crack direction as can be seen in Figure 5.3. The DIC-displacement in Figure 5.3 is from the 3 mm crack length for SENT specimen with the crack direction/path in the *x*-axis as was setup in the experiment. Once the user selects 'Yes' (Y) in the command line in Figure 5.3, one can then crop the data (see Figure 5.4 for a 'Yes/No' to crop the data) by selecting regions around the crack tip. The cropped area is the region of interest and will minimise computational cost and time when performing the finite element analysis. The interface for cropping is as shown in Figure 5.5, and Figure 5.6 depicts the region of interest around the crack tip that was cropped. Figure 5.6 also shows next step which is the selection of the crack tip and crack path direction (to conform with the crack path direction (*x*-axis) that was chosen in Figure 5.3). Here, the crack tip position is assessed, and a horizontal crack is inserted to define the crack as can be seen in Figure 5.8. To accommodate the crack, the region in the vicinity of the crack is masked for re-meshing when performing the finite element analysis as shown in Figure 5.7 and Figure 5.8.

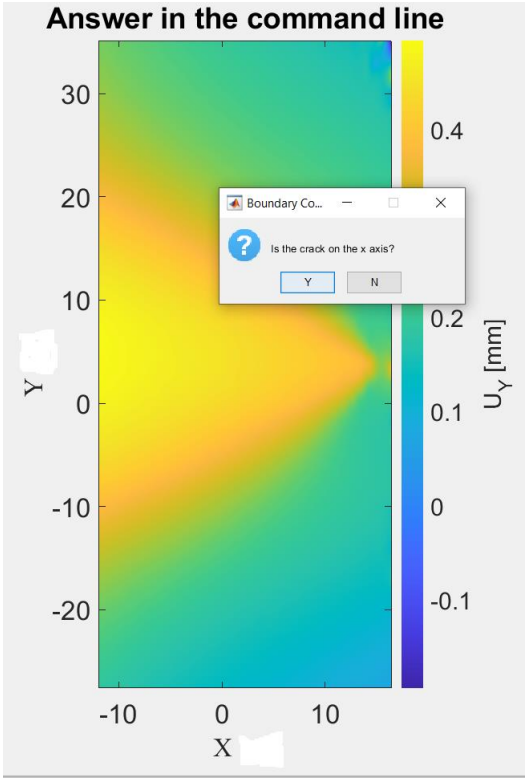

Figure 5.3: Command to define the crack path direction (dimensions in mm)

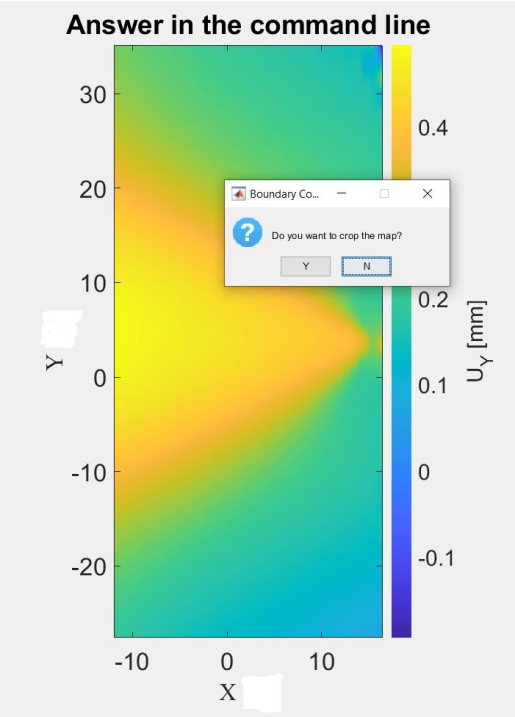

Figure 5.4: Command to accept an option to crop the displacement map (dimensions in mm)

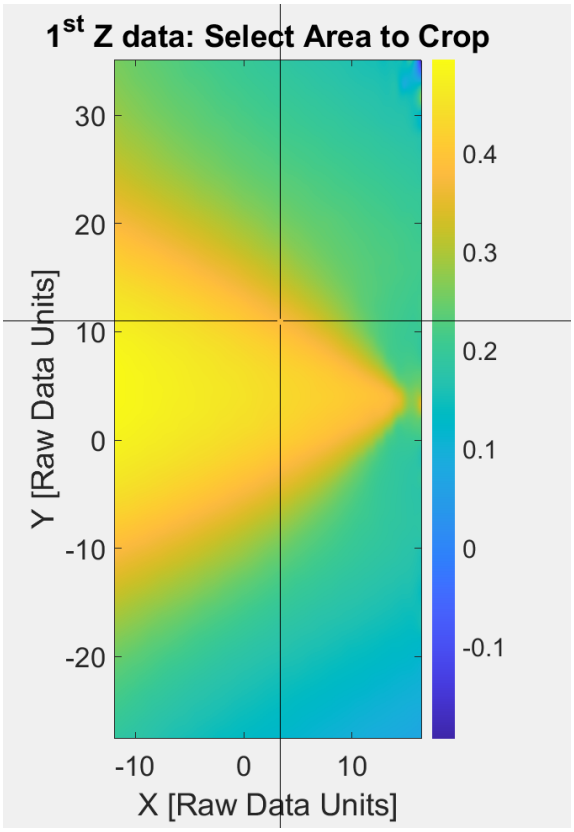

Figure 5.5: Region of interest around the crack to select (dimensions in mm)

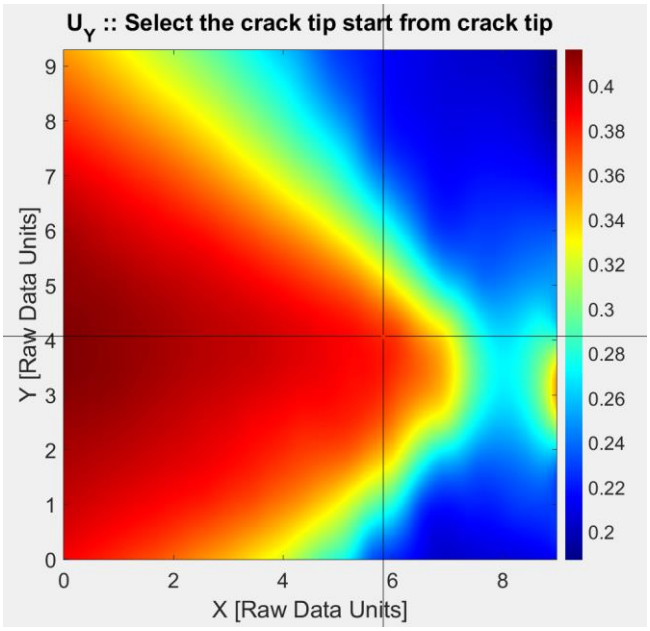

Figure 5.6: Crack path and crack tip position selection (dimensions in mm)

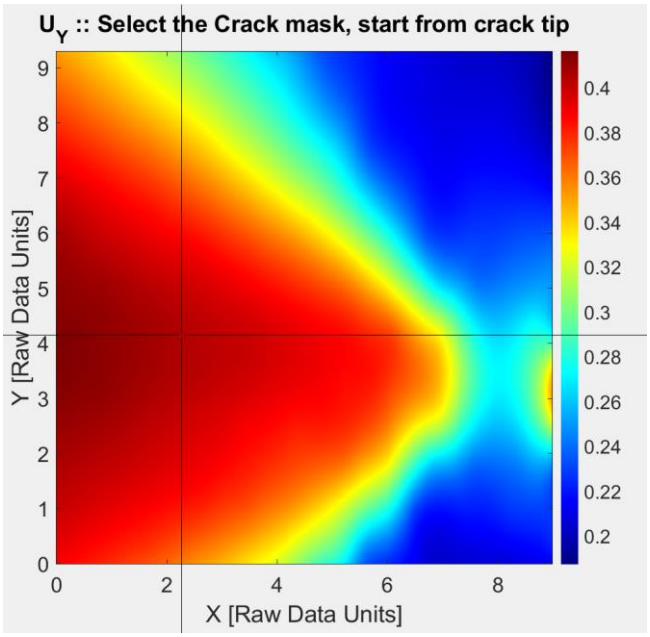

Figure 5.7: Displacement fields of a 3 mm SENT specimen showing an option to select region in the vicinity of the crack (dimensions in mm)

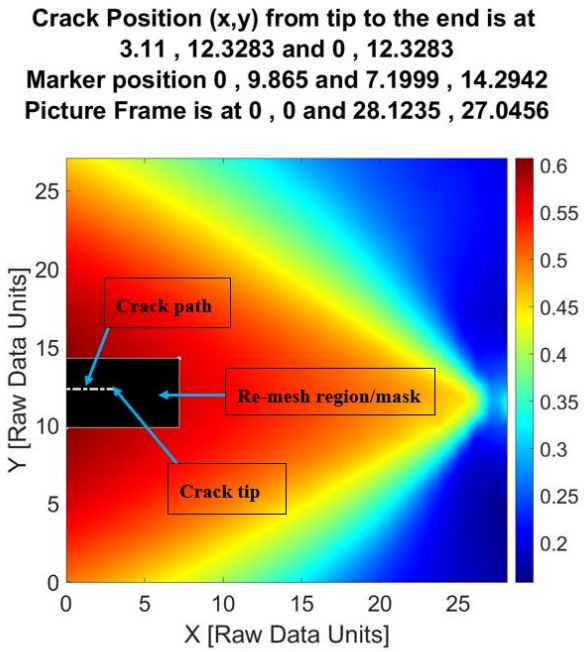

Figure 5.8: Displacement fields showing crack tip location and crack path for a 3 mm SENT specimen (dimensions in mm)

Once the DIC analysis is complete as in Figure 5.8 with the MATLAB computations, a Python script is generated with crack path and crack tip location. The data points obtained by DIC-measured displacement are injected as local boundary conditions, point by point within the Python script. The Python script is run in Abaqus to create the CAE file where material properties are then defined in the model. The material law examined in this work is the linear isotropic elastic model with properties of API 5L X65 steel (Young's modulus, E=207000 MPa and Poisson's ratio, $\nu = 0.3$). Note that the method is versatile and can be applied to any material model used in Abaqus. A finite element analysis using plane stress (CPS4) elements is performed to obtain the stress and strain fields and to compute the *J*-integral using the inbuilt algorithms (virtual crack extension) in the finite element software Abaqus version 2020).

The 2D finite element CAE generated from the Python script is shown Figure 5.9 indicating the region of interest, crack tip and crack path. Figure 5.10 shows the close-up of the re-meshed region around the crack that was masked in Figure 5.8. The load and boundary condition applied to the model are illustrated in Figure 5.11 and the contour plots for the *J*-integral are shown in Figure 5.12 and Figure 5.13. The values of *J* obtained from the experiments and those from this analysis are shown in Table 5.1. There was good agreement (less than 2% error for the three cases analysed) with the *J*-integral obtained from the DIC-FE treatment and that obtained from the experiment for

the 15 mm thick and 3 mm crack length SENT specimens analysed. This low percentage error indicate that the method is versatile and reliability, providing a close representation of the experiment and actual component being studied.

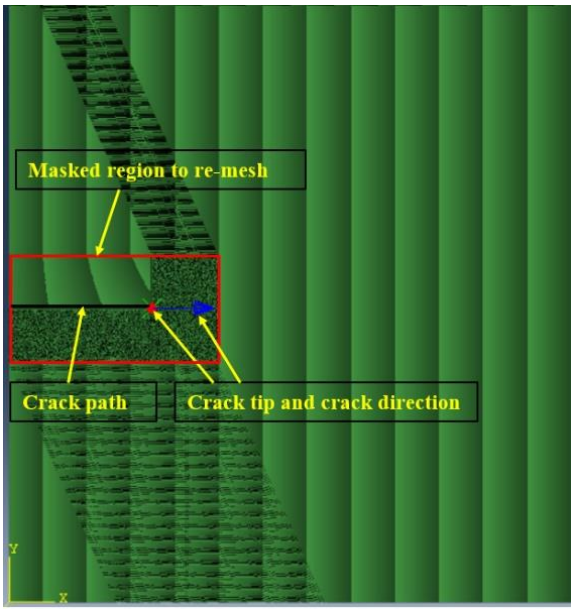

Figure 5.9: FE mesh registered with the DIC measured grid showing region containing the crack to be deleted and re-meshed

Table 5.1: Comparison of *J* values for SENT experimental and DIC-FE analysis

Specimen No.	a_0/W	J_0 **from experiments [N/mm]**	J **from DIC-FE [N/mm]**	**Error [%]**
SENT fracture tests/DIC-FE analysis at room temperature, 23℃				
M01-04	0.10	1399.9	1423.53	1.67
M01-05	0.11	1413.7	1416.30	0.18
M01-06	0.11	1344.9	1366.17	1.56

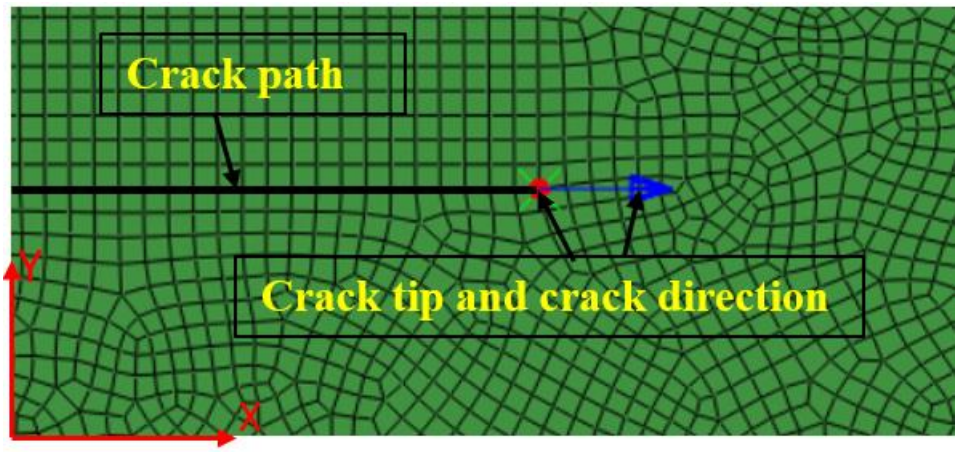

Figure 5.10: Close-up view of the re-meshed region in the vicinity of the crack

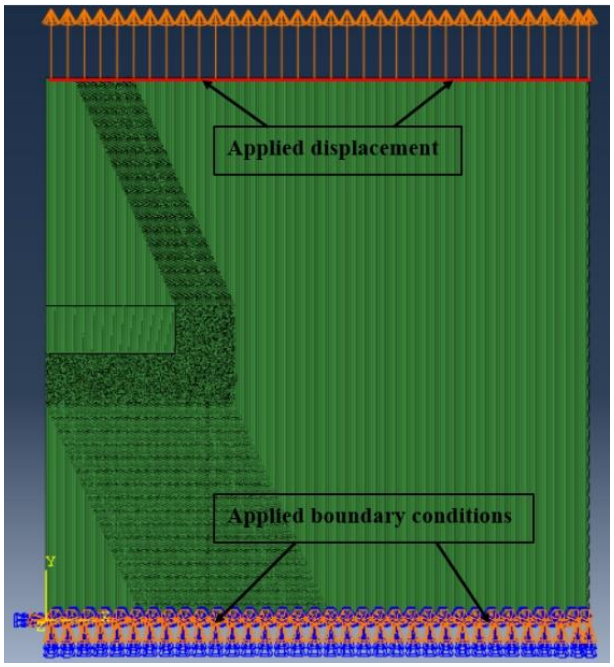

Figure 5.11: Boundary conditions and displacement load applied to the FE model

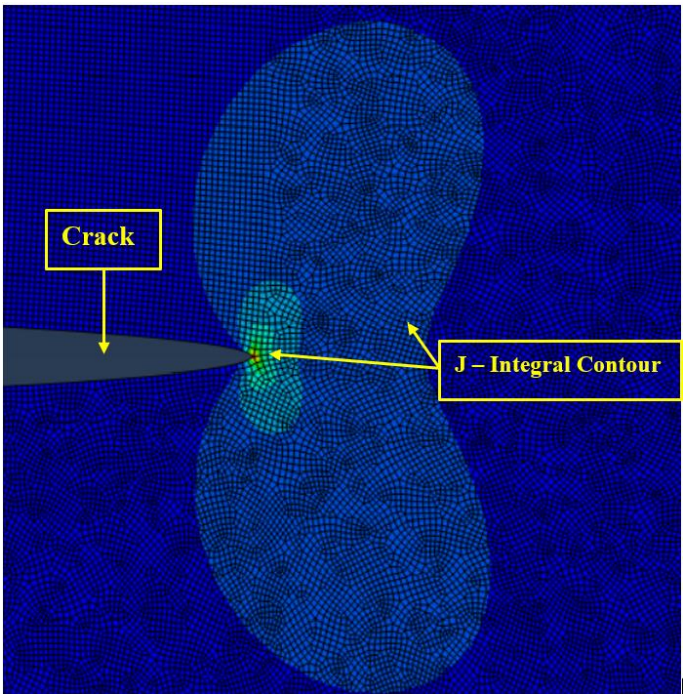

Figure 5.12: *J*-integral contour plot and crack for DIC-FE analysis of SENT specimen of 3 mm crack length

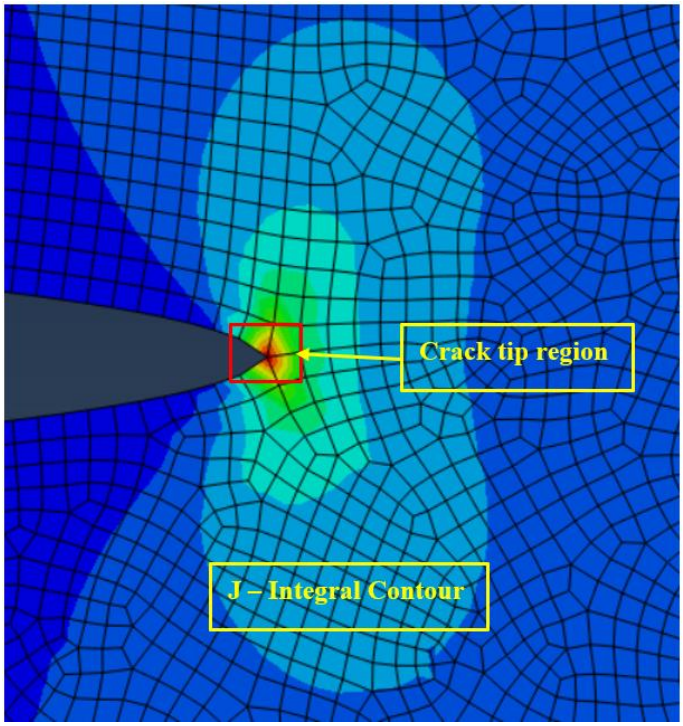

Figure 5.13: Close-up look of the *J*-integral contour plot and crack tip region for DIC-FE analysis of SENT specimen (3 mm crack length)

5.5 Summary and conclusion to this chapter

The prediction of structural failure/fatigue life is most difficult for shallow cracks, as their local conditions may differ from what is predicted using the remote applied loading and crack geometry of deep cracked specimens. Digital image correlation (DIC) can be utilised to analyse images from an optical microscope (OM), which facilitates the local characterisation of the crack field.

This chapter presented a novel finite element-based approach that uses DIC-measured displacement data to retrieve the crack field and quantify the local crack driving force (*J*-integral). With the assumption of linear elasticity (note that this approach can be applied to plastic/Ramberg-Osgood material models too) isotropic models, the change in Mode I crack intensity factors can be extracted using the interaction integral method. This allowed the determination of the local driving force for shallow crack propagation. The application of this method was demonstrated by the full-field analysis of short cracks in SENT specimen for API 5L X65 steel. This technique is robust and requires no prior knowledge of theoretical solutions or far-field boundary conditions, and it can be applied to the tip of a crack by defining an appropriate local frame of reference. The following are a summary and concluding remarks drawn from this chapter:

- A method to determine the *J*-integral as the crack driving force from measured displacement fields has been presented, using digital correlation image (DIC) datasets. The method uses a finite element framework and is easy to implement.
- For the study of short cracks, the full-field DIC measurements have been used as boundary conditions for finite element calculation of the local *J*-integral for elastic material models.
- It has been demonstrated in a shallow crack (3 mm in length) of SENT specimen that, this method is insensitive to the specimen geometry and does not require any prior knowledge of the applied loading and the total crack length.
- Only the local crack tip segment is used within this framework, and it can be applied when DIC measurements in the vicinity of the crack surface are not trustworthy, which allows for a precise evaluation of the local crack tip conditions.
- Application of the method to the SENT experimental data for elastic material model show the crack field (as a *J*-integral) can be obtained with good accuracy. However, care must be taken to ensure that the crack tip position and crack path are well determined.
- The work carried out in this chapter showed there is good agreement for the *J* values obtained using the DIC-FE approach to values determined from experimental tests. The values from the experiment and that from the DIC-FE novel approach were very close to each other with less than 2% error.
- As discussed in chapter 3, the DIC test was not performed at the low temperature due to frost and the environmental chamber needed to be closed to maintain uniform temperature. DIC tests conducted at room temperature can be inferred to provide valuable insights for analysis of cold temperature tests that were not able to utilize DIC due to frost-related issues.
- Although the environmental conditions and frost present during cold temperature tests may affect the feasibility of applying DIC directly, data obtained from the room temperature can be used to gain a better understanding of the material behaviour and deformation mechanisms under different conditions. Here are suggested ways on how DIC tests at room temperature can be leveraged for the analysis of cold temperature tests affected by frost:
    - Establish baseline behaviour: Conducting DIC tests at room temperature allows for the establishment of a baseline behaviour of the material. By understanding the material's deformation characteristics under normal conditions, it becomes possible to compare and assess the deviations observed during cold temperature tests affected by frost.

- Investigate material response: DIC provides detailed information about strain and deformation patterns. Analysing the room temperature DIC data can help identify the typical response of the material to external loading, such as the development of strain concentrations, stress redistribution or crack initiation and propagation. This knowledge can be used as a reference for evaluating the behaviour observed in cold temperature tests.
- Understand frost effects: Frost can introduce additional complexities to the material's response during cold temperature tests. By examining the room temperature DIC data alongside other relevant information, such as environmental conditions during cold tests, it becomes possible to infer the potential effects of frost on deformation and strain fields. This understanding can aid in interpreting the frost-induced changes in the material's behaviour during cold temperature tests.
- Validation and calibration: If possible, conducting controlled tests at room temperature that simulate the frost conditions encountered during cold temperature tests can provide a means to validate and calibrate the DIC technique. By comparing the DIC results from the simulated frost tests with the observed behaviour in the cold temperature tests, the accuracy and reliability of the DIC analysis can be assessed and refined.
- Modelling and simulation: DIC data obtained at room temperature can serve as input for modelling and simulation efforts aimed at predicting the behaviour of the material under cold temperature conditions. By incorporating the knowledge gained from room temperature DIC tests, the models can be calibrated to capture the effects of frost and predict the deformation response during cold temperature tests more accurately.

It is important to acknowledge DIC limitations and differences between room and cold temperature tests. The analysis of cold temperature tests affected by frost requires a careful consideration of the specific environmental conditions and their impact on the material's behaviour. Integrating the information obtained from room temperature DIC tests into the analysis can provide valuable insights and help in understanding the material's response under cold temperature conditions affected by frost.

6 Fracture assessment of aluminium 5083 alloy by X-ray computed tomography

6.1 Introduction

In this chapter an initial investigation using X-ray computed tomography (XCT) and digital volume correlation (DVC) to measure the through-thickness displacement and strain fields of a cheaper material (AL 5083) is presented. This was suggested as part of the research to assess the volumetric deformations of the aluminium material and compare the analyses to the DIC surface measurements performed in chapter 3 and 5 on the X65 steel grade. DVC extends the concept of DIC (2D surface measurements) to three-dimensional volumetric measurements providing a more comprehensive understanding of the material's behaviour in 3D space.

Offshore structures such as marine ships, oil pipes, liquefied natural gas (LNG) storage, LNG carriers (LNGC) for transportation and supply systems, floating storage regasification units (FSRU) and LNG fuel gas supply systems (FGSS), should be designed to ensure structural integrity under a wide range of loading conditions through the appropriate selection of materials. Typical materials applied to these structures include aluminium alloys, nickel alloy steels and stainless steel [147].

Most of these structures are exposed to several loading conditions, i.e., fatigue, sloshing impact and thermal loading [147]. These loading conditions can often result in the failure of the structural component with flaws. One of the most significant issues in the design and safe operation of offshore structures is a fracture assessment of the component or specimen with possible flaws to better understand the fracture behaviour.

To reveal crack formation and propagation processes as precisely as possible, scanning electron microscopy (SEM) and surface-based fractography are normally utilised to establish the relationships between fracture behaviour and mechanical properties. Though, these two-dimensional imaging techniques contribute to the achievements made in revealing the fracture behaviour to some extent, the effect of the internal microstructure under the 2D surface of the specimens on the crack regime are often neglected. In fact, the stress state of the crack on the surface differs significantly from the interior of the specimen and cracking always occurs within the interior [148]. Therefore, it is necessary to analyse fracture behaviour of engineering components using three-dimensional characterisation methods such as X-ray computed tomography (XCT) with digital volume correlation.

More recently, XCT technique, routinely used in hospitals for medical diagnoses, is now increasingly becoming an attractive tool for characterising engineering structural materials. This is because of its high resolution, non-destructive nature and clear visualisation capability in 3D. In the past decade, tremendous efforts have been made in applying the XCT to characterise and study the evolution of damage and fracture for a variety of materials, including ceramic matrix composites, 3D printed components, metal matrix composites etc. [137].

Therefore, as part of this research, it was agreed to utilise this technique to characterise and study the fracture behaviour of a 'softer' metal such as aluminium (AL 5083) to demonstrate the functionality of the digital volume correlation (DVC) approach. This was to allow for the analysis of full-field deformation and strain fields within a three-dimensional volume based on data obtained from XCT.

6.2 X-ray computed tomography

XCT is a technology that uses X-rays to produce tomographic images of a scanned object or specific area, allowing the user to see the interior of the object without cutting through it.

XCT is based on the fact that different components of an object have different attenuation rates on an X-ray beam which is caused by the absorption when penetrating the object. For a given incident intensity (I_0), the transmitted intensity $I(x)$ of the X-ray is computed by the equation 6.1 [148] [149]:

$$I(x) = I_0 e^{-\mu x} \tag{6.1}$$

where μ is the local linear attenuation/absorption coefficient which correlates with incoherent scattering, coherent scattering and photoelectric effect and x is the distance of the object transmitted by the X-rays.

When X-rays penetrate an object with multiple constituents, $I(x)$ of the X-rays changes with the variable absorption coefficients of the constituents. Accordingly, absorption-contrast is obtained, and the inner constituents of the object can be distinguished from each other. Two-dimensional tomography layers can be stacked to generate three-dimensional images, where a virtual replica of the object is created to reveal its internal structure and this forms the imaging principle of XCT [149].

Like other computed tomography-based imaging systems, the critical components of an XCT are an X-ray source, sample stage and a detector. The specimen to be tested is placed on a rotatable/turntable between the X-ray source and a detector where the specimen is rotated while

the X-ray hits it. After passing through the specimen, the X-rays are detected and sequential images (slices) are collected and compiled to create 3D representations that can be manipulated digitally to perform measurement and visualisation tasks. In order to achieve optimal data acquisition and interpretation, it is vital to select the scanning configuration properly: use of X-ray sources and detectors, careful calibration, energy of X-ray source, exposure and total scanning time as well as special attenuation and modes of artefact suppression.

There are many factors that can affect the quality of scanned images. First, is the material type, since the amount of material attenuation of X-rays is controlled by the density and atomic number of each component. Secondly, the X-ray intensity controls its ability to penetrate the specimen and affects the relationship between signal and noise in the image. High energy X-rays can pass through a greater thickness of a material or a similar thickness of a denser material before they are absorbed.

Therefore, the energy of the X-ray beam should be selected with utmost care depending on the size and composition of the material being investigated. In some cases, to obtain better contrast images, filters such as copper or aluminium can be used before the X-ray reaches the test specimen. The third factor is the distance between the X-ray source and the test piece on the turntable as well as sample stage and detector distance. For better scanned quality, a closer distance between the test specimen and X-ray source is ideal. In this case however, the X-rays should be emitted simultaneously across the specimen's width and should all be collected by the detector. Last but not the least, the specimen should be firmly mounted on the rotatable/turntable stage to ensure that the specimen does not move while the X-ray is scanning so as to obtain reliable slice images [150]–[154].

6.3 Image reconstruction

The most widespread image reconstruction technique is the so-called filtered back-projection, where the data are first convolved with a filter to create a set of filtered views. Each view is then successively superimposed over a square grid at an angle corresponding to its acquisition angle. After image reconstruction, the raw projection data are converted to CT numbers or grey values that have a certain range by the computer system, e.g., 8-bit or 16-bit etc. The reconstructed images are in the form of pixels in 2D (unit of 2D picture) or voxels in 3D. Each pixel or voxel in the reconstruction is allocated a grey value, from a grey scale as a representation of the attenuation coefficient of the element occupying that pixel/voxel [149].

6.4 Material and Experimental Procedure

The investigated aluminium 5083 alloy specimen was produced at The Welding Institute (TWI) in Cambridge, UK, by electro-discharge machining (EDM) from a (500 mm x 500 mm) flat square plate of 5 mm approximate thickness. A central, parallel sided gauge section of 5 mm x 10 mm with a thickness of 3 mm for the entire specimen was extracted retaining the as EDM finish ends allowed an interface to a pinned plate grip design to either end. Figure 6.1 illustrates schematic drawing of the specimen design on the left and the EDM finish is on the right.

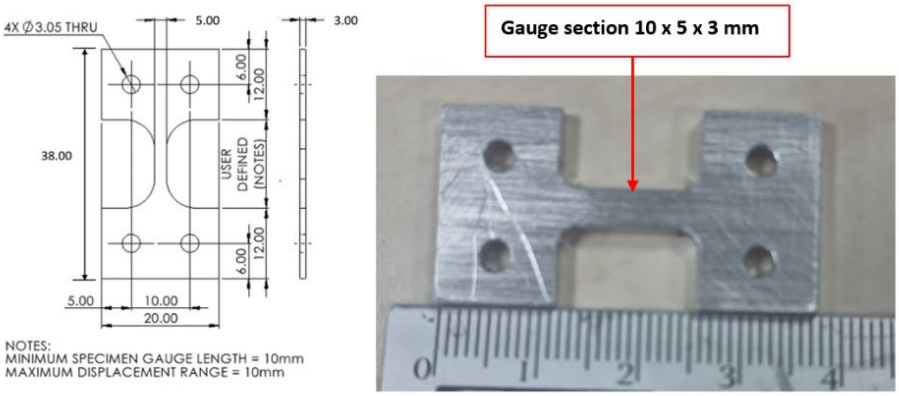

Figure 6.1: Specimen geometry, left (dimensions in mm) with tested specimen shown on the right

The in-situ experiments of the aluminium dog-bone specimen under tensile loading was carried out at the state-of-the-art Manchester X-ray imaging facility, at the University of Manchester, UK. The 225kV High Flux Bay and the CT5000 Deben loading system was used to perform the experiment. Figure 6.2 illustrates the setup. The Deben rig was used to apply tensile load to the specimen which was positioned on a rotating stage. The Perspex tube allows live observations, both by projection and sight view. Different combinations of the exposure time, voltage and beam current were tried, and the best ones were selected in terms of best resultant image quality and reasonable scanning time. Finally, the X-ray projections were acquired with an exposure time of 2.83s leading to a scan time of 1hr 34 minutes at an accelerating voltage of 140kV and a 36μA beam current using a tungsten target. For each scan, the specimen on the stage was rotated 360 degrees resulting in 2000 projections collected on a Perkin Elmer high resolution 16-bit flat panel detector, 2024 x 2024-pixel. A summary of the XCT parameters used during the experiment is given in Table 6.1.

The displacement-controlled loading was used to ensure that there would be no further movement during each scan at the successive loading steps, which otherwise would generate blurred images.

During the hold periods, approximately 14 minutes each in duration, the Deben rig displacement-controlled loading ensured the specimen remained stationary during the X-ray acquisition.

The first scan was conducted without loading the specimen (i.e., at 0N). A tensile load was then applied at a displacement rate of 0.1mm/min to 1000N, at which point the displacement was kept stable and the second scan was performed. As there was no noticeable elongation or defects in the reconstructed image for the 1000N loading step, the third scan was carried out at 3000 N at the same rate. The fourth scan was conducted at 3500N and the fifth scan at 3700N which was nearer the point of failure as per the offline test. However, crack propagation could not be captured after the fifth loading step before the specimen went into catastrophic failure at the supposedly final loading step when it reached the ultimate tensile stress (UTS). The last scan was performed at this failure load. It should be noted that, for each scan, the standard X-ray scanning procedure was followed. This include the specimen set-up, machine warming, pre-scan settings, energy checking, exposure time selection, detector and CT calibration and the displacement load was maintained during each scan.

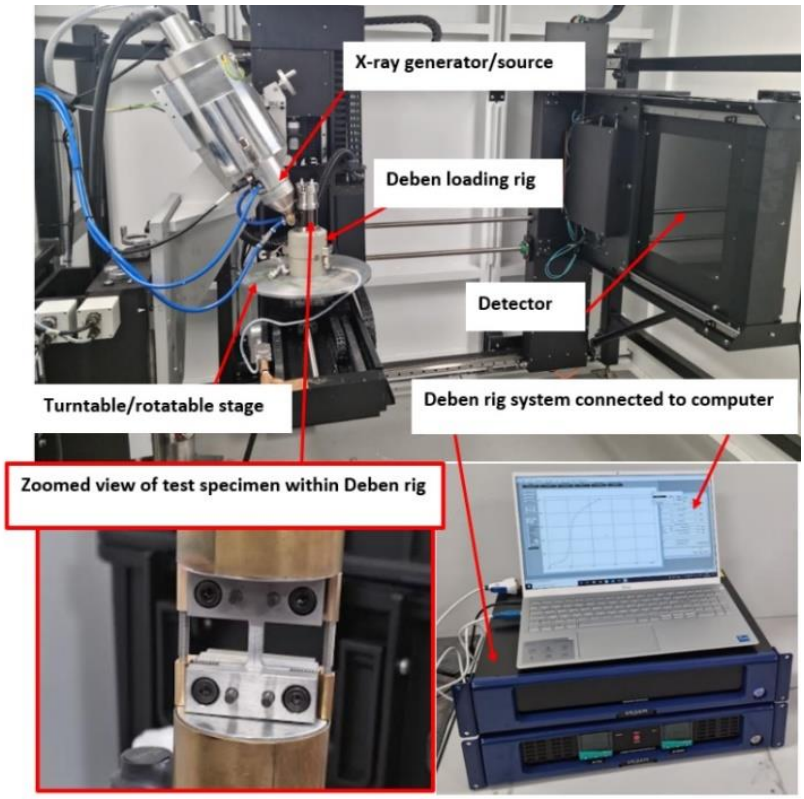

Figure 6.2: Experimental setup for the in-situ tensile test with the Deben loading rig within the X-ray source and the detector in view, showing an enlarged image of the dog-bone specimen mounted in the loading rig and the Deben computer system

Table 6.1: Summary of XCT parameters used for scanning

X-ray Parameter	Value
X-ray Energy (kV)	140
Current (μA)	36
Exposure time (minutes)	94
Projections	2000
Source to object distance (mm)	39
Source to detector distance (mm)	1404
Voxel size (mm)	0.0055

6.5 Data Import and Analysis

A three-dimensional XCT image of the aluminium specimen is presented in Figure 6.6. This was reconstructed from the XCT volumetric data acquired from the central gauge section of the specimen and recorded prior to loading the specimen. For all the loading steps, a 3D image was computationally reconstructed by a filtered back projection algorithm, using the projections acquired for each dataset. Commercially available CT Pro 3D and AVIZO software were used to reconstruct and visualise the raw datasets respectively, consisting of 2000 slices.

As shown in Figure 6.3 and Figure 6.4 there was deformation (i.e., elongation) during the loading. However, we were unable to capture the crack propagation before the specimen went into catastrophic failure. This is noticed from the force-elongation curve that the specimen failed after reaching the ultimate tensile stress (UTS) as illustrated in Figure 6.5 and Figure 6.7.

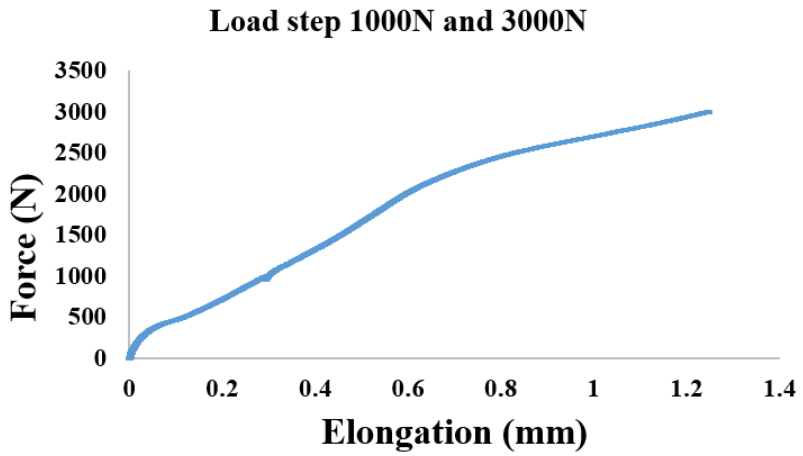

Figure 6.3: Loading steps 1000N and 3000N: Force vs elongation

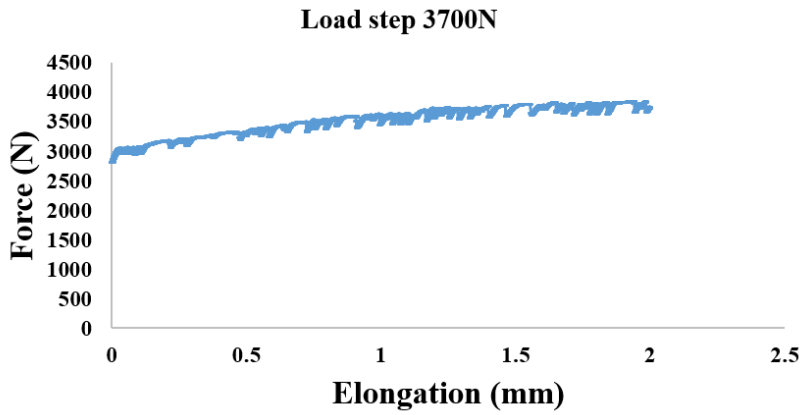

Figure 6.4: Loading step 3500N and 3700N: Force vs elongation

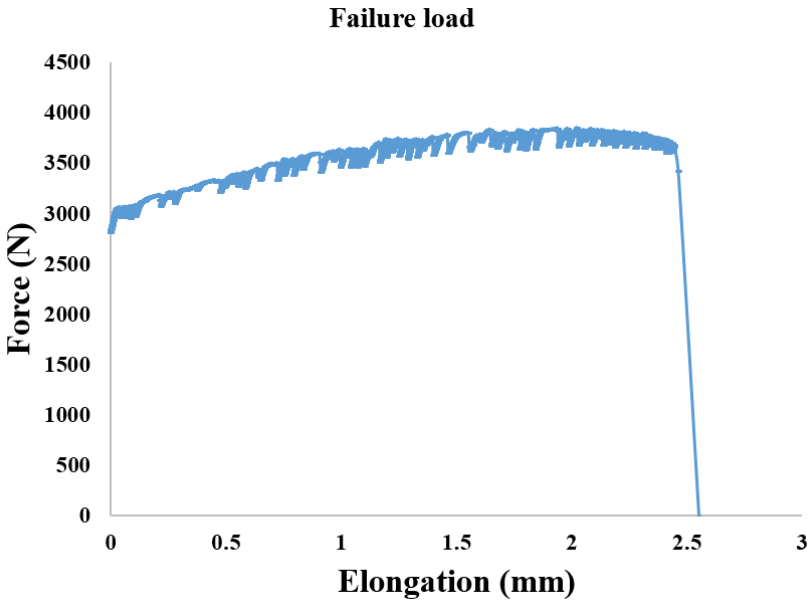

Figure 6.5: Catastrophic failure: Force vs elongation

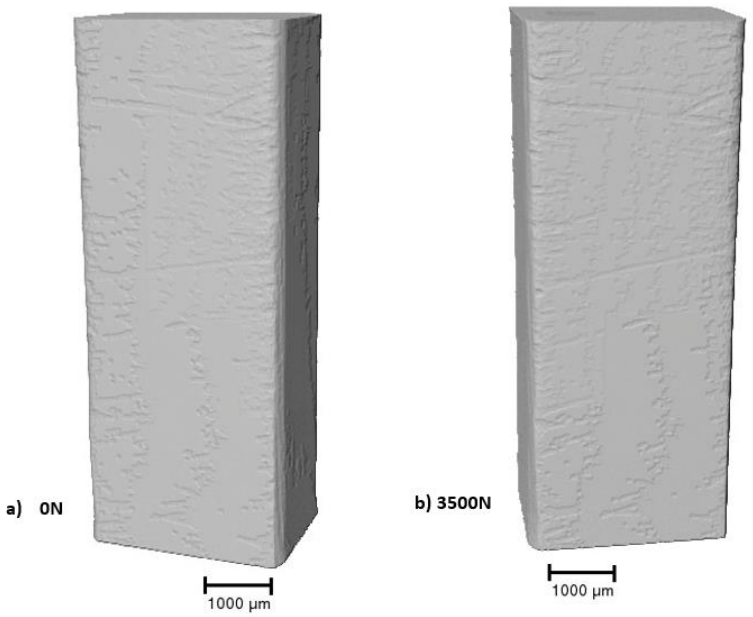

Figure 6.6: Three-dimensional XCT view of the gauge section prior to loading (0N) and loading to 3500N

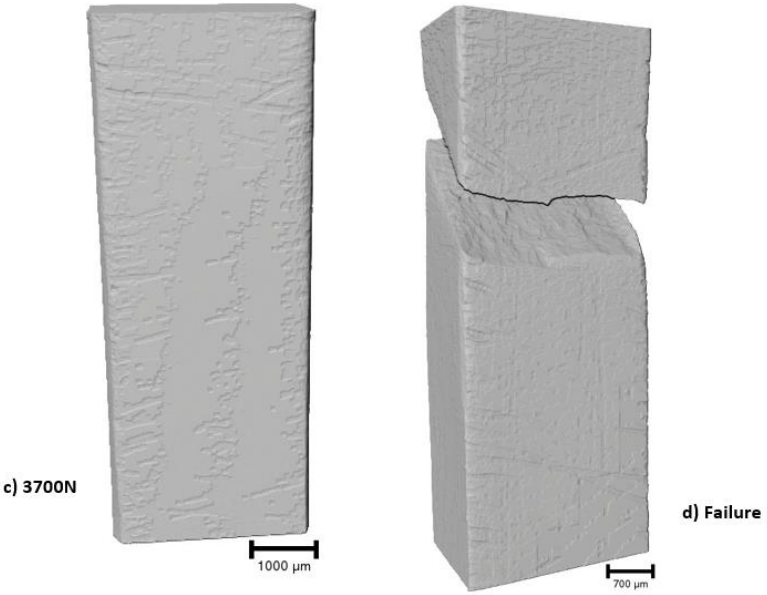

Figure 6.7: Three-dimensional XCT view of the gauge section at 3700N load and at failure

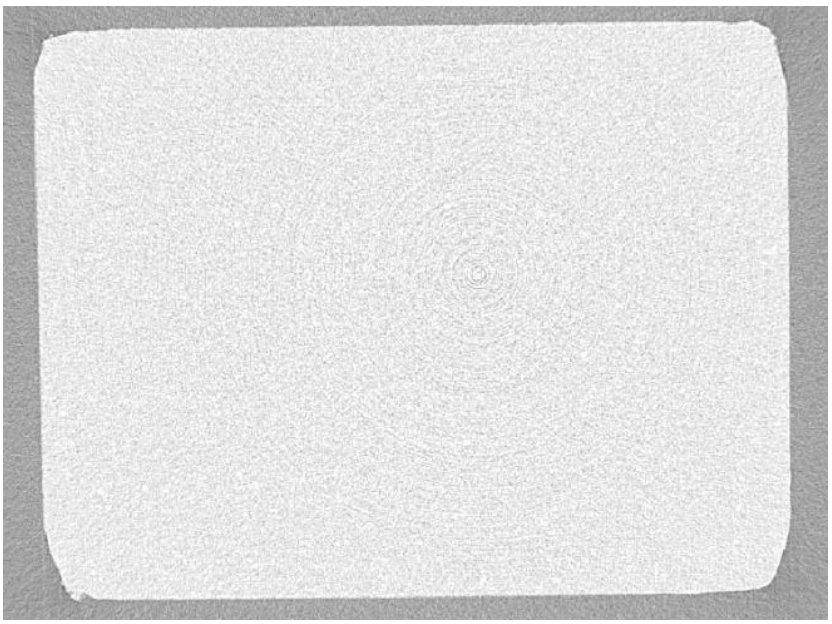

Figure 6.8: Image of ring artefacts on the aluminium 5083 specimen

6.6 Summary, conclusions and recommendations to this chapter

The fracture assessment of aluminium 5083 alloy using X-ray computed tomography (XCT) provides valuable insights into the fracture behaviour and integrity of the material. X-ray CT is a powerful non-destructive testing technique that allows for the detailed characterisation of internal defects, cracks and microstructural features within the material. By employing X-ray CT, engineers and researchers can accurately visualise and quantify the size, shape and distribution of internal flaws and cracks within the aluminium 5083 alloy. This information is crucial for fracture assessment, as it helps in determining the critical flaw size and predicting the material's fracture resistance. Moreover, X-ray CT allows for the assessment of the material's microstructure, including grain size, texture and presence of inclusions or voids. These microstructural features can influence the initiation and propagation of cracks and their characterisation is essential for understanding the fracture behaviour. In summary, the fracture assessment of a component by X-ray CT provides critical information about internal defects, crack morphology, crack growth mechanisms and microstructural features. This knowledge aids in understanding the material's fracture, predicting its fracture resistance and optimising the design and performance of structures and components.

This chapter presented an initial trial of in-situ XCT inspection of an aluminium 5083 specimen under static tensile loading. The following summarises the study conducted in this chapter:

- An aluminium 5083 specimen was tested under tensile load using a commercially available in-situ Deben CT5000 loading rig. XCT images were recorded at various stages during loading.
- The 225kV High Flux Bay system used can detect cracks. However, due to the specimen suddenly failing catastrophically, the detection of crack propagation in the aluminium 5083 specimen was not achieved. Process artefacts and general EDM finish architecture were visible illustrating the capability of the High Flux Bay to track any crack had the specimen not have suddenly failed.
- Ring artefacts are a common issue related to XCT images as shown in Figure 6.8. Such artefacts may be the result of defects or poor calibration of detectors, non-linear behaviour of detector materials, channel to channel variation of the detector array output. Among these, sensitivity of the detector plays an important role. It is important to have a constant sensitivity across the whole detector. In future experiments, checks should be done for faulty pixels on the detector prior to the start of testing to avoid ring-like artefacts in the reconstructed volumetric datasets.
- Repeat experiments should be planned in the future in order to gain confidence in the mechanical response of the loading rig, careful load increments selection closer to the failure load to enable recording of crack initiation and propagation just before any catastrophic failure.

The fracture assessment of aluminium 5083 alloy using X-ray computed tomography (CT) in this study did not yield the expected results due to the catastrophic failure of the specimen. Although the expected outcome was to obtain valuable insights into the fracture behaviour and integrity of the material, the specimen's failure hindered a comprehensive analysis using X-ray CT.

The catastrophic failure of the specimen may have been influenced by various factors such as the presence of pre-existing defects, flaws, or inconsistencies in the material's microstructure. These factors could have compromised the structural integrity of the specimen and led to premature failure, preventing a thorough assessment of the fracture behaviour using X-ray CT. It is essential to note that the failure of a specimen during a fracture assessment study can occur due to various reasons, including material defects, inadequate specimen preparation, or limitations in the testing procedure itself. In this case, the unexpected failure indicates the need for further investigation and

analysis to identify the root causes and determine the appropriate measures for future fracture assessment studies on aluminium 5083 alloy.

Despite the unexpected outcome, it is crucial to learn from this experience and consider alternative or complementary testing methods to assess the fracture behaviour of aluminium 5083 alloy or any component under X-ray CT test. Supplementing X-ray CT with other techniques such as scanning electron microscopy (SEM), optical microscopy, or mechanical testing can provide additional insights into the material's failure mechanisms and fracture characteristics.

In conclusion, even though the fracture assessment conducted in this research using X-ray CT did not yield the expected results due to the catastrophic failure of the specimen, the outcome highlights the importance of further investigation to identify the reasons for failure and consider alternative testing methods to gain a comprehensive understanding of the fracture behaviour of the material.

7 Summary, Concluding Remarks and Recommendations for Future Work

7.1 Summary

Engineering critical assessments are carried out to support the demonstration of structural integrity for high integrity components such as oil and gas pipelines. These assessments often consider deep notched specimens which results in high stresses around the crack tip leading to high constraint conditions and reduction in fracture toughness. This causes a problem when the resulting apparent limiting defect sizes are applied to real engineering components such as oil and gas pipelines. These pipelines often contain shallow cracks, leading to low stresses in the vicinity of the crack/low constraint conditions leading to an increase in fracture toughness. Consequently, it is worthwhile when considering defect assessment of critical components to consider the possibility of taking advantage of enhanced fracture toughness resulting from a loss of the crack tip constraint due to localised plasticity in the stress concentration region.

Analyses have been carried out in this research with supporting material fracture testing to demonstrate that the increased stress intensity factors (SIF) at the crack tip is offset by a reduction in crack tip constraint, such that the material exhibits a higher apparent fracture toughness. This enables a more simplistic defect assessment and leads to larger margins when assessing structural components. This work features the use of low constraint specimens: - pin-loaded single edge notched tension (SENT) and three-point shallow-notched bend (SENB) to demonstrate the material response when a load is applied. Crack size margins in defect tolerance assessments are often measured against the initiation of tearing, though failure of the material may occur at a higher load following stable crack extension. This work measured and assessed the benefit of reduced crack tip constraint on both crack initiation and ductile tearing, even though, the amount of tearing at the low temperature was limited compared to tests carried out at room temperature. This showed that the effect of constraint was valid with ductile tearing for this material and that there was additional margin available beyond the onset of tearing.

7.2 Concluding Remarks

The original objective of this work was to assess the effects of constraint on fracture toughness of high strength steels in low temperature applications, in order to reduce inherent conservatism in current defect assessment procedures. A thorough experimental and numerical investigation was

conducted in this respect. Although, several questions still remain unanswered, significant advances were made towards achieving this objective. Since a summary and conclusion was given for each chapter, a brief conclusion to the entire thesis is given as:

- Crack tip constraint is an important and relevant area of research within the field of materials engineering and structural integrity. Understanding the behaviour of cracks and the level of constraint at the crack tip is crucial for ensuring the safe and reliable operation of structures in harsh Arctic environments.
- Arctic conditions present unique challenges to high strength steel components due to extreme low temperatures, brittle fracture behaviour and the presence of ice and other environmental factors. The presence of cracks in these components further exacerbates the potential for failure and poses significant risks to the integrity of the structures.
- The findings from this research emphasise the significance of crack tip constraint in high strength steel components in Arctic conditions. The study highlighted that in Arctic conditions, where temperatures are extremely low, the crack tip constraint becomes even more critical. The combination of low temperatures and fracture toughness can significantly affect the crack propagation path and rate, as well as the overall structural integrity of high strength steel components.
- The findings of research in this area can contribute to the development of improved design guidelines, inspection procedures and maintenance strategies for high strength steel components operating in Arctic conditions. By better understanding the crack tip constraint, engineers and researchers can develop strategies to mitigate crack propagation and prevent catastrophic failures.
- The experimental data obtained in this investigation provided a demonstration of constraint effects on fracture toughness. It was apparent from the results that, size effects on fracture toughness can be attributed to constraint which was dependent on specimen size and geometry.
- With respect to constraint assessment, the linear elastic *T*-stress indicated the SENB specimen (a/W=0.5) to be highly constrained with positive normalised *T*-stress values of +0.01 and +0.13 at $-120℃$ and room temperature tested respectively.
- The normalised *T*-stress for SENT specimen (a/W=0.5) was shown to be -0.21 and -0.28 at $-120℃$ and room temperatures respectively. Though these values are negative, indicating loss of constraint, they are not significantly negative values. Similar trend was observed in the Q-parameter from the elastic-plastic finite element analyses conducted.

From the elastic-plastic Q-parameter analyses in chapter 5, the SENT specimen indicated loss of constraint more readily at small deformation levels than the SENB specimens.

- The findings conducted in this thesis show that there appear not to be any much constraint benefit from testing deeply cracked SENT specimens instead of deeply cracked SENB specimens and therefore, these could be interchangeable. However, it should be noted that, SENB specimens are much simpler to test and requires less material in comparison to the SENT (i.e., the British standard, BS 8571 requires SENT to have a H/W ratio of 10 compared to SENB H/W ratio of 4). Here, H is the so-called day-light length and W is the width of the specimen. Therefore, from an industrial perspective where additional material is required for testing, this increase in specimen size for the SENT would not be welcomed. This not only requires increasing material and increasing levels of sample machining, but also increases cost of specimen manufacture and testing. Thus, a change in specimen type also requires a change in testing procedure and testing rig.
- The enhanced toughness associated with loss of constraint implies that there is, in fact, an increased margin in assessment based on the constraint-modified FADs. This demonstrates the advantages of incorporating representative (enhanced) fracture toughness at low temperatures, to support more realistic design and repair decisions.
- The FE results indicated that for the relevant crack lengths of the pipe considered, the constraint in the shallow cracked SENT specimens is much closer to the constraint in the pipe models than the SENB specimens. This will reduce the conservatism inherent in defect assessment analyses, if shallow cracked SENT/SENB specimens are used to establish the fracture toughness. This can be an effective tool to establish acceptance criteria for pipes with defects.
- The cost reduction associated with using small-scale testing (SENT and shallow-cracked SENB) to quantify low temperature testing (brittle fracture) will enable industries to make use of the test methods developed in this work. This can be incorporated in defect assessment procedures (specifically, BS 7910) and allow for life extension programme of the structures.
- A novel approach using full-field DIC-measured data and finite element was developed and implemented to compute *J*-integral. There was good agreement for the *J* values obtained using the DIC-FE approach and the values determined from experimental tests. The values from the experiment and that from the DIC-FE novel approach were very close to each other with less than 2% error, indicating versatility and reliability of the method,

thereby providing a close representation of the experiment and actual component being studied.

- The research will also pave way for testing thin-walled and shallow cracked specimens that are representative of structural steel components, ensuring that the materials used for offshore applications in the Arctic regions are safe in preventing catastrophic failures. This outcome will be taken forward by Lloyd's Register Foundation to the BS 7910 committee for the incorporation of low constraint fracture toughness based on small-scale testing.
- Overall, the investigation of crack tip constraint in typical high strength steel components in Arctic conditions is a crucial aspect in ensuring the structural integrity and safety of critical infrastructure in extreme environments. Continued research and development in this area will contribute to the advancement of materials engineering and enhance the reliability of structures operating in Arctic regions.

7.3 Recommendations for Future Work

- **Experimental Investigations:** The experimental work carried in this research considered only three crack geometries. It is worth conducting more extensive experimental studies to characterise the crack tip constraint in high strength steel components under various loading conditions and environmental factors specific to Arctic conditions. This can include conducting fracture toughness tests, fatigue tests and full-scale component testing of different material types, crack/specimen geometries, loading conditions and environmental factors to obtain a comprehensive understanding of crack growth behaviour and constraint effects.

- **Advanced Numerical Modelling:** Enhance numerical modelling techniques to simulate crack propagation and evaluate crack tip constraint in high strength steel components. Develop advanced finite element models that can capture the complexities of crack tip behaviour, including crack branching and interaction with microstructural features. Incorporate temperature-dependent material properties, loading conditions and consider the influence of ice and other environmental factors specific to Arctic conditions to provide more accurate predictions of crack growth and failure.
- **Microstructural/Multi-Scale Analysis:** Investigate the effect of microstructural features, such as grain boundaries, phase constituents and inclusions, on crack tip constraint in high strength steel components. Focus on the impact of low temperatures, brittle behaviour and changes in microstructure on crack tip constraint. This can involve use of advanced

microscopy techniques to examine the microstructural characteristics near the crack tip and correlate them with the observed crack growth behaviour to gain a deeper understanding of crack propagation mechanisms.

- **Material Development:** Explore the potential for developing new high strength steel alloys or modifying existing alloys to improve crack tip constraint and fracture resistance in Arctic conditions. Investigate the influence of alloying elements/composition, heat treatment, microstructural characteristics, mechanical properties and fracture toughness on the crack growth behaviour and constraint of the developed materials.
- **Field Studies and Case Studies:** Conduct field and case studies and collect data from real-world high strength steel components operating in Arctic conditions. Analyse the behaviour of existing structures, including oil and gas installations, bridges or offshore platforms and assess the influence of crack tip constraint on their performance. This can involve inspections, monitoring crack growth and analyse the structural response to validate experimental and numerical findings and enhance the understanding of crack tip constraint in real-world scenarios. This can provide valuable insights into the practical implications and challenges associated with crack tip constraint in low temperature environments.
- It is important to acknowledge the DIC limitations and differences between room and cold temperature tests. The analysis of cold temperature tests affected by frost requires a careful consideration of the specific environmental conditions and their impact on the material's behaviour. Integrating the information obtained from room temperature DIC tests into the analysis can provide valuable insights and help in understanding the material's response under cold temperature conditions affected by frost.
- For the XCT and DVC work carried out in chapter 6, repeat experiments should be planned in the future in order to gain confidence in the mechanical response of the loading rig, careful load increments selection closer to the failure load to enable recording of crack initiation and propagation just before any catastrophic failure.

By pursuing these recommendations, future research in the field of crack tip constraint in typical high-strength steel components in Arctic conditions can contribute to the development of improved design guidelines, maintenance strategies and risk assessment methodologies/safety practices for structures operating in such extreme environments.

References

[1] P. Mohseni, Brittle and Ductile Fracture of X80 Arctic Steel, no. October. 2012.

[2] E. E. and H. L. X. Wu, "Fracture Mechanics of High Strength Steel Used in Arctic Offshore Structures," *J. Offshore Mech. Eng.*, 2000.

[3] R. H. Dodds, T. L. Anderson, and M. T. Kirk, "A framework to correlate a/W ratio effects on elastic-plastic fracture toughness (Jc)," *Int. J. Fract.*, vol. 48, no. 1, pp. 1–22, 1991.

[4] T. L. Anderson, Fracture Mechanics: Fundamentals and Applications, 4th Edition, 2017.

[5] A. Saxena, Advanced Fracture Mechanics and Structural Integrity, 2019

[6] W. D. Callister and J. G. David Rethwisch, Materials Science And Engineering: An Introduction, 2014.

[7] J. F. Knott, Fundamentals of Fracture Mechanics The Butterworth Group, London, 1973.

[8] T. Kundu, Fundamentals of Fracture Mechanics. Boca Raton: Taylor & Francis Group, 2012.

[9] H. A. Richard and M. Sander, Fundamentals of fracture mechanics, Solid Mechanics and its Applications, vol. 227, no. November, pp. 55–112, 2016.

[10] A. A. Griffith, The phenomena of rapture and flow in soilds, Philosophical Transactions of the Royal Society of London, vol. 221. pp. 163–198, 1920.

[11] C. E. Inglis, "Stress in a plate due to the presence of cracks and sharp corners," *Spring Meetings of the Fifty-fourth Session of the Institution of Naval Architects*. pp. 219–241, 1913.

[12] S. Kumar Maiti, Fracture Mechanics Fundamentals and Applications, 2015.

[13] G. R. Irwin, Analysis of Stresses and Strains Near the End of a Crack Traversing a Plate, Journal of Applied Mechanics, vol. 24, pp. 361–364, 1957.

[14] J. W. Hutchinson, Fundamentals of the phenomenological theory of nonlinear fracture mechanics, Journal of Applied Mechanics Transactions - ASME, vol. 50, no. 4, pp. 1042–1051, 1983.

[15] F. C. Campbell, Fatigue and fracture : Understanding the basics. ASM International, 2012.

[16] T. L. Anderson, Fracture Mechanics Fundamentals and Applications, third edition, 2005.

[17] H. M. Westergaard, Bearing Pressures and Cracks, Journal of Applied Mechanics Transactions - ASME, vol. 6, pp. 49–53, 1939.

[18] G. R. Irwin, Plastic zone near a crack and fracture toughness, in Sagamore Research Conference Proceedings, 1961, pp. 63–78.

[19] M. L. Williams, "On the Stress Distribution at the Base of a Stationary Crack," *J. Appl. Mech. Trans. ASME*, vol. 24, pp. 109–114, 1957.

[20] N. P. O'Dowd and C. F. Shih, "Family of crack-tip fields characterized by a triaxiality parameter-I. Structure of fields," *J. Mech. Phys. Solids*, vol. 39, no. 8, pp. 989–1015, 1991.

[21] James M. Gere and Barry J. Goodno, Mechanics of materials, 2017.

[22] Z. Shao Fuli Wang Wood, The Fracture Mechanics of Plant Materials, 2018.

[23] BS 7910 2019, "BSI Standards Publication Guide to methods for assessing the acceptability of flaws in metallic structures," 2019.

[24] R6, "British Energy Generation Limited: Assessment of the Integrity of Structures Containing Defects, R6 Revision 4," 2009.

[25] API, API 579-1/ASME FFS-1, Fitness-for-Service 2021.

[26] ASTM E399 (2012), "Standard Test Method for Linear-Elastic Plane-Strain Fracture Toughness, KIC of Metalic Materials." American Society of Testing and Materials International, West Conshohocken, PA, 2012.

[27] D. S. Dugdale, "Yielding of steel sheets containing slits," vol. D, pp. 100–104, 1953.

[28] G. I. Barenblatt, "The Mathematical Theory of Equilibrium Cracks in Brittle Fracture," vol. 129, pp. 55–129, 1962.

[29] F. M. Burdekin and D. E. W. Stone, "The crack opening displacement approach to fracture mechanics in yielding materials," Strain Anal. Eng. Des., 1966.

[30] H. Tada, Paul C. Paris and George R. Irwin Stress Analysis of Cracks Handbook , Third Edition. 2000.

[31] Abdel Salam Hamdy Makhlouf; Mahmood Aliofkhazraei, Handbook of Materials Failure Analysis With Case Studies from the Oil and Gas Industry. Elsevier, 2016.

[32] J. R. Rice, “A Path Independent Integral and the Approximate Analysis of Strain Concentration by Notches and Cracks,” J. Appl. Mech. Trans. ASME, vol. 35:379-386, 1968.

[33] A. A. Wells, “Unstable Crack Propagation in Metals, Cleavage and Fast Fracture,” in Proceedings of the Crack Propagation Symposium, 1961, p. 1:84.

[34] Rice J. R. and Rosengren G. F., “Plane Strain Deformation Near a Crack Tip in a Power Law Hardening Material,” J. Mech. Phys. Solids, vol. 16:1–12, 1968.

[35] J. R. Rice, “Fracture mechanics,” Appl. Mech. Rev., vol. 38, no. 10, pp. 1271–1275, 1985.

[36] J. D. Eshelby, “The elastic energy-momentum tensor,” vol. 5, no. November, pp. 321–335, 1975.

[37] J. R. Rice, “Mathematical Analysis in the Mechanics of Fracture,” Math. Fundam., vol. 2, no. B2, pp. 191–311, 1968.

[38] D. J. Griffith, Introduction to Quantum Mechanics, 2nd editio. 2013.

[39] D. J. Griffith, Introduction to Electrodynamics. 2017.

[40] C. F. Shih, “Relationships between the J-integral and the Crack Opening Displacement for Stationary and Extending Cracks,” J. Mech. Phys. Solids, vol. 29(4):305-, pp. 305-326., 1981.

[41] J. Yang, “The matching of crack-tip constraint between standard and non-standard specimen,” Adv. Mech. Eng., vol. 10, no. 4, pp. 1–8, 2018.

[42] M. Gintalas and R. A. Ainsworth, “Constraint based assessments of large-scale cracked straight pipes and elbows,” Am. Soc. Mech. Eng. Press. Vessel. Pip. Div. PVP, vol. 6A-2015, no. 2014, 2015.

[43] A. Y. Dakhel, M. Gáspár, Z. Koncsik, and J. Lukács, “Fatigue and burst tests of full-scale girth welded pipeline sections for safe operations,” Weld. World, vol. 67, no. 5, pp. 1193–1208, 2023.

[44] T. Obinata, F. Koshiga, N. Matsuo, K. Nishioka, and K. Ikeda, “Full Scale Burst Test of

Large Diameter, High Pressure Gas Pipelines.,” Trans. Iron Steel Inst. Japan, vol. 23, no. 5, pp. 453–459, 1982.

[45] N. P. O’Dowd, “Applications of two parameter approaches in elastic-plastic fracture mechanics,” Eng. Fract. Mech., vol. 52, no. 3, pp. 445–465, 1995.

[46] X. K. Zhu and J. A. Joyce, “Review of fracture toughness (G, K, J, CTOD, CTOA) testing and standardization,” Eng. Fract. Mech., vol. 85, pp. 1–46, 2012.

[47] Y. J. Chao and X. K. Zhu, “Constraint effects on plastic crack-tip fields for plane strain mode-I , II and III cracks in non-hardening materials,” no. 1976, pp. 187–207, 2000.

[48] ASTM E1820, “Standard Test Method for Measurement of Fracture Toughness” ASTM Int., no. August, pp. 1–58, 2019.

[49] BS ISO 12135:2021 Metallic materials — Unified method of test for the determination of quasistatic fracture toughness, 2021.

[50] J. A. Joyce; R. E. Link, “Effects of Constraint on Upper Shelf Fracture Toughness,” Fract. Mech., vol. 26, 1995.

[51] B. S. G. Larsson and A. J. Carlsson, Influence of Non-Singular Stress Terms and Specimen Geometry on Small-Scale Yielding at Crack Tips in Elastic-Plastic Materials, vol. 21, pp. 263–277, 1973.

[52] P. S. Leevers and J. C. Radon, “Inherent stress biaxiality in various fracture specimen geometries,” Int. J. Fract., vol. 19, no. 4, pp. 311–325, 1982.

[53] A. H. Sherry, C. . C. France, and M. R. Gpldthorpe, “Compendium of T-stress solutions for two and three Dimensional Cracked Geometries,” Fatigue Fract. Eng. Mater. Struct., vol. 18, no. 1, pp. 141–155, 1995.

[54] N. P. O’Dowd and C. F. Shih, “Family of crack-tip fields characterized by a triaxiality parameter-II. Fracture applications,” J. Mech. Phys. Solids, vol. 40, no. 5, pp. 939–963, 1992.

[55] J. Faleskog, “Effects of local constraint along three-dimensional crack fronts-a numerical and experimental investigation,” J. Mech. Phys. Solids, vol. 43, no. 3, 1995.

[56] Y. J. Chao, S. Yang, and M. A. Sutton, “On the fracture of solids characterized by one or two parameters: Theory and practice,” J. Mech. Phys. Solids, vol. 42, no. 4, pp. 629–647,

1994.

[57] S. Yang, F. G. Yuan, and X. Cai, “Higher Order Asymptotic Elastic-Plastic Crack-Tip Fields Under AntiPlane Shear,” no. 1, 1996.

[58] A. Neimitz and J. Galkiewicz, “Fracture toughness of structural components: Influence of constraint,” Int. J. Press. Vessel. Pip., vol. 83, no. 1, pp. 42–54, 2006.

[59] C. She and W. Guo, “The out-of-plane constraint of mixed-mode cracks in thin elastic plates,” Int. J. Solids Struct., vol. 44, no. 9, pp. 3021–3034, 2007.

[60] F. Yusof, “Three-dimensional assessments of crack tip constraint,” Theor. Appl. Fract. Mech., vol. 101, pp. 1–16, Jun. 2019.

[61] C. Fields, “Quantification of Constraint Loss in Three-Dimensional Non-hardening,” vol. 1, no. 7, pp. 57–63, 2019.

[62] G. Qian, V. F. Gonzalez-Albuixech, and M. Niffenegger, “In-plane and out-of-plane constraint effects under pressurized thermal shocks,” Int. J. Solids Struct., vol. 51, no. 6, pp. 1311–1321, 2014.

[63] O. A. Terfas and A. M. Kriama, “Out-of-plane constraint based fracture toughness,” Lect. Notes Eng. Comput. Sci., vol. 3 LNECS, pp. 2142–2145, 2013.

[64] W. Brocks, G. Künecke, H. D. Noack, and H. Veith, “On the transferability of fracture mechanics parameters from specimens to structures using fem,” Nucl. Eng. Des., vol. 112, no. C, pp. 1–14, 1989.

[65] G. Wanlin, “Elasto-plastic three-dimensional crack border field-III. Fracture parameters,” Eng. Fract. Mech., vol. 51, no. 1, pp. 51–71, 1995.

[66] W. Guo, “Elastoplastic three dimensional crack border field-I. Singular structure of the field,” Eng. Fract. Mech., vol. 46, no. 1, pp. 93–104, 1993.

[67] B. Zhang and W. Guo, “Three-dimensional stress state around quarter-elliptical corner cracks in elastic plates subjected to uniform tension loading,” Eng. Fract. Mech., vol. 74, no. 3, pp. 386–398, 2007.

[68] J. Zhao, W. Guo, and C. She, “The in-plane and out-of-plane stress constraint factors and K - T - Tz description of stress field near the border of a semi-elliptical surface crack,” Int. J. Fatigue, vol. 29, no. 3, pp. 435–443, 2007.

[69] C. H. Wang, G. X. Chen, and L. R. F. Rose, “A critical evaluation of superposition methods for cracks in grossly plastic gradient fields,” vol. 69, pp. 633–646, 2002.

[70] A. Neimitz, “Dugdale model modi ® cation due to the geometry induced plastic constraints,” vol. 67, pp. 251–261, 2000.

[71] B. I. N. Zhang and W. Guo, “T_z constraints of semi-elliptical surface cracks in elastic plates,” pp. 173–187, 2005.

[72] A. Pineau, A. A. Benzerga, and T. Pardoen, “Acta Materialia Failure of metals I : Brittle and ductile fracture,” vol. 107, pp. 424–483, 2016.

[73] A. Pineau, “Development of the local approach to fracture over the past 25 years: Theory and applications,” Int. J. Fract., vol. 138, no. 1–4, pp. 139–166, 2006.

[74] Marius Sævik and Ove B. Sunde, “Hydrogen Embrittlement of High-Strength Steels in Arctic Conditions,” J. Mater. Eng. Perform., 2013.

[75] Alan T. K. Liu, Chao Yang and Samuel Chih Ting, “Fracture and Fatigue of Welded Joints and Structures in Arctic Environments,” J. Offshore Mech. Arct. Eng., 1999.

[76] C. L. Walters, A. Alvaro, and J. Maljaars, “The effect of low temperatures on the fatigue crack growth of S460 structural steel,” Int. J. Fatigue, vol. 82, pp. 110–118, Jan. 2016.

[77] F. M. Beremin, A. Pineau, F. Mudry, J. C. Devaux, Y. D’Escatha, and P. Ledermann, “A local criterion for cleavage fracture of a nuclear pressure vessel steel,” Metall. Trans. A, vol. 14, no. 11, pp. 2277–2287, 1983.

[78] X. Gao, C. Ruggieri, and R. H. Dodds, “Calibration of Weibull stress parameters using fracture toughness data,” Int. J. Fract., vol. 92, no. 2, pp. 175–200, 1998.

[79] K. Wallin, “Fracture Toughness Transition Curve Shape for Ferritic Structural Steels,” Fract. Eng. Mater. Struct., no. August, pp. 83–88, 1991.

[80] I. Sattari-Far and K. Wallin, “Application of master curve methodology for structural integrity assessment of nuclear components,” SKI (Swedish Nucl. Power Insp. Rep., vol. 55, no. October, 2005.

[81] R. H. Dodds, T. L. Anderson, and M. T. Kirk, “A framework to correlate a / W ratio effects on elastic-plastic fracture toughness (J_c),” Int. J. Fract., vol. 48, no. 1, pp. 1–22, 1991.

[82] J. Billingham, J. Healy, and J. Spurrier, Current and Potential use of High Strength Steels in offshore Structures, London: Marine Technology Directorate Limited, 1995

[83] J. Billingham et al., Review of the performance of high strength steels used offshore, Health and Safety Executive, Cranfield University, Great Britain, 2003

[84] S. Chen, X. Qian, and A. Ahmed, "Cleavage fracture assessment for surface-cracked plates fabricated from high strength steels," Eng. Fract. Mech., vol. 161, pp. 1–20, 2016.

[85] X. Qian, S. Chen, and A. Ahmed, "Assessment of Cleavage Fracture in Specimens with a Curved Crack Front for High-Strength Steels in Offshore Applications," Procedia Struct. Integr., vol. 2, pp. 2046–2053, 2016.

[86] R. Willms, "High strength steel for steel constructions," Nord. steel Constr. Conf., pp. 597–604, 2009.

[87] M. Y. Demeri, Advanced high-strength steels : science, technology, and applications, ASTM International, 2013.

[88] F. Schroter, "Trends of using high strength steel for heavy steel structures." AG der Dillinger Huttenwerke, 2012.

[89] I. D. S. Bott, L. F. G. De Souza, J. C. G. Teixeira, and P. R. Rios, "High-strength steel development for pipelines: A Brazilian perspect," Metallurgical and Materials Transactions A, vol. 36 A, no. 2, pp. 443–454, 2005.

[90] H. Ban and G. Shi, "A review of research on high-strength steel structures," Proc. Inst. Civ. Eng. Struct. Build., vol. 171, no. 8, pp. 625–641, Aug. 2018.

[91] J. Kang, J. A. Gianetto, and W. R. Tyson, "Recent development in low-constraint fracture toughness testing for structural integrity assessment of pipelines," Front. Mech. Eng., vol. 13, no. 4, pp. 546–553, 2018.

[92] A. Pineau, "Modeling ductile to brittle fracture transition in steels - Micromechanical and physical challenges," Int. J. Fract., vol. 150, no. 1–2, pp. 129–156, 2008.

[93] Nina Fonstein, Advanced High Strength Sheet Steels Physical Metallurgy, Design, Processing, and Properties., 2015

[94] M. Mokhtarishirazabad and M. Mostafavi, "Some observations on failure of austenitic stainless steel: Effects of in- And out of plane constraint," in Procedia Structural Integrity,

2019, vol. 18, pp. 457–471.

[95] BSI, “BS 8571:2018 - Method of test for determination of fracture toughness in metallic materials using single edge notched tension (SENT) specimens,” *BSI*, pp. 1–24, 2018.

[96] Hancock J. W., Reuter W. G. and Parks D. M., Constraint and Toughness Parameterized by T, Constraint effects in Fracture,” pp. 21–40, 1993.

[97] Towers O. L. and Garwood S. J., “Influence of crack depth on resistance curves for three-point bend specimens in HY130,” *Fract. Mech.*, vol. 7, pp. 54–84, 1986.

[98] BS 7448-1, “Fracture mechanics toughness tests —Part 1: Method for determination of K_{IC}, critical CTOD and critical J values of metallic materials, no. 1, 1991.

[99] British Standard BS 7448-2, “Fracture mechanics toughness tests - Part 2: Method for determination of KIc, critical CTOD and critical J values of metallic materials, BSI, 1991.

[100] BS 7448-3, “Fracture mechanics toughness tests — Part 3: Method for determination of fracture toughness of metallic materials at rate of increase in stress intensity factor greater than 3.0 MPa $\sqrt{\text{ms}^{-1}}$ BSI, vol. 3, no. 1, 2005.

[101] BS 7448-4, “Fracture mechanics toughness tests — Part 4: Method for determination of fracture resistance curves and initiation values for stable crack extension in metallic materials, BSI, 1997.

[102] BS 5752 Methods for crack opening displacement (COD) testing.” 1979.

[103] A. R. Dowling and C. H. A. Townley, “The effect of defects on structural failure. A two-criteria approach,” Int. J. Press. Vessel. Pip., vol. 3, no. 2, pp. 77–107, 1975.

[104] U. Zerbst et al., Fitness-for-service fracture assessment of structures containing cracks: A workbook based on the European SINTAP/FITNET procedure, first edition, 2007

[105] S. Cravero and C. Ruggieri, “Structural integrity analysis of axially cracked pipelines using conventional and constraint-modified failure assessment diagrams,” *Int. J. Press. Vessel. Pip.*, vol. 83, no. 8, pp. 607–617, 2006.

[106] D. H. Moon, J. Y. Park, and M. H. Kim, “Effects of the crack tip constraint on the fracture assessment of an Al 5083-O weldment for low temperature applications,” *Materials (Basel).*, vol. 10, no. 7, 2017.

[107] Simulia, “Abaqus / CAE 6.14 User’s Manual,” pp. 1–1146, 2014.

[108] T. L. Sham, “The Determination of the Elastic T-Term using Higher Order Weight Functions,” *Int. J. Fract.*, vol. 30, pp. 301–315, 1986.

[109] S. Cicero, R. A. Ainsworth, and F. Gutiérrez-Solana, “Engineering approaches for the assessment of low constraint fracture conditions: A critical review,” *Eng. Fract. Mech.*, vol. 77, no. 8, pp. 1360–1374, May 2010.

[110] Y. K. Kim, B. T. Oh, and J. H. Kim, “Effects of crack tip constraint on the fracture toughness assessment of 9% ni steel for cryogenic application in liquefied natural gas storage tanks,” *Materials (Basel).*, vol. 13, no. 22, pp. 1–11, 2020.

[111] S. Cravero and C. Ruggieri, “Estimation procedure of J-resistance curves for SE(T) fracture specimens using unloading compliance,” *Eng. Fract. Mech.*, vol. 74, no. 17, pp. 2735–2757, 2007.

[112] J. Xu, Z. L. Zhang, E. Østby, B. Nyhus, and D. B. Sun, “Constraint effect on the ductile crack growth resistance of circumferentially cracked pipes,” *Eng. Fract. Mech.*, vol. 77, no. 4, pp. 671–684, 2010.

[113] J. Xu, Z. L. Zhang, E. Østby, B. Nyhus, and D. B. Sun, “Effects of crack depth and specimen size on ductile crack growth of SENT and SENB specimens for fracture mechanics evaluation of pipeline steels,” *Int. J. Press. Vessel. Pip.*, vol. 86, no. 12, pp. 787–797, 2009.

[114] B. Nyhus, M. L. Polanco, and O. Orjasaether, “SENT Specimens an alternative to SENB Specimens,” 2003.

[115] J. Xu, X. Zhuo, P. Li, Y. Fan, and Z. Sun, “Constraint effect on the ductile fracture behavior of high-strength pipeline steels,” *Mater. Sci. Forum*, vol. 850, pp. 899–904, 2016.

[116] J. Xu and Y. Fan, “Effects of temperature and crack tip constraint on cleavage fracture toughness in the weld thermal simulated X80 pipeline steels,” *Adv. Mater. Res.*, vol. 197–198, pp. 1595–1598, 2011.

[117] C. Ruggieri, “Low constraint fracture toughness testing using SE(T) and SE(B) specimens,” *Int. J. Press. Vessel. Pip.*, vol. 156, pp. 23–39, 2017.

[118] D. F. B. Sarzosa and C. Ruggieri, “A numerical investigation of constraint effects in circumferentially cracked pipes and fracture specimens including ductile tearing,” *Int. J. Press. Vessel. Pip.*, vol. 120–121, no. 1, pp. 1–18, 2014.

[119] “TWI software 2020, CrackWISE® version 6.0 (CW6), R44569. ‘https://www.twisoftware.com/software/integrity-management-software/crackwise/.’” .

[120] “‘BS EN ISO 6892-1-2019, Metallic materials- tensile testing: Part 1 Method of test at room temperature.’, 2019.” .

[121] I. Jones *et al.*, “A Good Practices Guide for Digital Image Correlation,” *Int. Digit. Image Correl. Soc.*, p. 94, 2018.

[122] “GOM Correlate 2019: GOM Software, Hotfix 6, Rev. 125216, Build 2020-02-27.” 2020.

[123] “BS EN ISO 148-1-2016, Metallic materials — Charpy pendulum impact test, 2016.

[124] R. A. Ainsworth, “A constraint-based failure assessment diagram for fracture assessment,” *Int. J. Press. Vessel. Pip.*, vol. 64, no. 3, pp. 277–285, 1995.

[125] R. A. Ainsworth and N. O’Dowd, “Constraint in the failure assessment diagram approach for fracture assessment,” *J. Press. Vessel Technol. Trans. ASME*, vol. 117, no. 3, pp. 260–267, 1995.

[126] M. M. Hossain, “‘Simplied Design and Integrity Assessment of Pressure Components and Structures’, PhD thesis , Memorial University, 2009.,” pp. 1–23, 2016.

[127] A. H. Sherry, D. G. Hooton, D. W. Beardsmore, and D. P. G. Lidbury, “Material constraint parameters for the assessment of shallow defects in structural components. Part II: Constraint-based assessment of shallow defects,” *Eng. Fract. Mech.*, vol. 72, no. 15, pp. 2396–2415, 2005.

[128] W. Y. Peng, H. J. Jin, and S. J. Wu, “Structural Integrity Analysis of Cracked Pressure Vessel Welds Using Conventional and Constraint-modified Failure Assessment Diagrams,” *Procedia Eng.*, vol. 130, pp. 835–844, 2015.

[129] R. A. Ainsworth, “Failure assessment diagrams for use in R6 assessments for austenitic components,” *Int. J. Press. Vessel. Pip.*, vol. 65, no. 3, pp. 303–309, 1996.

[130] O. Bouledroua, M. Hadj Meliani, and G. Pluvinage, “Assessment of Pipe Defects Using a Constraint-Modified Failure Assessment Diagram,” *J. Fail. Anal. Prev.*, vol. 17, no. 1, pp.

144–153, 2017.

[131] I. Hadley and A. Horn, “Treatment of constraint in BS 7910:2013, ISO 27306 and DNVGL-RP-F108,” *Int. J. Press. Vessel. Pip.*, vol. 169, no. November 2018, pp. 77–93, 2019.

[132] C. Rodriguez, F. J. Belzunce, T. E. Garcia, and I. Peñuelas, “Constraint dependence of the fracture toughness of reduced activation ferritic-martensitic Eurofer steel plates,” *Eng. Fract. Mech.*, vol. 103, pp. 60–68, 2013.

[133] I. Hadley and S. A. Karger, Effect of Crack Tip Constraint on Fracture Toughness of a533B Steel and Validation of the SINTAP Constraint Procedure, TWI Rep. No SINTAP/TWI/012, no. March, 1999.

[134] I. MacLennan and J. W. Hancock, “Constraint-based failure assessment diagrams,” *Int. J. Press. Vessel. Pip.*, vol. 64, no. 3, pp. 287–298, 1995.

[135] A. H. Sherry, M. A. Wilkes, D. W. Beardsmore, and D. P. G. Lidbury, “Material constraint parameters for the assessment of shallow defects in structural components - Part I: Parameter solutions,” *Eng. Fract. Mech.*, vol. 72, no. 15, pp. 2373–2395, 2005.

[136] Abaqus, “Abaqus 6.11." Dassault Systemes Simulia Corporation,” 2011.

[137] N. Nourpanah and F. Taheri, “A numerical study on the crack tip constraint of pipelines subject to extreme plastic bending,” *Eng. Fract. Mech.*, vol. 78, no. 6, pp. 1201–1217, 2011.

[138] C. K. Seal and A. H. Sherry, “Predicting the effect of constraint on cleavage and ductile fracture toughness using area contour toughness scaling,” *Eng. Fract. Mech.*, vol. 186, pp. 347–367, 2017.

[139] Rob S. Kulka, “Influence of Material and Constraint Variation on the Fracture Toughness Behaviour of Steels,” 2012.

[140] M. Nevalainen and R. H. Dodds, Numerical Investigation of 3-D Constraint Effects on Brittle Fracture in SE(B) and C(T) Specimens, Civil Engineering Studies, Structural Research Series No. 598, 1995.

[141] B. A. Dahl et al., Effect of low temperature tensile properties on crack driving force for Arctic applications, Theoretical and Applied Fracture Mechanics, vol. 93, pp. 88–96, Feb.

2018.

[142] G. L. G. Gonzáles et al., A J-integral approach using digital image correlation for evaluating stress intensity factors in fatigue cracks with closure effects, Theoretical and Applied Fracture Mechanics, vol. 90, pp. 14–21, 2017.

[143] J. Górszczyk, K. Malicki, and T. Zych, "Application of digital image correlation (DIC) method for road material testing," *Materials (Basel).*, vol. 12, no. 15, 2019.

[144] Philip Reu, Introduction to Digital Image Correlation: Best Practices and Applications, 2012.

[145] S. M. Barhli, M. Mostafavi, A. F. Cinar, D. Hollis, and T. J. Marrow, "J-Integral Calculation by Finite Element Processing of Measured Full-Field Surface Displacements," *Exp. Mech.*, vol. 57, no. 6, pp. 997–1009, 2017.

[146] S. M. Barhli, "Advanced quantitative analysis of crack fields, observed by 2D and 3D image correlation, volume correlation and diffraction mapping," vol. c, p. 229, 2017.

[147] Mohamed A. El-Reedy, Offshore structures : design, construction and maintenance. Gulf Professional Publication, 2012.

[148] C. Xu et al., 3D visualized characterization of fracture behavior of structural metals using synchrotron radiation computed microtomography, Quantum Beam Science, vol. 3, no. 1, 2019.

[149] R. K. Sun, W, Brown, S B, Leach, An overview of industrial X-ray computed tomography, Engineering Measurements, January, 2012.

[150] J. Marrow et al., 3D Studies of Damage by Combined X-ray Tomography and Digital Volume Correlation, Procedia Material Science, vol. 3, pp. 1554–1559, 2014.

[151] A. Al Mahbub and A. Haque, "X-ray computed tomography imaging of the microstructure of sand particles subjected to high pressure one-dimensional compression," *Materials (Basel).*, vol. 9, no. 11, pp. 7–15, 2016.

[152] H. Toda et al., "In-situ observation of ductile fracture using X-ray tomography technique," vol. 59, no. 5, pp. 1995–2008, 2011.

[153] J. Hendl et al., "In situ ct tensile testing of an additively manufactured and heat-treated metastable ß-titanium alloy (Ti-5al-5mo-5v-3cr)," Appl. Sci., vol. 11, no. 21, 2021.

[154] M. R. Bache, P. I. Nicholson, and E. Williams, “In-situ assessment of fracture in SiCF/SiC under computed x-ray tomography,” Proc. ASME Turbo Expo, vol. 6, pp. 1–10, 2018.

This page intentionally left blank

APPENDICES

Appendix A CHARPY V-NOTCH TEST RESULTS

Table A.1: Charpy V-notch test results

Specimen No.	Temperature [℃]	Absorbed energy [J]	Lateral expansion [mm]	Crystallinity [%]
M04-01	21	226	2.39	0.00
M04-02	-90	200	2.22	0.00
M04-03	-150	9	0.12	96.00
M04-04	-120	10	0.11	93.00
M04-05	-100	232	2.15	0.00
M04-06	-110	153	1.86	30.00
M04-07	0	298	2.55	0.00
M04-08	-40	306	2.50	0.00
M04-09	-60	302	2.43	0.00
M04-10	-100	126	1.55	33.00

Appendix B : SENT AND SENB FRACTURE TEST RESULTS

Table B.1: Actual dimensions of SENT specimens with nominal crack depth of a_0/W = 0.1

Specimen No.	B [mm]	W [mm]	a_0 [mm]	a_0/W
Fracture tests at cold temperature, -120℃				
M01-01	15	30	3.15	0.11
M01-02	15	30	3.16	0.11
M01-03	15	30	3.24	0.11
Fracture tests at room temperature, 23℃				
M01-04	15	30	3.10	0.10
M01-05	15	30	3.17	0.11
M01-06	15	30	3.24	0.11

Table B.2: Actual dimensions of SENT specimens with nominal crack depth of a_0/W = 0.3

Specimen No.	B [mm]	W [mm]	a_0 [mm]	a_0/W
Fracture tests at cold temperature, -120℃				
M01-07	15	30	9.21	0.31
M01-08	15	30	8.70	0.29
M01-09	15	30	9.19	0.31
Fracture tests at room temperature, 23℃				
M01-10	15	30	9.32	0.31
M01-11	15	30	9.25	0.31
M01-12	15	30	9.29	0.31

Table B.3: Actual dimensions of SENT specimens with nominal crack depth of a_0/W = 0.5

Specimen No.	B [mm]	W [mm]	a_0 [mm]	a_0/W
Fracture tests at cold temperature, -120℃				
M01-13	15	30	15.14	0.50
M01-14	15	30	15.02	0.50
M01-15	15	30	15.26	0.51
Fracture tests at cold temperature, 23℃				
M01-16	15	30	15.10	0.50
M01-17	15	30	15.36	0.51
M01-18	15	30	15.50	0.52

Table B.4: Actual dimensions of SENB specimens with nominal crack depth of a_0/W = 0.1

Specimen No.	B [mm]	W [mm]	a_0 [mm]	a_0/W
Fracture tests at cold temperature, -120℃				
M02-01	15	30	3.18	0.11
M02-02	15	30	3.02	0.10
M02-03	15	30	3.31	0.11
Fracture tests at room temperature, 23℃				
M02-04	15	30	3.38	0.11
M02-05	15	30	3.38	0.11
M02-06	15	30	3.50	0.11

Table B.5: Actual dimensions of SENB specimens with nominal crack depth of a_0/W = 0.3

Specimen No.	B [mm]	W [mm]	a_0 [mm]	a_0/W
Fracture tests at cold temperature, -120℃				
M02-07	15	30	9.26	0.31
M02-08	15	30	9.31	0.31
M02-09	15	30	9.15	0.31
Fracture tests at room temperature, 23℃				
M02-10	15	30	9.55	0.32
M02-11	15	30	9.23	0.31
M02-12	15	30	9.47	0.32

Table B.6: Actual dimensions of SENB specimens with nominal crack depth of a_0/W = 0.5

Specimen No.	B [mm]	W [mm]	a_0 [mm]	a_0/W
Fracture tests at cold temperature, -120℃				
M02-13	15	30	15.24	0.51
M02-14	15	30	15.37	0.51
M02-15	15	30	15.91	0.53
Fracture tests at room temperature, 23℃				
M02-16	15	30	15.25	0.51
M02-17	15	30	15.56	0.52
M02-18	15	30	15.39	0.51

The fracture mechanics tests result for the SENT and SENB specimens at room and cold temperature are shown in Table B.7 and Table B.8 respectively, and include the single point values of J_0 at the first attainment of a maximum/fracture load with the appropriate material toughness, K_{mat}, computed using equation (B.1).

$$K_{mat} = \sqrt{\frac{J_0 E}{(1-\nu^2)}} \qquad (B.1)$$

Table B.7: Fracture tests results for SENT specimens

Specimen No.	**a/W**	**J_0 [kJ/m^2]**	**CTOD [mm]**	**Tear length [mm]**	**Max/Fracture load [kN]**	**K_{mat} [MPa.m$^{0.5}$]**
Fracture Tests at cold temperature, -120℃						
M01-01	0.11	329.4	0.53	0.12	273.4	277.7
M01-02	0.11	746.9	1.15	0.39	287.6	418.1
M01-03	0.11	540.6	0.84	0.23	279.0	355.7
M01-07	0.31	958.5	0.89	0.22	215.9	473.7
M01-08	0.29	278.3	0.29	0.02	196.9	255.2
M01-09	0.31	225.3	0.23	0.01	184.3	229.6
M01-13	0.51	46.6	0.05	0.00	68.2	104.4
M01-14	0.50	181.9	0.19	0.02	102.3	206.4
M01-15	0.51	426.5	0.42	0.08	125.6	315.6
Fracture Tests at room temperature, 23℃						
M01-04	0.10	1399.9	2.74	1.69	242.9	564.3
M01-05	0.11	1413.7	2.67	2.54	243.3	567.1
M01-06	0.11	1344.9	2.53	1.50	242.4	553.1
M01-10	0.31	2270.3	2.62	1.78	184.2	718.6
M01-11	0.31	2438.2	2.85	1.59	185.8	744.7
M01-12	0.31	2279.9	2.58	1.49	185.9	720.2
M01-16	0.50	2148.4	2.26	4.83	139.4	699.1
M01-17	0.51	2152.4	2.39	1.37	135.7	699.7
M01-18	0.52	1865.6	2.05	1.21	133.6	651.4

Table B.8: Fracture tests results for SENB specimens

Specimen No.	a/W	J_0 [kJ/m^2]	CTOD [mm]	Tear length [mm]	Max/Fracture load [kN]	K_{mat} [MPa.m$^{0.5}$]
Fracture Tests at cold temperature, -120℃						
M02-01	0.11	674.9	0.84	0.34	82.9	397.5
M02-02	0.11	380.5	0.52	0.18	79.4	298.4
M02-03	0.11	783.0	1.19	0.61	83.9	428.1
M02-07	0.31	32.7	0.03	0.004	32.2	87.6
M02-08	0.29	99.6	0.11	0.00	42.1	152.7
M02-09	0.31	247.8	0.24	0.00	46.4	240.8
M02-13	0.51	48.5	0.04	0.00	20.1	106.5
M02-14	0.50	85.0	0.09	0.00	22.4	142.7
M02-15	0.51	141.6	0.13	0.00	25.4	182.0
Fracture Tests at room temperature, 23℃						
M02-04	0.10	1496.6	2.97	2.59	71.8	583.5
M02-05	0.11	1806.5	3.02	2.54	72.2	641.0
M02-06	0.11	1885.9	3.17	2.56	71.4	655.0
M02-10	0.31	1494.5	2.04	1.97	43.1	583.1
M02-11	0.31	1641.8	2.21	2.19	45.2	611.1
M02-12	0.31	1675.6	2.29	2.14	44.4	617.4
M02-16	0.50	1320.4	1.61	1.66	23.6	548.1
M02-17	0.51	1293.1	1.66	1.78	22.6	542.4
M02-18	0.52	1324.9	1.78	1.55	23.4	549.0

Appendix C : TENSILE TEST REPORTS

FLAT TENSILE 33650 M03-04

Test date	24/01/2023
Technician	Craig Moss
Test machine	INSTRON 8500 B488
Control mode	DISPLACEMENT
Test standard	BS EN ISO 6892-3:2015 A22

Client	
Project leader	Paul Sukpe
Investigator's signature	
Compiled by	Craig Moss
Signed	

SPECIMEN DETAILS

Initial Width	20.00	mm
Initial Thickness	3.02	mm
Initial XSA	60.333	mm²
Final XSA	19.293	mm²
Estimated Youngs modulus	217020	N/mm²
Test temperature	-120.0	°C
Extensometer gauge length	50.00	mm
Initial Gauge length	79.80	mm
Final gauge length	101.18	mm
Initial Stressing rate	17.301	N/mm²/s
Initial Straining rate	0.000085	Strain/s
Initial Displacement rate	0.02275	mm/s

RESULTS

Strain %	Extension mm	Load kN	Stress, Rp N/mm²
0.1	0.186	35.64	590.7
0.2	0.244	37.80	626.5
0.5	0.404	39.59	656.1
1.0	0.654	40.37	669.2
2.0	1.158	41.31	684.6
UTS		45.24	749.8

Reduction in area	68.02 %
Elongation	26.79 %

Note: Extensometer out of travel

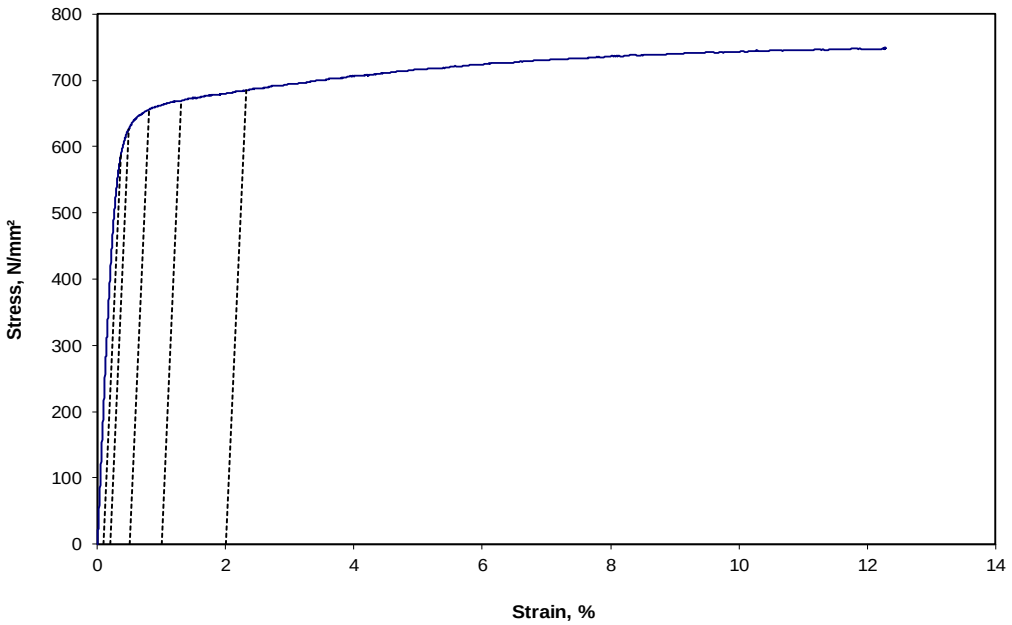

LVGENPLOT V 1.67.4 08-Dec-2022

25 January 2023 SI/FRA/F/24 REV0.0

ROUND TENSILE 33650 M03-01

Test date	28/07/2022
Technician	Craig Moss
Test machine	INSTRON 8500 B488
Control mode	DISPLACEMENT
Test standard	BS EN ISO 6892-1:2019 A22

Client	PhD	
Project leader	Yin Jin Janin	(Paul Sukpe)
Investigator's signature		
Compiled by	Craig Moss	
Signed		

SPECIMEN DETAILS

Initial diameter	9.95	mm
Initial XSA	77.704	mm²
Final XSA	17.423	mm²
Estimated Youngs modulus	216269	N/mm²
Test temperature	23.0	°C
Extensometer gauge length	50.00	mm
Initial Gauge length	49.98	mm
Final gauge length	63.61	mm
Initial Stressing rate	9.687	N/mm²/s
Initial Straining rate	0.000055	Strain/s
Initial Displacement rate	0.015134	mm/s

RESULTS

Strain %	Extension mm	Load kN	Stress, Rp N/mm²
0.1	0.146	31.51	405.5
0.2	0.206	34.62	445.5
0.5	0.365	37.54	483.1
1.0	0.619	39.18	504.2
2.0	1.126	41.00	527.6
UTS		44.99	579.0

Reduction in area	77.58	%
Elongation	27.27	%

Note: Extensometer removed before max load
Note: Extensometer out of travel

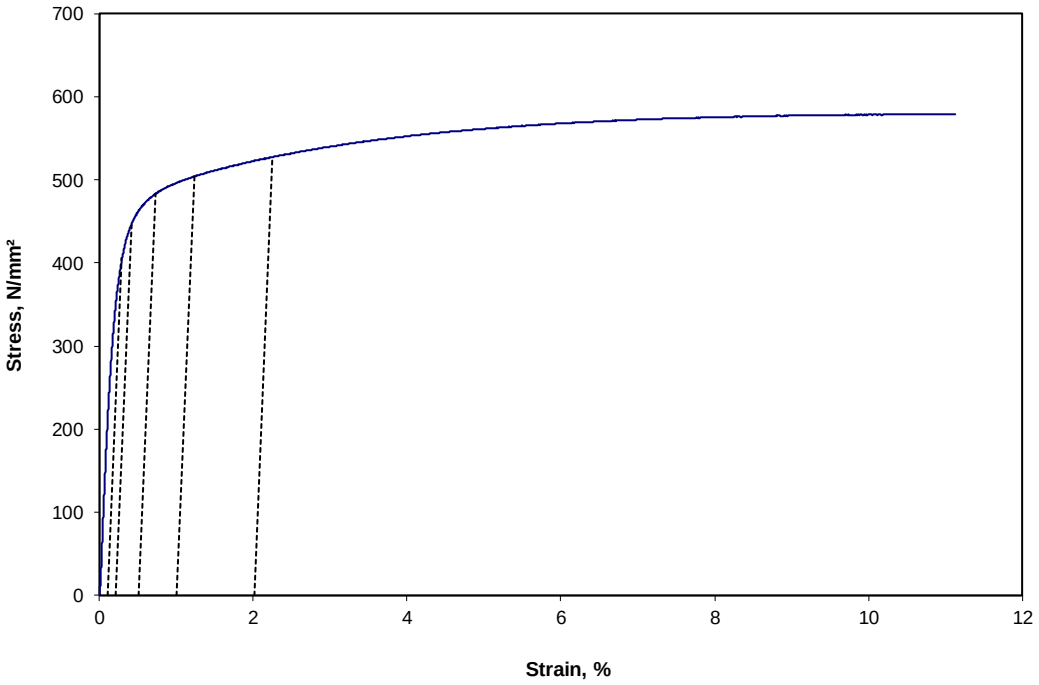

LVGENPLOT V 1.65.4 28-Jul-2022

28 July 2022 SI/FRA/F/24 REV0.0

ROUND TENSILE 33650 M03-02

Test date	28/07/2022
Technician	Craig Moss
Test machine	INSTRON 8500 B488
Control mode	DISPLACEMENT
Test standard	BS EN ISO 6892-3:2015 A22

Client	PhD	
Project leader	Yin Jin Janin	(Paul Sukpe)
Investigator's signature		
Compiled by	Craig Moss	
Signed		

SPECIMEN DETAILS

Initial diameter	9.93	mm
Initial XSA	77.392	mm²
Final XSA	20.030	mm²
Estimated Youngs modulus	224491	N/mm²
Test temperature	-120.0	°C
Extensometer gauge length	50.00	mm
Initial Gauge length	50.02	mm
Final gauge length	66.44	mm
Initial Stressing rate	10.675	N/mm²/s
Initial Straining rate	0.000052	Strain/s
Initial Displacement rate	0.015134	mm/s

RESULTS

Strain %	Extension mm	Load kN	Stress, Rp N/mm²
0.1	0.165	42.90	554.3
0.2	0.224	45.90	593.1
0.5	0.381	48.46	626.1
1.0	0.635	49.66	641.6
2.0	1.141	51.15	661.0
UTS		57.75	746.2

Reduction in area	74.12	%
Elongation	32.83	%

Note: Extensometer removed before max load
Note: Extensometer out of travel

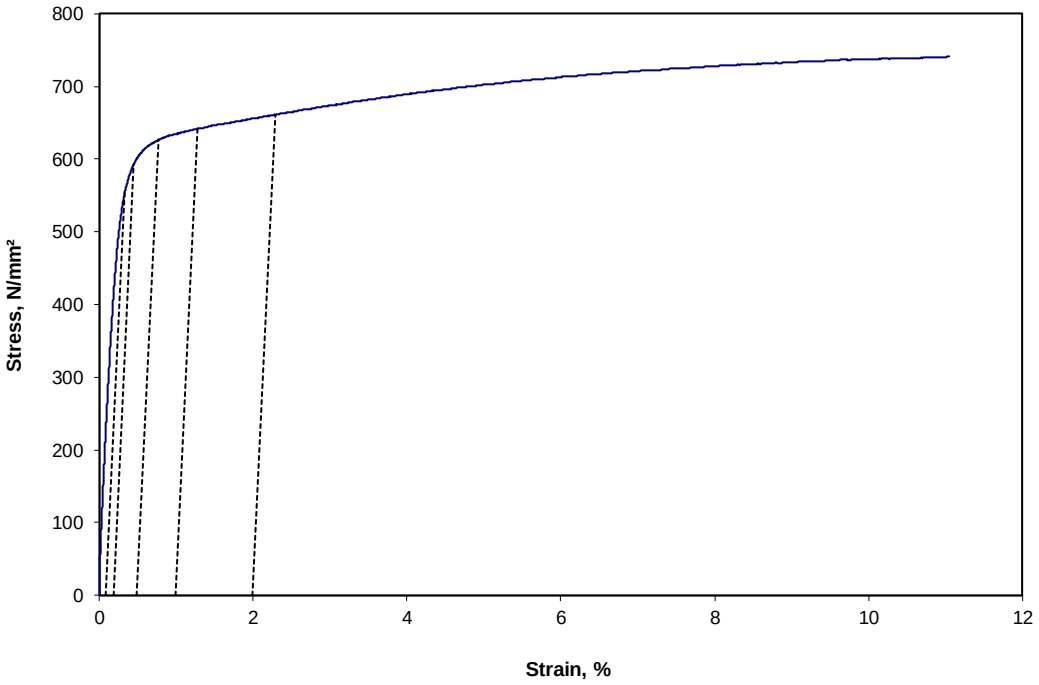

LVGENPLOT V 1.65.4 28-Jul-2022

Appendix D : SENT TEST REPORTS

SENT FRACTURE TEST 33650 M01-01

Client	PhD	
Project leader	Rob Kulka	Signed:

Data source

Data logging program	LVGENLOG V 1.55.10 02-Aug-2022
Program used to calculate CTOD/J	LVGENPLOT V 1.66.0 04-Oct-2022
Calculation date of CTOD/J	17 Oct 2022

Specimen details

Material	API 5L X65	
Specimen type	Subsize, Pin-loaded SENT	
Crack plane orientation	Y-X	
Type of notch tip	Fatigue	
Notch tip location	Parent material	
Specimen width	30.120	mm
Specimen thickness	14.980	mm
Initial crack length	3.148	mm
Side-grooved?	NO	
Original PM 1 thickness	23.80	mm

Test details

Test standard(s)	BS 8571:2018	
Test date	29/09/2022	
Test time	13:49:00	
Test technician	Jack Bradford	Signed:
Test machine	INSTRON 8500 B107	
Test environment	Environmental chamber	
Test temperature	-120.0	°C
Soak time @ test temperature	15.0	minutes
Knife edge heights	2.000, 12.000	mm
Knife edge attachment spacing	12.00	mm
Initial K-rate	0.413	$MPa.m^{0.5}/s$
Crosshead displacement rate	0.998	mm/min
Gauge length	0.0	mm

Material properties

Yield strength for pre-cracking	445.5	MPa	Measured at RT
Tensile strength for pre-cracking	579.0	MPa	Measured at RT
Yield strength for testing	593.0	MPa	Measured at test temperature
Tensile strength for testing	746.0	MPa	Measured at test temperature
Poisson's ratio	0.3		Assumed
Young's modulus	213	GPa	Measured

Fatigue details

Stress ratio, R	0.100	
Final force, F_f	16.00	kN
Final K	21.2	$MPa.m^{0.5}$
Fatigue temperature	21.0	°C
Loading span, S	120.0	mm

Analysis details

CMOD type	DOUBLE CLIP
J calculated from	CMOD
CTOD calculated from	DOUBLE CLIP

Compiled by: Jack Bradford **Signed:**

Result relates only to specimen tested.

Tensile properties are not determined as part of this test and are not part of the accredited result.

Result falls within the bounds of TWI's flexible scope of accreditation.

SENT FRACTURE TEST 33650 M01-01

Qualification checks

		Value	Allowed
ISO 12135:2016 Fig 8			
Knife edge attachment spacing	**Pass**	14.76	15.06
ISO 12135:2016 5.4.2.4.1			
Stress ratio <= 0.1	**Pass**	0.1	0.1
ISO 12135:2016 5.4.2.4.3			
The final fatigue precracking force <= F_f	**Pass**	16	19.34671
ISO 12135:2016 5.8.2			
Minimum fatigue length (c)	**Fail**	1.2	1.3
Fatigue crack within envelope (d)	**Pass**		
BS 8571:2018 5.2			
Minimum gauge length	**Fail**	0	120.014
BS 8571:2018 7.4.3			
W/B limit	**Fail**	2	0.5 - 1.0
BS 8571:2018 6.3			
Initial K-rate between 0.2 MPa.m$^{0.5}$s^{-1} and 3.0 MPa.m$^{0.5}$	**Pass**	0.413294	0.2 - 3.0
BS 8571:2018 9.1			
a_0/W Limit (b)	**Fail**	0.104519	0.3 - 0.5
Crack shape (c)	**Pass**	0.44	0.629625
Δa differences within limit (d)	**Pass**	0.44	0.653875
BS 8571:2018 9.2			
No out of plane tearing	**Pass**		

SENT FRACTURE TEST 33650 M01-01

Test date	29/09/2022	Client	PhD
Technician	Jack Bradford	Project leader	Rob Kulka
Test machine	INSTRON 8500 B107	Investigator's signature	
Control mode	Displacement	Compiled by	Jack Bradford

SPECIMEN DETAILS

Force, F	273.43	kN
Width, W	30.120	mm
Thickness, B	14.980	mm
Crack length, a_0	3.148	mm
Yield strength	593.0	MPa
Young's modulus	213	GPa
Poisson's ratio	0.300	
Test temperature	-120.0	°C

RESULTS

δ	0.529	mm
Elastic K @ calculation point	71.7	MPa.m$^{0.5}$
F_{max}/F_Q	2.07	
K_Q	34.68	MPa.m$^{0.5}$
Total area under F vs CMOD	144.98	kNmm
J_0	329.36	kJ/m²
Plastic area under F vs CMOD	138.54	kNmm
Type of result	δ/J_c	
Test standard(s)	BS 8571:2018	
Result qualified to standard(s)	NO	

LOWER CLIP GAUGE VALUES

Knife edge height	2.00	mm
Vg	0.607	mm
Vp	0.556	mm

UPPER CLIP GAUGE VALUES

Knife edge height	12.00	mm
Vg	0.726	mm
Vp	0.656	mm

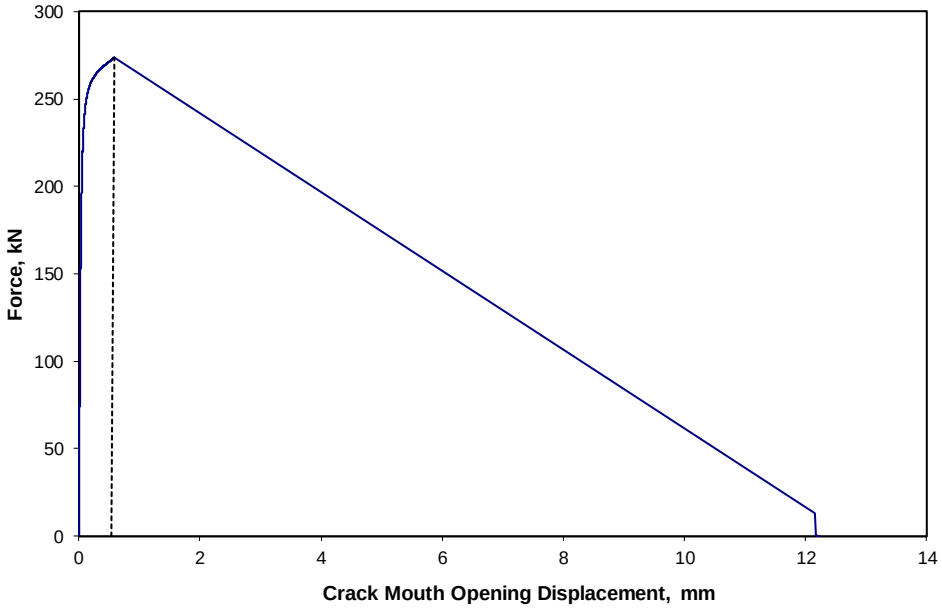

SENT FRACTURE TEST 33650 M01-01

Specimen width, W	30.120	mm
Specimen thickness, B	14.980	mm
Machined notch depth, M	1.580	mm
Machined notch width, h	0.350	mm
Surface crack length, a_{S1}	2.680	mm
Surface crack length, a_{S2}	2.930	mm
a_{max}	3.400	mm
a_{min}	2.780	mm

Diagram of fracture face

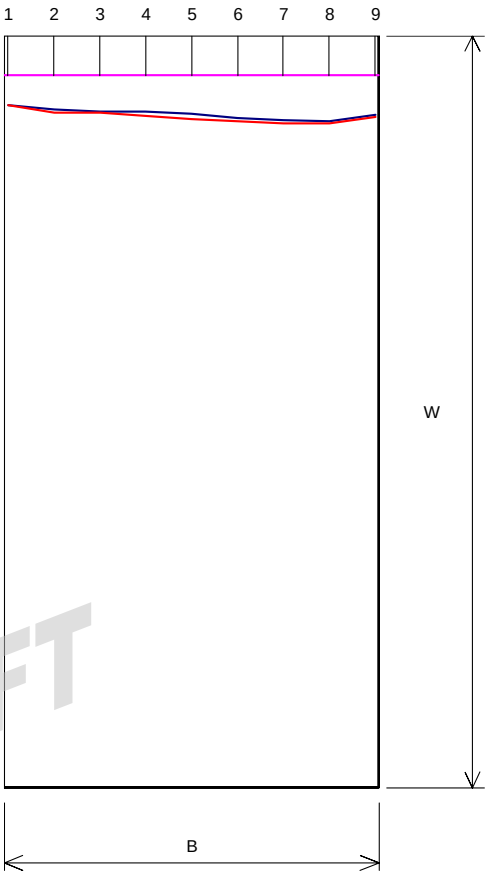

Comments

Measurement Line	Fatigue crack length a_0, mm	Slow stable crack extension + fatigue crack a_p, mm	Slow stable crack extension including stretch zone, Δ_a, mm
1	2.780	2.780	0.000
2	2.960	3.090	0.130
3	3.030	3.080	0.050
4	3.020	3.190	0.170
5	3.130	3.340	0.210
6	3.280	3.420	0.140
7	3.390	3.520	0.130
8	3.400	3.510	0.110
9	3.170	3.230	0.060
Weighted Average	**3.148**	**3.269**	**0.121**

Measured by: Jack Bradford **Signed:**

SENT FRACTURE TEST 33650 M01-04

Client	PhD	
Project leader	Rob Kulka	Signed:

Data source

Data logging program	LVGENLOG V 1.55.10 02-Aug-2022
Program used to calculate CTOD/J	LVGENPLOT V 1.66.0 04-Oct-2022
Calculation date of CTOD/J	17 Oct 2022

Specimen details

Material	API 5L X65	
Specimen type	Subsize, Pin-loaded SENT	
Crack plane orientation	Y-X	
Type of notch tip	Fatigue	
Notch tip location	Parent material	
Specimen width	30.240	mm
Specimen thickness	14.990	mm
Initial crack length	3.104	mm
Side-grooved?	NO	
Original PM 1 thickness	23.80	mm

Test details

Test standard(s)	BS 8571:2018	
Test date	28/09/2022	
Test time	10:15:00	
Test technician	Jack Bradford	Signed:
Test machine	INSTRON 8500 B107	
Test environment	Air	
Test temperature	22.0	°C
Soak time @ test temperature	0.0	minutes
Knife edge heights	2.000, 12.000	mm
Knife edge attachment spacing	12.00	mm
Initial K-rate	0.386	MPa.m$^{0.5}$/s
Crosshead displacement rate	1.00	mm/min
Gauge length	0.0	mm

Material properties

Yield strength for pre-cracking	445.5	MPa	Measured at RT
Tensile strength for pre-cracking	579.0	MPa	Measured at RT
Yield strength for testing	445.5	MPa	Measured at test temperature
Tensile strength for testing	579.0	MPa	Measured at test temperature
Poisson's ratio	0.3		Assumed
Young's modulus	207	GPa	Measured

Fatigue details

Stress ratio, R	0.100	
Final force, F_f	16.00	kN
Final K	20.9	$MPa.m^{0.5}$
Fatigue temperature	21.0	°C
Loading span, S	120.0	mm

Analysis details

CMOD type	DOUBLE CLIP
J calculated from	CMOD
CTOD calculated from	DOUBLE CLIP

Compiled by: Jack Bradford **Signed:**

Result relates only to specimen tested.

SENT FRACTURE TEST 33650 M01-04

Qualification checks		Value	Allowed
ISO 12135:2016 Fig 8			
Knife edge attachment spacing	**Pass**	14.76	15.12
ISO 12135:2016 5.4.2.4.1			
Stress ratio <= 0.1	**Pass**	0.1	0.1
ISO 12135:2016 5.4.2.4.3			
The final fatigue precracking force <= F_f	**Pass**	16	25.39543
ISO 12135:2016 5.8.2			
Minimum fatigue length (c)	**Fail**	1.28	1.3
Fatigue crack within envelope (d)	**Fail**		
BS 8571:2018 5.2			
Minimum gauge length	**Fail**	0	120.292945
BS 8571:2018 7.4.3			
W/B limit	**Fail**	2	0.5 - 1.0
BS 8571:2018 6.3			
Initial K-rate between 0.2 MPa.$m^{0.5}s^{-1}$ and 3.0 MPa.$m^{0.5}s^{-1}$	**Pass**	0.38553	0.2 - 3.0
BS 8571:2018 9.1			
a_0/W Limit (b)	**Fail**	0.102637	0.3 - 0.5
Crack shape (c)	**Pass**	0.39	0.62075
Δa differences within limit (d)	**Fail**	1.85	0.959875
BS 8571:2018 9.2			
No out of plane tearing	**Pass**		

SENT FRACTURE TEST 33650 M01-04

Test date	28/09/2022	Client	PhD
Technician	Jack Bradford	Project leader	Rob Kulka
Test machine	INSTRON 8500 B107	Investigator's signature	
Control mode	Displacement	Compiled by	Jack Bradford

SPECIMEN DETAILS

Force, F	242.97	kN
Width, W	30.240	mm
Thickness, B	14.990	mm
Crack length, a_0	3.104	mm
Yield strength	445.5	MPa
Young's modulus	207	GPa
Poisson's ratio	0.300	
Test temperature	22.0	°C

RESULTS

δ	2.738	mm
Elastic K @ calculation point	62.8	MPa.m$^{0.5}$
F_{max}/F_Q	2.37	
K_Q	26.50	MPa.m$^{0.5}$
Total area under F vs CMOD	641.13	kNmm
J_0	1399.96	kJ/m²
Plastic area under F vs CMOD	632.53	kNmm
Type of result	δ/J_m	
Test standard(s)	BS 8571:2018	
Result qualified to standard(s)	NO	

LOWER CLIP GAUGE VALUES

Knife edge height	2.00	mm
Vg	2.827	mm
Vp	2.758	mm

UPPER CLIP GAUGE VALUES

Knife edge height	12.00	mm
Vg	2.903	mm
Vp	2.848	mm

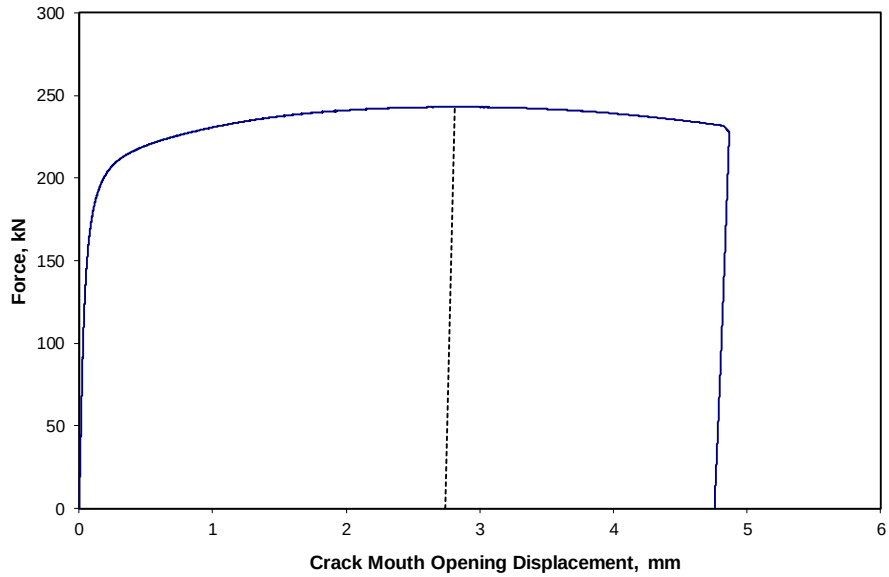

SENT FRACTURE TEST 33650 M01-04

Specimen width, W	30.240	mm
Specimen thickness, B	14.990	mm
Machined notch depth, M	1.630	mm
Machined notch width, h	0.340	mm
Surface crack length, a_{S1}	2.930	mm
Surface crack length, a_{S2}	2.850	mm
a_{max}	3.320	mm
a_{min}	2.910	mm

Diagram of fracture face

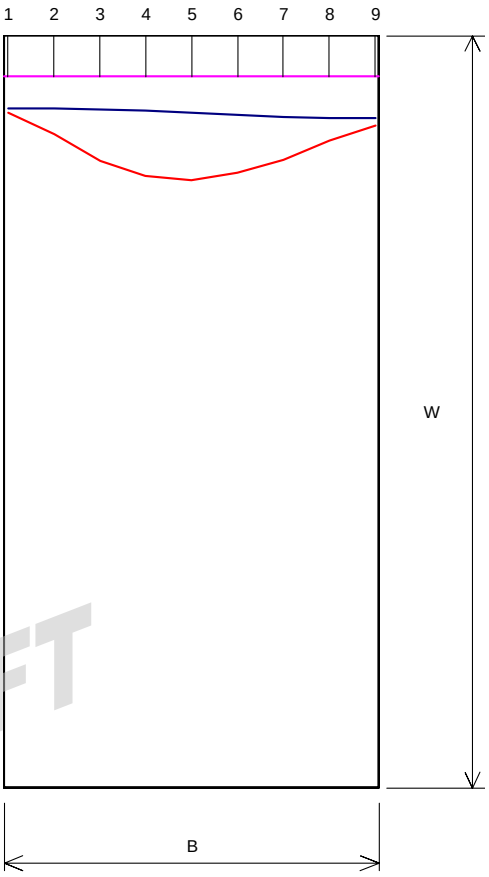

Comments

Measurement Line	Fatigue crack length a_0, mm	Slow stable crack extension + fatigue crack a_p, mm	Slow stable crack extension including stretch zone, Δ_a, mm
1	2.910	3.100	0.190
2	2.930	3.950	1.020
3	2.970	5.010	2.040
4	3.000	5.630	2.630
5	3.080	5.800	2.720
6	3.170	5.490	2.320
7	3.260	4.980	1.720
8	3.320	4.190	0.870
9	3.290	3.590	0.300
Weighted Average	**3.104**	**4.799**	**1.696**

Measured by: Jack Bradford **Signed:**

Appendix E : SENB TEST REPORTS

TWI FATIGUE PRE-CRACKING CHECK FOR SENB SPECIMENS TO ISO 12135:2016

SPECIMEN DETAILS		
Width, W	30.00	mm
Thickness, B	15.00	mm
Notch depth	1.63	mm
Desired a/W	0.10	
Est. surface a	2.93	mm
Est. a0	3.00	mm

FATIGUE DETAILS		
Fat. load, initial	21.00	kN
Fat. load, final	15.00	kN
Fat. span (400mm max)	120.0	mm
R ratio	0.1	

RESULTS		
a init / W	0.066	
Kq (relevant to K1c tests only)	3000.0	N/mm^1.5
K init	720.9	N/mm^1.5
Kf est. from desired a/W	618.5	N/mm^1.5
Kf est. from est. a0	618.5	N/mm^1.5

PROJECT NUMBER	SPECIMEN NO.	
33650	M02	01-06

MECHANICAL PROPERTIES	Measured or assumed, M / A		
:- At test temperature			
Yield strength, Sys	594.0	N/mm^2	A
Tensile strength, Sts	720.2	N/mm^2	A
Young's modulus, E	207000	N/mm^2	A
:- At fatigue temperature			
Yield strength, Sysp	479.0	N/mm^2	A
Tensile strength, Stsp	602.0	N/mm^2	A

CHECKS to ISO 12135:2016				
5.4.2.4.3 (1) and (2)	Limit Ff <	20.48	kN	
	Actual Ff	15.00	kN	Pass
6.2.4 (15)	If valid K1C test, limit Ff <	35.20	kN	K1c only
	Actual Ff	15.00	kN	N/A

Form compiled by : Jack Bradford Signature : _____

Date : 28/07/2022

YFUNa init	0.705
YFUNad	0.847
YFUNa0	0.847

UKAS TESTING
0088

TWI

SENB FRACTURE TEST 33650 M02-01

Client	PhD	
Project leader	Yin Jin Janin	Signed:

Data source

Data logging program	LVGENLOG V 1.55.10 02-Aug-2022
Program used to calculate CTOD/J	LVGENPLOT V 1.65.6 10-Aug-2022
Calculation date of CTOD/J	28 Sep 2022

Specimen details

Material	API 5L X65	
Specimen type	Subsize, SENB	
Crack plane orientation	Y-X	
Type of notch tip	Fatigue	
Notch tip location	Parent material	
Specimen width	30.010	mm
Specimen thickness	14.990	mm
Initial crack length	3.180	mm
Side-grooved?	NO	
Original PM 1 thickness	23.80	mm

Test details

Test standard(s)	BS ISO 12135:2021	
Test date	09/08/2022	
Test time	10:05:00	
Test technician	Jack Bradford	Signed:
Test machine	INSTRON 8500 B107	
Test environment	Environmental chamber	
Test temperature	-120.0	°C
Soak time @ test temperature	15.0	minutes
Knife edge heights	2.500, 12.500	mm
Knife edge attachment spacing	2.00	mm
Initial K-rate	0.759	$MPa.m^{0.5}/s$
Crosshead displacement rate	0.500	mm/min
Loading span	120.0	mm
Double roller diameter	18.00	mm
Single roller diameter	18.00	mm

Material properties

Yield strength for pre-cracking	445.5	MPa	Measured at RT
Tensile strength for pre-cracking	579.0	MPa	Measured at RT
Yield strength for testing	593.0	MPa	Measured at test temperature
Tensile strength for testing	746.0	MPa	Measured at test temperature
Poisson's ratio	0.3		Assumed
Young's modulus	213	GPa	Measured

Fatigue details

Stress ratio, R	0.100	
Final force, F_f	15.00	kN
Final K	20.1	$MPa.m^{0.5}$
Fatigue temperature	21.0	°C
Loading span, S	120.0	mm

Analysis details

LLD type	DOUBLE CLIP
CMOD type	DOUBLE CLIP
J calculated from	LLD
CTOD calculated from	CMOD
K_Q point from Load vs	SINGLE CLIP (LOWER)

Compiled by: Jack Bradford **Signed:**

Result relates only to specimen tested.

Tensile properties are not determined as part of this test and are not part of the accredited result.

Result falls within the bounds of TWI's flexible scope of accreditation.

SENB FRACTURE TEST 33650 M02-01

Qualification checks

		Value	Allowed
BS ISO 12135:2021 Fig 8			
Knife edge attachment spacing	**Pass**	2	15.005
BS ISO 12135:2021 5.4.2.4.1			
Fatigue stress ratio <= 0.1	**Pass**	0.1	0.1
BS ISO 12135:2021 5.4.2.4.3			
Final precracking force <= F_f	**Pass**	15	19.13759
BS ISO 12135:2021 5.6.4			
Single roller diameter	**Pass**	18	Min. 15.0
Double roller diameter	**Pass**	18	15.0 - 30.0
BS ISO 12135:2021 5.7.1.1			
Loading span	**Pass**	120	118.839600 - 121.240400
BS ISO 12135:2021 5.7.5			
Initial K-rate between 0.2 MPa.$m^{0.5}s^{-1}$ and 3.0 MPa.m$^{($	**Pass**	0.758937	0.2 - 3
BS ISO 12135:2021 5.8.2			
a_0/W check (a)	**Fail**	0.105965	0.45 - 0.7
Fatigue crack shape (b)	**Pass**	0.13	0.318
Minimum fatigue length (c)	**Fail**	0.98	1.3
Fatigue crack within envelope (d)	**Pass**		
BS ISO 12135:2021 5.8.3			
Final crack shape	**Pass**	0.205625	0.352438

UKAS TESTING
0088

TWI

SENB FRACTURE TEST 33650 M02-01

Test date	09/08/2022
Technician	Jack Bradford
Test machine	INSTRON 8500 B107
Control mode	Displacement

Client	PhD
Project leader	Yin Jin Janin
Investigator's signature	
Compiled by	Jack Bradford

SPECIMEN DETAILS

Force, F	82.85	kN
Width, W	30.010	mm
Thickness, B	14.990	mm
Crack length, a_0	3.180	mm
Loading span, S	120.0	mm
Yield strength	593.0	MPa
Young's modulus	213	GPa
Poisson's ratio	0.300	
Test temperature	-120.0	°C

RESULTS

δ_0	0.803	mm
Elastic K @ calculation point	110.8	MPa.m$^{0.5}$
F_{max}/F_Q	2.55	
K_Q	43.47	MPa.m$^{0.5}$
Total area under F vs LLD	145.69	kNmm
J_0	674.93	kJ/m²
Plastic area under F vs LLD	131.76	kNmm
Type of result	δ/J_c	
Test standard(s)	BS ISO 12135:2021	
Result qualified to standard(s)	NO	

LOWER CLIP GAUGE VALUES

Knife edge height	2.50	mm
Vg	1.191	mm
Vp	1.086	mm

UPPER CLIP GAUGE VALUES

Knife edge height	12.50	mm
Vg	1.883	mm
Vp	1.666	mm

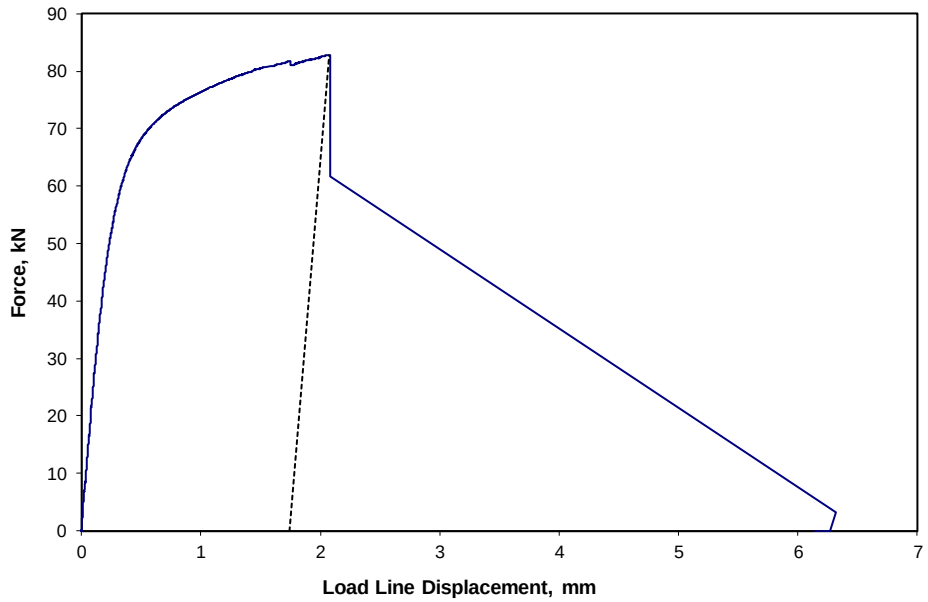

SENB FRACTURE TEST 33650 M02-01

Specimen width, W	30.010	mm
Specimen thickness, B	14.990	mm
Machined notch depth, M	1.640	mm
Machined notch width, h	0.360	mm
Surface crack length, a_{S1}	2.930	mm
Surface crack length, a_{S2}	2.800	mm
a_{max}	3.310	mm
a_{min}	2.620	mm

Comments

Diagram of fracture face

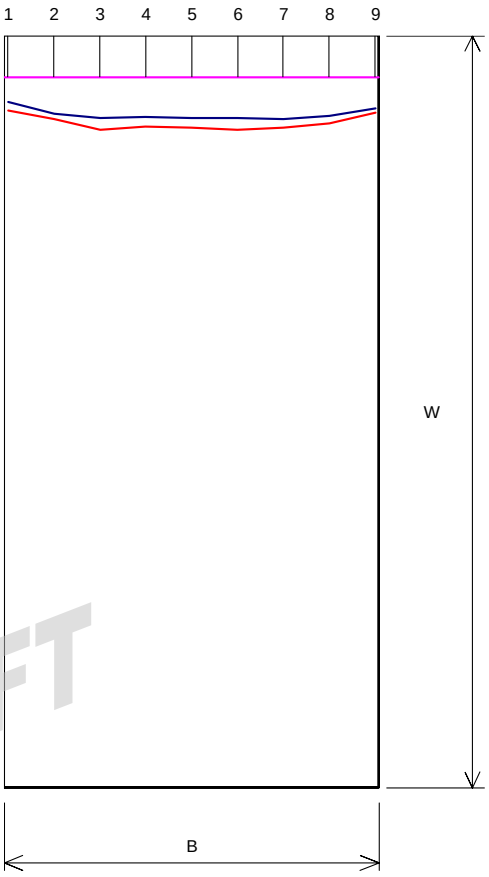

Measurement Line	Fatigue crack length a_0, mm	Slow stable crack extension + fatigue crack a_p, mm	Slow stable crack extension including stretch zone, Δ_a, mm
1	2.620	2.960	0.340
2	3.130	3.320	0.190
3	3.270	3.730	0.460
4	3.240	3.610	0.370
5	3.270	3.660	0.390
6	3.280	3.730	0.450
7	3.310	3.650	0.340
8	3.190	3.480	0.290
9	2.880	3.070	0.190
Weighted Average	**3.180**	**3.524**	**0.344**

Measured by: Jack Bradford **Signed:**

SENB FRACTURE TEST 33650 M02-04

Client	PhD	
Project leader	Yin Jin Janin	Signed:

Data source

Data logging program	LVGENLOG V 1.55.10 02-Aug-2022
Program used to calculate CTOD/J	LVGENPLOT V 1.65.6 10-Aug-2022
Calculation date of CTOD/J	28 Sep 2022

Specimen details

Material	API 5L X65	
Specimen type	Subsize, SENB	
Crack plane orientation	Y-X	
Type of notch tip	Fatigue	
Notch tip location	Parent material	
Specimen width	30.000	mm
Specimen thickness	14.990	mm
Initial crack length	3.376	mm
Side-grooved?	NO	
Original PM 1 thickness	23.80	mm

Test details

Test standard(s)	BS ISO 12135:2021	
Test date	08/08/2022	
Test time	10:47:00	
Test technician	Jack Bradford	Signed:
Test machine	INSTRON 8500 B107	
Test environment	Air	
Test temperature	24.0	°C
Soak time @ test temperature	0.0	minutes
Knife edge heights	2.500, 12.500	mm
Knife edge attachment spacing	2.00	mm
Initial K-rate	0.765	MPa.m$^{0.5}$/s
Crosshead displacement rate	0.501	mm/min
Loading span	120.0	mm
Double roller diameter	18.00	mm
Single roller diameter	18.00	mm

Material properties

Yield strength for pre-cracking	445.5	MPa	Measured at RT
Tensile strength for pre-cracking	579.0	MPa	Measured at RT
Yield strength for testing	445.5	MPa	Measured at test temperature
Tensile strength for testing	579.0	MPa	Measured at test temperature
Poisson's ratio	0.3		Assumed
Young's modulus	207	GPa	Assumed

Fatigue details

Stress ratio, R	0.100	
Final force, F_f	15.00	kN
Final K	20.6	$MPa.m^{0.5}$
Fatigue temperature	21.0	°C
Loading span, S	120.0	mm

Analysis details

LLD type	DOUBLE CLIP
CMOD type	DOUBLE CLIP
J calculated from	LLD
CTOD calculated from	CMOD
K_Q point from Load vs	SINGLE CLIP (LOWER)

Compiled by: Jack Bradford **Signed:**

Result relates only to specimen tested.

Tensile properties are not determined as part of this test and are not part of the accredited result.

Result falls within the bounds of TWI's flexible scope of accreditation.

SENB FRACTURE TEST 33650 M02-04

Qualification checks		Value	Allowed
BS ISO 12135:2021 Fig 8			
Knife edge attachment spacing	**Pass**	2	15
BS ISO 12135:2021 5.4.2.4.1			
Fatigue stress ratio <= 0.1	**Pass**	0.1	0.1
BS ISO 12135:2021 5.4.2.4.3			
Final precracking force <= F_f	**Pass**	15	24.096062
BS ISO 12135:2021 5.6.4			
Single roller diameter	**Pass**	18	Min. 15.0
Double roller diameter	**Pass**	18	15.0 - 30.0
BS ISO 12135:2021 5.7.1.1			
Loading span	**Pass**	120	118.800000 - 121.200000
BS ISO 12135:2021 5.7.5			
Initial K-rate between 0.2 MPa.m$^{0.5}$s^{-1} and 3.0 MPa.m$^{0.5}$s^{-1}	**Pass**	0.764678	0.2 - 3
BS ISO 12135:2021 5.8.2			
a_o/W check (a)	**Fail**	0.112521	0.45 - 0.7
Fatigue crack shape (b)	**Pass**	0.045625	0.337562
Minimum fatigue length (c)	**Pass**	1.68	1.3
Fatigue crack within envelope (d)	**Pass**		
BS ISO 12135:2021 5.8.3			
Final crack shape	**Fail**	1.280625	0.596938

SENB FRACTURE TEST 33650 M02-04

Test date	08/08/2022	Client	PhD
Technician	Jack Bradford	Project leader	Yin Jin Janin
Test machine	INSTRON 8500 B107	Investigator's signature	
Control mode	Displacement	Compiled by	Jack Bradford

SPECIMEN DETAILS

Force, F	71.80	kN
Width, W	30.000	mm
Thickness, B	14.990	mm
Crack length, a_0	3.376	mm
Loading span, S	120.0	mm
Yield strength	445.5	MPa
Young's modulus	207	GPa
Poisson's ratio	0.300	
Test temperature	24.0	°C

RESULTS

δ_0	2.931	mm
Elastic K @ calculation point	98.7	MPa.m$^{0.5}$
F_{max}/F_Q	3.10	
K_Q	31.88	MPa.m$^{0.5}$
Total area under F vs LLD	314.43	kNmm
J_0	1496.64	kJ/m²
Plastic area under F vs LLD	305.38	kNmm
Type of result	δ/J_m	
Test standard(s)	BS ISO 12135:2021	
Result qualified to standard(s)	NO	

LOWER CLIP GAUGE VALUES

Knife edge height	2.50	mm
Vg	4.171	mm
Vp	4.062	mm

UPPER CLIP GAUGE VALUES

Knife edge height	12.50	mm
Vg	5.788	mm
Vp	5.596	mm

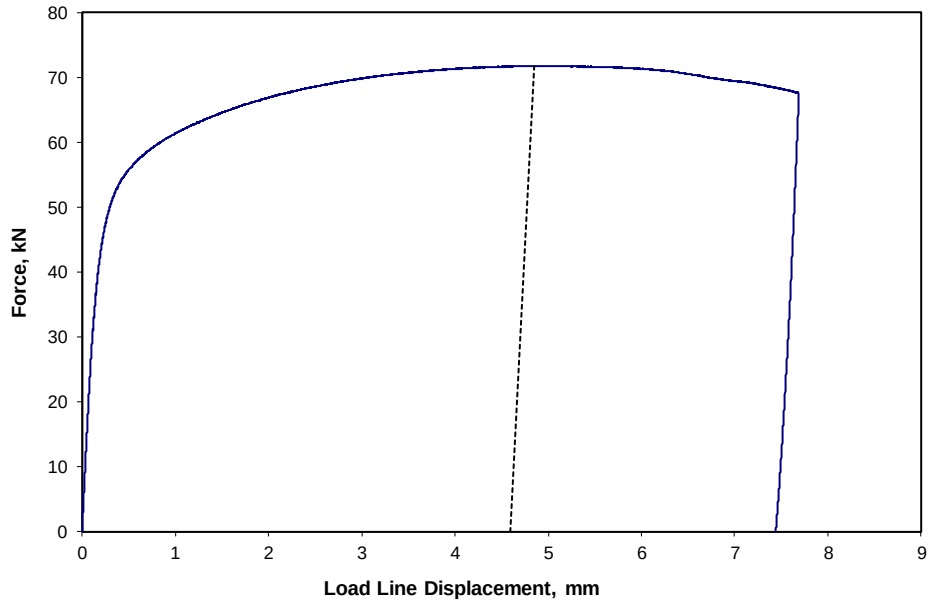

SENB FRACTURE TEST 33650 M02-04

Specimen width, W	30.000	mm
Specimen thickness, B	14.990	mm
Machined notch depth, M	1.650	mm
Machined notch width, h	0.350	mm
Surface crack length, a_{S1}	2.910	mm
Surface crack length, a_{S2}	2.760	mm
a_{max}	3.420	mm
a_{min}	3.330	mm

Comments

Diagram of fracture face

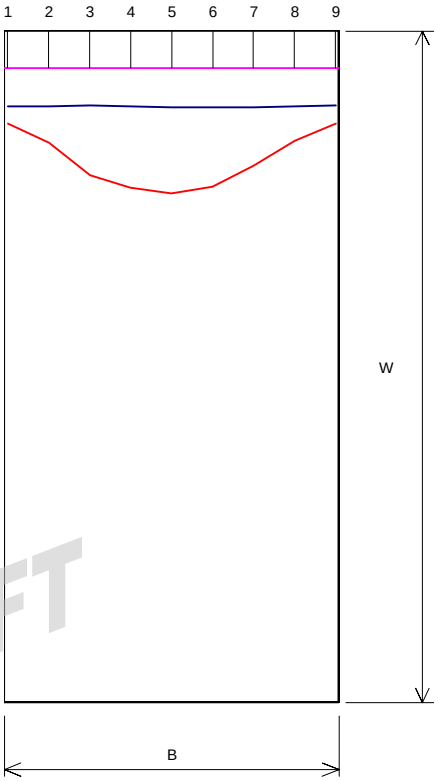

Measurement Line	Fatigue crack length a_o, mm	Slow stable crack extension + fatigue crack a_p, mm	Slow stable crack extension including stretch zone, Δ_a, mm
1	3.380	4.150	0.770
2	3.360	4.980	1.620
3	3.330	6.460	3.130
4	3.360	7.000	3.640
5	3.400	7.250	3.850
6	3.400	6.970	3.570
7	3.420	6.030	2.610
8	3.380	4.920	1.540
9	3.330	4.140	0.810
Weighted Average	**3.376**	**5.969**	**2.594**

Measured by: Jack Bradford **Signed:**

Appendix F : CRACKWISE FADs REPORTS

Project Information

Project Title	Constraint-Modified FADs SENB Roon Temperature
Project Leader	Paul Sukpe
Date	16 May 2023
Project Number	33650
Comments	

Problem Setup

Assessment Type	Fracture

Flaw details

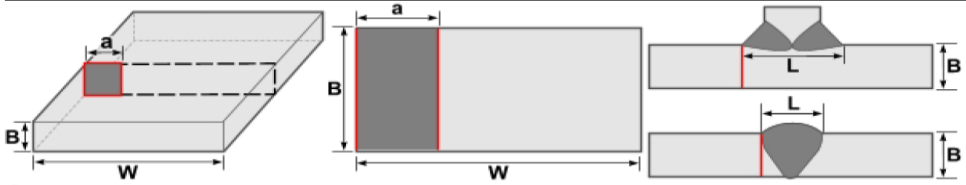

Geometry

Geometry	Flat Plate
Flaw	Edge
Stress intensity solution	M.3.2
Reference stress solution	P.4.2
Section thickness (B)	15 mm
Section width (W)	30 mm

Flaw

Flaw length (a)	15 mm

Tensile Properties

FAD	Option 1 (Tensile Properties)
Yield strength (Assessment temp)	446 MPa
Tensile strength (Assessment temp)	579 MPa
Youngs modulus, E	2.07E+05 MPa
Poisson's ratio	0.3
No yield discontinuity	

Toughness

Toughness Parameter	J
Toughness value	1293.1 kJ/m²

Primary Stresses

Membrane stress, Pm	0 MPa
Bending stress, Pb	603.47 MPa
Stress concentration factor, ktm	1
Stress concentration factor, ktb	1

Secondary Stresses

Condition	Known residual stresses
Plasticity Interaction Factor	ρ
Thermal membrane stress, Qtm	0 MPa
Thermal bending stress, Qtb	0 MPa
Membrane stress, Qm	0 MPa
Bending stress, Qb	0 MPa

TWI Software, Granta Park, Great Abington Cambridge, CB21 6AL, UK
Tel:+44(1223) 899000, Email: crackwise@twi.co.uk

Results

Fracture Results

Assessment result	Unacceptable
Lr	1.8041
Kr	0.6866
Qm used	0

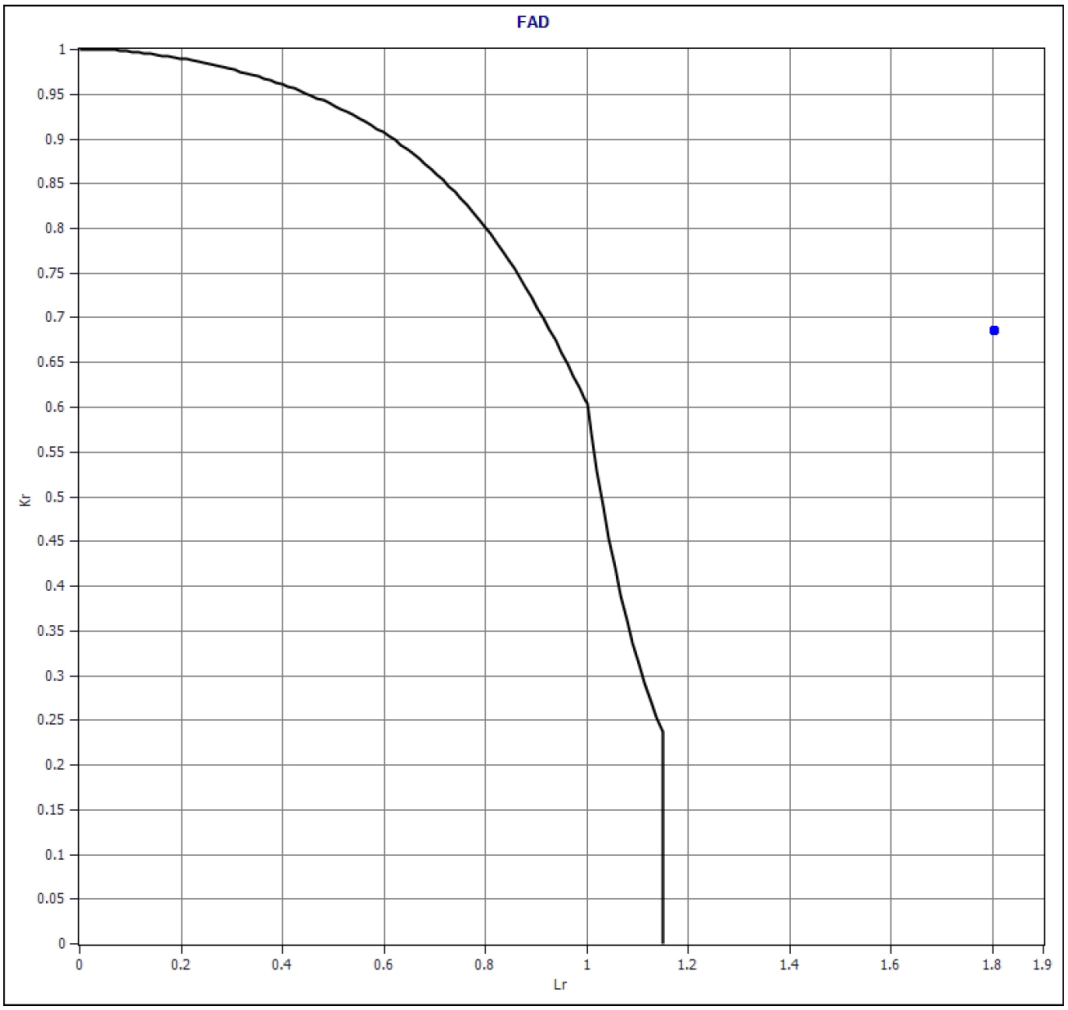

Project Information

Project Title	Constraint-Modified FADs SENB Roon Temperature
Project Leader	Paul Sukpe
Date	16 May 2023
Project Number	33650
Comments	

Problem Setup

Assessment Type	Fracture

Flaw details

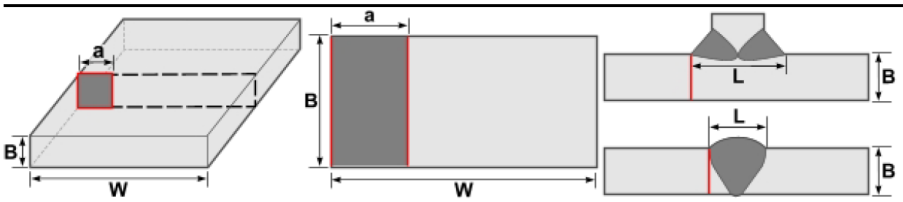

Geometry

Geometry	Flat Plate
Flaw	Edge
Stress intensity solution	M.3.2
Reference stress solution	P.4.2
Section thickness (B)	15 mm
Section width (W)	30 mm

Flaw

Flaw length (a)	3 mm

Tensile Properties

FAD	Option 1 (Tensile Properties)
Yield strength (Assessment temp)	446 MPa
Tensile strength (Assessment temp)	579 MPa
Youngs modulus, E	2.07E+05 MPa
Poisson's ratio	0.3
No yield discontinuity	

Constraint

α	6.907
β	-0.573
k	2.56

Toughness

Toughness Parameter	J
Toughness value	1496.6 kJ/m²

Primary Stresses

Membrane stress, Pm	0 MPa
Bending stress, Pb	1902.9 MPa
Stress concentration factor, ktm	1
Stress concentration factor, ktb	1

Secondary Stresses

Condition	Known residual stresses
Plasticity Interaction Factor	ρ
Thermal membrane stress, Qtm	0 MPa

TWI Software, Granta Park, Great Abington Cambridge, CB21 6AL, UK
Tel:+44(1223) 899000, Email: crackwise@twi.co.uk

Thermal bending stress, Qtb	0 MPa
Membrane stress, Qm	0 MPa
Bending stress, Qb	0 MPa

Results

Fracture Results

Assessment result	Unacceptable
Lr	3.1605
Kr	0.3750
Qm used	0

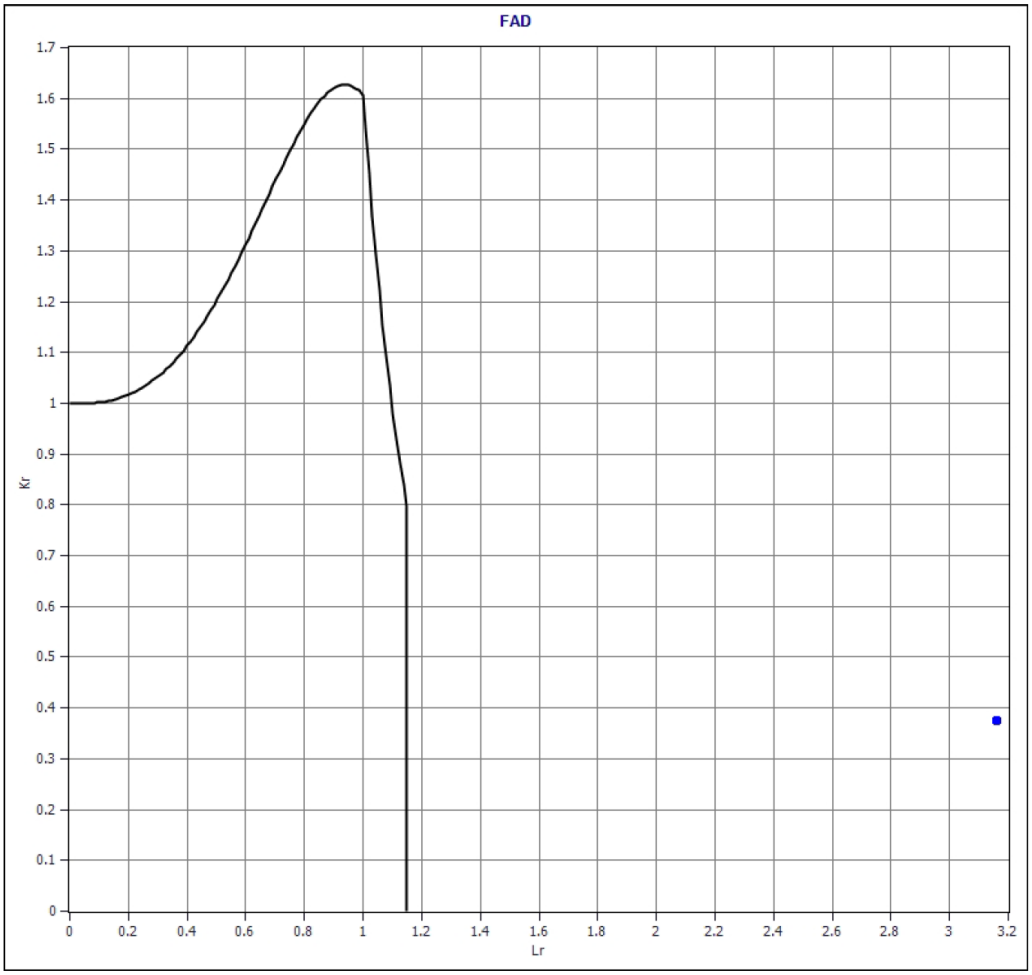

Project Information

Project Title	Constraint-Modified FADs SENB Low Temperature
Project Leader	Paul Sukpe
Date	16 May 2023
Project Number	33650
Comments	

Problem Setup

Assessment Type	Fracture

Flaw details

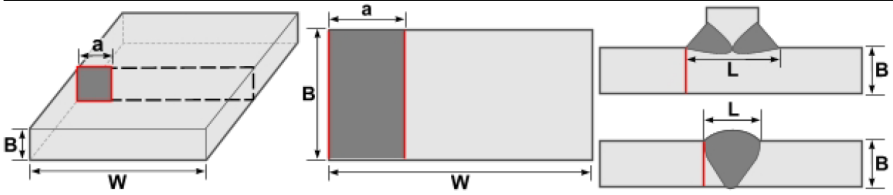

Geometry

Geometry	Flat Plate
Flaw	Edge
Stress intensity solution	M.3.2
Reference stress solution	P.4.2
Section thickness (B)	15 mm
Section width (W)	30 mm

Flaw

Flaw length (a)	3 mm

Tensile Properties

FAD	Option 1 (Tensile Properties)
Yield strength (Assessment temp)	593 MPa
Tensile strength (Assessment temp)	746 MPa
Youngs modulus, E	2.13E+05 MPa
Poisson's ratio	0.3
No yield discontinuity	

Constraint

α	6.821
β	-0.602
k	2.57

Toughness

Toughness Parameter	J
Toughness value	380.5 kJ/m²

Primary Stresses

Membrane stress, Pm	0 MPa
Bending stress, Pb	2209.3 MPa
Stress concentration factor, ktm	1
Stress concentration factor, ktb	1

Secondary Stresses

Condition	Known residual stresses
Plasticity Interaction Factor	ρ
Thermal membrane stress, Qtm	0 MPa

TWI Software, Granta Park, Great Abington Cambridge, CB21 6AL, UK
Tel:+44(1223) 899000, Email: crackwise@twi.co.uk

Thermal bending stress, Qtb	0 MPa
Membrane stress, Qm	0 MPa
Bending stress, Qb	0 MPa

Results

Fracture Results

Assessment result	Unacceptable
Lr	2.7598
Kr	0.8512
Qm used	0

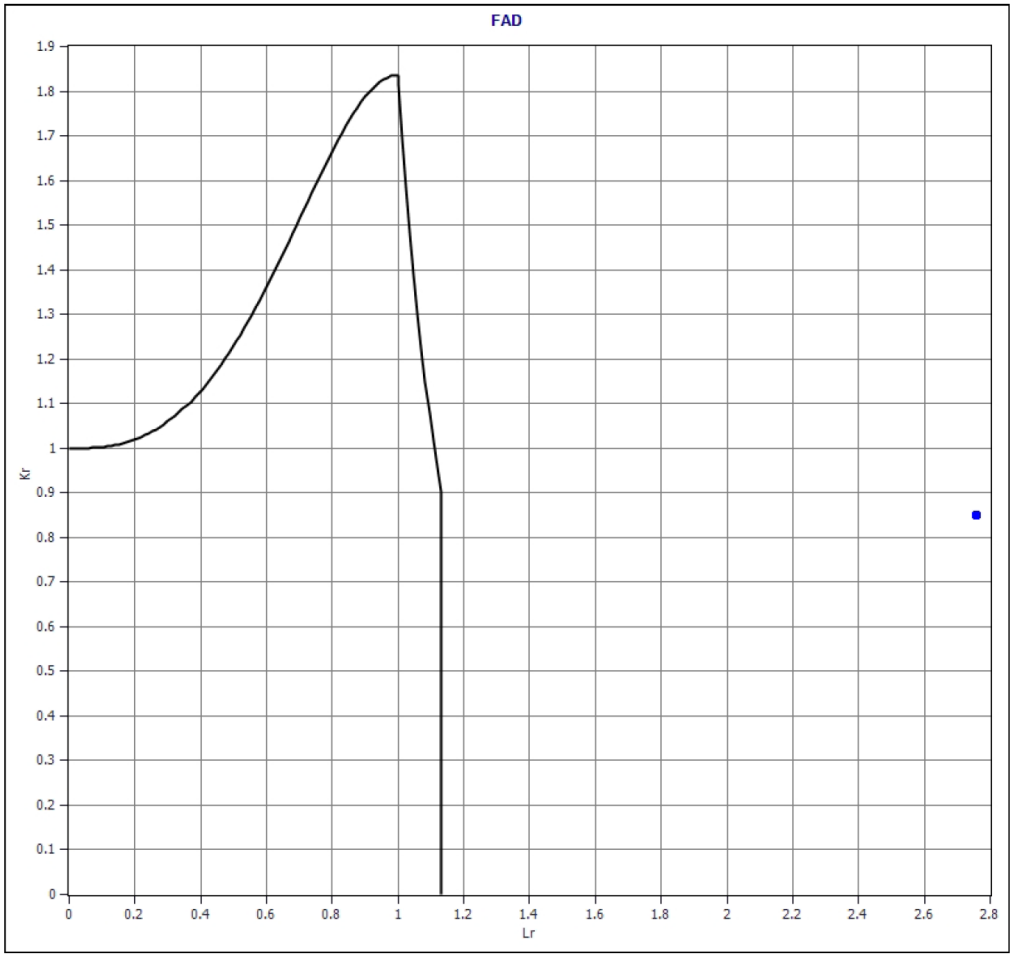

Project Information

Project Title	Constraint-Modified FADs SENT Room Temperature
Project Leader	Paul Sukpe
Date	16 May 2023
Project Number	33650
Comments	

Problem Setup

Assessment Type	Fracture

Flaw details

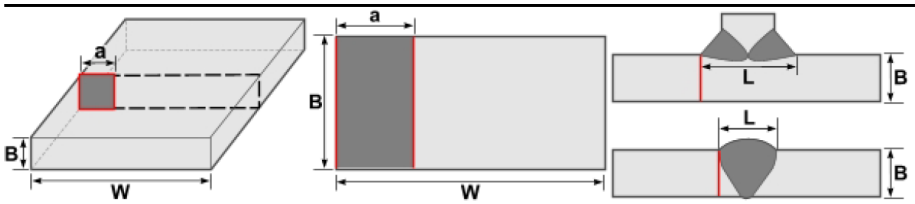

Geometry

Geometry	Flat Plate
Flaw	Edge
Stress intensity solution	M.3.2
Reference stress solution	P.4.2
Section thickness (B)	15 mm
Section width (W)	30 mm

Flaw

Flaw length (a)	15 mm

Tensile Properties

FAD	Option 1 (Tensile Properties)
Yield strength (Assessment temp)	446 MPa
Tensile strength (Assessment temp)	579 MPa
Youngs modulus, E	2.07E+05 MPa
Poisson's ratio	0.3
No yield discontinuity	

Toughness

Toughness Parameter	J
Toughness value	1865.6 kJ/m²

Primary Stresses

Membrane stress, Pm	296.89 MPa
Bending stress, Pb	0 MPa
Stress concentration factor, ktm	1
Stress concentration factor, ktb	1

Secondary Stresses

Condition	Known residual stresses
Plasticity Interaction Factor	ρ
Thermal membrane stress, Qtm	0 MPa
Thermal bending stress, Qtb	0 MPa
Membrane stress, Qm	0 MPa
Bending stress, Qb	0 MPa

TWI Software, Granta Park, Great Abington Cambridge, CB21 6AL, UK
Tel:+44(1223) 899000, Email: crackwise@twi.co.uk

Results

Fracture Results

Assessment result	Unacceptable
Lr	1.3313
Kr	0.2812
Qm used	0

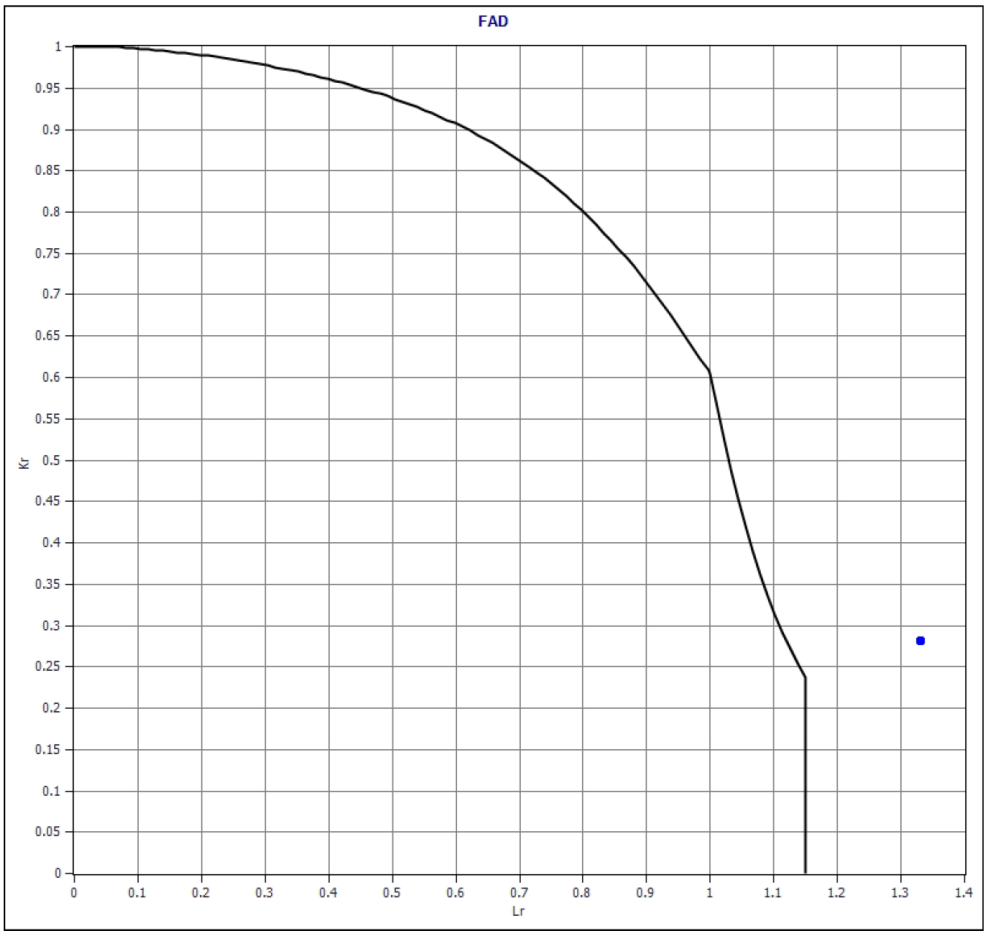

Project Information

Project Title	Constraint-Modified FADs SENT Room Temperature
Project Leader	Paul Sukpe
Date	16 May 2023
Project Number	33650
Comments	

Problem Setup

Assessment Type	Fracture

Flaw details

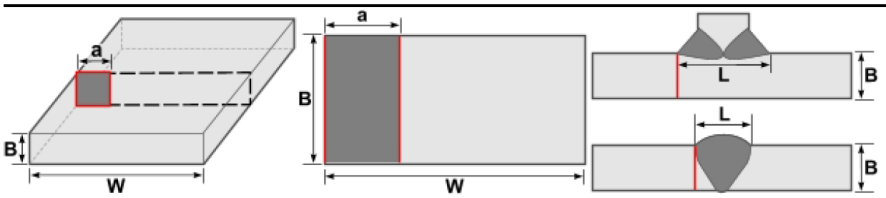

Geometry

Geometry	Flat Plate
Flaw	Edge
Stress intensity solution	M.3.2
Reference stress solution	P.4.2
Section thickness (B)	15 mm
Section width (W)	30 mm

Flaw

Flaw length (a)	3 mm

Tensile Properties

FAD	Option 1 (Tensile Properties)
Yield strength (Assessment temp)	446 MPa
Tensile strength (Assessment temp)	579 MPa
Youngs modulus, E	2.07E+05 MPa
Poisson's ratio	0.3
No yield discontinuity	

Constraint

α	6.907
β	-0.58
k	2.56

Toughness

Toughness Parameter	J
Toughness value	1344.9 kJ/m²

Primary Stresses

Membrane stress, Pm	538.57 MPa
Bending stress, Pb	0 MPa
Stress concentration factor, ktm	1
Stress concentration factor, ktb	1

Secondary Stresses

Condition	Known residual stresses
Plasticity Interaction Factor	ρ
Thermal membrane stress, Qtm	0 MPa

TWI Software, Granta Park, Great Abington Cambridge, CB21 6AL, UK
Tel:+44(1223) 899000, Email: crackwise@twi.co.uk

Thermal bending stress, Qtb	0 MPa
Membrane stress, Qm	0 MPa
Bending stress, Qb	0 MPa

Results

Fracture Results

Assessment result	Unacceptable
Lr	1.3417
Kr	0.1120
Qm used	0

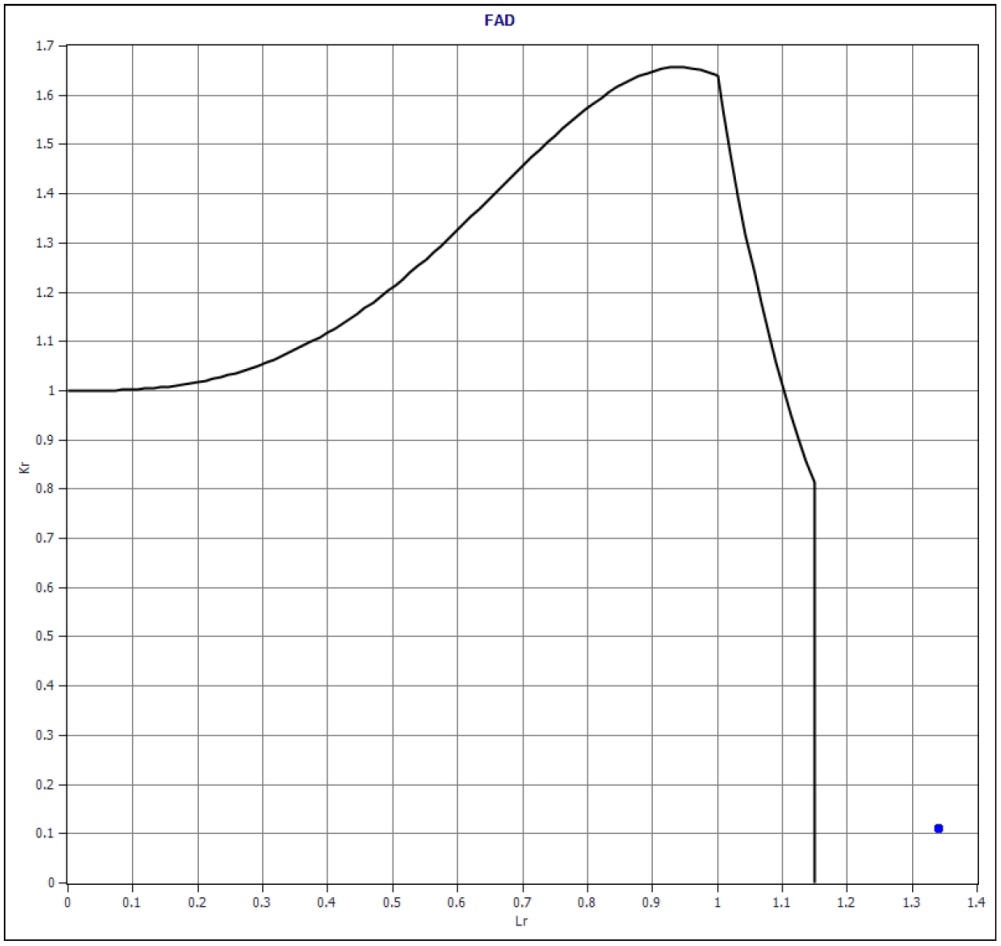

Project Information

Project Title	Constraint-Modified FADs SENT Low Temperature
Project Leader	Paul Sukpe
Date	16 May 2023
Project Number	33650
Comments	

Problem Setup

Assessment Type	Fracture

Flaw details

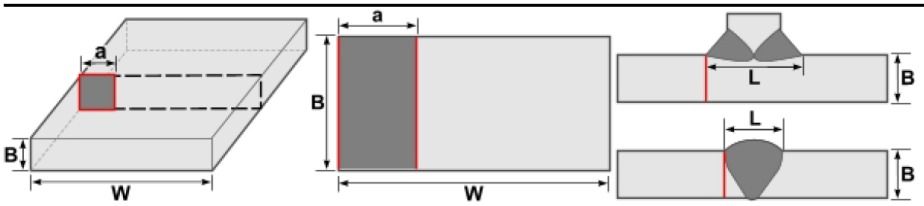

Geometry

Geometry	Flat Plate
Flaw	Edge
Stress intensity solution	M.3.2
Reference stress solution	P.4.2
Section thickness (B)	15 mm
Section width (W)	30 mm

Flaw

Flaw length (a)	3 mm

Tensile Properties

FAD	Option 1 (Tensile Properties)
Yield strength (Assessment temp)	593 MPa
Tensile strength (Assessment temp)	746 MPa
Youngs modulus, E	2.13E+05 MPa
Poisson's ratio	0.3
No yield discontinuity	

Constraint

α	6.821
β	-0.579
k	2.57

Toughness

Toughness Parameter	J
Toughness value	329.4 kJ/m²

Primary Stresses

Membrane stress, Pm	607.62 MPa
Bending stress, Pb	0 MPa
Stress concentration factor, ktm	1
Stress concentration factor, ktb	1

Secondary Stresses

Condition	Known residual stresses
Plasticity Interaction Factor	ρ
Thermal membrane stress, Qtm	0 MPa

TWI Software, Granta Park, Great Abington Cambridge, CB21 6AL, UK
Tel:+44(1223) 899000, Email: crackwise@twi.co.uk

Thermal bending stress, Qtb	0 MPa
Membrane stress, Qm	0 MPa
Bending stress, Qb	0 MPa

Results

Fracture Results

Assessment result	Unacceptable
Lr	1.1385
Kr	0.2516
Qm used	0

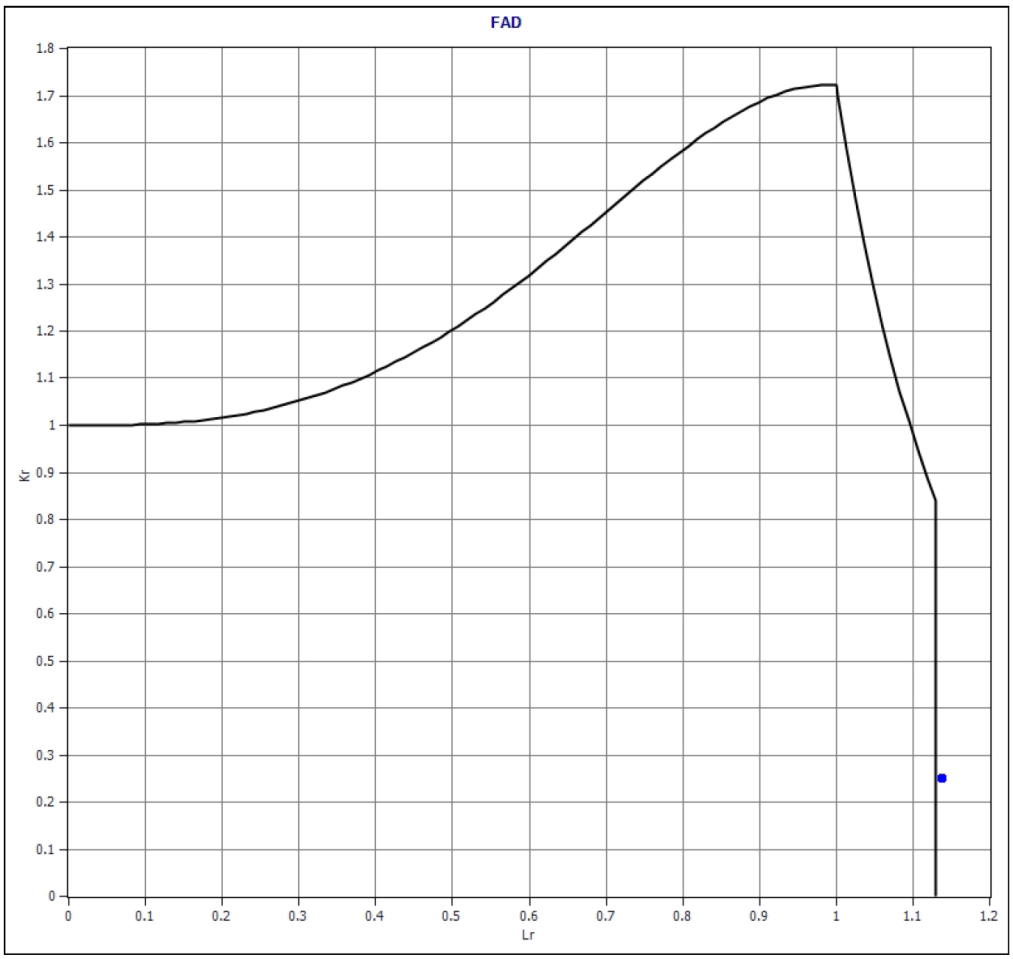

Appendix G : MATLAB CODE FOR TREATMENT OF DIC DATA

MAIN.m

```
% A code to prepare API 5L X65 displacement and strain data to be inputted to Abaqus. The data is
% inputted as received from the fracture tests (SENT/SENB)with DIC at room temperature.
close all;     restoredefaultpath; warning off;       addpath(genpath(pwd));
clc;clear;     set(0,'defaultAxesFontSize',20);       set(0,'DefaultLineMarkerSize',12)
DS = com.mathworks.mde.desk.MLDesktop.getInstance();  DS.closeGroup('Variables');

%% Setting the scene
Dir.fullpath     = 'D:\GOM DIC data\33650 M01 04\33650_M01_04_330'; % file Directory
Dir.fillname     = 'M01_04_330';       % DONT include extension,in .mat or .dat format
Dir.input_unit   = 'mm';        % meter (m) or milmeter (mm) or micrometer(um);
Operation        = 'DIC';       % calculation mode\n Str = Strain, DIC for Displacement
Dir.tri          = 1;

%% INPUT MATERIAL PROPERTIES AND DATA
% Poisson's ratio,          Young's Modulus [MPa],
  Dir.nu    = 0.3;          Dir.E  = 207000;                Dir.Mat = 'Ferrite';
  Dir.type  = 'E'; % 'E' for Elastic or 'R' for Ramberg-Osgood or 'A' for Elastic-Anisotropic
% if 'Ramberg-Osgood' type of material input               Yield Stress [Pa]
  Dir.Exponent = 26.67;     Dir.Yield_offset = 1.24;        Dir.yield = 4E9;
% if 'Elastic-Anisotropic' you need to define the stifness tensor Dir.Stifness

%% %%%%%%%%%%%%%%%%%%%%%%%%%%%%%%%% END of USER INTERFACE %%%%%%%%%%%%%%%%%%%%%%%%%%%%%%%%%%%%
%% Load, MESHING, Integration
if Operation ~= 'DIC'
    % loadUD output is in meter
    [mesh,Dir] = loadUd(Dir.input_unit,Dir.fullpath, Dir.fillname,Operation,Dir);
    if mesh.selct == 'F' || mesh.selct == 'f'
        [mat]      = matprop(Dir.E,Dir.nu,Dir.yield,Dir.stressstat,Dir.input_unit); % material props.
        [el,mesh]  = meshDIC(mesh); % create mesh for data
        %runs isoparametric FE analysis to solve for strain and stress at Gauss points
        [el]       = FEanalysisStrains(el,mat,mesh);
        % % STRAIN INTEGRATION, gl.dy & dx
        [~,~,gl]   = StrainInegration(mesh,el,Dir); % STRAIN INTEGRATION, gl.dy & dx
        % Debugged(gl,Dir); %% debug
        alldata   = [gl.Ux(:) gl.Uy(:) gl.dx(:) gl.dy(:)];    % all in input units
    else
        alldata = [Maps.X1(:), Maps.Y1(:),Maps.Ux(:),Maps.Uy(:)];
    end
else
    Dir.results = [Dir.fullpath '\' Dir.fillname];
    alldata = 0;
end
if Dir.tri ~=1; Dir.results = [Dir.results '.' num2str(Dir.tri)]; end

%% Locate crack and prepare python code :: CROP AND DATA FOR ABAQUS
[DATA,Dir.results,UnitOffset] = Locate_Crack(alldata,Dir.results,Operation,Dir);
fprintf('\nDone, For  results and python code Check %s \n',Dir.results); close all

%% Once Abaqus analysis are done
% PlotKorJ(Dir.fullpath,Dir.E,UnitOffset)
```

Appendix H : PYTHON SCRIPTS FOR FINITE ELEMENT POST-PROCESSING

```python
"""
This script performs post-processing to the SENB model:
1. Extract J-integral
2. Extract normalised crack opening stress (S11) at a specified distance from the crack tip
3. Write above data to a text file
"""
# Import necessary modules
from abaqus import *
from odbAccess import *
from abaqusConstants import *
import visualization
import xyPlot
import displayGroupOdbToolset as dgo
import numpy as np
import os

sy = 593      # Yield strength, MPa
odbName = 'SENT_Cold_aW01'      # Name of odb file
stepName = 'Step-1'                          # Name of load step

# 1. Open odb file and Abaqus viewer session
myOdb = session.openOdb(odbName + '.odb')
session.viewports['Viewport: 1'].setValues(displayedObject=myOdb)
myFrame = myOdb.steps[stepName].frames

# 2. Extract J values for each time increment
region = myOdb.steps[stepName].historyRegions['ElementSet  ALL ELEMENTS']
contourNum = 22

if contourNum < 10:
    contour_num_str = 'Contour_0' + str(contourNum)
else:
    contour_num_str = 'Contour_' + str(contourNum)

J_keys = []
for key in region.historyOutputs.keys():
    if 'J at ' and 'Contour_' + str(contourNum) in key:
        J_keys.append(key)

JData = region.historyOutputs[J_keys[0]].data

J_list = []                    # Create an empty list for containing J values
for J in JData:                # Add J value for each time increment to the list created
    J_list.append(J[1])
```

```python

# 3. Extract S11 along the path starting from the crack tip
# 3.1 Create a path starting with crack tip node and ending with a node far
#     enough from crack tip
node1_ID = 22             # Crack tip node
node2_ID = 18          # Node away from crack tip
session.Path(name='Path-1', type=NODE_LIST, expression=(('SENB_B15MM-1', (node1_ID,
    node2_ID, )), ))
pth = session.paths['Path-1']

# In the SENB model, the crack opening stress is s11. Make sure you
# pick the crack opening stress in the model.
result_File = open(odbName+'_S11.txt', 'w')
result_File.write('J-integral'.rjust(10) + 'S11'.rjust(30) +'\n')
for i in range(1,len(myFrame)):
    session.viewports['Viewport: 1'].odbDisplay.setFrame(step=0, frame=i)
    session.viewports['Viewport: 1'].odbDisplay.setPrimaryVariable(
        variableLabel='S', outputPosition=INTEGRATION_POINT, refinement=(
        COMPONENT, 'S11'),)
    xy1 = xyPlot.XYDataFromPath(path=pth, includeIntersections=True,
        projectOntoMesh=False, pathStyle=PATH_POINTS, numIntervals=10,
        projectionTolerance=0, shape=UNDEFORMED, labelType=TRUE_DISTANCE_Y)
    S11_list = []               # Create an empty list for containing S11
    norm_S11_list = []          # Create an empty list for containing normalised S11
    distance_list = []          # Create an empty list for containing the distance from the crack tip
    norm_distance_list = []     # Create an empty list for containing the normalised distance from the crack tip
    for xy in xy1:
        S11_list.append(xy[1])        # Add s11 from each node along the path to the s11 list
        distance_list.append(xy[0])   # Add distance from each node along the path to the distance list
    for S11 in S11_list:
        norm_S11_list.append(S11/sy)  # Add normalised s11 from each node along the path to the normalised s11 list
    for distance in distance_list:
        norm_distance_list.append(distance*sy/J_list[i-1])     # Add normalised distance from each node along the path to the normalised distance list
    # Perform linear interpolation to calculate the normalised s11 at the required distance
    S11_extracted = np.interp(2.0, norm_distance_list, norm_S11_list)
    # Write J and normalised S11 at x*sy/J=2.0 to the text file created
    result_File.write(str(J_list[i-1]).rjust(10) + str(S11_extracted).rjust(30) +'\n')
result_File.close()
```

```python
"""
This script performs post-processing to the SENT model:
1. Extract J-integral
2. Extract normalised crack opening stress (S11) at a specified distance from the crack tip
3. Write above data to a text file
"""
# Import necessary modules
from abaqus import *
from odbAccess import *
from abaqusConstants import *
import visualization
import xyPlot
import displayGroupOdbToolset as dgo
import numpy as np
import os

sy = 593     # Yield strength, MPa
odbName = 'SENT_Cold_aW05'     # Name of odb file
stepName = 'Step-1'                          # Name of load step

# 1. Open odb file and Abaqus viewer session
myOdb = session.openOdb(odbName + '.odb')
session.viewports['Viewport: 1'].setValues(displayedObject=myOdb)
myFrame = myOdb.steps[stepName].frames

# 2. Extract J values for each time increment
region = myOdb.steps[stepName].historyRegions['ElementSet  ALL ELEMENTS']
contourNum = 22

if contourNum < 10:
    contour_num_str = 'Contour_0' + str(contourNum)
else:
    contour_num_str = 'Contour_' + str(contourNum)

J_keys = []
for key in region.historyOutputs.keys():
    if 'J at ' and 'Contour_' + str(contourNum) in key:
        J_keys.append(key)

JData = region.historyOutputs[J_keys[0]].data

J_list = []                    # Create an empty list for containing J values
for J in JData:                # Add J value for each time increment to the list created
    J_list.append(J[1])
```

```python
# 3. Extract S22 along the path starting from the crack tip
# 3.1 Create a path starting with crack tip node and ending with a node far
#     enough from crack tip
node1_ID = 33            # Crack tip node
node2_ID = 22          # Node away from crack tip
session.Path(name='Path-1', type=NODE_LIST, expression=(('PART-1-1', (node1_ID,
    node2_ID, )), ))
pth = session.paths['Path-1']

# In the SENT model, the crack opening stress is s11. Make sure you
# pick the crack opening stress in your model.
result_File = open(odbName+'_S11.txt', 'w')
result_File.write('J-integral'.rjust(10) + 'S11'.rjust(30) +'\n')
for i in range(1,len(myFrame)):
    session.viewports['Viewport: 1'].odbDisplay.setFrame(step=0, frame=i)
    session.viewports['Viewport: 1'].odbDisplay.setPrimaryVariable(
        variableLabel='S', outputPosition=INTEGRATION_POINT, refinement=(
        COMPONENT, 'S11'),)
    xy1 = xyPlot.XYDataFromPath(path=pth, includeIntersections=True,
        projectOntoMesh=False, pathStyle=PATH_POINTS, numIntervals=10,
        projectionTolerance=0, shape=UNDEFORMED, labelType=TRUE_DISTANCE_Y)
    S11_list = []              # Create an empty list for containing S11
    norm_S11_list = []         # Create an empty list for containing normalised S11
    distance_list = []         # Create an empty list for containing the distance from the crack tip
    norm_distance_list = []    # Create an empty list for containing the normalised distance from the crack tip
    for xy in xy1:
        S11_list.append(xy[1])        # Add s11 from each node along the path to the s11 list
        distance_list.append(xy[0])   # Add distance from each node along the path to the distance list
    for S11 in S11_list:
        norm_S11_list.append(S11/sy)  # Add normalised s11 from each node along the path to the normalised s11 list
    for distance in distance_list:
        norm_distance_list.append(distance*sy/J_list[i-1])     # Add normalised distance from each node along the path to the normalised distance list
    # Perform linear interpolation to calculate the normalised s11 at the required distance
    S11_extracted = np.interp(2.0, norm_distance_list, norm_S11_list)
    # Write J and normalised S11 at x*sy/J=2.0 to the text file created
    result_File.write(str(J_list[i-1]).rjust(10) + str(S11_extracted).rjust(30) +'\n')
result_File.close()
```

```python
"""
This script performs post-processing to the pipe model:
1. Extract J-integral
2. Extract normalised crack opening stress (S11) at a specified distance from the crack tip
3. Write above data to a text file
"""
# Import necessary modules
from abaqus import *
from odbAccess import *
from abaqusConstants import *
import visualization
import xyPlot
import displayGroupOdbToolset as dgo
import numpy as np
import os

sy = 446     # Yield strength, MPa
odbName = 'Pressure_Bending_a_6_0'     # Name of odb file
stepName = 'Step-1'           # Name of load step
stepName = 'Step-Bending'           # Name of load step

# 1. Open odb file and Abaqus viewer session
myOdb = session.openOdb(odbName + '.odb')
session.viewports['Viewport: 1'].setValues(displayedObject=myOdb)
myFrame = myOdb.steps[stepName].frames

# 2. Extract J values for each time increment
region = myOdb.steps[stepName].historyRegions['ElementSet  ALL ELEMENTS']
contourNum = 10

if contourNum < 10:
    contour_num_str = 'Contour_0' + str(contourNum)
else:
    contour_num_str = 'Contour_' + str(contourNum)

J_keys = []
for key in region.historyOutputs.keys():
    if 'J at ' and 'Contour_' + str(contourNum) in key:
        J_keys.append(key)

JData = region.historyOutputs[J_keys[0]].data

#JOutput = 'J_' + odbName + '.txt'
#JFile = open(JOutput + '.txt', 'w')
#JFile.write('Time'.rjust(20) + 'J-integral'.rjust(20) + '\n')
J_list = []                # Create an empty list for containing J values


# 3. Extract opening stress along the path starting from the crack tip
# 3.1 Create a path starting with crack tip node and ending with a node far
#     enough from crack tip
node1_ID = 56            # Crack tip node
node2_ID = 52         # Node away from crack tip
session.Path(name='Path-1', type=NODE_LIST, expression=(('PART-1-1', (node1_ID,
    node2_ID, )), ))
pth = session.paths['Path-1']

# In my pipe model, the crack opening stress happens to be s11. Make sure you
# pick the crack opening stress in your model.
result_File = open(odbName+'_S11.txt', 'w')
result_File.write('J-integral'.rjust(10) + 'S11'.rjust(30) +'\n')
for i in range(1,len(myFrame)):
    session.viewports['Viewport: 1'].odbDisplay.setFrame(step=0, frame=i)
    session.viewports['Viewport: 1'].odbDisplay.setPrimaryVariable(
        variableLabel='S', outputPosition=INTEGRATION_POINT, refinement=(
        COMPONENT, 'S11'),)
    xy1 = xyPlot.XYDataFromPath(path=pth, includeIntersections=True,
        projectOntoMesh=False, pathStyle=PATH_POINTS, numIntervals=10,
        projectionTolerance=0, shape=UNDEFORMED, labelType=TRUE_DISTANCE_Y)
    S11_list = []               # Create an empty list for containing S11
    norm_S11_list = []          # Create an empty list for containing normalised S11
    distance_list = []          # Create an empty list for containing the distance from the crack tip
    norm_distance_list = []     # Create an empty list for containing the normalised distance from the crack tip
    for xy in xy1:
        S11_list.append(xy[1])        # Add s11 from each node along the path to the s11 list
        distance_list.append(xy[0])   # Add distance from each node along the path to the distance list
    for S11 in S11_list:
        norm_S11_list.append(S11/sy)  # Add normalised s11 from each node along the path to the normalised s11 list
    for distance in distance_list:
        norm_distance_list.append(distance*sy/J_list[i-1])     # Add normalised distance from each node along the path to the normalised distance list
    # Perform linear interpolation to calculate the normalised s11 at the required distance
    S11_extracted = np.interp(2.0, norm_distance_list, norm_S11_list)
    # Write J and normalised S11 at x*sy/J=2.0 to the text file created
    result_File.write(str(J_list[i-1]).rjust(10) + str(S11_extracted).rjust(30) +'\n')
result_File.close()
```

The bending moment of the pipe with diameter, D_o= 1219 mm, thickness, t = 15 mm, length, L=1500 mm and internal pressure of 2 MPa used in chapter 4 is calculated as: Calculate the hoop stress in the pipe caused by the applied pressure σ = (P x r)/ t

where:

σ is the hoop stress in the pipe
P is the applied internal pressure
r is the radius of the pipe (1219 mm / 2 = 609.5 mm)
t is the thickness of the pipe (15 mm)

Substituting the values: σ = (2 x 609.5) / 15 = 81.27 MPa

Calculate the moment of inertia of the pipe cross-section: $I = (\pi/64) \times (D_o^4 - (D_o - 2t)^4)$

Substituting the values: $I = (\pi/64) \times (1219^4 - (1219 - 2x15)^4) = 1.0261 \times 10^{10}$ mm^4

Calculate the distance from the neutral axis of the pipe to the point where the bending moment is being measured. For a pipe with a circular cross-section, this distance is equal to half of the diameter: $y = D_o/2 = 1219/2 = 609.5$ mm

Calculate the bending moment: M = (σ x I) / y

Substituting the values: $M = (81.27 \times 1.025 \times 10^{10}) / 609.5 = 1.368 \times 10^9$ N-mm or 1.368 MN-m

Therefore, the bending moment of the pipe with diameter 1219 mm and thickness 15 mm, length of 1500 mm, and an applied pressure of 2 MPa is approximately 1.368 MN-m

Appendix I : MATERIAL PROPERTY USED IN FEA

Cold		Room	
true plastic stress [MPa]	true plastic strain [%]	true plastic stress [MPa]	true plastic strain [%]
627.28	0.0000	444.97	0.0000
628.12	0.0018	450.22	0.0065
629.17	0.0019	451.96	0.0066
630.56	0.0019	454.50	0.0067
638.39	0.0023	460.60	0.0070
639.11	0.0023	463.64	0.0072
641.25	0.0025	468.02	0.0073
643.86	0.0027	469.93	0.0076
647.62	0.0030	473.70	0.0079
650.06	0.0032	476.58	0.0099
653.38	0.0037	484.84	0.0119
653.68	0.0038	491.79	0.0136
654.18	0.0038	498.10	0.0153
655.40	0.0040	505.36	0.0163
658.94	0.0044	512.07	0.0175
662.35	0.0050	519.83	0.0195
665.72	0.0058	526.15	0.0210
672.07	0.0075	531.72	0.0223
677.35	0.0094	537.83	0.0233
677.49	0.0095	543.53	0.0259
677.52	0.0095	547.84	0.0271
681.19	0.0107	553.18	0.0301
685.85	0.0128	557.78	0.0317
688.33	0.0136	561.41	0.0327
692.83	0.0161	566.68	0.0366
692.84	0.0162	569.76	0.0388
693.05	0.0162	572.05	0.0407
693.27	0.0163	575.04	0.0427
693.28	0.0163	576.43	0.0441
693.38	0.0164	579.10	0.0457
699.06	0.0190	584.34	0.0488
700.41	0.0197	590.12	0.0521
703.24	0.0205	597.03	0.0569
706.52	0.0224	606.25	0.0641
710.97	0.0245	609.52	0.0681
715.49	0.0265	616.16	0.0730
720.19	0.0289	622.54	0.0791
723.92	0.0309	632.05	0.0906
728.42	0.0327	637.05	0.0963
729.38	0.0334	644.42	0.1085
731.64	0.0346		
733.16	0.0351		
736.88	0.0377		
738.58	0.0385		
741.98	0.0404		
744.99	0.0415		
747.28	0.0434		
748.83	0.0439		
754.89	0.0476		
759.82	0.0505		
763.35	0.0527		
766.18	0.0548		
778.13	0.0623		
788.25	0.0702		
790.32	0.0719		
790.60	0.0720		
797.78	0.0764		
811.10	0.0893		
819.03	0.0958		
819.44	0.0959		
828.02	0.1047		
828.62	0.1051		
835.30	0.1118		
835.95	0.1119		

This page intentionally left blank

This page intentionally left blank